

**Porous two-dimensional materials (MXenes) for high capacity  
energy storage**

Submitted by Philip Adam Maughan, MChem

For the degree of Doctor of Philosophy

Lancaster University

September 2019



# **Porous two-dimensional materials (MXenes) for high capacity energy storage**

Submitted by Philip Adam Maughan, MChem

For the degree of Doctor of Philosophy

Lancaster University

September 2019

## **Abstract**

Energy storage is becoming a key challenge of the 21<sup>st</sup> century as the global energy system transitions away from the use of fossil fuels, which have been linked to damaging climate change and increasing air pollution. Electrochemical energy storage devices, such as batteries and supercapacitors, offer great potential to enable the clean energy transition, but require significant improvements to their performance characteristics such as energy density, power density and lifetime. The design and study of new electrode materials is key to achieving these improvements. MXenes are a new class of two-dimensional transition metal carbides and nitrides which have shown early promise in the field of electrochemical energy storage. Particularly interesting is the discovery of pseudocapacitive intercalation as their charge storage mechanism, since this could enable high power and energy densities with long cycling lifetimes into one device. However, the performance of MXene electrodes greatly depends on the electrode architecture, with multilayered or restacked MXenes showing unsatisfactory performances.

This thesis reports on the development of pillaring techniques to increase the interlayer spacing between MXene ( $\text{Ti}_3\text{C}_2$  and  $\text{Mo}_2\text{TiC}_2$ ) sheets creating porous electrode architectures. This is shown to lead to large increases in the interlayer spacings, with up to 60-fold increases in the specific surface areas, among the highest reported for MXenes to-date. The pillared MXenes are then tested in a variety of systems for metal-ion capacitor applications, including organic Li-ion and Na-ion and aqueous Zn-ion systems. It was found that the pillared materials outperformed the non-pillared materials in each system studied, with improvements in capacities, rate capabilities, cycling stabilities and coulombic efficiencies. In addition, the pillaring and electrochemical mechanisms are studied using a combination of microscopy, spectroscopy and electrochemical techniques, providing important understanding to assist with the further development of this field.

## Table of Contents

Abstract.....	I
Table of Contents.....	II
List of Figures.....	VI
List of Tables.....	XIII
Dissemination.....	XII
Acknowledgments.....	XIII
Declaration of Authorship.....	XIV
1. Introduction.....	1
1.1. Scope and Motivation.....	2
1.2. Structure of Thesis.....	3
2. Background.....	5
2.1. Introduction.....	6
2.2. Energy Storage.....	6
2.3. Electrochemical Energy Storage.....	7
2.3.1. Batteries.....	7
2.3.1.1. Lithium-ion Batteries.....	9
2.3.1.2. Sodium-ion Batteries.....	10
2.3.1.3. Zinc-ion Batteries.....	11
2.3.2. Supercapacitors.....	14
2.3.2.1. Electric Double Layer Supercapacitors.....	15
2.3.2.2. Pseudocapacitors.....	15
2.3.2.3. Hybrid metal-ion capacitors.....	16
2.3.3. Electrolytes.....	17
2.3.3.1. Aqueous Electrolytes.....	17
2.3.3.2. Organic Electrolytes.....	18
2.3.3.3. Ionic Liquid Electrolytes.....	18
2.3.4. Mechanisms of Charge Storage.....	19
2.3.5. Battery Charge Storage Mechanisms.....	19
2.3.5.1. Intercalation Reactions.....	20
2.3.5.2. Conversion Reactions.....	21
2.3.5.3. Alloying Reactions.....	22
2.3.6. Supercapacitor Mechanisms.....	22
2.3.6.1. Electric double layer capacitance.....	23
2.3.6.2. Pseudocapacitive charge storage mechanisms.....	24
2.3.6.3. Intercalation pseudocapacitance.....	25

2.4.	MXenes.....	27
2.4.1.	Synthesis and Precursors.....	27
2.4.1.1.	HF-based MXene Synthesis.....	29
2.4.1.2.	Non-HF Etching Methods.....	36
2.4.1.3.	HCl-F Salt Etching.....	37
2.4.1.4.	Comparisons Between Etching Methods.....	39
2.4.1.5.	Delamination.....	42
2.4.2.	MXenes as Electrochemical Energy Storage Materials.....	43
2.4.2.1.	Non-structured MXenes.....	44
2.4.2.1.1.	Theoretical Studies.....	44
2.4.2.1.2.	Li-ion Systems.....	46
2.4.2.1.3.	Na-ion Systems.....	50
2.4.2.1.4.	Multivalent-ion Systems.....	52
2.4.2.1.5.	Aqueous Electrolytes.....	54
2.4.2.1.6.	Intercalation Hybrid Metal-ion Supercapacitors.....	56
2.4.2.2.	Porous MXene Electrodes.....	57
2.5.	Pillaring.....	59
2.5.1.	Pillars.....	60
2.5.1.1.	Oxide Pillars.....	60
2.5.1.2.	Ionic Surfactants.....	61
2.5.1.3.	Molecular Surfactants.....	61
2.5.1.4.	Co-pillars.....	62
2.5.2.	Pillaring of 2D Materials.....	62
2.5.3.	Pillared MXenes.....	63
2.6.	Aims and Objectives.....	68
3.	Materials and Methods.....	70
3.1.	Introduction and Materials.....	71
3.2.	Methods.....	72
3.2.1.	Materials Synthesis.....	72
3.2.1.1.	Ti <sub>3</sub> C <sub>2</sub> MXene.....	72
3.2.1.2.	Mo <sub>2</sub> TiC <sub>2</sub> MXene.....	73
3.2.2.	Pillaring Experiments.....	73
3.2.2.1.	Amine-assisted Pillaring.....	73
3.2.2.2.	Pillaring of Ti <sub>3</sub> C <sub>2</sub> .....	75
3.2.2.3.	Pillaring of Mo <sub>2</sub> TiC <sub>2</sub> .....	75
3.2.2.4.	CTAB Pillaring.....	76
3.2.2.5.	Ex-situ CTAB Pillaring.....	76
3.2.2.6.	In-situ CTAB Pillaring.....	76
3.2.3.	Characterisation.....	76
3.2.3.1.	X-ray Powder Diffraction.....	76
3.2.3.2.	Raman Spectroscopy.....	79

3.2.3.3.	Infrared Spectroscopy.....	81
3.2.3.4.	Scanning Electron Microscopy.....	82
3.2.3.5.	Transmission Electron Microscopy.....	83
3.2.3.6.	Energy Dispersive X-ray Spectroscopy.....	84
3.2.3.7.	X-ray Photoelectron Spectroscopy.....	86
3.2.3.8.	Nuclear Magnetic Resonance Spectroscopy.....	87
3.2.3.9.	Gas sorption.....	89
3.2.3.10.	Thermogravimetric Analysis.....	90
3.2.3.11.	Electrochemical Characterisation.....	90
3.2.3.12.	Galvanostatic charge-discharge Testing.....	91
3.2.3.13.	Cyclic Voltammetry.....	93
3.2.3.14.	Summary.....	95
4.	SiO <sub>2</sub> -Pillared Ti <sub>3</sub> C <sub>2</sub> for Na and Li-ion systems.....	97
4.1.	Introduction.....	98
4.2.	Results and Discussion.....	99
4.2.1.	Controlling the MXene Surface Chemistry.....	99
4.2.2.	DDA-TEOS Pillaring.....	102
4.2.2.1.	Synthesis and Characterisation.....	102
4.2.2.2.	Effect of Starting Material Ratios.....	113
4.2.2.3.	Intercalation Mechanism.....	114
4.2.3.	Electrochemical Performance.....	118
4.2.3.1.	Sodium-ion System.....	118
4.2.3.2.	Lithium-ion System.....	126
4.3.	Conclusions.....	132
5.	SiO <sub>2</sub> -Pillared Mo <sub>2</sub> TiC <sub>2</sub> for Li and Na-ion systems.....	133
5.1.	Introduction.....	134
5.2.	Results and Discussion.....	135
5.2.1.	MAX Phase and MXene Synthesis.....	135
5.2.2.	Pillaring of Mo <sub>2</sub> TiC <sub>2</sub> .....	139
5.2.3.	Electrochemical Testing.....	148
5.2.3.1.	Lithium-ion System.....	148
5.2.3.2.	Sodium-ion System.....	159
5.3.	Conclusions.....	165
6.	MXenes in Zn-ion Systems.....	167
6.1.	Introduction.....	168
6.2.	Ti <sub>3</sub> C <sub>2</sub> in Aqueous Zn Electrolyte.....	169
6.2.1.	Synthesis, Pillaring and Characterisation.....	169
6.2.2.	Electrochemical Testing.....	174
6.2.3.	Structural Changes During Cycling.....	180
6.2.3.1.	Ex-situ Powder X-ray Diffraction.....	180
6.2.3.2.	Ex-situ Raman Spectroscopy.....	183

6.2.3.3.	Ex-situ X-ray Photoelectron Spectroscopy.....	188
6.3.	SiO <sub>2</sub> -pillared Ti <sub>3</sub> C <sub>2</sub> in Aqueous Zn Electrolyte.....	190
6.4.	Mo <sub>2</sub> TiC <sub>2</sub> in Aqueous Zn Electrolyte.....	191
6.5.	MXenes in Organic Zn Electrolytes.....	192
6.5.1.	CTAB-pillared Ti <sub>3</sub> C <sub>2</sub> .....	192
6.5.2.	SiO <sub>2</sub> -pillared Ti <sub>3</sub> C <sub>2</sub> .....	193
6.6.	Conclusions.....	194
7.	Conclusions and Further Work.....	196
7.1.	Concluding Remarks.....	197
7.2.	Future Work.....	201
7.2.1.	Amine-assisted Pillaring Method.....	201
7.2.2.	Mo <sub>2</sub> TiC <sub>2</sub> .....	203
7.2.3.	Zinc-ion Systems.....	204
8.	Bibliography.....	205
	Appendix.....	225

## List of Figures

Figure 2.1. Comparison of the different battery technologies in terms of volumetric and gravimetric energy density.....	8
Figure 2.2. Schematic representation of a rechargeable lithium-ion battery.....	10
Figure 2.3. Pourbaix diagram for Zn metal in aqueous electrolytes.....	13
Figure 2.4. Ragone plot comparing energy and power densities of supercapacitors to various battery technologies.....	14
Figure 2.5. Example salts and solvents that make up typical a) aqueous b) organic and c) ionic liquid electrolytes.....	17
Figure 2.6. Schematic representing the different class of redox-based charge storage mechanisms displayed by electrochemical energy storage materials.....	25
Figure 2.7. Periodic table highlighting elements that make up MAX phases.....	28
Figure 2.8. Crystal structures of the 211, 312, and 413 MAX phases.....	29
Figure 2.9. Schematic of the exfoliation process for $Ti_3AlC_2$ .....	30
Figure 2.10. SEM image for MXene stacked layers, showing the typical morphology for HF etched MXenes ( $Ti_3C_2$ ).....	31
Figure 2.11. Schematic illustration of the concept of in- and out-of-plane ordered MAX phases.....	35
Figure 2.12. XRD patterns of samples produced by etching in LiF + HCl solution.....	38
Figure 2.13. SEM images of MXene samples.....	40
Figure 2.14. Composition of the $Ti_3C_2T_x$ surface functional groups produced by etching of the $Ti_3AlC_2$ in HF and LiF–HCl solutions.....	40
Figure 2.15. Schematic of the intercalation and delamination of an MXene.....	42
Figure 2.16. Capacity and ionic radius for adsorption on both sides of an MXene sheet in different ion systems.....	44
Figure 2.17. Cell voltage and theoretical gravimetric capacity for intercalation of two ions of $Li^+$ , $Na^+$ , $K^+$ , or $Mg^{2+}$ per formula unit into $M_2CT_2$ .....	45
Figure 2.18. CV curves demonstrating the effect of increasing the interlayer spacing on the shape of the voltammogram for $Ti_3C_2$ in a Li-ion half-cell.....	48

Figure 2.19. Schematic representation of the pillaring process, showing the insertion of pillars which separate the layers of a material creating new pores.....	60
Figure 2.20. Illustration showing the chemical structure of a molecular surfactant (top, DDA) and ionic surfactant (bottom, CTAB), which are both used in this thesis.....	61
Figure 3.1. Schematic representation of the etching set-up for MXene synthesis.....	72
Figure 3.2. Diagram illustrating the TEOS hydrolysis reaction pathway to form the SiO <sub>2</sub> pillars.....	74
Figure 3.3. Schematic illustrating the amine-assisted pillaring method.....	74
Figure 3.4. Schematic illustration of the arrangement of the co-pillars in the intercalated materials.....	75
Figure 3.5. Schematic illustration of diffraction according to the Bragg equation.....	77
Figure 3.6. Diagram showing the unit cell of Ti <sub>3</sub> C <sub>2</sub> and demonstrating the use of the (002) plane to calculate the interlayer spacing and gallery height.....	78
Figure 3.7. Schematic illustrating the Raman Effect in terms of the changes in energy levels which occur when visible light scatters from a material.....	80
Figure 3.8. Illustration of the vibrational modes predicted to occur for Ti <sub>3</sub> C <sub>2</sub> terminated with –OH and –O groups.....	81
Figure 3.9. Schematic representation of some of the effects of the interaction of the focused electron beam with a sample.....	83
Figure 3.10. Schematic diagram of the generation of an x-ray for EDS analysis.....	85
Figure 3.11. Schematic diagram showing the ejection of a photoelectron by an x-ray which can then be analysed by XPS.....	86
Figure 3.12. Photo of coin cell parts used in this thesis for the electrochemical characterisation.....	90
Figure 3.13. Load curve diagram illustrating the two main types of load curve features observed for electrochemical energy storage materials.....	93
Figure 3.14. Schematic cyclic voltammograms and corresponding galvanostatic discharge curves for various kinds of energy-storage materials.....	94

Figure 4.1. Schematic illustrating the pillaring process used.....	100
Figure 4.2. XRD and SEM characterisation of $Ti_3C_2$ .....	101
Figure 4.3. EDS spectra of the as-etched $Ti_3C_2$ , confirming the selective removal of the Al layer.....	101
Figure 4.4. Raman spectra of the alkali and acid treated MXene, and the acid treated intercalated and calcined at 400 °C pillared MXene.....	102
Figure 4.5. Low angle XRD of the acid and alkali treated MXenes after the intercalation experiments.....	103
Figure 4.6. Microscopy studies of the intercalated MXene.....	104
Figure 4.7. SEM-EDS analysis of $Ti_3C_2$ -OH-Si.....	105
Figure 4.8. IR spectroscopy of $Ti_3C_2$ -OH-Si recorded between 500-4,000 $cm^{-1}$ .....	105
Figure 4.9. Analysis of $Ti_3C_2$ -OH dispersed in TEOS at room temperature for 4 h and recovered by vacuum filtration before being dried at 60 °C.....	106
Figure 4.10. XRD results showing the shift in the (002) diffraction peak when calcined at 300, 400 and 500 °C.....	107
Figure 4.11. TGA and DSC plot from the heating of $Ti_3C_2$ -OH-Si to 600 °C under $N_2$ .....	108
Figure 4.12. a) EDS of $Ti_3C_2$ -OH-Si-400. b) IR spectroscopy results of $Ti_3C_2$ -OH-Si-400 after calcination under argon.....	108
Figure 4.13. TEM and EDS studies of the pillared MXene post calcination.....	109
Figure 4.14. XRD plot of $Ti_3C_2$ -OH-Si-400 sample between 4 and 50° 2 $\theta$ .....	110
Figure 4.15. Adsorption isotherms from $N_2$ adsorption-desorption experiments. The BET surface area is also given in each panel.....	111
Figure 4.16. Pore size distributions derived from the isotherms using the NL DFT method.....	112
Figure 4.17. XRD analysis of the effect of the starting ratios for pillaring.....	113
Figure 4.18. Solid-state NMR spectra (16.4 T, 29-30 kHz Magic Angle Spinning (MAS)) of $Ti_3C_2$ -O, $Ti_3C_2$ -OH, $Ti_3C_2$ -OH-Si and $Ti_3C_2$ -OH-Si-400.....	115
Figure 4.19. XRD of $Ti_3C_2$ -OH intercalated with octylamine and TEOS.....	117
Figure 4.20. Galvanostatic data from half-cell tests against Na metal at 20 mA $g^{-1}$ in the voltage range 0.01-3 V.....	119

Figure 4.21. Cyclic voltammograms at 0.01-3 V vs. Na metal at a scan rate of 0.2 mV s <sup>-1</sup> for a) the non-pillared and b) pillared MXene.....	120
Figure 4.22. CV analysis at different rates for non-pillared and pillared Ti <sub>3</sub> C <sub>2</sub> at scan rates of 0.2, 0.5, 2 and 5 mV s <sup>-1</sup> in the voltage window 0.01-3 V vs. Na <sup>+</sup> / Na.....	122
Figure 4.23. Rate capability tests for the pillared and non-pillared MXene at rates of 20, 50, 200, 500 and 1,000 mA g <sup>-1</sup> .....	123
Figure 4.24. Ex-situ XPS Si 2p spectra for Ti <sub>3</sub> C <sub>2</sub> -OH-Si-400 at OCV, after discharge to 0.01 V and charging to 3 V.....	124
Figure 4.25. Galvanostatic charge-discharge tests for the non-calcined pillared MXene, Ti <sub>3</sub> C <sub>2</sub> -OH-Si. The electrodes were cycled at 20 mA g <sup>-1</sup> for 100 cycles between 0.01-3V against Na <sup>+</sup> / Na.....	125
Figure 4.26. Galvanostatic data from half-cell tests against Li metal at 20 mA g <sup>-1</sup> in the voltage range 0.01-3 V using 1 M LiPF <sub>6</sub> in EC:DEC (1:1 wt. ratio) as the electrolyte.....	128
Figure 2.27. Rate capability tests for the pillared and non-pillared MXene at rates of 20, 50, 200, 500 and 1,000 mA g <sup>-1</sup> vs. Li <sup>+</sup> / Li.....	129
Figure 4.28. Galvanostatic charge-discharge data for SiO <sub>2</sub> -pillared Ti <sub>3</sub> C <sub>2</sub> in a Li-ion half-cell tested for 500 cycles at a rate of 1 A g <sup>-1</sup> in a voltage window of 0.01-3 V vs. Li <sup>+</sup> / Li.....	130
Figure 4.29. CV data from Ti <sub>3</sub> C <sub>2</sub> -Si-400 in the Li-ion system. Cells were run in a voltage window of 0.01-3 V vs. Li <sup>+</sup> / Li using 1 M LiPF <sub>6</sub> in EC:DEC (1:1 wt. ratio) as the electrolyte.....	131
Figure 5.1. XRD patterns of Mo <sub>2</sub> TiAlC <sub>2</sub> MAX phase (bottom) and Mo <sub>2</sub> TiC <sub>2</sub> MXene (top).....	136
Figure 5.2: SEM micrographs of as-synthesised Mo <sub>2</sub> TiC <sub>2</sub> flakes.....	137
Figure 5.3. EDS analysis of as-etched Mo <sub>2</sub> TiC <sub>2</sub> .....	138
Figure 5.4. TGA plot of mass loss (mg) against temperature.....	139
Figure 5.5. Low angle XRD diffraction pattern of the intercalated, Mo <sub>2</sub> TiC <sub>2</sub> -Si, and calcined, Mo <sub>2</sub> TiC <sub>2</sub> -Si-400 samples.....	140
Figure 5.6. Low angle XRD pattern showing the (002) diffraction peak in the pillared Mo <sub>2</sub> TiC <sub>2</sub> after calcination at 400 °C.....	140
Figure 5.7. SEM-EDS studies of the Si intercalated Mo <sub>2</sub> TiC <sub>2</sub> MXene.....	142

Figure 5.8. SEM micrographs of the SiO <sub>2</sub> pillared Mo <sub>2</sub> TiC <sub>2</sub> MXene after calcination at 400 °C for 5 h under argon.....	143
Figure 5.9. SEM-EDS studies of the SiO <sub>2</sub> pillared Mo <sub>2</sub> TiC <sub>2</sub> MXene after calcination at 400 °C for 5 h under argon.....	144
Figure 5.10. Raman spectroscopy of the non-pillared, intercalated pillared and calcined pillared Mo <sub>2</sub> TiC <sub>2</sub> MXene materials.....	145
Figure 5.11. Mo 3d XPS spectra for the non-pillared and SiO <sub>2</sub> -pillared Mo <sub>2</sub> TiC <sub>2</sub> after calcination at 400 °C.....	146
Figure 5.12. Ti 2p XPS spectra for the non-pillared and SiO <sub>2</sub> -pillared Mo <sub>2</sub> TiC <sub>2</sub> after calcination at 400 °C.....	147
Figure 5.13. XPS analysis of a) O 1s spectrum of non-pillared Mo <sub>2</sub> TiC <sub>2</sub> b) O 1s spectrum of the pillared MXene Mo <sub>2</sub> TiC <sub>2</sub> -Si-400 and c) Si 2p spectrum of the pillared MXene Mo <sub>2</sub> TiC <sub>2</sub> -Si-400.....	147
Figure 5.14. Galvanostatic charge-discharge testing of Mo <sub>2</sub> TiC <sub>2</sub> samples in Li-ion half cells.....	150
Figure 5.15. Discharge capacity and coulombic efficiency of Mo <sub>2</sub> TiC <sub>2</sub> -Si-400 for 500 cycles at a rate of 1 A g <sup>-1</sup> in a voltage window of 0.01-3 V vs. Li <sup>+</sup> / Li.....	151
Figure 5.16. Cyclic Voltammograms for the a) non-pillared and b) pillared Mo <sub>2</sub> TiC <sub>2</sub> MXene materials. In both cases scan rates of 0.2 mV s <sup>-1</sup> were used in a voltage window of 0.01-3 V vs. Li <sup>+</sup> / Li.....	152
Figure 5.17. Cyclic voltammograms for the a) non-pillared and b) pillared Mo <sub>2</sub> TiC <sub>2</sub> MXene materials. In both cases increasing scan rates of 0.2, 0.5, 2 and 5 mV s <sup>-1</sup> were used in a voltage window of 0.01-3 V vs. Li <sup>+</sup> / Li.....	154
Figure 5.18. Plot of b-values against voltage vs. Li <sup>+</sup> / Li. a) Non-Pillared Mo <sub>2</sub> TiC <sub>2</sub> b) Pillared-Mo <sub>2</sub> TiC <sub>2</sub> .....	156
Figure 5.19. Ex-situ XPS of SiO <sub>2</sub> -pillared Mo <sub>2</sub> TiC <sub>2</sub> .....	157
Figure 5.20. Galvanostatic charge-discharge testing of Mo <sub>2</sub> TiC <sub>2</sub> samples in Na-ion half cells at 20 mA g <sup>-1</sup> in a voltage window of 0.01-3 V vs. Na <sup>+</sup> / Na.....	160
Figure 5.21. Rate capability testing at 20, 50, 200, 500, 1,000 mA g <sup>-1</sup> for five cycles at each rate for the pillared and non-pillared samples.....	161
Figure 5.22. Cyclic voltammograms collected at a scan rate of 0.2 mV s <sup>-1</sup> in a voltage window between 0.01-3 V vs. Na <sup>+</sup> / Na for a) the non-pillared Mo <sub>2</sub> TiC <sub>2</sub> and b) pillared Mo <sub>2</sub> TiC <sub>2</sub> -Si-400.....	162

Figure 5.23. Cyclic voltammograms collected at increasing scan rates of 0.2, 0.5, 2 and 5 $\text{mV s}^{-1}$ in a voltage window of 0.01-3 V vs. $\text{Na}^+/\text{Na}$ for a) the non-pillared $\text{Mo}_2\text{TiC}_2$ and b) pillared $\text{Mo}_2\text{TiC}_2\text{-Si-400}$ .....	163
Figure 5.24. Plot of $b$ -values against voltage vs. $\text{Na}^+/\text{Na}$ . a) Non-pillared $\text{Mo}_2\text{TiC}_2$ , b) pillared- $\text{Mo}_2\text{TiC}_2$ .....	164
Figure 6.1. XRD comparison of a) the commercial $\text{Ti}_3\text{AlC}_2$ MAX phase precursor and b) the etched $\text{Ti}_3\text{C}_2$ MXene.....	170
Figure 6.2. SEM and EDS analysis of the as-etched non-pillared $\text{Ti}_3\text{C}_2$ MXene. a) SEM micrograph of $\text{Ti}_3\text{C}_2$ b) EDS results of $\text{Ti}_3\text{C}_2$ .....	170
Figure 6.3. Schematic illustrating the in-situ pillaring process.....	171
Figure 6.4. XRD comparison of $\text{Ti}_3\text{C}_2$ pillared with CTAB using the a) in-situ method and b) ex-situ method.....	172
Figure 6.5. TGA and DSC studies comparing a) the non-pillared $\text{Ti}_3\text{C}_2$ as-made material and b) the CTAB ex-situ pillared material. Figure c shows the difference in mass between the as-made MXene as the CTAB pillared MXene.....	173
Figure 6.6. CV scans at 1 $\text{mV s}^{-1}$ between 0.01 V and 1.5 V to determine stable voltage window for $\text{Ti}_3\text{C}_2$ in a) $\text{ZnSO}_4$ and b) $\text{ZnSO}_4$ with CTAB additive.....	174
Figure 6.7. Galvanostatic charge-discharge testing of the $\text{Ti}_3\text{C}_2$ electrodes in 0.1 $\text{ZnSO}_4$ .....	175
Figure 6.8. Rate capability tests of the non-pillared ( $\text{Ti}_3\text{C}_2$ ) and in-situ pillared ( $\text{Ti}_3\text{C}_2$ in-situ pillared) materials. The cells were run at increasing rates of at rates of 20, 50, 200, 500 and 1,000 $\text{mA g}^{-1}$ .....	176
Figure 6.9. Cyclic voltammograms for: a) non-pillared $\text{Ti}_3\text{C}_2$ at 0.1 $\text{mV s}^{-1}$ for five cycles, b) $\text{Ti}_3\text{C}_2$ at 0.1, 0.5, 2 and 5 $\text{mV s}^{-1}$ , c) in-situ pillared $\text{Ti}_3\text{C}_2$ at 0.1 $\text{mV s}^{-1}$ , d) in-situ pillared $\text{Ti}_3\text{C}_2$ at 0.1, 0.5, 2 and 5 $\text{mV s}^{-1}$ .....	178
Figure 6.10. Plot of the $b$ -value against voltage for the un-pillared and in-situ pillared $\text{Ti}_3\text{C}_2$ . a) Cathodic current. b) Anodic current.....	180
Figure 6.11. Ex-situ XRD of the non-pillared $\text{Ti}_3\text{C}_2$ . a) Load curve showing the depth of charge each electrode was stopped at. b) Corresponding diffraction patterns.....	181
Figure 6.12. Ex-situ XRD data of the in-situ pillared $\text{Ti}_3\text{C}_2$ material at different states of charge in the voltage window 0.01-1 V.....	182
Figure 6.13. Ex-situ Raman spectroscopy of the non-pillared $\text{Ti}_3\text{C}_2$ .....	184

Figure 6.14. Ex-situ XRD of in-situ pillared $\text{Ti}_3\text{C}_2$ at OCV after 48 h of drying for the removal of interlayer water.....	185
Figure 6.15. Ex-situ Raman spectroscopy of the in-situ pillared $\text{Ti}_3\text{C}_2$ .....	186
Figure 6.16. Ex-situ XPS Ti 2p spectra of in-situ pillared $\text{Ti}_3\text{C}_2$ at selected states of charge during the first cycle.....	189
Figure 6.17. Galvanostatic charge-discharge testing of $\text{SiO}_2$ -pillared $\text{Ti}_3\text{C}_2$ in 0.1 M $\text{ZnSO}_4$ at 20 $\text{mA g}^{-1}$ in a voltage window of 0.01-1 V vs. $\text{Zn}^{2+}/\text{Zn}$ . ....	191
Figure 6.18. Galvanostatic charge-discharge testing of $\text{Mo}_2\text{TiC}_2$ in 0.1 M $\text{ZnSO}_4$ at 20 $\text{mA g}^{-1}$ in a voltage window of 0.01-1 V vs. $\text{Zn}^{2+}/\text{Zn}$ .....	192
Figure 6.19. Galvanostatic charge-discharge testing of CTAB-pillared $\text{Ti}_3\text{C}_2$ in 1 M $\text{Zn(TFSI)}_2$ at 20 $\text{mA g}^{-1}$ in a voltage window of 0.01-2 V vs. $\text{Zn}^{2+}/\text{Zn}$ .....	193
Figure 6.20. Galvanostatic charge-discharge testing of $\text{SiO}_2$ -pillared $\text{Ti}_3\text{C}_2$ in 1 M $\text{Zn(TFSI)}_2$ at 20 $\text{mA g}^{-1}$ in a voltage window of 0.01-2 V vs. $\text{Zn}^{2+}/\text{Zn}$ .....	194

## List of Tables

Table 2.1. Comparison of sodium vs. lithium.....	11
Table 2.2. Currently synthesised MXenes, with the parent MAX phase and the respective reference.....	33
Table 2.3. Reaction conditions for selected MXenes.....	36
Table 2.4. Summary of selected MXene synthesis conditions used with HCl / LiF etching solution.....	39
Table 2.5. Summarized EDS values of various etching and washing procedures. Results are normalised with respect to Ti content.....	41
Table 3.1. Experimental parameters used for MAS solid-state NMR experiments.....	89
Table 3.2. Components used in test cells for different electrochemical systems.....	91
Table 6.1. Ex-situ EDS data showing increased Zn content during discharging and decreased Zn content during charging.....	182
Table A.1. Raman Spectroscopy band assignments and peak fittings for $Ti_3C_2$ at selected stages of pillaring.....	226
Table A.2. Ex-situ Si 2p XPS peak assignments and fitting errors for $Ti_3C_2$ -OH-Si-400 at selected states-of-charge in a Na-ion half-cell.....	226
Table A.3. Mo 3d XPS peak assignments and fitting errors for $Mo_2TiC_2$ .....	227
Table A.4. Mo 3d XPS peak assignments and fitting errors for $Mo_2TiC_2$ -Si-400.....	227
Table A.5. Ti 2p XPS peak assignments and fitting errors for $Mo_2TiC_2$ .....	227
Table A.6. Ti 2p XPS peak assignments and fitting errors for $Mo_2TiC_2$ -Si-400.....	227
Table A.7. Ex-situ O 1s XPS peak assignments and fitting errors for $Mo_2TiC_2$ -Si-400 at selected states-of-charge in a Li-ion half-cell.....	227
Table A.8. Ex-situ Si 2p XPS peak assignments and fitting errors for $Mo_2TiC_2$ -Si-400 at selected states-of-charge in a Li-ion half-cell.....	228
Table A.9. Raman spectroscopy band assignments and peak analysis results for $Ti_3C_2$ at selected states-of-charge in the aqueous Zn-ion system.....	228
Table A.10. Ex-situ Ti 2p XPS peak assignments and fitting errors for $Mo_2TiC_2$ -Si-400 at selected states-of-charge in a Li-ion half-cell.....	229

## Dissemination

### Journal Publications

At the time of writing the author has submitted two manuscripts based on the contents of this thesis. Manuscript 1 reports on the development of the amine-assisted SiO<sub>2</sub> pillaring methods and the performance of the pillared Ti<sub>3</sub>C<sub>2</sub> in a Na-ion battery system, which form the basis of Chapter 4 of this thesis. Manuscript 2 is based on the results obtained from in-situ pillaring Ti<sub>3</sub>C<sub>2</sub> with CTAB, and the behaviour of these materials in an aqueous Zn-ion system, which are reported in Chapter 6.

1. Philip A. Maughan, Valerie R. Seymour, Ramon Bernardo-Gavito, Daniel J. Kelly, Shouqi Shao, Supakorn Tantisriyanurak, Robert Dawson, Sarah J. Haigh<sup>4</sup>, Robert J. Young, Nuria Tapia-Ruiz, and Nuno Bimbo, Porous Silica-Pillared MXenes with Controllable Interlayer Distances for Long-life Na-ion Batteries, 2019, Under Review.
2. Philip A. Maughan, Nuria Tapia-Ruiz and Nuno Bimbo In-situ pillared Ti<sub>3</sub>C<sub>2</sub> MXene for Zinc-ion hybrid capacitors", 2019, Under Review.

### Conference Presentations

The author has presented the following oral and poster presentations, based on the results in Chapter 4 and Chapter 6.

#### Oral Presentations

1. **NECEM International Conference on Energy Materials and Interfaces**, 29<sup>th</sup> July- 1<sup>st</sup> August 2019, Newcastle, UK, In-situ pillared Ti<sub>3</sub>C<sub>2</sub> MXene for Zinc-ion hybrid capacitors.
2. **RSC International conference on Materials Chemistry (MC-14)**, 8<sup>th</sup>-11<sup>th</sup> July 2019, Birmingham, UK, Silicon Pillared Ti<sub>3</sub>C<sub>2</sub> MXene with Controllable Interlayer Spacing for Enhanced Performance for Na-ion batteries.
3. **Graphene NOWNANO CDT summer conference**, July 2018, Cheshire, UK, Silicon Pillared Porous Ti<sub>3</sub>C<sub>2</sub> MXene.
4. **Departmental conference**, July 2017, Lancaster, UK, Porous MXenes for High Capacity Energy Storage.

#### Poster Presentations

1. **European Materials Research Society (E-MRS) Spring Meeting**, 27<sup>th</sup>-30<sup>th</sup> May 2019, Nice, France, Silicon Pillared Ti<sub>3</sub>C<sub>2</sub> MXene as a long-life Na-ion battery Electrode.
2. **Graphene NOWNANO CDT summer conference**, July 2017, Cambridge, UK, Porous MXenes for High Capacity Energy Storage.

3. **Graphene NOWNANO CDT summer conference**, July 2016, Cheshire, UK, Porous MXenes for High Capacity Energy Storage.

### **Acknowledgements**

The work presented in this thesis has only been possible with the contributions of many people at the Universities of Lancaster and Manchester, who have trained, taught and helped me throughout this PhD. Special thanks must go to Dr Nuno Bimbo, my supervisor, who devised the project, and has always been available to guide me through it to completion. Luc Bouscarrat has also been invaluable with his assistance with MXene synthesis, and constant willingness to discuss our work with MXenes.

Several people at Lancaster University also helped train me on equipment without which this thesis would not have happened. Drs Ramon Bernardo-Gavito and Rob Young allowed me to use and trained me on their Raman spectrometer. Drs Nathan Halcovitch and Sara Baldock trained me on the Lancaster University SEM and XRD facilities, and were always available to assist with problems and questions. The chemical engineering technicians, Peter Jones and Jess Fisher, have been invaluable with their assistance with experiments run in the chemical engineering labs, from lab maintenance to training and advice for specific experiments. NMR experiments were carried out by Dr Valerie Seymour, who was always keen to discuss NMR experiments and the results.

The electrochemical parts of this thesis would not have been possible without the help, guidance and equipment from Dr Nuria Tapia-Ruiz, who in many ways acted as an extra supervisor. The members of her group, Dr Mangai Nagarathinam, Sara Costa and Cindy Soares must also be thanked for always being willing to help with organising my experiments and any questions I had on the electrochemical side of things.

Important contributions were also made by people from other universities. Dan Kelly (a fellow Graphene NOWNANO CDT student) was always keen to discuss microscopy related work that could be done for me, and, with Shouqi Shao, under the supervision of Professor Sarah Haigh (my co-supervisor) helped devise, run and analyse the TEM based experiments reported in this thesis. Supakorn Tantisriyanurak and Dr Robert Dawson, at the University of Sheffield, carried out BET experiments and analysis on my samples.

Finally, special thanks should go to my wonderful wife, Liz, who has supported me throughout the PhD, and made sure I think about other things besides batteries and MXenes!

## **Declaration of Authorship**

The work presented in this thesis, except for the following exceptions, was carried out by the author with supervision and guidance from his academic supervisor, Dr Nuno Bimbo, Lecturer of Chemical Engineering in the Department of Engineering at Lancaster University. The work presented has not been submitted in substantially the same form towards the award of a degree or other qualification.

NMR experiments were carried out by Dr Valerie Seymour in the Department of Chemistry at Lancaster University. NMR analysis was a joint effort between the author and Valerie Seymour.

TEM and TEM-EDS experiments and analysis (used in Chapter 4) was carried out by Daniel Kelly and Shouqi Shao under the supervision of Professor Sarah Haigh in the School of Materials at the University of Manchester.

BET experiments and analysis (used in Chapter 4) were carried by Supakorn Tantisriyanurak under the supervision of Dr Robert Dawson at the Department of Chemistry at the University of Sheffield.

XPS experiments were carried out by Dr Shaoliang Guan at the national XPS facility at Harwell Campus. All analysis and peak fittings were carried out by the author.

Copyrighted material in this thesis is identified and used with permission from the copyright owner.

# **Chapter One**

## **Introduction**

## 1.1 Scope and Motivation

Energy storage is gaining increasing attention worldwide as concerns grow about the continuing use of fossil fuels, which have powered the industrialised world for over 150 years. In particular, greenhouse gas emissions produced by the use of these fuels have been linked to causing severe shifts in the global climate systems, with potentially catastrophic consequences. Other fossil fuel emissions, such as particulate matter and nitrous oxides, have been linked with worsening and unsafe air quality, which causes premature deaths of millions each year. Finally, the finite nature of fossil fuels combined with an ever increasing global energy demand has led to increasing worries about the security of supply, with the remaining reserves often located in politically unstable countries and being more technically challenging and costly to extract than previous resources. This has led to a growing focus on developing low carbon, non-fossil fuel energy sources such as nuclear fission power stations, and renewable technologies such as wind, solar and wave.

However, these alternative energy sources bring their own challenges, in particular with regards to matching energy supply with demand. Nuclear power stations suffer from long start-up times, which means that they cannot be rapidly deployed to fill a sudden increase in demand. Emerging renewable technologies, such as solar and wind power, are widely known to be highly intermittent in nature, since the energy generated depends on uncontrollable factors such as whether it is sunny or windy. Therefore, there is an urgent need to develop energy storage technologies which could facilitate the alignment of energy supply with demand. Such energy storage technologies must be affordable, scalable and have the desired performance criteria such as high efficiency, power density, energy density and long lifetimes. Electrochemical energy storage devices, such as batteries and supercapacitors, have recently attracted significant interest as potential technologies to fulfil this application. In addition, transportation has so far proven to be a difficult sector to decarbonise, and solar, wind or nuclear powered vehicles are not considered practical. Recently, mainstream electric vehicles, powered by Li-ion batteries, have been commercialised, with major manufacturers and economies setting targets for further electrification of transport in the near future. This offers a way of removing greenhouse gas and other emissions from the tailpipe of vehicles, which would have significant effect on climate change and air quality. However, the performance of current generation supercapacitors and batteries, which is dictated by the electrode materials used to make them, is not sufficient to meet the requirements that will be demanded of them. In addition, Li-ion batteries in particular also have associated concerns surround the supply and manufacture of some of the materials used. Therefore, there is an urgent need to develop safer, more abundant and higher

performing electrode materials in these devices, with a particular focus on combining high energy density (characteristic of a battery) with high power density and long lifetime (characteristic of a supercapacitor) into one device (such as a metal-ion capacitor), which could meet the demanding requirements of these new applications.

This thesis investigates the development of pillaring processes to create porous and stable architectures of the family of two-dimensional (2D) layered materials known as MXenes. These are a family of 2D transitional metal carbides and nitrides discovered in 2011, which have shown early promise in the area of electrochemical energy storage, but have limited performance when their layers stack closely together, giving a non-porous material with low capacities and poor charging rates. Therefore, porous MXenes ( $\text{Ti}_3\text{C}_2$  and  $\text{Mo}_2\text{TiC}_2$ ) are investigated as potential electrode materials for metal-ion capacitor applications (specifically lithium, sodium and zinc systems) with the aim to improve the capacity, rate capability and cycling lifetime of this promising class of materials. As well as electrochemical characterisation, the role of surface groups, which terminate the MXenes, on the pillaring process is investigated. Furthermore, a series of ex-situ structural characterisation techniques are used to determine the charge storage mechanisms of the pillared MXenes in the different electrolyte systems.

## **1.2 Structure of thesis**

This thesis consists of seven main chapters. Chapter 1 (this chapter) introduces the thesis, describing the motivation, scope and structure. Chapter 2 describes the background to the thesis, introducing energy storage, MXenes and pillaring, including a review on the current state of research in these areas. This chapter does not aim to be a complete review of all works carried out under these topics, but instead focuses on key concepts and reports which are most relevant to understanding the contents and context of this thesis. Chapter 3 is the materials and methods chapter, which introduces the materials and methods used to carry out the work described in the results chapter of this thesis. As well as explaining what experimental techniques and methods were used, some basic background theory is also explored. The background theory for each technique is presented only to the level needed to interpret the results reported in this thesis, and is not intended to be a thorough review of each technique described. Chapters 4, 5 and 6 are results chapters, which describe the bulk of the work carried out for this thesis. Chapter 4 reports on the development and application of an amine-assisted pillaring method to  $\text{Ti}_3\text{C}_2$  MXene, which successfully expanded the interlayer and created porous  $\text{Ti}_3\text{C}_2$ . The pillared  $\text{Ti}_3\text{C}_2$  was then tested as a negative electrode in organic Na and Li-ion systems, and compared to the non-pillared MXene to determine the effect on performance of the porous structure. Chapter 5 applies this amine-assisted pillaring method to the out-of-plane

ordered MXene  $\text{Mo}_2\text{TiC}_2$ , which consists of Mo-only outer metal layers. This allows for the effect of the metal (M) element on the pillaring process to be studied. The pillared  $\text{Mo}_2\text{TiC}_2$  MXene was also studied as a negative electrode in Li and Na-ion systems, with ex-situ XPS experiments being used to investigate a suspected conversion reaction in the Li-ion system. Chapter 6 reports on the use of MXenes (in particular  $\text{Ti}_3\text{C}_2$ ) in Zn-ion systems, with a focus on aqueous electrolytes. A series of ex-situ spectroscopic techniques were applied in addition to electrochemical characterisation techniques to determine the charge storage mechanism in this system. Chapter 7 summarises the results presented in this thesis, giving the main conclusions and some recommendations for further work. The final chapter, Chapter 8, contains the bibliography for the works referred to in this thesis.

# **Chapter Two**

## **Background**

## 2.1 Introduction

As mentioned in Chapter 1, this thesis investigates the development of pillaring processes to create porous and stable architectures of the family of two-dimensional (2D) layered materials known as MXenes. These materials have shown early potential in the area of electrochemical energy storage, but have limited performance when their layers stack closely together, giving a non-porous material. Therefore, this thesis investigates methods to create porous MXenes ( $\text{Ti}_3\text{C}_2$  and  $\text{Mo}_2\text{TiC}_2$ ) which are investigated as potential electrode materials for metal-ion capacitor applications (specifically lithium, sodium and zinc systems) with the aim to improve the capacity, rate capability and cycling lifetime of this promising class of materials. Therefore, this chapter introduces the main background and concepts for this thesis, including electrochemical energy storage, MXenes and pillaring techniques, and concludes with the aims and objectives for the thesis.

## 2.2 Energy Storage

Energy storage is becoming more important now that at any previous point in human history. Over the last 150 years, industrial development has relied greatly on the use of fossil fuels. However, there are multiple concerns about the continuing use of fossil fuels, which have been linked to climate change, air pollution and geopolitical tensions. In addition, as global energy use generally continues to rise, the non-renewable nature of fossil fuels has led to growing fears about the finite nature of remaining reserves, which also tend to be more challenging and costly to extract than the resources already exploited.

This has led to the development and increasing deployment of alternative (such as nuclear fission) and renewable energy sources such as wind, solar and tidal power stations. However, an energy system dominated by these power sources needs significant contributions from energy storage technologies to be able to provide a stable grid system which can efficiently match supply and demand.<sup>1</sup> For example, typical nuclear fission power stations cannot rapidly change their power output, regardless of demand.<sup>2</sup> Instead it can take several days to start up one of these power stations to full output. On the other hand, renewable energy sources such as wind and solar are highly intermittent in nature, generating energy whenever it is windy or when the Sun is shining, not when it is needed.<sup>3</sup> Being able to store the generated energy for when it is needed is crucial for the widespread development of these clean fossil fuel free energy systems.

In addition to the drive to decarbonise the energy generation systems, there is growing focus on developing alternative powertrains for the transport sector, where the use of fossil fuels causes significant greenhouse gas emissions linked to climate change, and is attributed to high air pollution, especially in city centres. For example,

in the UK, there are several areas with illegal levels of pollutants such as NO<sub>x</sub> (nitrous oxides), which predominantly arise from fossil fuel powered vehicles. Air pollution has been linked to directly causing the deaths of over 40,000 people a year in the UK alone.<sup>4</sup> This has led to a significant push to electrify the transport sector, since this would remove the emission of these pollutants from the exhaust of vehicles. Since vehicles cannot currently be powered directly by non-fossil fuel energy sources, this transition is reliant on energy storage technologies, with batteries and fuel cells (using hydrogen as the energy carrier) currently the most promising technologies for this application.

There has also been a remarkable growth in portable electronics in the last few decades, such as mobile phones and laptops. This has been enabled by the commercialisation and continuing development of lithium-ion batteries (LIBs), without which the increasingly energy consuming electronic devices would not be able to be powered to a similar scale.<sup>5</sup>

There are a variety of energy storage technologies under development for different scales of energy storage and with different cost, power density and energy density characteristics. These include pumped hydroelectric energy storage, thermal energy storage, compressed air energy storage, chemical energy storage and electrochemical energy storage.<sup>1</sup> Of these, the electrochemical energy storage technologies have potential applications in all three of the areas described above, and therefore are the focus of significant research and development programs.

## **2.3 Electrochemical Energy Storage**

There are two main technologies for electrochemical energy storage: batteries and supercapacitors. These will both be discussed in detail and compared in the following sections.

### **2.3.1 Batteries**

There are many different types of battery chemistries, each with their own properties and applications. These include lead-acid batteries, nickel-cadmium, nickel-metal hydride, metal-ion (such as lithium-ion, sodium-ion and zinc-ion), metal-oxygen (such as lithium-oxygen and zinc-oxygen), molten salt and redox flow batteries. These technologies have different properties, with varying energy densities, power densities and device lifetime (cycling stability). A plot of relative energy densities (gravimetric and volumetric) for a selection of these technologies is shown in Figure 2.1.

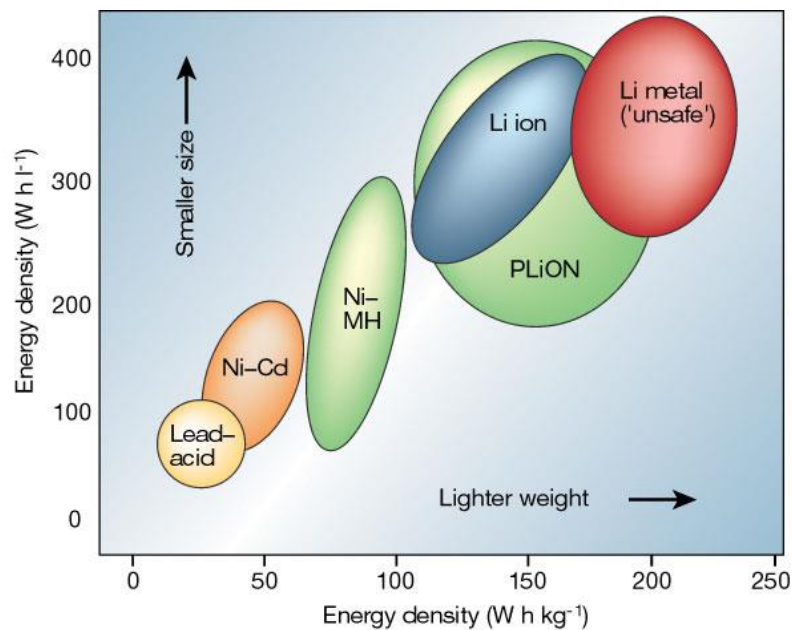


**Figure 2.1.** Comparison of the different battery technologies in terms of volumetric and gravimetric energy density. Note that P in PLiON stands for polymer. Reproduced from Springer Nature, Nature, Tarascon et al., 2001, with permission.<sup>6</sup>

Lead-acid batteries are the oldest type of secondary (rechargeable) battery listed, which stores charge via the reversible reactions between Pb (negative electrode), PbO<sub>2</sub> (positive electrode) and H<sub>2</sub>SO<sub>4</sub> (electrolyte), but suffer from the lowest energy densities, making them both heavy and bulky. There are also safety concerns associated with the corrosive sulphuric acid electrolyte. They have however been reliably used in a number of applications for decades, including in cars.<sup>7</sup>

Nickel-cadmium batteries, which are based on the reversible oxidation of Cd and NiO to Cd(OH)<sub>2</sub> and Ni(OH)<sub>2</sub> respectively with a KOH electrolyte, have a higher energy density than lead-acid batteries, but cadmium is a toxic element, and is therefore being replaced in many countries. They are being replaced by nickel-metal hydride (NMH) batteries, which work in a similar way, based on the formation of a metal hydride (such a Co hydride) rather than Cd(OH)<sub>2</sub>, but have a slightly higher energy density and contain only low toxicity elements.<sup>8</sup> The biggest drawback from nickel-metal hydride batteries is that they are prone to self-discharge, and therefore must not be left in a charged state for too long, otherwise they return a reduced capacity. In industrial uses, when multiple cells are stacked into a larger battery pack, the self-discharge leads to a variation in the state of charge that each cell is in. This can cause cells to be over-discharged, which can damage the lifetime of the cell.<sup>9</sup> However, NMH batteries do have good lifetimes overall, and are low cost with relatively high power densities for a battery. These characteristics have led to them being developed for a variety of applications including consumer electronics, hybrid-electric cars<sup>10</sup> and power grids.<sup>9</sup> Research here focuses on minimising cost and

toxicity of materials used (Co is still used in commercial cells), while improving the lifetime and power and energy densities. It is also desirable to eliminate problems from self-discharge. Another similar issue with these types of batteries is the memory effect. This is where a battery is charged before it has finished a full discharge cycle (this partial discharge will result in a smaller discharge capacity that cycle), and subsequently shows a reduced capacity on further cycles.<sup>11,12</sup>

### **2.3.1.1 Lithium-ion Batteries**

Lithium-ion batteries (LIBs) have dominated the consumer electronics market since being commercialised by Sony in 1991.<sup>13</sup> They have high energy densities and good power densities, which has made them widely used as lightweight batteries in a variety of portable applications from cameras and laptops to phones, and transport applications such as battery-electric and battery-hybrid electric cars. Lithium is the lightest and smallest metallic element which gives lithium-ion batteries these desirable properties. More recently LIBs are being studied as possible batteries for grid-scale energy storage<sup>14</sup>.

LIBs work by the reversible intercalation (or insertion) of  $\text{Li}^+$  between the electrodes. The positive electrode, e.g. a layered transition metal oxide such as  $\text{LiCoO}_2$ ,  $\text{LiNi}_{1/3}\text{Mn}_{1/3}\text{Co}_{1/3}\text{O}_2$  and  $\text{LiNi}_x\text{Co}_y\text{Al}_z\text{O}_2$ , is typically fabricated in the discharged state containing Li. The negative electrode (normally graphite) is a material that can act as a host for Li. Upon charging,  $\text{Li}^+$  ions are extracted from the positive electrode, move through the organic electrolyte, and insert into the negative electrode (Figure 2.2). During discharge this process is reversed. Ideally this can be repeated many times, giving a long-life rechargeable battery. The electrode materials are therefore key to the performance of the battery.

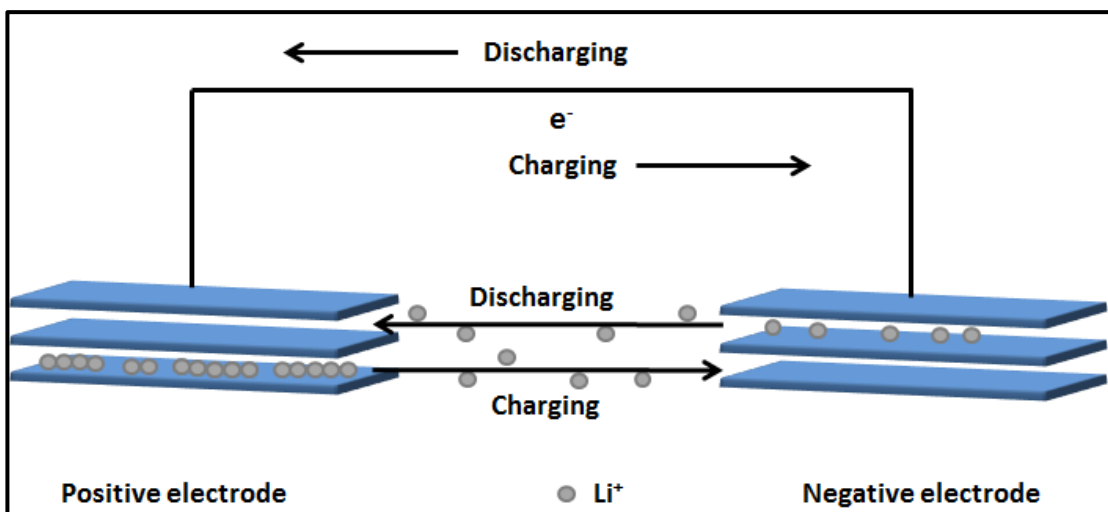


**Figure 2.2.** Schematic representation of a rechargeable lithium-ion battery, showing the  $\text{Li}^+$  ions and electrons,  $e^-$ , moving from the positive electrode to the negative electrode upon charging, and from the negative electrode to the positive electrode upon discharging.

Despite their commercial success, there are several problems with LIBs. One is that lithium is not an easily accessible element, with most reserves in politically sensitive countries, making these batteries relatively expensive. Another is safety, with LIBs having been implicated in a number of high-profile incidents over the last few years. Other limitations of LIBs include environmental and toxicity impacts of elements (e.g. Co) in electrode materials, flammability and lithium plating of electrolytes, relatively low power densities and low energy densities compared to some other technologies and the complexity of stacks of cells for large scale energy storage.<sup>15</sup> In addition, the charging times are typically slow (multiple hours) compared to what is required for many of the new more demanding application areas such as electric vehicles and grid stabilisation and storage (where charge times of minutes would be desirable).

There is a large volume of research currently being carried out on LIBs, with electrolytes, electrode materials and the overall battery management system all under investigation to improve performance. Recently, 2D nanomaterials have shown excellent potential for electrode materials, with high rate capabilities (improving power) and capacities, compared to bulk materials. However, stability issues with these nanomaterials as electrode have so far limited their take up in commercial systems.<sup>16,17,18</sup>

### 2.3.1.2 Sodium-ion Batteries

Sodium-ion batteries (NIBs) are analogous to LIBs, with the only difference being that  $\text{Na}^+$  is the active ion, not  $\text{Li}^+$ . They are the subject of renewed interest in the last few years, after researchers abandoned them in the 1980's to focus on the higher performing LIBs. The resurgence of NIBs is due to the issues with LIBs outlined above, with the cost and abundance of Na a clear advantage over Li. NIBs are expected to be

cheaper and safer with fewer toxicity and environmental issues than LIBs. NIBs do have lower energy and power densities than LIBs, due to the larger ionic size and electrochemical potential of Na<sup>+</sup> compared to Li<sup>+</sup> (Table 2.1).

**Table 2.1.** Comparison of sodium vs. lithium. Adapted from Slater et al.<sup>19</sup>

	Lithium	Sodium
Potential (V vs. SHE)	-3.04	-2.70
Ionic radii (Å)	0.69	1.04
Mass (atomic units)	6.941	22.99
Price (£ per ton, carbonates)	3320	99

This makes them unlikely to replace LIBs in portable applications, but more competitive in stationary applications, such as grid storage, where cost rather than weight is the primary concern. However, they could find future uses as cheaper alternatives to LIBs in transport applications, especially in low-energy vehicles. Research here also focuses on similar challenges to LIBs, with electrode materials again a major topic of research. Since cost is the main driver for NIBs development, it is particularly important to consider the cost of materials for NIBs, although the highest capacity materials reported are based on more expensive 2D materials.

The best performing materials for NIBs currently reported exhibit higher capacities than current commercially used LIBs materials, showing that NIBs can achieve high energy densities. However, these materials have much lower capacities than those reported for the leading LIB electrode materials at equivalent stages of development. For example, Yan et al. reported a reduced graphene oxide/carbon nanotubes sponge negative electrode with a capacity of 436 mAh g<sup>-1</sup> after 100 cycles at a current density of 50 mA g<sup>-1</sup>.<sup>20</sup> Hung et al. reported a large capacity of 241 mAh g<sup>-1</sup> for a P2-NaLi<sub>0.2</sub>Mn<sub>0.8</sub>O<sub>2</sub> positive electrode when cycled between 1.5-4.5 V, with a capacity retention of 78% over 40 cycles.<sup>21</sup> For comparison, LiCoO<sub>2</sub> and LiFePO<sub>4</sub>, typical commercial LIB positive electrode materials, have capacities of around 140<sup>22</sup> and 170<sup>16</sup> mAh g<sup>-1</sup> respectively, while graphite, the typical LIB negative electrode, has a capacity of 372 mAh g<sup>-1</sup>.<sup>22</sup>

### 2.3.1.3 Zinc-ion batteries

Due to the disadvantages of the Li and Na based batteries described above, other metal-ion batteries have been proposed, with some research focusing on multivalent ions, for example, Al-, Zn- and Mg-ion batteries. These systems have some very high theoretical energy densities, since each ion can utilise two or three electrons. However, these batteries are in very early stages of development, with low capacities and generally poor cycling stabilities reported.<sup>23,24</sup>

Of these multivalent batteries, zinc systems are gaining significant interest, in particular for aqueous energy storage systems.<sup>6,7</sup> Zinc is relatively wide-spread in nature, has a large theoretical capacity (over 800 mAh g<sup>-1</sup>) and a low potential (-0.76 vs. standard hydrogen electrode (SHE)).<sup>8,9</sup> Importantly, this potential sits in the stable voltage window for water, making zinc metal compatible with aqueous electrolytes, unlike most elements under consideration for rechargeable energy storage systems.<sup>10</sup> Aqueous electrolytes are of interest since they are inherently non-flammable, which gives them significant safety advantages over systems based on organic electrolytes. However, aqueous electrolytes have significantly reduced voltage windows compared to organic electrolytes, due to the hydrogen and oxygen evolution reactions.<sup>11,12</sup> This gives a thermodynamically stable window of 1.23 V, which limits considerably the energy density of aqueous systems and makes the need to find high energy density electrode materials an urgent priority for these systems.

Zinc is already widely used in primary (non-rechargeable) batteries, but commercial rechargeable systems have not yet been realised, partly due to a lack of electrode materials that can reversibly store Zn<sup>2+</sup> ions. Another reason is because zinc metal forms dendrites (analogous to the Li metal electrodes in organic electrolytes) when used with certain electrolytes, making the systems non-rechargeable in the long-term. However, it is now known that in some neutral and mildly acidic aqueous electrolytes (pH 4 to 6), such as 1 M zinc sulphate (ZnSO<sub>4</sub>) in water, zinc can be reversibly cycled for long duration times without losing significant capacity.<sup>6</sup> This development makes the investigation of electrode materials for zinc-ion systems significantly more feasible.

This is explained by the Pourbaix diagram for Zn metal in an aqueous system, which shows how Zn behaves in different pH conditions (Figure 2.3).<sup>25</sup> This reveals that only in electrolytes in pH 8 or above is Zn able to reversibly plate without involvement of OH side-products, which are known to irreversibly precipitate to ZnO, preventing Zn metal from being able to cycle multiple times in basic conditions. It should also be noted that at pH values below 4, Zn corrosion becomes the dominant process, also preventing stable cycling.<sup>25</sup> Therefore, Zn metal is suitable to use as a reversible electrode in aqueous systems so long as the pH at the electrode surface is in the range of 4-7. Using mildly acidic electrolytes, such as those used in this thesis, in the pH range 4-6 enables the Zn pH to remain in the stable regime even if there are local pH changes near the electrode during cycling. Figure 2.3 also reveals that the potential at which the Zn/Zn<sup>2+</sup> reaction occurs is independent of pH in acidic electrolytes, as long as the local pH does not drop below 8, which should allow its use as a reference electrode in half-cells as is common practice for Li and Na metal in Li- and Na-ion half-cells.

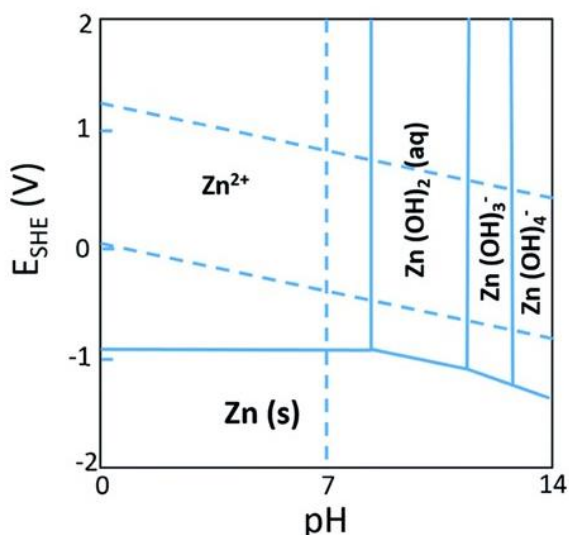


**Figure 2.3.** Pourbaix diagram for Zn metal in aqueous electrolytes. Reproduced with permission from the RSC.<sup>25</sup>

The majority of electrode materials belong to the oxide family and are based on manganese ( $Mn^{4+}/Mn^{2+}$ )<sup>26</sup> and vanadium (e.g.  $V^{5+}/V^{4+}$  in  $V_2O_5$ )<sup>27</sup> redox couples, which store charge based on intercalation mechanisms. However, despite having relatively high capacities, typically between 100-350 mAh  $g^{-1}$ , manganese oxides tend to suffer from poor cycling stability due to manganese dissolution in the electrolyte.<sup>28-30</sup> Vanadium oxides generally have better cycling stability, but lower voltages than manganese-based ones. The capacities are typically around 170-300 mAh  $g^{-1}$ .<sup>31-33</sup> In addition, Prussian blue analogues have recently been studied as a new class of zinc-ion electrode, but have shown low capacities (50-65 mAh  $g^{-1}$ ) despite reasonably high operating voltages (greater than 1.2 V).<sup>34-36</sup> So far, none of these materials classes have been able to meet the demands of a commercial zinc-ion energy storage system.<sup>7</sup> Therefore, there is an urgent need for widespread research into new  $Zn^{2+}$  hosts with stable and reversible electrochemical performance. One difficulty has been that the smaller Zn ion size (0.67 Å) and 2+ charge give rise to poor diffusion kinetics, which has limited the range of available materials. In addition, the materials need to contain multivalent redox centres to allow them to be redox active with Zn. One group of materials which have received lots of attention in other ion systems has been two-dimensional (2D) materials such as graphene.<sup>37-40</sup> These are considered promising electrode materials due to the potential for high surface areas, large open structures between nanosheets, and high electrical conductivity which can result in hybrid capacitor mechanisms giving a combination of high energy densities, high rates and long cycle life. However, there have only been limited reports on the use of 2D materials in zinc-ion systems so far, with the work at a very early stage.<sup>41-43</sup>

### 2.3.2 Supercapacitors

Supercapacitors are often described as a bridge between low power, high energy density batteries and high power, low energy density capacitors (Figure 2.4). Conventional dielectric capacitors have very high power densities, but the capacitance is typically measured in micro-farads, which leads to tiny energy densities. Consequently, they are typically only used in a few applications where a small amount of energy is required to be delivered quickly. On the other hand, supercapacitors can have capacitances measuring over 1,000 F, while maintaining high power densities. They can be charged and discharged very rapidly (in seconds if required) and are stable for thousands of cycles giving them long life. Therefore, they have complementary properties to typical batteries.

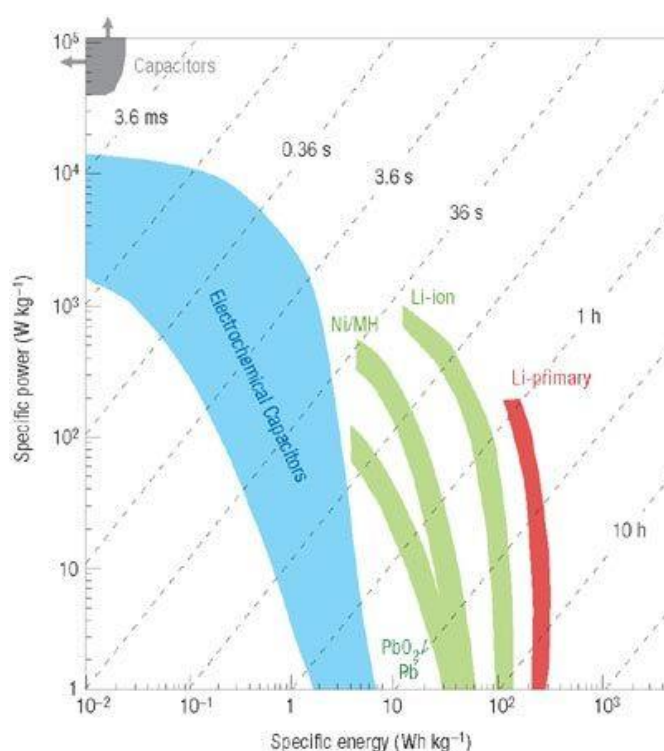


**Figure 2.4.** Ragone plot comparing energy and power densities of supercapacitors to various battery technologies. Reproduced from Springer Nature, Nature Materials, Simon et al., 2008, with permission.<sup>44</sup>

The differences in the properties of supercapacitors and batteries arise from the different charge storage mechanisms which occur in each device. In batteries, energy is stored in the bulk of the material, allowing higher energy density (none of the active material is wasted) but leading to slower reaction kinetics, which limits the power. In supercapacitors, energy is stored only on the surface, which allows for fast reactions kinetics (high power) but low energy density since atoms below the surface cannot participate in storing energy.

There are two main classes of supercapacitors: electric double layer (EDL) supercapacitors and pseudocapacitors. The names are related to the charge storage mechanism. Hybrid capacitors that make use of both mechanisms also exist.

### **2.3.2.1 Electric Double Layer Supercapacitors**

In EDL supercapacitors, energy is stored through the formation of an electric double layer at the interface between the electrode and the electrolyte. They form whenever a charged solid is placed into a liquid. To counteract the charge that accumulates on the surface of the solid, the ions in the liquid self-organise with ions holding the opposite charge on the surface accumulating in the liquid near the interface. In supercapacitors, this occurs on both electrodes. When a supercapacitor is charged, electrons migrate through an external circuit from the positive electrode to the negative electrode. This causes charge imbalance that is counteracted by cations forming an EDL near the surface of the negative electrode and anions congregating at the positive electrode. While simple models exist for describing the behaviour of ions in EDLs, e.g. Helmholtz model, these are insufficient for the complex behaviour in porous electrodes used in supercapacitors. This has led to the development of more complex models for these systems, but to date, none provide full understanding for the behaviour of ions in supercapacitors.<sup>45</sup>

### **2.3.2.2 Pseudocapacitors**

In pseudocapacitors, charge is stored through fast highly reversible reactions on the surface of the electrodes. This leads to higher energy densities than for EDL capacitors (capacitance can be up to 100x higher), but the reactions can cause volume changes and potentially cracking in the electrodes, in a similar way to what occurs in batteries, which could reduce the lifetime of the cell. The power density is often lower than for EDL capacitors, since charge storage processes are slower than electric double layer formation. There are a variety of mechanisms that are classed as pseudocapacitive including redox reactions, intercalation and reversible doping which is often seen in polymer electrode materials. Pseudocapacitive materials can be classed as either intrinsic or extrinsic. In extrinsic capacitive materials, capacitance is introduced to materials that do not usually show capacitive energy storage via materials processing, for example, nanosizing.<sup>46</sup>

The charge storage mechanism may be identified by a variety of characterisation techniques such as cyclic voltammetry, galvanostatic cycling and impedance spectroscopy. Often a combination of techniques will be needed, since the differences can be very subtle.<sup>46</sup> The mechanism of charge storage is dictated by the properties of the electrode material and electrolyte used.

### 2.3.2.3 Hybrid Metal-ion Capacitors

Hybrid, or asymmetric, capacitors are a third class on supercapacitor devices. In these devices two different electrode materials are used on the negative and positive electrode. Typically this would be a carbon electrode with an alternative pseudocapacitive electrode. These can give a higher energy density than typical supercapacitors due to increasing the electrochemically active voltage range.<sup>45</sup> In addition, the combination of charge storage from EDL and pseudocapacitive mechanisms allows for a greater capacitance (and therefore energy density) than symmetric supercapacitors and faster charge storage (and therefore power densities) than batteries or all redox pseudocapacitors. When a typical battery electrode is paired with a capacitive electrode (EDL or pseudocapacitive) in a battery electrolyte, these hybrid asymmetric capacitors are called hybrid metal-ion capacitors. For example, a graphite negative electrode paired with an activated carbon positive electrode using a LiPF<sub>6</sub> EC-DEC electrolyte is called a lithium-ion (hybrid) capacitor.

These devices have large voltage windows due to the highly stable LIB electrolytes (which can perform up to around 4.5 V in LIBs), relatively fast charge times (less than 10 min) due to the EDL capacitive charge storage on the activated carbon positive electrode and high energy densities (over 4 times that of EDL supercapacitors) as a result of the high capacity graphite intercalation electrode. This type of device has already been commercialised by Taiyo Yuden Ltd., who claim their devices can achieve up to 100,000 charge-discharge cycles and deliver 4 times the energy density of EDL capacitors with a voltage of 3.8 V.<sup>47</sup> Therefore they are considered a promising technology to bridge the energy-power gap between traditional supercapacitors and batteries.

However, due to the differing charge storage mechanisms, these devices suffer from kinetic and capacity mismatches between the two electrodes. Battery materials cannot store charge as rapidly as EDL electrodes, and EDL electrodes store many times less charge per weight than the battery electrodes, leading to significantly thicker EDL electrodes compared to the battery side. This means that there is an urgent need to develop materials which can store charge in similar quantities as typical battery materials and at similar rates to EDL electrodes. MXenes have shown early promise in this technology area, therefore metal-ion capacitors is the application chosen to develop the porous MXenes towards in this thesis. As well the Li-ion capacitors, Na-ion and Zn-ion capacitors are also studied, due to the advantages of using these elements in energy storage systems as outlined in the battery section (Section 2.3.1).

### 2.3.3 Electrolytes

The energy ( $E$ ) stored in a supercapacitor is given by Equation 2.1:

$$E = 0.5 C V^2 \quad \text{Equation 2.1}$$

where  $C$  is the capacitance and  $V$  is the working voltage of the cell. Therefore, while high capacitance electrode materials are clearly important for the development of supercapacitors with a high energy density, it is equally important to increase the voltage that the cell can work at (since this contributes to the energy stored with a power of two). The major route to improving this is the electrolyte, since it is generally the decomposition voltage of the electrolyte that dictates the stable voltage window for the cell. There are three main types of electrolyte for supercapacitors: aqueous, organic and ionic liquids.

#### 2.3.3.1 Aqueous Electrolytes

There are a number of different aqueous electrolytes, with different conductivities and ionic radii. This influences the capacitance, energy density and kinetics (power). Typically, aqueous electrolytes are stable between 0-1.0 V. This is because of decomposition of water via electrolysis at higher cell voltages, which limits the voltage window of aqueous electrolytes.<sup>48</sup> They are generally safer and cheaper than organic electrolytes, with higher concentrations and smaller ionic radii which allows for higher capacitance. The smaller ionic radii allows for access to smaller pores, which may be inaccessible to organic electrolyte ions. Common aqueous electrolyte salts include,  $\text{NaSO}_4$ ,  $\text{MgSO}_4$ ,  $\text{NaCl}$ ,  $\text{H}_2\text{SO}_4$ ,  $\text{KOH}$  and  $\text{ZnSO}_4$ , which are dissolved in water as the solvent (Figure 2.5a).

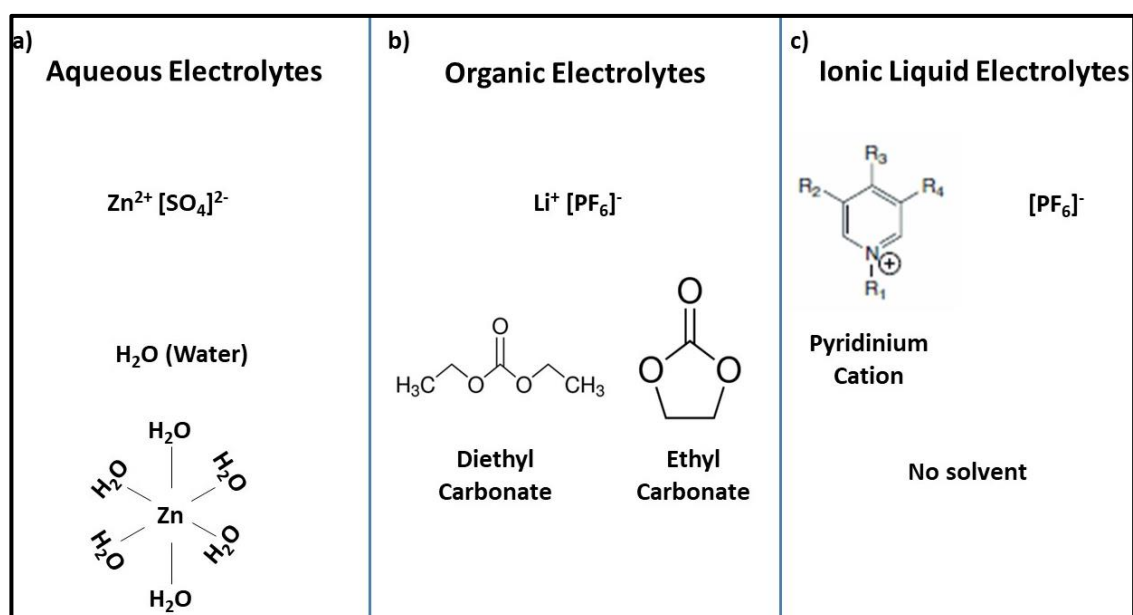


**Figure 2.5.** Example salts and solvents that make up typical a) aqueous b) organic and c) ionic liquid electrolytes.

Due to the water splitting reactions severely limiting the useable voltage window in aqueous systems, there has also been research carried out on extending the voltage window. This has included using different electrode materials to make asymmetric capacitors and by studying the effect of electrolyte concentration on the water splitting reactions. For example, more concentrated electrolytes will have less free water, since most molecules are in the solvation shells. Taken to extremes, this has led to the development of water-in-salt electrolytes, where the number of water molecules present in the electrolyte is less than the number of salt ions. This means that there is almost no free water in the electrolyte, giving voltage windows up to 3 V, similar to many organic systems.<sup>49</sup> However, these systems will have significant extra mass and cost from such high salt loadings, which may limit their future use. In addition, these are relatively early in their development, and not currently fully understood. Therefore, the work on aqueous electrolytes in this thesis focuses on more traditional electrolytes, with concentrations less than 1 M.

### **2.3.3.2 Organic electrolytes**

Organic electrolytes use organic solvents rather than water as the solvent to dissolve the salts (Figure 2.5b). They are more electrochemically stable than aqueous ones, and therefore can be cycled in a wider voltage window, with up to 3.5 V achievable.<sup>50</sup> This leads to organic supercapacitors generally having a higher energy density than aqueous ones, and explains why they are generally used commercially. Disadvantages of organic electrolytes include lower ionic conductivity (lower power), larger ionic radii (lower capacitance), flammability, safety and cost.<sup>51</sup> A large aspect of the cost is the need to remove water from the electrolyte, otherwise water electrolysis would occur. Common organic electrolyte solvents include acetonitrile, diethyl carbonate and propylene carbonate with tetraethylammonium tetrafluoroborate, tetraethylphosphonium tetrafluoroborate, triethylmethylammonium tetrafluoroborate and  $\text{LiPF}_6$  used as salts.<sup>51</sup> Toxicity can also be an issue with organic electrolytes, for example in acetonitrile, which is a common solvent.<sup>45</sup>

### **2.3.3.3 Ionic liquid electrolytes**

Ionic liquids are salts which are liquid (or molten) at relatively low temperatures, removing the need for a solvent to be used to dissolve a salt, as is the case in aqueous and organic electrolytes (Figure 2.5c). For energy storage applications, the most suitable ionic liquids are molten in the temperature range from around -20 to 60 °C, which is a desirable temperature range for devices. They have very wide voltage stability windows, with up to 6 V has being reported, but have the largest ionic radii, highest cost, and lowest conductivity (typically) of the three classes of electrolyte.<sup>45</sup> Despite having the largest ionic radii, the absence of any solvent means

that the solvation shell (and therefore the total ion size) is better known. The high voltages may enable high energy densities in future supercapacitors.

#### **2.3.4. Mechanisms of Charge Storage**

As mentioned previously, there are several different charge storage mechanisms which can be exploited in electrochemical energy storage devices. These vary depending on the choice of electrode materials and electrolyte, and have a significant impact on the overall device performance characteristics. Consequently, the charge storage mechanism should be considered and understood as well as possible when designing new electrode materials. Therefore, the different charge storage mechanisms, with example electrode materials, are now discussed in more detail.

#### **2.3.5 Battery Charge Storage Mechanisms**

Battery materials store charge via faradaic charge transfer redox reactions.<sup>6</sup> For example, in a lithium-ion battery,  $\text{Li}^+$  ions are reversibly gained and lost from the active electrode materials, which also simultaneously gains or loses one electron per  $\text{Li}^+$  ion. These electrons travel round the external circuit (between the electrode materials) where they either power the desired device (discharge) or are forced across by an applied current (charge).<sup>6</sup> When a current is neither being drawn nor applied the electrons are stored with the  $\text{Li}^+$  ions in the electrode material. Therefore, electrode materials must be able to: reversibly store  $\text{Li}^+$  ions (they must have available sites and have the ability to undergo redox reactions with  $\text{Li}^+$  ions at suitable potentials), transfer  $\text{Li}^+$  ions (be good  $\text{Li}^+$  conductors) and transfer electrons (good electrical conductors).<sup>52</sup> Since most  $\text{Li}^+$  sites in typical battery materials are located within the bulk of the structure (not on or near the surface) the  $\text{Li}^+$  ions must undergo solid state diffusion through the electrode material to reach the active site.<sup>46</sup> This gives battery materials their slow charging times, which is problematic for their development in metal-ion capacitors. There are several strategies that have been proposed for improving the diffusion rates and therefore charging times for these materials including nanosizing and nano-structuring techniques.<sup>52,53</sup>

Typically, the charge transfer reactions utilised in battery materials are accompanied by phase changes (structural changes) in the material. These give rise to voltage plateaus on the charge-discharge curves for these materials, which gives the battery its characteristic nearly constant operating voltage.<sup>46</sup> In turn, these voltage plateaus give batteries higher energy densities than supercapacitors, since they typically lead to higher energy densities. For example, a battery may operate near its maximum voltage for its entire charge/ discharge, giving it a high average voltage. On the other hand, a supercapacitor, which has a linear voltage profile, would have an average voltage half that of its maximum.<sup>46</sup> Since energy density is the product of charge

stored and voltage, the average operating voltage, and therefore location (voltage) at which any plateau exists, has a large impact on the overall energy density of the cell.<sup>5,54</sup> It should be noted that the total cell voltage is the voltage of the positive electrode minus that of the negative electrode. Therefore, it is desirable for a positive electrode to have an operating voltage as high as possible and for a negative electrode to have an operating voltage as low as possible, whilst being aware of metal plating concerns around 0 V vs.  $M^+/M$ , which can cause safety issues if the metal, M, can form dendrites.<sup>5</sup>

As well as giving rise to distinctive voltage plateaus, these phase transitions are often a source of capacity fade upon repeated cycling within battery cells.<sup>54</sup> This can be as a result of the phase transitions not being fully reversible, and need to accommodate (at least) two crystal structures within an electrode. This may cause significant size mismatches, causing mechanical failures in the electrode upon multiple cycles.<sup>52</sup> This explains why battery materials often have significantly reduced cycling lifetimes compared to supercapacitor electrodes, which do not undergo such phase transitions.<sup>46</sup>

There are four distinct classes of charge storage reactions found in battery materials: intercalation, insertion, conversion and alloying reactions. Of these, intercalation, conversion and alloying reactions have relevance to the materials studied in this thesis, and so are discussed in more detail below.

#### **2.3.5.1 Intercalation Reactions**

Intercalation reactions are where the charge carrying ion, for example  $Li^+$  in Li-ion systems, enters the space between two layers of a layered material to undergo the charge storage reaction. They can be thought of as an insertion reaction, but where the host material is layered (insertion materials typically have channels or tunnels which do not arise from layered structures). This is the charge storage mechanism utilised in common commercial Li-ion battery materials, where both the positive electrode (e.g.  $LiMO_2$ , where M is one of or a combination of transition metals such as Co, Mn or Ni) and the negative electrode (graphite) are layered materials where the  $Li^+$  ions enter/ leave between the layers (intercalate/ de-intercalate).<sup>54</sup> Intercalation materials often can achieve high specific capacities and charging rates as a result of 2D diffusion channels between each layer which allows for large amounts of ions to be stored and easy diffusion through the 2D channels. Depending on whether the intercalation products are solid solutions or new phases, intercalation reactions can give voltage profiles with sloping profiles or plateaus.

The intercalation of layered materials by ions is typically associated with a volume change as the layers separate, expanding the interlayer space to accommodate the intercalating ion. These volume changes can cause capacity fade over long term

cycling.<sup>54</sup> Therefore, there is significant interest in developing zero-strain materials that do not show large volume changes upon intercalation. In addition, the amount of charge that can be stored is often limited by the available space for ions between the layers.

The interlayer spacing is known to be highly important for intercalation electrodes. If the interlayer spacing is too small, the charge carrying ion cannot enter between the layers, which prevents that material being a usable electrode. For example, it is well known that Na<sup>+</sup> cannot intercalate into graphite, which prevents its use in Na-ion batteries. If expanded graphite, with a larger interlayer spacing is used, then reversible Na<sup>+</sup> intercalation becomes possible.<sup>55</sup> Hard carbons, which cannot transform to graphite, have open structures that can allow relatively high Na-ion capacities (between 280-400 mAh g<sup>-1</sup>), which makes them the current state-of-the-art for Na-ion negative electrodes.<sup>56</sup> MXenes have been shown to store charge in both Li and Na-ion systems via intercalation processes, which makes these results significant for the further development of MXene electrodes.

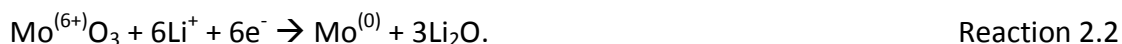
### 2.3.5.2 Conversion reactions

Conversion reactions are a group of reactions which involve the formation of entirely new products during cycling, with the charge carrying ion typically reacting to reduce the active transition metal and form a product with an anionic species such as oxygen sulphur or fluorine. This is demonstrated by Reaction 2.1.<sup>57</sup>



Here Tm<sup>(n)</sup>X is a transition metal oxide, sulphide or fluoride where the transition metal has an oxidation state greater than 0, ion<sup>+</sup> is the charge carrying ion (e.g. Li<sup>+</sup>) and e<sup>-</sup> is the electron consumed/ generated. Ideally, this would be a fully reversible reaction to allow for multiple charge-discharge cycles. Typical materials which undergo conversion reactions include transitional metal oxides such as Mn<sub>3</sub>O<sub>4</sub>, MoO<sub>3</sub> and Fe<sub>3</sub>O<sub>4</sub> and transition metal sulphides such as MoS<sub>2</sub>, Fe<sub>2</sub> and TiS<sub>2</sub>.<sup>57</sup>

For example, the lithiation of MoO<sub>3</sub> can undergo the following conversion reaction:



Conversion reactions are considered very promising for the development of the next generation high capacity negative electrode materials since they provide very high specific capacities, potentially up to 1,500 mAh g<sup>-1</sup>, which are much larger than what is typically achieved by intercalation electrodes.<sup>58</sup> For example, each MoO<sub>3</sub> unit can accommodate six Li<sup>+</sup>, whereas each C in graphite only stores 1/6 Li<sup>+</sup> (i.e. the lithiation product is C<sub>6</sub>Li, where each Li<sup>+</sup> is stored within a C<sub>6</sub> ring).<sup>59</sup> However, since the reactions produce products which are completely different to the starting reactants,

this mechanism is accompanied by large volume changes, with the products often having volumes many times that of the starting materials.<sup>58</sup> This leads to severe particle and electrode cracking, which hinders the reversibility of these reactions and causes significant capacity fade over multiple cycles.

There have been several different strategies attempted to overcome this capacity fade, including alternative binders, composite electrodes and nanosizing/nanostructuring. For example, combining conversion electrodes with conductive carbon materials has been shown to help overcome the low electrical conductivity of the conversion material, while the carbon material may provide structural support to the electrode.<sup>57</sup> Nanostructuring can reduce the ion diffusion pathways, and make the materials more structurally stable to the large volume changes, particularly if the structure contains free space to accommodate the conversion product during cycling.<sup>60,61</sup>

### 2.3.5.3 Alloying reactions

Alloying reactions have some similar features to conversion reactions, in that they involve the formation of products which are very different to the starting materials, have very high theoretical capacities and undergo huge volume expansions which cause rapid capacity fade upon repeated cycling.<sup>54</sup> The products are alloys of the starting material with the charge carrying ion. For example, Si undergoes an alloying reaction with Li as shown in Reaction 2.3.



This reaction gives Si a theoretical capacity of  $3,780 \text{ mAh g}^{-1}$ , which is similar to metallic Li itself.<sup>62,63</sup> However, the volume expansion is over 300%, which severely limits the capacity on multiple cycles. Other alloying electrodes include Sn, Ge,  $\text{SiO}_2$ , and P, all of which share similar characteristics.<sup>64,65</sup>

As for conversion reactions, there has been significant research to try and overcome the volume changes and subsequent capacity fade, which have mostly focused on alternative binders, composite electrodes and nanosizing/nanostructuring.<sup>63</sup>

As well as the idealised cases where only one of these mechanisms occurs, electrodes can display mixtures of mechanisms (e.g. intercalation followed by conversion) depending on the state of charge and electrode chemistry.

### 2.3.6 Supercapacitor Mechanisms

There are two main mechanisms for capacitive charge storage, electric double layer and pseudocapacitance. Pseudocapacitance can then be divided into redox pseudocapacitance and intercalation pseudocapacitance. These mechanisms are outlined in more detail in this section.

### 2.3.6.1 Electric double layer capacitance

Electric double layer capacitance (EDL) occurs when a charged electrode is placed into an electrolyte. Charge builds up on the surface of the electrode, which is charge balanced by the build-up of counter ions (of the opposite charge) from the electrolyte at the electrode-electrolyte interface. This is a strictly physical mechanism, with no charge transfer or other chemical reaction occurring.<sup>66</sup> This allows for electrodes to store charge very rapidly, limited only by the speed at which counter ions can reach the electrode surface. This gives supercapacitors which utilise this type of charge storage (usually based on high surface area carbons) very high rates (charging times can be seconds) and long cycling lifetimes (up to 1,000,000 cycles).<sup>67</sup> However, energy densities are low, (typically an order of magnitude lower than batteries) and they also suffer from high self-discharge rates if not discharged soon after charging (as a results of ions not being chemically bonded to the electrodes). Since no phase changes occur, this charge storage mechanism give very linear voltage profiles, with no plateaus, which means that the device voltage varies continually on cycling.<sup>67</sup>

The amount of charge stored depends highly on the surface area available for charge storage, i.e. how much of the electrode surface is exposed to the electrolyte. This means that a large amount of research aiming to improve the performance of EDL electrode materials for supercapacitors focused on ways to increase the surface area of the electrode materials.<sup>68</sup> More recently, the importance of pore size has also been highlighted, with it being demonstrated that the capacitance can significantly increase when the pore size is close to that of the electrolyte ions being stored.

Specifically, it has been reported that pore sizes of less than 1 nm lead to an increase in capacitance.<sup>69</sup> This was put down to a desolvation effect, meaning that only the electrolyte ion with no solvation shell is adsorbed onto the surface, which maximises the ion concentration on the surface.<sup>70</sup> However, some studies have been carried out recently finding no increase in capacitance with sub-nanometre pores.<sup>71</sup> It should also be noted that if pores are less than the ionic radii of the electrolyte (typically about 0.5 nm) then these pores will not be utilised for charge storage.<sup>72</sup> It is also thought that it is beneficial to have some larger pores to act as fast ion transport channels, which allows for fast rates since ions can quickly reach adsorption sites in the material. It has also been reported that the optimal pore size depends upon the operating voltage, with a higher voltage device benefitting from a larger pore size.<sup>73</sup> More recently, it has also been shown that charge screening by the ions as they pack inside the pores plays an important role in the increases in capacitance in sub-nanometre pores. Overall it is accepted that it is important to carefully control the pore size and structure in potential electrode materials, and to match the material structure to the electrolyte used. Largeot et al. claimed that even a 1 Å mismatch

between the ion and pore sizes led to a decrease in capacitance.<sup>70</sup> The ideal electrode structure likely features a large number of small pores which allow for efficient ion packing and high charge storage while also containing several large pores which act as fast transport channels for the ions to allow for fast rate performance.

It has also been discovered recently that the classical model for EDL capacitors whereby counter ions are brought into pores to counter an applied charge is not necessarily correct. NMR studies have demonstrated that ions (of both charges) enter the pores even without charging.<sup>74</sup> This leads to three possible mechanisms for charge storage. One is for further counter ions (ions with the opposite charge to the electrode) to enter the pore, as per the classical model which was called counter-ion adsorption. Another is for a co-ion (with the same charge as the electrode) to be expelled from the pore, which was termed co-ion expulsion. Finally, ion exchange may occur, where a co-ion is expelled and a counter-ion adsorbed into the pore. While these studies have mainly focused on carbon electrodes, it has been shown using in-situ Raman Spectroscopy, that depending on the electrolyte used, MXenes also show different ion movements depending on the electrolyte used.<sup>75</sup>

It should be noted that EDL capacitance will occur for any charged electrode placed in an electrolyte, therefore even traditional battery materials have some contribution from EDL capacitance. However, because the specific surface area of these materials is typically very low, this contribution is generally negligible compared to the total charge stored via the redox reactions.

### **2.3.6.2 Pseudocapacitive charge storage mechanisms**

Pseudocapacitive charge storage differs from EDL capacitance in that ions are not just physically stored on the electrode surface, but undergo a charge transfer (faradaic) reaction with the electrode.<sup>46</sup> This allows higher levels of charge to be stored than EDL capacitance (since ions are typically desolvated for redox reactions and efficiently stored at active redox sites), and, since the ions are chemically bonded to the electrode, gives significantly lower self-discharge rates. Unlike battery mechanisms, these reactions occur without major phase changes, which avoids the volume and structure changes that typically cause capacity fade, and generally occur on or near the surface, which avoids the solid-state diffusion which causes slow charging times.<sup>46</sup> This gives pseudocapacitive materials energy and power densities between that of EDL capacitance and battery mechanisms. Typically, pseudocapacitive reactions are classed as surface redox reactions, such as is known for transition metal oxides such as RuO<sub>2</sub> and MoO<sub>2</sub>.

RuO<sub>2</sub> was the first material reported to show pseudocapacitance in 1971.<sup>76</sup> This comes from faradaic charge transfer reactions like those seen in batteries ( $\text{Ru}^{4+} \rightarrow$

Ru<sup>3+</sup>), but showed capacitor behaviour on cyclic voltammograms (rectangular). It has many desirable properties as a supercapacitor electrode material including high capacitance and high electrical conductivity. Studies on RuO<sub>2</sub> have shown that the pore structure of RuO<sub>2</sub> is very important, since the redox behaviour occurs on at near the surface, with capacitance values over 700 F g<sup>-1</sup> being reported for nanostructured hydrated RuO<sub>2</sub>.<sup>77</sup> Hydration gives the material high proton conductivity, which balances the Ru<sup>4+</sup> / Ru<sup>3+</sup> redox couple through Reaction 2.4.



The main disadvantage of RuO<sub>2</sub> is the very high cost, which makes it impractical for use in commercial capacitors.

MnO<sub>2</sub> is another heavily studied material that shows pseudocapacitive behaviour. Like RuO<sub>2</sub>, it has shown high capacitance but has the advantage of being cheap and abundant, giving it an economic advantage. However it has a low electrical conductivity (10<sup>-3</sup> S cm<sup>-1</sup> compared to 10<sup>4</sup> S cm<sup>-1</sup> for RuO<sub>2</sub>)<sup>78</sup> which lowers the capacitance by restricting charge storage to a very thin surface layer. Another issue is that Mn<sup>3+</sup> is known to disproportionate which reduces the stability and lifetime of the electrode. High capacitance is only seen in thin films (over 1,000 F g<sup>-1</sup> has been reported), but in thicker more practical samples, 250 F g<sup>-1</sup> is more typical.<sup>46</sup> The studies on MnO<sub>2</sub> have shown two interesting trends related to electrode structure. One is that crystalline materials showed higher capacitance than amorphous ones, due to ion intercalation as an additional pseudocapacitance mechanism in these materials.<sup>78</sup> The second is that capacitance was not strongly correlated to surface area, as had widely been assumed. This indicates charge storage beneath the surface, thought to be through shallow ion intercalation.<sup>46</sup> V<sub>2</sub>O<sub>5</sub> and TiO<sub>2</sub> also show pseudocapacitance through shallow ion intercalation, with increased capacitance seen for materials with larger gaps between the layers.<sup>46,79</sup>

Typically however, traditional redox pseudocapacitors utilise only the electrode surface, or near surface, for charge storage, giving charge storage levels significantly below that of battery mechanisms.

### 2.3.6.3 Intercalation pseudocapacitance

A promising solution to this problem is intercalation pseudocapacitance. This charge storage mechanism relies on the intercalation of ions between layers with a subsequent redox reaction, as discussed for battery mechanisms, but occurs across a wide voltage range without phase transitions giving a sloping voltage profile, as observed for capacitors.<sup>46</sup> Most importantly, these intercalation reactions are not diffusion-limited as is the case in typical battery materials, but by the electron transfer at the electrode surface.<sup>80</sup> This means that ions can be stored in the bulk of the electrode, not restricted to the surface as for typical capacitive mechanisms, but

with rapid ion diffusion the charging and discharge times are also fast.<sup>81</sup> Therefore, intercalation pseudocapacitance provides the opportunity to combine the high charge storage characteristics and low self-discharge of battery materials with the fast charging and long lifetimes of supercapacitor mechanisms (Figure 2.6).<sup>46</sup> This suggests that devices based upon this charge storage mechanism may be able to deliver high power and energy densities for 1,000s of charge-discharge cycles. Since hybrid metal-ion capacitors need to address the kinetic imbalance between the EDL mechanism on the carbon electrode and the battery-type electrode,<sup>82</sup> materials based on a pseudocapacitive intercalation charge storage mechanism seem to be well suited for this device class. As was the case for EDL capacitance, the electrode structure has a significant effect on intercalation pseudocapacitive materials, especially when nanostructured, and needs to be well designed to achieve both high charge storage and fast charging times.<sup>80</sup>

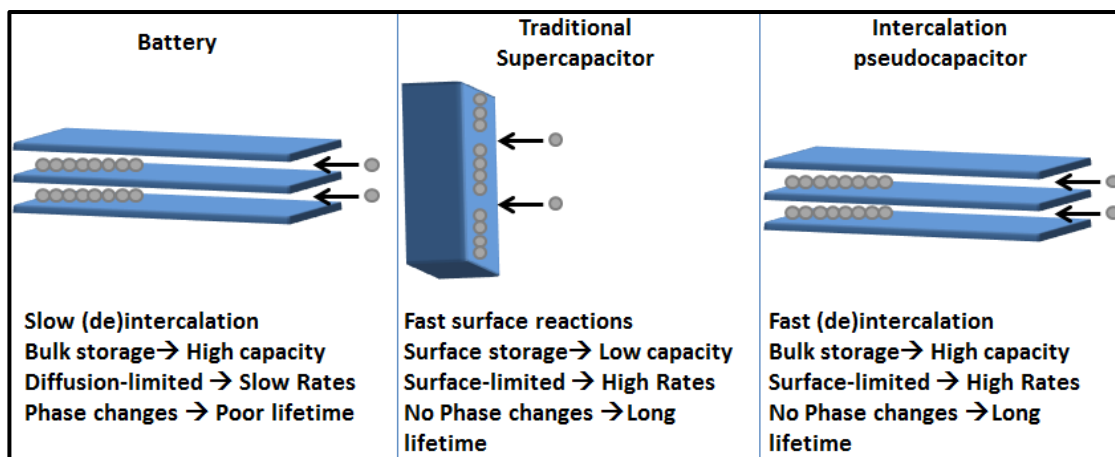


**Figure 2.6.** Schematic representing the different class of redox-based charge storage mechanisms displayed by electrochemical energy storage materials.

Perhaps the most studied class of materials displaying this charge storage mechanism are niobium oxides, which have been shown to undergo intercalation pseudocapacitance in organic Li-ion systems. In particular, orthorhombic T-Nb<sub>2</sub>O<sub>5</sub>, which is a layered material with large 2D ion-diffusion channels, has shown large capacities (90-145 mAh g<sup>-1</sup>) even at very high rates (2-5 A g<sup>-1</sup>).<sup>83</sup> Although these results were typically obtained from electrodes with low mass loadings, Sun et al. showed that capacities of 145 mAh g<sup>-1</sup> could be achieved at 2 A g<sup>-1</sup> even at a mass loading of 11 mg cm<sup>-2</sup>, which is comparable to practical commercial cells.<sup>83</sup> It should be noted that Nb<sub>2</sub>O<sub>5</sub> has relatively low electrical conductivity, which means it is often combined with carbons such as graphene to achieve these high rate electrodes. Apart from cost, a main drawback of Nb<sub>2</sub>O<sub>5</sub> is that the capacities obtained at low rates are significantly less than graphite, with 160-185 mAh g<sup>-1</sup> typically reported.<sup>83</sup> In addition, the capacity is stored above 1 V vs. Li<sup>+</sup>/Li, which limits the energy density of a full cell. This is a similar problem to lithium titanate, an alternative high power

(insertion) electrode, the use of which in lithium-ion capacitors has been limited due to the high potential (1.55 V vs.  $\text{Li}^+/\text{Li}$ ) and low capacities (125-175  $\text{mAh g}^{-1}$ ), despite good rate performance (e.g. 110-130  $\text{mAh g}^{-1}$  at 10C, 6 min charge).<sup>84</sup> Therefore, even niobium oxides do not sufficiently bridge the gap between high power and high energy materials.

In real electrochemical systems, it can be common to observe complex charge storage mechanisms whereby a combination of the above mechanisms occurs simultaneously and each contribute to the total charge storage. This is particularly the case for nanomaterials, where small particle sizes mean that the faradaic contributions are particularly sensitive to electrode architecture as to whether they are diffusion-limited (battery-like) or surface-limited (pseudocapacitive-like).<sup>85</sup> In addition, the inherently larger surface areas of nanomaterials compared to bulk materials means that the contribution from EDL capacitance is no longer negligible as it is for the bulk counterparts. If a material is nanosized below a certain threshold, it has also been reported that typical phase transitions seen in battery materials (such as  $\text{LiCoO}_2$ ) may be suppressed, which further complicates the assigning of the charge storage mechanisms of different materials.<sup>53</sup> Surface functional groups, which can make up a much higher proportion of the overall nanomaterial compared to bulk materials, can also contribute to the charge storage processes, potentially with different mechanisms to the underlying material.<sup>80</sup> Overall, this means that understanding the charge storage mechanism of nanomaterials, including MXenes, can be very complicated, and should be carefully investigated to allow for the effect of different electrode architectures to be understood as well as possible.

## **2.4 MXenes**

### **2.4.1 Synthesis and Precursors**

MXenes are a family of recently discovered 2D “graphene-like” materials. They were discovered by Naguib et al. in 2011,<sup>86</sup> and have since become increasingly studied as materials with an interesting mix of properties, making them potentially suitable for a large variety of applications, including electrochemical energy storage. They are generally derived from a parent “MAX” phase, which are a class of hexagonal ternary layered materials that have been studied for several decades. The term “MAX” phase was first used in 2000 and relates to the chemical composition of the compounds.<sup>87</sup> The M elements are early transition metals, namely: Sc, Ti, V, Cr, Zr, Nb, Mo, Hf, Y W, and Ta. The A elements are from columns 13-16 of the periodic table: Al, Si, P, S, Ga, Ge, As, In, Sn, Tl and Pb (Cd, group 12, has also been reported to act as an A element). X elements are either C and / or N. This is summarised in Figure 2.7.



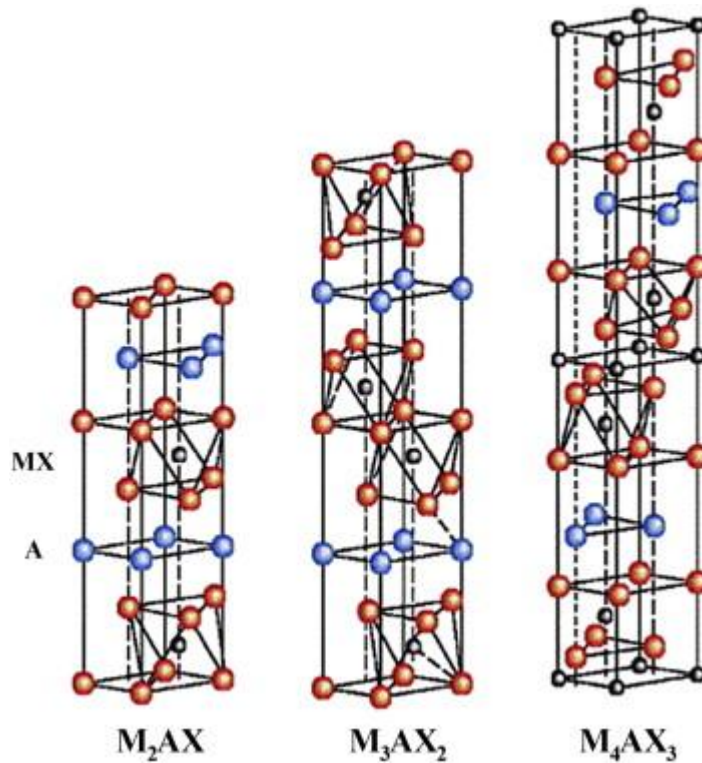


**Figure 2.8.** Crystal structures of the 211, 312, and 413 MAX phases. Reproduced from *Thin Film Solids, The  $M_{n+1}AX_n$  phases: Materials science and thin-film processing, 1851-1878, 2010, Eklund et al. with permission from Elsevier.*<sup>89</sup>

Several possible ways of synthesising MAX phases have been reported such as sputtering to synthesise thin films,<sup>90</sup> however by far the most common method is to use a simple solid state reaction at high temperatures under an inert atmosphere. For example,  $Ti_3AlC_2$  is normally made by mixing stoichiometric amounts of Ti, Al and C (as graphite) using a ball mill before reacting at 1,400-1,700 °C under argon gas for 1-4 h. Although reaction conditions vary slightly, this is a very common synthesis method and how the vast majority of MAX phases are synthesised in the literature.

#### 2.4.1.1 HF-based MXene synthesis

In 2011, it was reported that the A layer could be selectively etched by immersion in hydrofluoric acid (HF), without altering the M and X layers. This created 2D-like layered materials, which were dubbed MXenes by the authors. This was to signify the close relation to the MAX phases, with M and X relating to the same elements as in the parent phases. The suffix “ene” was added to emphasise the similarity with graphene, the most famous 2D material known which can be made down to monolayers one atom thick and has a number of interesting and potentially useful properties. Therefore MXenes are part of the growing family of 2D materials which includes graphene, transition metal dichalcogenides such as  $MoS_2$  and  $WS_2$ , and hexagonal boron nitride. The removal of the A layers means that the M and X elements are no longer fully co-ordinated, therefore surface terminations have been

shown to form, namely O, OH and F. This gives a full formula for MXenes as  $M_{n+1}X_nT_x$  where  $M_{n+1}X_n$  is derived from the parent MAX compound, and T is the surface termination group present. This is a simplification however; in most real systems a mixture of the possible T groups are present. The termination groups come from the solution the etching was carried out in. Aqueous solutions of HF are used in the synthesis which is the source of the O and OH groups. F terminations originate from the F ions from the etching solution. This process is represented in Figure 2.9.

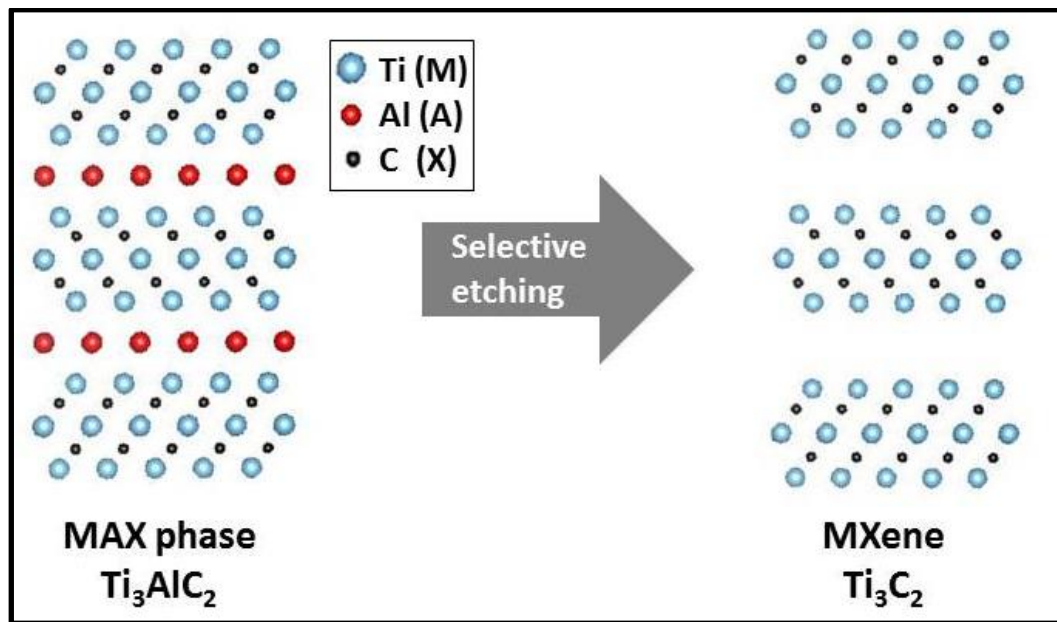


**Figure 2.9.** Schematic of the exfoliation process for  $Ti_3AlC_2$ . The termination groups have been removed for simplicity.

The 2D layers are of course not as thin as graphene, since even a monolayer of bare  $M_2X$  (the MXene with the smallest number of constituent layers), still contains three layers of atoms, as well as termination groups. The etching reaction with HF is thought to proceed according to the three reactions shown below.



Reaction 2.5 explains the removal of the Al (the A) layer, giving the bare MXene,  $Ti_3C_2$ . Reactions 2.6 and 2.7 show idealised reactions for the formation of OH and F terminating groups, ignoring any mixing of different surface groups. These reactions show the origin of the OH and F terminating groups. O has been shown to form by oxidation of OH when the MXene has been left in air. Reaction 2.5 also shows that it is the  $F^-$  ions which are the active species in removing the A layer. This synthesis

route gives a characteristic “accordion-like” structure which can be seen either with SEM or TEM (Figure 2.10).

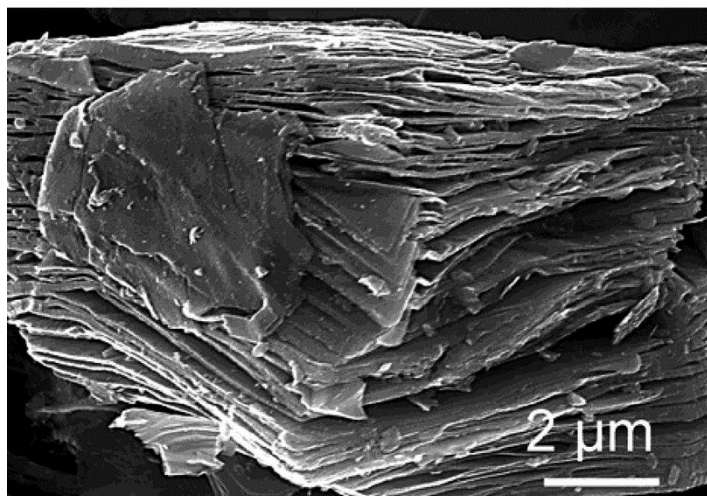


**Figure 2.10.** SEM image for MXene stacked layers, showing the typical morphology for HF etched MXenes ( $\text{Ti}_3\text{C}_2$ ). Reproduced from Naguib et al. with permission from ACS.<sup>91</sup>

The detailed synthesis of the first etching in HF to form an MXene involved adding  $\text{Ti}_3\text{C}_2$  to 50 wt.% HF solution at room temperature for 2 h. The resulting suspension was then washed several times using deionized (DI) water and centrifuged to separate the powders. Nanosheets were separated out by sonication in methanol, giving flakes and scrolls similar to exfoliated graphene.<sup>86</sup> Filtration can be used instead of centrifuging to separate the solid from solution and washing with ethanol is sometimes done in addition to DI water.<sup>92</sup>

Several parameters can be altered in this synthesis: HF concentration, reaction time and reaction temperature. Mashtalir et al. investigated the effect of reaction time and temperature on the synthesis of  $\text{Ti}_3\text{C}_2$  in 50 wt.% and found that pure MXene phases were obtained after 2 hours at 50 °C, but took over 15 h when reacted at room temperature.<sup>93</sup> They also found that having a smaller MAX particle size decreased the time taken for a pure MXene phase to form. It is also possible to remove some surface terminating groups using post synthetic treatments.<sup>94</sup> For example, both Mashtalir et al.<sup>93</sup> and Wang et al.<sup>94</sup> found that OH groups could be removed by heating in inert atmosphere (Ar) up to 450-500 °C. It was also reported that above 500 °C  $\text{TiO}_2$  began to form, presumably due to reactions between Ti and O or OH terminating groups. The  $\text{TiO}_2$  content increases all the way up to 1,200 °C, where large amounts of rutile phase  $\text{TiO}_2$  form on the surface. A solid solution of  $\text{TiC}_x\text{O}_{1-x}$  ( $0 < x < 1$ ) from the reaction of  $\text{Ti}_3\text{C}_2$  and  $\text{TiO}_2$  was also seen. Apart from this, the nanosheets were seen as thermally stable up to 1,200 °C.<sup>94</sup> Rakhi et al. looked at the effect of different annealing gases for this post synthesis treatment and found that  $\text{N}_2/\text{H}_2$  gave the lowest F terminations and the highest C content overall, with the

largest interlayer spacings (assumed to be due to the removal of more functional groups).<sup>92</sup> This gave the best performance as a supercapacitor electrode.

Typically, higher  $n$  MXenes require more concentrated HF, higher temperatures and longer times, due to a greater stability of the MAX phase. Table 2.2 shows all of the currently synthesised MXenes found in this review.

**Table 2.2.** Currently synthesised MXenes, with the parent MAX phase and the corresponding reference. Terminating functional groups have been neglected for simplicity.

MXene	MAX phase	Reference
Ti <sub>3</sub> C <sub>2</sub>	Ti <sub>3</sub> AlC <sub>2</sub>	86
Ti <sub>3</sub> C <sub>2</sub>	Ti <sub>3</sub> SiC <sub>2</sub>	95
Ti <sub>2</sub> C	Ti <sub>2</sub> AlC	91
Ta <sub>4</sub> C <sub>3</sub>	Ta <sub>4</sub> AlC <sub>3</sub>	91
[Ti <sub>0.5</sub> ,Nb <sub>0.5</sub> ] <sub>2</sub> C	[Ti <sub>0.5</sub> ,Nb <sub>0.5</sub> ] <sub>2</sub> AlC	91
[V <sub>0.5</sub> ,Cr <sub>0.5</sub> ] <sub>3</sub> C <sub>2</sub>	[V <sub>0.5</sub> ,Cr <sub>0.5</sub> ] <sub>3</sub> AlC <sub>2</sub>	91
Ti <sub>3</sub> CN	Ti <sub>3</sub> AlCN	91
V <sub>2</sub> C	V <sub>2</sub> AlC	96
V <sub>4</sub> C <sub>3</sub>	V <sub>4</sub> AlC <sub>3</sub>	97
Nb <sub>2</sub> C	Nb <sub>2</sub> AlC	98
Nb <sub>4</sub> C <sub>3</sub>	Nb <sub>4</sub> AlC <sub>4</sub>	99
Mo <sub>2</sub> TiC <sub>2</sub>	Mo <sub>2</sub> TiAlC <sub>3</sub>	100
Mo <sub>2</sub> Ti <sub>2</sub> C <sub>3</sub>	Mo <sub>2</sub> Ti <sub>2</sub> AlC <sub>4</sub>	100
Mo <sub>2</sub> ScC <sub>2</sub>	Mo <sub>2</sub> ScAlC <sub>2</sub>	101
Cr <sub>2</sub> TiC <sub>2</sub>	Cr <sub>2</sub> TiAlC <sub>2</sub>	100
Mo <sub>2</sub> C	Mo <sub>2</sub> Ga <sub>2</sub> C	102
[Nb <sub>0.8</sub> ,Ti <sub>0.2</sub> ] <sub>4</sub> C <sub>3</sub>	[Nb <sub>0.8</sub> ,Ti <sub>0.2</sub> ] <sub>4</sub> AlC <sub>3</sub>	103
[Nb <sub>0.8</sub> ,Zr <sub>0.2</sub> ] <sub>4</sub> C <sub>3</sub>	[Nb <sub>0.8</sub> ,Zr <sub>0.2</sub> ] <sub>4</sub> AlC <sub>3</sub>	103
Nb <sub>1.33</sub> C <sub>2</sub>	[Nb <sub>0.66</sub> ,Sc <sub>0.33</sub> ] <sub>2</sub> AlC <sub>2</sub>	104
Zr <sub>3</sub> C <sub>5</sub>	Zr <sub>3</sub> Al <sub>3</sub> C <sub>5</sub>	105
Hf <sub>3</sub> C <sub>2</sub>	Hf <sub>3</sub> (Al, Si) <sub>4</sub> C <sub>6</sub>	106
Mo <sub>1.33</sub> C	[Mo <sub>0.66</sub> Sc <sub>0.33</sub> ] <sub>2</sub> AlC	107
Mo <sub>1.33</sub> C	[Mo <sub>0.66</sub> Y <sub>0.33</sub> ] <sub>2</sub> AlC	108
W <sub>1.33</sub> C	[W <sub>0.66</sub> Sc <sub>0.33</sub> ] <sub>2</sub> AlC	109
W <sub>1.33</sub> C	[W <sub>0.66</sub> Y <sub>0.33</sub> ] <sub>2</sub> AlC	109
[Mo <sub>0.66</sub> Y <sub>0.33</sub> ] <sub>2</sub> C	[Mo <sub>0.66</sub> Y <sub>0.33</sub> ] <sub>2</sub> AlC	108
Ti <sub>4</sub> N <sub>3</sub>	Ti <sub>4</sub> AlN <sub>3</sub>	110
Ti <sub>2</sub> N	Ti <sub>2</sub> AlN	111
V <sub>2</sub> N	V <sub>2</sub> AlC	112
Mo <sub>2</sub> N	Mo <sub>2</sub> Ga <sub>2</sub> C	112

To date, around 30 different MXenes have been successfully synthesised from a variety of MAX phases. These have included  $n = 1, 2$  and  $3$  MXenes, Ti, Nb, Ta, Mo, Cr, V, W, Y, Zr, Hf and Sc based M elements (all the M elements highlighted in the MAX phase periodic table in Figure 2.7), and C, N and CN X elements. Precursors with Al, Si and Ga as A elements have been used so far.

Whilst the majority of MXenes have been synthesised from Al containing MAX phases there are some notable exceptions. Mo<sub>2</sub>C was synthesised from Mo<sub>2</sub>Ga<sub>2</sub>C which is not strictly speaking a MAX phase compound, since two Ga layers separate each Mo<sub>2</sub>C block, rather than one.<sup>102</sup> This was done due to difficulty with

synthesising Mo containing MXenes from MAX phases and remains the only example found of an MXene where Mo is the only M element. This route potentially opens up the synthesis of other new MXenes, which are also considered difficult to make from the MAX family. For example,  $\text{Mo}_2\text{C}$ , and  $\text{Zr}_2\text{C}$  are theoretically possible MXenes, but neither have known equivalent Al containing MAX phases.  $\text{Zr}_3\text{C}_2$  and  $\text{Hf}_3\text{C}_2$  have also been synthesised from non-MAX compounds for the same reasons.<sup>105,106</sup> Whilst the precursors used for these three MXenes are not MAX phases, they have clear similarities with MAX phases since they are layered materials with the same chemistries as MAX phases, and the MXenes are synthesised by the selective etching of layers. The synthesis of  $\text{Zr}_3\text{C}_2$  also introduces the use of Si as an A element, and the potential benefits of solid-solutions in the MAX phase, since the mixture of Si and Al elements in the A layer were shown to weaken the A-M bonding, allowing successful etching.<sup>105</sup> There has also been a report of  $\text{Ti}_3\text{C}_2$  synthesis using  $\text{Ti}_3\text{SiC}_2$  as the MAX phase precursor, which opens up non-Al MAX phases for etching.<sup>95</sup> However,  $\text{H}_2\text{O}_2$  was added to the HF etching solution as an oxidant, which introduces an extra hazard to the synthesis procedure.

Table 2.2 also includes the synthesis of solid solution and ordered MXenes where multiple M elements are present. This opens up the possibility of creating very carefully designed MXenes with hybrid properties as a result of combining two or more M elements into one material. There is also the possibility of incorporating otherwise difficult elements such as Mo into ordered MXene compounds, such as done by Anasori et al. with  $\text{Mo}_2\text{TiC}_2$  and  $\text{Mo}_2\text{Ti}_2\text{C}_3$ ,<sup>100</sup> and by solid solution MXenes as done by Yang et al. with Zr into  $(\text{Nb}_{0.8},\text{Zr}_{0.2})_4\text{C}_3$ .<sup>103</sup> As previously mentioned, no Al containing MAX phases based on Mo or Zr are known.

Ordering on the M layers when multiple M elements are used in the MAX phase can give rise to ordered MXenes, when the ordering present in the MAX phase survives the etching process. This gives rise to two sub-classes of MXenes: in-plane ordered MXenes, where the MAX phases were dubbed *i*-MAX, and out-of-plane ordered MXenes, from *o*-MAX phases. In-plane ordered MXenes are characterised by ordering by the M elements within each M layer. The in- and out-of-plane ordered MAX phases are illustrated in Figure 2.11.

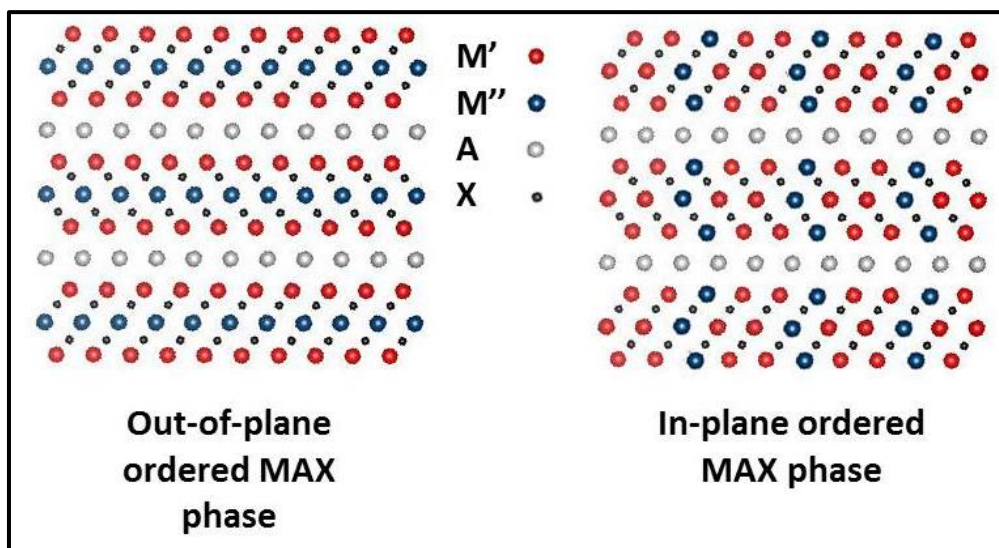


**Figure 2.11.** Schematic illustration of the concept of in- and out-of-plane ordered MAX phases.

For example, in  $[\text{Mo}_{0.66}\text{Y}_{0.33}]_2\text{C}$ , the Mo and Y elements order as Mo-Y-Mo-Mo-Y-Mo-Mo-Y across each M layer. Out-of-plane ordered MXenes also contain multiple M elements, but each layer contains only one. For example,  $\text{Mo}_2\text{TiC}_2$ , which is studied in Chapter 5, has only Mo on the outer layers, while Ti only occupies the central M layer.<sup>100</sup> This arises as a result of the different preferred environment of the different elements within the MAX phase structure. For example, Mo elements have been shown to be unstable in a face centred cubic arrangement with the C atoms, which is the case in  $\text{Mo}_3\text{C}_2$ .<sup>100</sup> Instead, Mo is more stable in a hexagonal environment. Therefore, if Mo exists only on the surface M layers, it can achieve its preferred environment and avoid the face centred cubic arrangement with the C atoms. Ti, which is stable in the face centred cubic sites, then occupies the central M layer to stabilise the structure, giving rise to the out-of-plane ordered double transition metal MAX phases and the corresponding MXenes.<sup>100,113</sup> This allows the effect of different surface M elements to be studied, since this is the only difference between  $\text{Mo}_2\text{TiC}_2$  and  $\text{Ti}_3\text{C}_2$ , which are the two MXenes studied in this thesis.

If one of the M elements is more reactive than the other, then the M chemistry of the MAX phase does not necessarily translate into the resulting MXene. However, the ordering of the M element sites may still be retained in the MXene, resulting in so-called divacancy MXenes. This was first reported for  $\text{Mo}_{1.33}\text{C}$  after selective etching from  $[\text{Mo}_{0.66}\text{Sc}_{0.33}]_2\text{AlC}$ , where Sc acts a sacrificial M element and is removed during the etching to leave vacancies where it was situated.<sup>107</sup> For example, each M layer is ordered as Mo-Mo- $V_{\text{Sc}}$ -Mo-Mo- $V_{\text{Sc}}$ -Mo where  $V_{\text{Sc}}$  indicates a vacancy on a Sc site. This adds a further layer of diversity to MXene chemistry and structure, and gives MXenes with lower unit masses than the non-vacancy containing counterparts,

which may be useful for electrochemical energy storage applications. Sc and Y are the only two sacrificial elements that have been used to date.

Table 2.2 also shows that the chemistry of the parent MAX phase does not necessarily dictate the chemistry of the final MXene if a suitable post-etching treatment is used. For example,  $V_2N$  and  $Mo_2N$  have both been reported as synthesised from the carbide precursors,  $V_2AlC$  and  $Mo_2Ga_2C$  respectively. A nitration process was then carried out at 600 °C, which exchanged the C atoms for N atoms. This gives further tools to synthesise MXenes which cannot easily be etched from MAX phases.<sup>112</sup>

The existing reports on MXene synthesis show that it appears to be more difficult to synthesise materials with higher  $n$  values, with harsher synthesis conditions seemingly required. Table 2.3 shows the reported synthesis conditions for selected MXenes listed in Table 2.2. It can clearly be seen that for higher  $n$  values (and higher atomic masses of the M element), higher HF concentration and temperatures and longer reaction times are required.

**Table 2.3.** Reaction conditions for selected MXenes. Where “room temperature” was stated, this has been taken to mean 25 °C.

MXene	Etchant and concentration	Reaction temperature (°C)	time (h)	Reference
$Ti_3C_2$	50 wt% HF	25	2	86
$Ti_2C$	10 wt% HF	25	10	91
$Ta_4C_3$	50 wt% HF	25	72	91
$[Ti_{0.5}, Nb_{0.5}]_2C$	50 wt% HF	25	28	91
$Ti_3CN$	30 wt% HF	25	18	91
$V_2C$	50 wt% HF	25	8	96
$V_4C_3$	40 wt% HF	25	165	97
$Nb_2C$	50 wt% HF	25	90	98
$Nb_4C_3$	50 wt% HF	25	96	99
$Mo_2C$	50 wt% HF	50	3	102
$Mo_2TiC_2$	50 wt% HF	25	48	100
$Mo_2Ti_2C_3$	50 wt% HF	55	90	100
$[Nb_{0.8}, Ti_{0.2}]_4C_3$	50 wt% HF	50	96	103

#### 2.4.1.2 Non-HF Etching Methods

While using concentrated HF solutions gives good yields and can be applied to a variety of MXenes, HF is a highly toxic chemical, the use of which requires careful health and safety precautions. Therefore, some alternative MXene synthesis methods have been developed.

In 2014, Ghidui et al. reported the first synthesis of an MXene which didn't involve handling concentrated HF solutions.<sup>114</sup> Instead, they dissolved a fluoride salt, LiF, into a HCl solution (6 M) and used this to synthesise  $Ti_3C_2$  from  $Ti_3AlC_2$  following a procedure that was otherwise very similar to the HF etching process. While this method avoids directly handling concentrated HF solutions, small amounts of HF still form during etching, which means that this method still requires significant health and safety precautions to be taken.

Therefore, other methods have been developed to try and overcome the use of HF containing solutions in MXene synthesis. Urbankowski et al. used a molten mixture of fluoride salts, LiF, NaF and KF, heated at 550 °C under argon to synthesise  $Ti_4N_3$  from  $Ti_4AlN_3$ .<sup>115</sup> This was the first synthesis of a nitride MXene, but still relies on the use of fluorides. A fluoride-free synthesis route was developed by Li et al., who used a hydrothermal etching route where the  $Ti_3AlC_2$  MAX phase was heated in an autoclave to 270 °C in 27 M NaOH.<sup>116</sup> While this is fluoride-free, the conditions are harsh, and the resulting MXenes, which will have very different surface chemistries compared to traditional etching methods, have not been studied in detail so far. Electrochemical etching methods have also been investigated, with  $Ti_2C$  being synthesised from  $Ti_2AlC_2$  in dilute HCl.<sup>117</sup> However, the MXene yields were small, with large amounts of carbide derived carbon also formed. Yang et al. used a binary electrolyte system, based on ammonium chloride and hydroxide, to synthesise  $Ti_3C_2$  from  $Ti_3AlC_2$ , with a five hour reaction time and reasonable yields.<sup>118</sup> The ammonium cations also intercalated between the layers and aided the delamination, to give around 90% double or single layer sheets in the recovered product. Very recently,  $Ti_3C_2$  and  $Ti_2C$  were synthesised with  $ZnCl_2$  in a molten-salt method via  $Ti_3ZnC_2$  and  $Ti_2ZnC$  (Al was exchanged for Zn before the exfoliation step).<sup>119</sup> This gave mostly Cl terminated MXenes with good yields.

#### **2.4.1.3 HCl-F Salt Etching**

Despite the formation of a small amount of HF, this method is significantly less hazardous than full HF etching, and allows for high yields of MXenes to be synthesised reproducibly in quantities up to 10 g, which is suitable for energy storage research. Therefore, this method was selected for use in this thesis, and is discussed in more detail in this section, including comparisons with HF-etched MXenes.

In their initial paper, Ghidui et al. investigated the impact of the etching time and temperature with these new reagents.<sup>114</sup> They found that using 35 °C for 24 h rather than 40 °C for 45 h gave a product with persistent MAX-phase peaks in the XRD patterns (Figure 2.12), and higher Al content revealed by EDS.

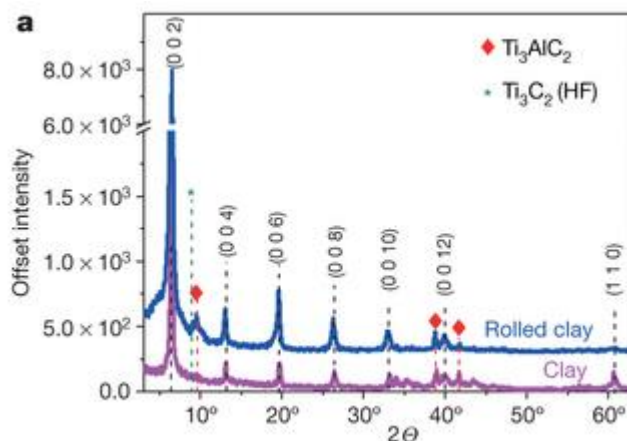


**Figure 2.12.** XRD patterns of samples produced by etching in LiF + HCl solution. The pink trace is for multilayer  $\text{Ti}_3\text{C}_2\text{T}_x$ , showing a sharp, intense diffraction peak (002) and higher-order (00l) peaks, corresponding to a  $c$  lattice parameter of 28 Å and high order in the  $c$  direction. The blue trace is for the same sample after rolling into an approximately 40- $\mu\text{m}$ -thick film;  $c$ -direction peaks are preserved, but the prominent (110) peak is no longer observed, showing substantial reduction of order in non-basal directions. In both cases, traces of  $\text{Ti}_3\text{AlC}_2$  are still present (red diamonds). The MXene (002) diffraction peak is at a lower angle than that typical of MXene produced by HF (green star), signifying an increased interlayer spacing. Reproduced from Ghidui et al. with permission from Springer Nature, Nature, 2014.<sup>114</sup>

These products did however have reliably high yields of delaminated flakes upon sonication. When etched at higher temperatures the products had lower Al content but did not always readily delaminate and disperse by sonication. Therefore the reported conditions were taken to be optimal. Despite these conditions being reported as optimal, subsequent reports of this synthesis route did not always use these same conditions, even when carried out by the same group for the same MXene. This may have been due to preferring ease of delamination over MAX phase impurities or vice versa,<sup>120</sup> depending on if a longer or shorter time was used (or a more concentrated solution). A selection of reports of this HCl-LiF etching method and the reaction conditions can be seen in Table 2.4.

**Table 2.4.** Summary of selected MXene synthesis conditions used with HCl/ LiF etching solution.

MXene	Etchant	Temp (°C)	Time (h)	Reference
Ti <sub>3</sub> C <sub>2</sub>	6 M HCl and LiF	40	45	114
Ti <sub>2</sub> C	6 M HCl and LiF	40	45	114
Nb <sub>2</sub> C	6 M HCl and LiF	40	45	114
Ti <sub>3</sub> C <sub>2</sub>	6 M HCl and LiF	35	45	121
Cr <sub>2</sub> TiC <sub>2</sub>	6M HCl and LiF	55	42	100
Ti <sub>3</sub> AlC <sub>2</sub>	HCl-LiF	60	48	122
[Nb <sub>0.8</sub> ,Zr <sub>0.2</sub> ] <sub>4</sub> C <sub>3</sub>	12M HCl and LiF	50	168	103
Ti <sub>3</sub> C <sub>2</sub>	9 M HCl and LiF	35	24	123
Ti <sub>3</sub> C <sub>2</sub>	6 M HCl and LiF	40	24	120
Ti <sub>3</sub> C <sub>2</sub>	6 M HCl and LiF	35	24	124
Ti <sub>3</sub> C <sub>2</sub>	9 M HCl and LiF	35	24	125
Ti <sub>2</sub> C	6 M HCl and LiF	50	48	126
Mo <sub>2</sub> C	12 M HCl and LiF	35	16 days	127

#### 2.4.1.4 Comparisons Between Etching Methods

The MXene flakes obtained by HCl / LiF etching show several differences compared to those from HF etching. These were noticed in the original paper by Ghidui et al. and studied in more detail by Hope et al. who used solid state NMR, EDS and XRD to directly compare Ti<sub>3</sub>C<sub>2</sub> samples synthesised via HF and HCl / LiF etching respectively.<sup>120</sup>

The first difference noted was the presence of intercalated water molecules (and possibly other cations) which was not the case for HF etched samples. This gave rise to a more compact morphology in contrast to the HF etched samples with the open “accordion-like” structures (Figure 2.13). The intercalated water also caused this material to be easier to delaminate through sonication, and gave it mouldable clay-like properties. This allowed it to be rolled into free-standing binder-less films, which is potentially useful for electrochemical applications. Attempts to make hydrated rollable films of HF etched MXenes had been unsuccessful, suggesting that the water molecules act as a lubricant, allowing the sliding of the layers over one another.<sup>114</sup> The presence of sharper narrower peaks with a high intensity compared to HF samples was also taken as evidence for water / cation intercalation, which keeps the layers more ordered than the HF etched versions.

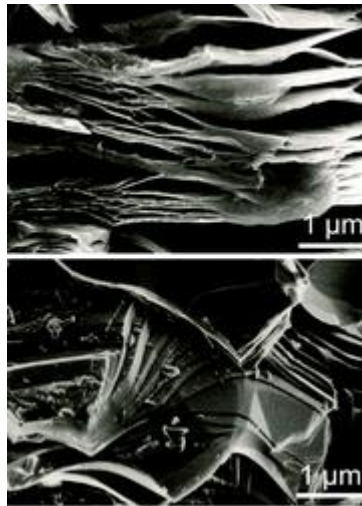


**Figure 2.13.** SEM images of MXene samples. HF-etched  $Ti_3C_2T_x$ , with accordion-like structure (top). LiF–HCl etched  $Ti_3C_2T_x$ , with a more compact structure (bottom). Reproduced from Hope et al., which was published by the PCCP Owner Societies.<sup>120</sup>

NMR studies by Hope et al. confirmed many of the original observations of differences between the two etching techniques. The NMR results also showed that the relative amounts of each type of surface termination were significantly affected by the synthesis route used. In particular it was noticed that etching with HCl / LiF led to a product where the surface chemistry was dominated by O terminations, while in HF etched products F termination was the most common group (Figure 2.14). This provides a way of matching the surface chemistry of MXenes to match the desired application, since it is known that the surface terminations have a significant effect on the MXene properties, which in turn affects application performance.

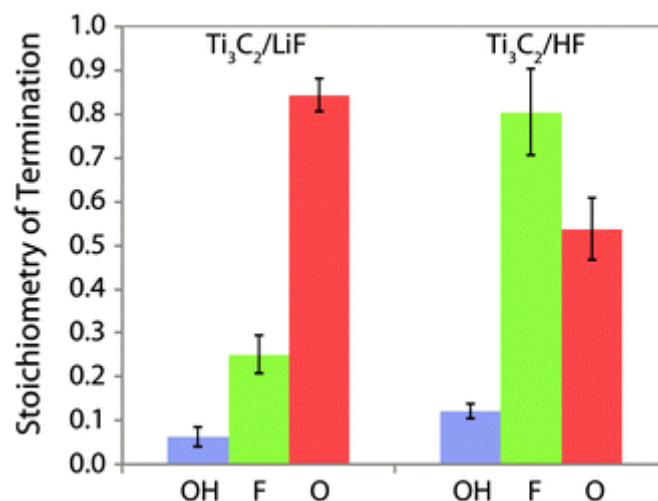


**Figure 2.14.** Composition of the  $Ti_3C_2T_x$  surface functional groups produced by etching of the  $Ti_3AlC_2$  in HF and LiF–HCl solutions, per  $Ti_3C_2$  formula unit, i.e.  $Ti_3C_2(OH)_xF_yO_z$ , as determined by solid-state NMR. Reproduced from Hope et al., which was published by the PCCP Owner Societies.<sup>120</sup>

Hope et al. also used EDS to look at the different elemental compositions of the etched MXenes, including the effect of adding an acid wash to the cleaning steps for HCl / LiF synthesis. It was shown that acid washing (with 6 M HCl) in addition to the standard washing with DI water removes  $\text{AlF}_3$  and LiF, and  $\text{Li}_3\text{AlF}_6$  impurities which led to better estimates for unreacted MAX-phase impurities, as well as giving guidance for improving MXene purity. Their EDS analysis also showed that the HCl / LiF etched products contained lower amounts of Al compared to HF etched samples (Table 2.5). However due to the lack of MAX-phase peaks in the XRD for HF etched samples, the authors assumed that this Al content was due to  $\text{AlF}_3$  and LiF impurities, not an unreacted MAX-phase. No attempt was made to acid wash the HF samples. It was also thought possible that acid washing may affect properties of the products. Since the use of HCl acid washes had been shown to successfully remove impurities, the MXenes synthesised in this thesis were all washed with HCl after etching.

**Table 2.5.** Summarized EDS values of various etching and washing procedures. Results are normalised with respect to Ti content. Reproduced from Hope et al., which was published by the PCCP Owner Societies.<sup>120</sup>

	HF etching	LiF-HCl@ 40 °C	
	Normal washing	Normal washing	Acid washing
<b>Ti</b>	3.00	3.00	3.00
<b>Al</b>	0.40	0.25	0.10
<b>C</b>	2.80	2.12	1.76
<b>O</b>	1.98	1.08	1.15
<b>F</b>	3.25	5.80	0.86
<b>Cl</b>	-	0.16	0.18

It should be noted that the reaction equations listed for HF etching are also thought to be valid for the HCl / LiF method.  $\text{F}^-$  ions are still present for Reactions 2.5 and 2.7 (although much lower amounts of F termination noted in the NMR study suggests that reaction 2.7 occurs much less when LiF is the  $\text{F}^-$  ion source). Water is still present for Reaction 2.6. However, due to the presence of Li in the etching solution,  $\text{Li}_3\text{AlF}_6$  can form as an etching product in addition to  $\text{AlF}_3$ . Cl terminations are also formed analogously to F terminations, which can give MXenes produced with HCl-LiF etching larger interlayer spacing than the HF etched counterparts.<sup>128</sup> This can lead to significantly improved electrochemical performance.

Since the requirements for the etching process appears to be presence of  $\text{F}^-$  ions and water, any acidic fluoride containing aqueous solution should be able to carry out the reaction. The original HCl / LiF study reported that many different  $\text{F}^-$  containing salts could be used in the production of MXenes, albeit with varying success. Specifically they mentioned use of NaF, KF, CsF, tetrabutylammonium fluoride and  $\text{CaF}_2$  as fluoride containing salts, claiming that they had similar etching behaviour.<sup>114</sup> Liu et al. investigated the use of LiF, NaF, KF and  $\text{NH}_4\text{F}$  in HCl to synthesise  $\text{Ti}_2\text{C}$  and  $\text{Ti}_3\text{C}_2$  and

found that all four salts could be used to synthesise high purity MXenes, though the etching temperature and times varied slightly for each salt.<sup>129</sup>

#### 2.4.1.5 Delamination

While the original paper in 2011 looked only at sonication to separate the nanosheets, this results in low delamination yields unless certain HCl-LiF etching conditions are used, where  $\text{Li}^+$  intercalates between nanosheets during etching and aids the delamination process. Therefore, like with graphene, research has been carried out into how to best delaminate the powders into single (and few) layer sheets. The most successful attempts at this have been via intercalation of organic molecules such as dimethyl sulfoxide (DMSO)<sup>130</sup> and amines<sup>131</sup> followed by sonication. Intercalation breaks the bonding forces between the sheets, making single layers much easier to separate (Figure 2.15). This is also known to be the case for graphite to graphene exfoliation.

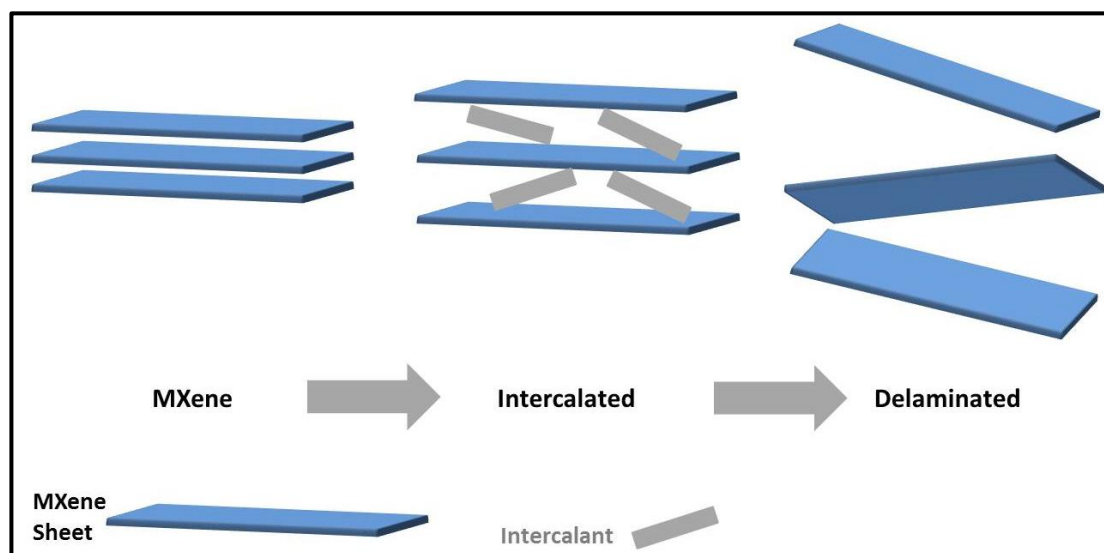


**Figure 2.15.** Schematic of the intercalation and delamination of an MXene.

For example, Mashtalir et al. first reported delamination of MXenes, ( $\text{Ti}_3\text{C}_2$ ,  $\text{Ti}_3\text{CN}$  and  $\text{TiNbC}$ ) by intercalation of a range of organic molecules including thiophene, ethanol, acetone, tetrahydrofuran, formaldehyde, chloroform, toluene, hexane, DMF, DMSO and urea. They found that only urea and DMSO properly intercalated (with a significant increase in the  $c$ -parameter) and DMSO intercalated compounds were easily separated by sonication in water.<sup>130</sup> The delaminated flakes also exhibited enhanced surface areas, with  $\text{Ti}_3\text{CN}$  achieving  $98 \text{ m}^2 \text{ g}^{-1}$  compared to around  $20 \text{ m}^2 \text{ g}^{-1}$  which is typical for MXenes.

It has been reported that other than the MXenes listed ( $\text{Ti}_3\text{C}_2$ ,  $\text{Ti}_3\text{CN}$  and  $\text{TiNbC}$ ), DMSO was not an effective delamination agent. However amines have also shown promise,<sup>131</sup> for example with  $\text{Nb}_2\text{C}$ , meaning that it should be possible to delaminate

a range of different MXenes. In addition, a range of bases (e.g.  $(C_4H_9)_4NOH$ ) have been shown to be effective for MXene delamination, and also provides promise for a large scale route.<sup>132</sup> Overall, however DMSO is still the most commonly used intercalant for  $Ti_3C_2$  delamination.<sup>133,134,135</sup> To keep the synthesis and processing of the MXenes used in this thesis as simple as possible, delamination steps were not attempted for this work, since pillared materials should contain well separated sheets in the final product. However, the finding that amines can successfully intercalate into MXenes is significant for the development of the amine-assisted pillaring method reported in this thesis.

Overall, this section has shown that there are a variety of MXenes that can be synthesised from layered precursor materials, which are predominately MAX phases, via selective etching processes. Different MXene chemistries, structures and surface chemistries can be developed by choice of precursor material and synthesis process.  $Ti_3C_2$  is the most studied MXene to date, and so was chosen as the model MXene to be investigated in this thesis. The out-of-plane double ordered MXene  $Mo_2TiC_2$  was also chosen for study, since this allows for the effect of the surface M element to be studied by comparing to  $Ti_3C_2$ . In addition, both MXenes are composed of affordable and abundant elements, which is important when considering energy storage applications. The etching method chosen for this thesis is HCl-LiF etching, since this avoids the handling of concentrated HF solutions and was already widely used in literature. In addition, etching with HCl-LiF leads to a higher concentration of O-based termination groups than the HF etched counterparts, which is advantageous for electrochemical energy storage applications, as is discussed in the next section.

#### **2.4.2 MXenes as Electrochemical Energy Storage Materials**

The bulk of research carried out on MXenes as electrochemical energy storage materials has focused on metal-ion batteries/ capacitor systems. Both experimental and theoretical studies have shown that MXenes can intercalate a large number of cations, including  $Li^+$ ,  $Na^+$ ,  $K^+$ ,  $Mg^{2+}$  and  $Al^{3+}$ . All of these are potential metal-ion battery chemistries.<sup>136</sup> The reversible intercalation of non-lithium ions is significant, since there are few materials known to act as intercalation hosts for these systems. This is due to the larger ion size of  $Na^+$  and  $K^+$  systems, and the high charge density of multivalent ions such as  $Mg^{2+}$  and  $Al^{3+}$ , which prevents standard materials for LIBs such as graphite being used in such systems.

## 2.4.2.1 Non-structured MXenes

### 2.4.2.1.1 Theoretical studies

Several early theoretical studies were carried out to gain insight into the potential of MXenes in different metal-ion systems, and to guide the research to the most promising MXene elements and surface chemistries. Er et al. used DFT to investigate the intercalation of Li, Na, K, and Ca ions on  $\text{Ti}_3\text{C}_2$ .<sup>137</sup> They found fast kinetics, but noticed that Na, K and Ca showed decreased adsorption energies as coverage increased (unlike Li) due to the large effective ionic radii. Their calculated capacities in fact followed ionic radii very closely, with highest capacity for Li and lowest for K (Figure 2.16).

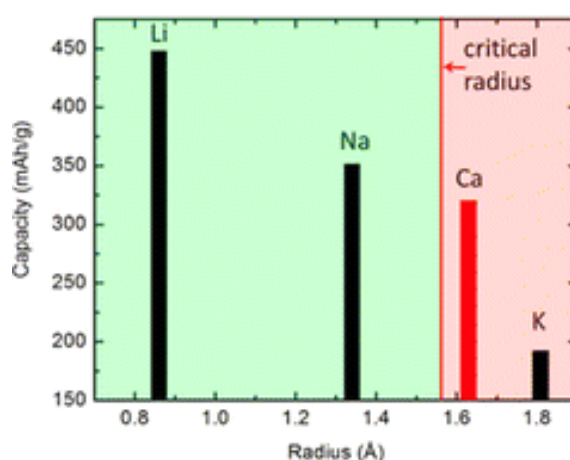


**Figure 2.16.** Capacity and ionic radius for adsorption on both sides. Reprinted with permission from Er et al., *ACS Appl. Mater. Interfaces*, 2014, 6, 14, 11173-11179.<sup>137</sup> Copyright (2014) American Chemical Society.

Eames et al. studied the intercalation of a variety of ions ( $\text{Li}^+$ ,  $\text{Na}^+$ ,  $\text{K}^+$ , and  $\text{Mg}^{2+}$ ) into selection of  $\text{M}_2\text{C}$ -based compounds ( $\text{M} = \text{Sc}, \text{Ti}, \text{V}, \text{Cr}, \text{Zr}, \text{Nb}, \text{Mo}, \text{Hf}, \text{Ta}$ ) with F, H, O, and OH terminating groups.<sup>138</sup> They found that  $\text{Li}^+$  or  $\text{Mg}^{2+}$  provide higher gravimetric capacities than  $\text{Na}^+$  or  $\text{K}^+$  (all other factors being equal), again due to the ion size. The capacity and voltage were both affected by the surface groups and the M element. O terminations gave the highest capacity (followed by bare) with the light M elements Sc, Ti, V, and Cr giving the highest gravimetric capacities. The theoretical capacities of Mg based systems were higher even than that of Li (Figure 2.17), due to the two electron redox activity of  $\text{Mg}^{2+}$  compared to  $\text{Li}^+$ . Double layer intercalation was also found to be possible for these materials, contributing to high capacities. Overall the materials with light transition metals and O or no terminations look promising for further work as negative electrodes for Li and Mg batteries especially.

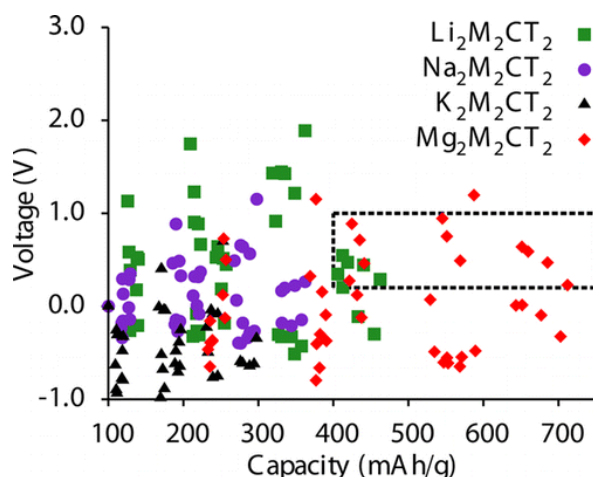


**Figure 2.17.** Cell voltage and theoretical gravimetric capacity for intercalation of two ions of  $\text{Li}^+$ ,  $\text{Na}^+$ ,  $\text{K}^+$ , or  $\text{Mg}^{2+}$  per formula unit into  $\text{M}_2\text{CT}_2$ . The dashed box indicates an approximate window of desired negative electrode voltages (0.2–1.0 V) and capacities (>400 mAh  $\text{g}^{-1}$ ). Reproduced from Eames et al. *J. Am. Chem. Soc.*, 2014, 136, 46, 16270-16276, <https://pubs.acs.org/doi/10.1021/ja508154e>, with permission.<sup>138</sup> Further permissions related to the material reproduced should be directed to the ACS.

Yu et al. used DFT to study in detail the intercalation of  $\text{Mg}^{2+}$  into  $\text{Ti}_2\text{C}$ .<sup>139</sup> They found that  $\text{Mg}^{2+}$  intercalation is favourable with the stable compound  $\text{Ti}_2\text{MgC}$  forming. This is analogous to  $\text{LiC}_6$  formation in graphite for LIBs. The theoretical capacity based on this intercalation compound was high (497 mAh  $\text{g}^{-1}$  compared to around 375 mAh  $\text{g}^{-1}$  for graphite in LIBs) with results suggesting intercalation of two layers of Mg may be possible ( $\text{Ti}_2\text{Mg}_2\text{C}$ ), which could offer even higher capacities. The rate of  $\text{Mg}^{2+}$  was fast due to the low energy of intercalation and the material cell voltage was low (0.10 V). These results suggest  $\text{Ti}_2\text{C}$  would be a promising negative electrode material for a high performing Mg-ion battery. The same paper also studied  $\text{Al}^{3+}$  intercalation and found that it showed similar behaviour to  $\text{Mg}^{2+}$ , but with higher intercalation energies and with only one layer of Al intercalation likely.

Xie et al. used DFT and some experimental testing to study  $\text{Na}^+$ ,  $\text{K}^+$ ,  $\text{Mg}^{2+}$ ,  $\text{Ca}^{2+}$ , and  $\text{Al}^{3+}$  intercalation into  $\text{M}_2\text{C}$  ( $\text{M} = \text{Nb}$ ,  $\text{Ti}$  and  $\text{V}$ ) and  $\text{Ti}_3\text{C}_2$  with F, O and OH terminations. Again, bare and O-terminations were found to be best (although this time bare was claimed to have a higher capacity), and Al and Mg are expected to have stable multi-layer adsorption, increasing their theoretical capacities.  $\text{Ti}_2\text{CO}_2$  was reported to have the highest capacity for each ion battery type, with 288, 264, 570, 487, and 552 mAh  $\text{g}^{-1}$  for Na, K, Mg, Ca, and Al respectively. This gives a similar set of results to the previously discussed papers. Na and K-ion batteries were then built with  $\text{Ti}_3\text{C}_2$  as the negative electrode. While high first cycle capacities were observed, subsequent cycles were much lower, possibly due to the formation of a solid-electrode interphase (SEI). K-ion shows greater capacity fade than Na-ion, probably due to the larger ion size causing greater electrode deformation. The results of this paper follow similar lines to the others previously discussed, but confirm the

reversible intercalation of non-lithium ions into MXenes for reversible battery applications experimentally. They also potentially confirm the multilayer ion intercalation of  $\text{Na}^+$  and  $\text{K}^+$  (first cycle capacities correspond to 2.79  $\text{Na}^+$ , 1.96  $\text{K}^+$  per  $\text{Ti}_3\text{C}_2\text{T}_x$ ), though side-reactions with the electrolyte also likely contribute to these large first cycle capacities.

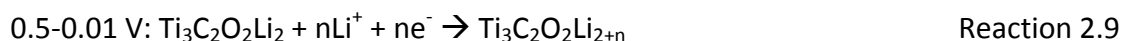
#### 2.4.2.1.2 Li-ion Systems

After the early computational screening studies implied that MXenes have potential as Li-ion negative electrodes, further work was carried out experimentally to probe the charge storage mechanisms and to benchmark the performance of multilayered MXenes. Li-ion systems have been extensively studied as an application for MXenes, with the initial screening studies suggesting the potential for large capacities from titanium and molybdenum-based MXenes. This section discusses some of the early work on Ti and Mo-based MXenes for Li-ion systems, with a focus on multilayered MXenes and the charge storage mechanisms involved.

The first report on the applications of MXenes in 2012 focused on the application of  $\text{Ti}_2\text{C}$  in an organic Li-ion system.<sup>140</sup> Here it was shown that  $\text{Ti}_2\text{C}$  had a reasonable reversible capacity of about 160  $\text{mAh g}^{-1}$ , albeit with a large capacity loss on the first cycle, (40%) which was attributed to SEI formation and  $\text{Li}^+$  trapping. At a 10C rate (6 min charge), 60  $\text{mAh g}^{-1}$  was retained, demonstrating promising high rate performance. The CV curves showed peaks similar to lithiated  $\text{TiO}_2$ , which led the authors to propose that the  $-\text{O}$  terminations were involved in the lithiation reactions. A follow up report was published by Come et al., who studied the mechanism using in-situ XRD and CV kinetic studies.<sup>141</sup> The XRD data showed the shift of the (002) diffraction peak to lower angles on lithiation, corresponding to the expansion of the interlayer spacing. On charging, this was only partially reversed, suggesting some  $\text{Li}^+$  trapping. No major phase changes were observed, suggesting that the lithiation was purely an intercalation process, with no conversion reactions occurring. Kinetic analysis showed that the current was almost entirely surface-limited, suggesting pseudocapacitive intercalation was the mechanism here, which explains the promising rate performance and matches the sloping load curve.

The lithiation mechanism was studied in more detail using a combination of simulations and experiments by Xie et al.<sup>98</sup> They found that  $-\text{OH}$  terminations could not give the experimentally realised capacities, but  $-\text{O}$  terminated  $\text{Ti}_3\text{C}_2$  could, which supported earlier expectations that  $-\text{O}$  were actively involved in the charge storage process. Interestingly, they showed that the lithiation product, which many previous reports had taken to be  $\text{Li}_2\text{Ti}_3\text{C}_2$ , was in fact  $\text{Li}_4\text{Ti}_3\text{C}_2$ , with the adsorption of a second Li layer on top of the lithiated  $\text{Ti}_3\text{C}_2$ . In-situ x-ray absorption near edge spectroscopy (XANES) analysis was carried out, and found that the oxidation state of Ti decreased upon lithiation, consistent with the Ti being reduced upon lithiation. After charging,

the oxidation state increased again, but not completely back to its initial state, suggesting that some Li may be retained (or another irreversible reduction process occurs) which contributes to the first cycle capacity loss. At low potentials (less than around 0.5 V vs.  $\text{Li}^+/\text{Li}$ ), the oxidation state of Ti was actually constant. This was assigned to the formation of the second adsorption layer on top of  $\text{Li}_2\text{Ti}_3\text{C}_2$ , which does not directly impact on the Ti oxidation state. They found that their simulations supported this interpretation, and actually suggested that two more layers of Li may be stably adsorbed on to this second layer. This would lead to a capacity over 600  $\text{mAh g}^{-1}$  if achieved experimentally, and is more adsorption layers than had been reported for Na-ion systems. Therefore, up to  $\text{Li}_8\text{Ti}_3\text{C}_2\text{T}_x$  may be possible as a lithiation product, however this has not yet been confirmed experimentally. Their results show that between 3-0.5 V Li intercalation occurs with a corresponding reduction in the Ti oxidation state, and between 0.5 and 0.01 V adsorption layers form on top of this lithiated product. In other words, the mechanism for lithiation of  $\text{Ti}_3\text{C}_2$  can be summarised by Reactions 2.8 and 2.9, where  $n = 3-6$ .



Chen et al. used a combination of ex-situ XRD and CV analysis to study the effect of the structure on the lithiation of multilayered  $\text{Ti}_3\text{C}_2$ .<sup>142</sup> They observed two redox couples in their CV analysis, which they matched to two different interlayer spacings using ex-situ XRD, which revealed a split in the (002) diffraction peak. This led them to propose that when the interlayer spacing is not even, with wide and narrow interlayer slits present, a sequential lithiation occurs whereby the wider slits are lithiated first, followed by the narrow slit. On delithiation, the narrow slits are vacated first, followed by the wider slits. After pre-intercalating with  $\text{NH}_4^+$  to increase the interlayer spacing, only one redox peak was seen, and no split in the ex-situ XRD was observed, which supports the assignment of the redox to  $\text{Li}^+$  intercalation into different sized interlayers (Figure 2.18). This work could also provide an explanation for why CV curves for MXenes in these systems seem to vary between papers, which has been observed when carrying out this review; the precise stacking structure of the MXene flakes may vary between reports.

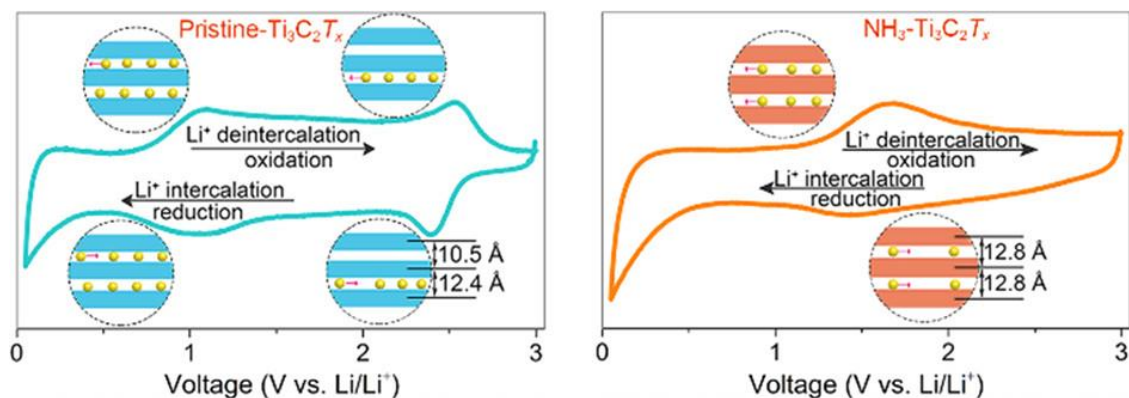


**Figure 2.18.** CV curves demonstrating the effect of increasing the interlayer spacing on the shape of the voltammogram for  $\text{Ti}_3\text{C}_2$  in a Li-ion half-cell. Reproduced with permission from Chen et al., *J. Phys. Chem. C*, 2019, 123, 2, 1099-1109. Copyright 2019 American Chemical Society.<sup>142</sup>

Kinetic analysis showed that a mixture of surface-limited (capacitive) and diffusion-limited (battery-like) processes contributed to the charge storage, with the intercalation processes which give rise to the redox peaks have a higher proportion of diffusion limitations. The capacities reported were around  $170 \text{ mAh g}^{-1}$  at low rates for the  $\text{NH}_4^+$  intercalated MXene compared to around  $100 \text{ mAh g}^{-1}$  for the multilayered MXene. At high rates (10C), both showed similar capacities, which was explained by only capacitive processes contributing to capacity at these rates. In other words, the increase in initial interlayer spacing (from 9.9 to 12.3 Å) was not sufficient to allow for the more diffusion-limited intercalation to occur. Using sub-micron MXene flakes offered some improvement to this at high rates, owing to a smaller diffusion distance for intercalation.

Several papers have studied the effect of surface chemistry on the Li storage properties. Xie et al. used a mixture of DFT (including on  $\text{Ti}_2\text{C}$ ,  $\text{Ti}_3\text{C}_2$ ) and experiments ( $\text{Ti}_3\text{C}_2$ ) to study the effect of O, OH and water content.<sup>98</sup> O terminations were found to lead to the highest Li capacities, OH and water were unfavourable, but could be removed upon vacuum annealing (673 and 773 K for 40 h and confirmed by in-situ X-ray adsorption spectroscopy (XAS)).

Chen et al. also used DFT to investigate  $\text{Ti}_2\text{C}$ ,  $\text{V}_2\text{C}$ , and  $\text{Nb}_2\text{C}$ , focusing on the effect of the effect of F surface groups.<sup>143</sup> They found F groups should stabilise the lithiated structures and enhance the conductivity, however O and OH terminations were not considered.

F terminations were studied experimentally by Sun et al. and found to be beneficial to the electrode performance, who achieved capacities close the theoretical maximums for  $\text{Ti}_3\text{C}_2\text{F}_2$ , and suggested maximising F terminations would maximise performance.<sup>144</sup> They also looked at the effect of delamination with DMSO and found

that this also led to increased capacity vs. their un-intercalated samples (124 mAh g<sup>-1</sup> vs. 107 mAh g<sup>-1</sup> at a 1C rate).

Cheng et al. used different heat treatments to change the surface of Ti<sub>3</sub>C<sub>2</sub> (heating to 400 °C under argon/H<sub>2</sub> and argon/ H<sub>2</sub>O atmospheres.<sup>142</sup> This removed some OH and F surface groups, as well as causing a small amount of TiO<sub>2</sub> to form, showing that they oxidised the MXene. The initial coulombic efficiencies were shown to increase after treatment from 58% to 64%, suggesting that the –OH and –F groups are involved in irreversible reactions with Li<sup>+</sup>, contributing to that high initial capacity loss.

Overall, it can be seen that titanium-based MXenes such as Ti<sub>3</sub>C<sub>2</sub> have promise for high rate Li-ion storage, but that multilayered flakes do not give capacities close to the theoretical capacities.

### **Molybdenum-based MXenes**

Anasori et al. discovered that out-of-plane ordered double MXenes could be a way of incorporating otherwise difficult elements into the M site of the MXenes.<sup>100</sup> They demonstrated that Mo<sub>2</sub>TiC<sub>2</sub>T<sub>x</sub> displayed very different electrochemical behaviour to the purely Ti equivalent, suggesting that the electrochemistry was dominated by the Mo on the surface instead.

Mo<sub>2</sub>TiC<sub>2</sub> has been studied for lithium-ion battery applications, with the performance showing several promising features which make it worthy for further investigation. For example, the first cycle capacity loss was only 14%, which is much lower than for other MXenes, which is promising for full cells. In addition, 85% of the total capacity was obtained below 1 V, which would lead to higher energy densities in a full cell. Unlike the fairly linear voltage profile observed for other MXenes, the load curve for Mo<sub>2</sub>TiC<sub>2</sub> displayed a plateau below 0.6 V, suggesting a phase change and charge storage mechanism clearly different to other MXenes. Therefore, the lithiation of Mo<sub>2</sub>TiC<sub>2</sub> is a two-stage mechanism. In the first stage, at an average voltage of around 1.6 V, Li<sup>+</sup> is intercalated on to the MXene surface, forming Mo<sub>2</sub>TiC<sub>2</sub>O<sub>2</sub>Li<sub>2</sub> in a similar mechanism to the Ti<sub>3</sub>C<sub>2</sub> MXene (Reaction 2.10). Computational studies suggested that this plateau was as a result of a conversion reaction between the lithiated Mo-O surface groups and the Li as shown by Reaction 2.11.



In the second stage, the lithiated MXene reacts further to form Li<sub>2</sub>O, which gives a large boost to capacity. The theoretical capacity of the intercalated MXene is just 150 mAh g<sup>-1</sup>, whereas when the conversion reaction is included this increases to 356 mAh

$\text{g}^{-1}$ . If more than one layer of Li can intercalate, the theoretical capacity could increase further, but the feasibility of this was not investigated.<sup>100</sup>

The proposed conversion reaction is similar to the lithiation mechanism of Mo oxides, where it is known to be accompanied by large volume changes which cause significant capacity fade.<sup>57</sup> This could explain the relatively high fade seen in the initial  $\text{Mo}_2\text{TiC}_2$  study, where 8% of the capacity was lost over just 25 cycles. If this could be stabilised, then this would significantly enhance the potential of this material.

$\text{Mo}_2\text{C}$  has also been studied, but in less detail. However, it is known to have Mo-O surface groups too, and the CV curves showed very similar shapes to  $\text{Mo}_2\text{TiC}_2$ , suggesting that a conversion reaction may also occur here.<sup>127</sup> The capacities were high, with  $560 \text{ mAh g}^{-1}$  reported after 70 cycles at  $0.4 \text{ A g}^{-1}$ ,  $250 \text{ mAh g}^{-1}$  after 1,000 cycles at  $5 \text{ A g}^{-1}$  and  $76 \text{ mAh g}^{-1}$  after 1,000 cycles at  $10 \text{ A g}^{-1}$ . However, the electrodes tested were free-standing electrodes only  $3 \mu\text{m}$  thick, with a mass loading of  $0.9 \text{ mg cm}^{-2}$ , which will give higher capacity, especially at fast rates, than thicker electrodes such as those casted using doctor blades. As was observed for  $\text{Mo}_2\text{TiC}_2$ , the initial coulombic efficiency, at 76%, was higher than for titanium-based MXenes, and over 66% of the capacity was below 0.5 V, which suggests that molybdenum-based MXenes have some advantages over titanium-based MXenes for Li-ion applications and are worth further investigation. No reports of molybdenum-based MXenes in non-lithium-ion systems (e.g. Na, Mg) have been found to-date.

#### **2.4.2.1.3 Na-ion Systems**

As for Li-ion systems, Na-ion has been a relatively heavily studied system for MXenes, although there has been a large focus on titanium-based MXenes. With the exception of one report on  $\text{V}_2\text{C}$  (as a positive electrode), all work found on MXenes in Na-ion systems focuses on titanium-based MXenes,  $\text{Ti}_3\text{C}_2$  and  $\text{Ti}_2\text{C}$ .

The first experimental report of MXenes in organic Na-ion systems was by Wang et al., who used DFT and STEM (scanning transmission electron microscopy) to investigate the structure of Na intercalated  $\text{Ti}_3\text{C}_2$ .<sup>145</sup> A double Na-atomic layer was found within the  $\text{Ti}_3\text{C}_2\text{X}$  interlayer towards the end of the first discharge cycle, giving experimental evidence to multilayer intercalation. However, the majority of the layers shown had only one  $\text{Na}^+$  layer present. The two  $\text{Na}^+$  layers were around 0.23 nm apart. In-situ XRD during the first cycle showed a reversible shift in the (002), (004), and (006) peaks to lower angles, suggesting reversible expansion upon intercalation, which is a sodiated product of  $\text{NaTi}_3\text{C}_2\text{T}_x$ . Electron energy loss spectroscopy (EELS) showed subtle changes in the Ti spectra, suggesting that Ti was reduced during intercalation. They tested  $\text{Ti}_3\text{C}_2$  nanosheets as a negative electrode to investigate the capacities and other predictions about electrode performance

(stability, rate) and found the rate performance was good (around 60 mAh g<sup>-1</sup> at 400 mA g<sup>-1</sup>). At 25 mA g<sup>-1</sup>, initial capacities were around 150 mAh g<sup>-1</sup>, but this quickly decreased to around 100 mAh g<sup>-1</sup> over the first 10-15 cycles, but stabilised after this initial decrease. Coulombic efficiency was close to 100% after the 20 initial cycles during which it steadily increased.

Multilayered Ti<sub>2</sub>C was studied in detail including its charge storage mechanism.<sup>146</sup> They found initial discharge capacities of 330 mAh g<sup>-1</sup>, but only 230 mAh g<sup>-1</sup> (which is similar to the reported theoretical capacities) was recovered on the subsequent charge, giving an initial coulombic efficiency of around 60%. After around 10 cycles, the capacity stabilised at around 175 mAh g<sup>-1</sup>, around 75% higher than had been reported for Ti<sub>3</sub>C<sub>2</sub>. The mechanism was then carefully studied using ex-situ XRD, TEM, and EDS. It was found that Na<sup>+</sup> did not spontaneously intercalate into the MXene, as had been reported for aqueous Na-based electrolytes, but did intercalate when current was applied. EDS gave the sodiated product as Na<sub>0.9</sub>Ti<sub>2</sub>CT<sub>x</sub>, similar to Wang et al.<sup>146</sup> This was accompanied by a shift to lower angles by the (002) diffraction peak, showing an increase in interlayer spacing. This spacing then became fixed, and did not change even after desodiation. Ex-situ TEM confirmed these XRD results. This suggested that after the initial expansion, due to intercalation of Na<sup>+</sup> ion and possibly solvent molecules, the electrode experienced no further volume change during cycling. This is in slight contrast to Wang et al., whose in-situ XRD showed reversible (002) shifts, which are potentially missed by ex-situ analysis.<sup>145</sup> The rate capability of this material was also promising, with around 110 mAh g<sup>-1</sup> retained at 1 A g<sup>-1</sup>, though a low mass loading of 1 mg cm<sup>-2</sup> was used.

Yu looked at the sodium storage capacity, mobility, and volume change during intercalation in Ti<sub>3</sub>C<sub>2</sub> using DFT.<sup>147</sup> They found high capacity and mobility, with only very small volume changes (which should lead to a more stable electrode). They found that the slightly enlarged interlayer spacing caused by some Na intercalation allowed for easy formation of multilayer adsorption, offering significantly increased capacities. This partial in-situ pillaring was investigated and confirmed using <sup>23</sup>Na solid state NMR by Kajiyama et al.<sup>148</sup> They also found that the solvent molecules also intercalate between the layers and help keep the interlayer distance slightly enlarged. This led to minimal changes in the interlayer spacing during cycling as shown by their ex-situ XRD data, confirming the work of Yu et al., and similar to Ti<sub>2</sub>C. The multilayered MXene showed initial reversible capacities of around 130 mAh g<sup>-1</sup>, but this quickly decreased across the first 10-15 cycles to around 100 mAh g<sup>-1</sup>. After this initial relatively rapid fade, the material stabilised and the rate of fade was substantially reduced. Ex-situ NMR showed that desolvated Na<sup>+</sup> was found in the intercalated material, confirming an intercalation redox reaction. Interestingly, ex-situ XANES on the Ti found no change in the oxidation state of Ti during cycling, but ex-situ XPS did detect clear changes in the oxidation state of oxygen. This suggests

that the redox reaction occurs on the surface O groups rather than the Ti in the MXene, but is in slight contrast to Wang et al., whose EELS results report very subtle changes in the Ti oxidation state.<sup>145</sup> They also confirmed the formation of a stable SEI layer using ex-situ NMR, which showed a consistent Na environment throughout cycling. CV analysis revealed that the charge storage was predominantly surface controlled, indicating pseudocapacitive intercalation mechanisms.

Luo et al. also reported that the Ti 2p XPS spectra of  $Ti_3C_2$  is unchanged in a Na-ion system, but did not study the O 1s to confirm any redox activity here.<sup>149</sup> Instead they partially oxidised the MXene surface using NaOH, forming  $TiO_x$  oxides, which then stored  $Na^+$  via Ti redox reactions. The NaOH treatment also increases the initial coulombic efficiency from around 40% to 60%.

Overall MXenes have been predicted to have high capacities with multilayer  $Na^+$  intercalation possible, fast rates and good stabilities. Experimental studies on multilayered materials appear to confirm these expectations. Light transition metals and bare or O terminated MXenes are predicted to give the best results, and Ti-O groups appear to be redox active in the charge storage mechanism, which can be best described as intercalation pseudocapacitance dominated. A stable SEI is thought to form after the first cycle, but contributes to low initial coulombic efficiencies (less than 60%). Therefore MXenes seem to be a good candidate for further development as negative electrodes for Na-ion systems, although much more work is required in this field, including on determining the charge storage mechanism in detail.

#### **2.4.2.1.4 Multivalent-ion Systems**

Multivalent-ion systems such as  $Mg^{2+}$ ,  $Zn^{2+}$  and  $Al^{3+}$  are attracting substantial interest since they are based on elements which are cheaper, more abundant and / or more widely distributed than  $Li^+$ , but offer higher energy densities than  $Na^+$  and  $K^+$  systems since each ion can contribute two or more electrons for redox processes. However, these systems suffer from a lack of host electrode materials which can reversibly store the small, highly charged ions at satisfactory rates. Initial theoretical studies predicted that MXenes could be promising materials in this area, which led to some experimental work being carried out to further develop MXenes for these applications. These are discussed briefly in this section, since Zn-ion systems are studied in Chapter 6 of this thesis.

Only one report has been found on MXenes in Al-ion systems, with  $V_2C$  being used as a positive electrode.<sup>150</sup> The capacity was around 170 mAh  $g^{-1}$  on the second cycle, with 112 mAh  $g^{-1}$  and a coulombic efficiency of 90% being reported by 20 cycles. Ex-situ XRD showed no shift in the (002) diffraction peak after the first discharge and charge, suggesting that the interlayer distance remained constant during cycling. The

CV curve showed clear redox peaks, suggesting the charge storage was faradaic in nature.

Initial attempts to investigate the Mg-ion capacity of  $\text{Ti}_3\text{C}_2$  MXene in an organic system concluded that the capacity was negligible. Instead, Byeon et al. used  $\text{Ti}_3\text{C}_2$  and  $\text{Mo}_2\text{C}$  MXenes as positive electrodes in a hybrid Li/ Mg battery, where the negative electrode was Mg metal and the MXene reversibly intercalated Li.<sup>151</sup> While the performance was good ( $100 \text{ mAh g}^{-1}$  at a rate of 0.1C), this system does not utilise  $\text{Mg}^{2+}$  storage in the MXene positive electrode.

Xu et al. used a cationic surfactant, CTAB, to intercalate  $\text{CTA}^+$  between  $\text{Ti}_3\text{C}_2$  layers, increasing the interlayer distance and lowering the  $\text{Mg}^{2+}$  diffusion barrier. This led to reversible  $\text{Mg}^{2+}$  intercalation, giving capacities of around  $100 \text{ mAh g}^{-1}$ , demonstrating that  $\text{Ti}_3\text{C}_2$  can be made to store  $\text{Mg}^{2+}$  ions.<sup>152</sup> Zhao et al. used a sacrificial PMMA template combined with pre-intercalating  $\text{Mg}^{2+}$  (using  $\text{MgCl}_2$ ), to achieve high capacities up to  $200 \text{ mAh g}^{-1}$ , though after 60 cycles at 1C rate (one hour charge) less than  $50 \text{ mAh g}^{-1}$  was retained (compared to  $140 \text{ mAh g}^{-1}$  at 1C initially).<sup>153</sup> This was attributed to possible conversion reactions after  $\text{Mg}^{2+}$  intercalation forming  $\text{MgO}$ , which has poor reversibility. No major phase changes were observed in the MXene after cycling. However, the precise reaction mechanism requires further investigation to be determined. Without pre-intercalation, the Mg capacity was negligible, though increased slightly over multiple cycles.

Liu et al. recently used a  $\text{Ti}_3\text{C}_2$  carbon nanosphere sandwich electrode as a Mg-ion positive electrode, which had a surface area of  $104 \text{ m}^2 \text{ g}^{-1}$ .<sup>154</sup> This resulted in large capacities, up to  $200 \text{ mAh g}^{-1}$  at  $10 \text{ mA g}^{-1}$  and  $120 \text{ mAh g}^{-1}$  at  $200 \text{ mA g}^{-1}$ . Ex-situ XRD revealed a reversible shift in the (002) diffraction peak, corresponding to the expansion and shrinkage of the MXene as Mg intercalates and de-intercalates between the layers. Interestingly, CV analysis revealed that the current was almost entirely surface-limited, not diffusion-limited, suggesting that the charge storage in the porous electrode was highly capacitive in nature. Like Zhao et al., they proposed that  $\text{MgO}$  could form by reaction of the  $\text{Mg}^{2+}$  ions with the Ti-O surface groups, but no evidence of this was given in their XRD patterns.

No reports have been found on the use of MXenes for  $\text{Zn}^{2+}$  intercalation. However, Yang et al. have recently reported the use of  $\text{Ti}_3\text{C}_2$  as a positive electrode (charging from OCV) against a Zn metal negative electrode in 1 M  $\text{ZnSO}_4$  in a Zn-ion capacitor.<sup>155</sup> Here the MXene stored charge via EDL capacitance by acting as sulphate hosts, while the negative electrode stored charge through the reversible electrodeposition of  $\text{Zn}^{2+}$  on the Zn metal surface. This demonstrates the flexibility of MXenes as potential electrode materials. A similar mechanism was exploited by Wang et al., who used  $\text{Ti}_3\text{C}_2$ -rGO aerogels as the positive electrode in a Zn-ion capacitor, where the MXene aided in the charge storage via EDL capacitance based

on  $\text{SO}_4^{2-}$  adsorption, giving a capacity of around  $35 \text{ mAh g}^{-1}$ .<sup>156</sup> This is similar to charge storage with carbon-based positive electrodes in this system, although oxygen functional groups often give a mixture of EDL and pseudocapacitance. Carbons (including activated carbons and carbon nanotubes) have been reported to have capacities in the range of  $27 - 125 \text{ mAh g}^{-1}$ .<sup>157</sup>

Overall, the results from this section on multivalent systems suggest that MXenes could have promise as Zn-ion electrodes since they can reversibly store charge in several multivalent systems, with the performance of  $\text{Ti}_3\text{C}_2$  in Mg-ion systems, which are also divalent, particularly encouraging. The exact charge storage mechanism in each system is not well understood so far, but appears to vary depending on the system being studied. Electrode structure can be seen to play an important role for MXene electrode performance, with the porous  $\text{Ti}_3\text{C}_2$  structure reported by Liu et al. showing excellent performance for Mg-ion storage. It is worth noting that with the exception of the Zn-ion system, all the reports discussed above have been in water-free organic systems, since water is detrimental to Al and Mg metal electrodes.

#### **2.4.2.1.5 Aqueous Electrolytes**

As previously mentioned (Section 2.3.3.1), aqueous electrolytes are considered safer than organic electrolytes due to being inherently non-flammable and (depending on the pH and specific salt used) non-toxic. In addition, high ionic conductivities are often reported in aqueous electrolytes, resulting in superior rate performance. Therefore there is significant interest in developing high energy aqueous energy storage systems. MXenes are stable in aqueous electrolytes, and have shown promising performance in certain systems. For Zn-ion systems, aqueous electrolytes are the most studied to date, consequently, an aqueous system ( $0.1 \text{ M ZnSO}_4$ ) was chosen to be studied in Chapter 6. Since MXenes had not previously been reported for  $\text{Zn}^{2+}$  intercalation, a short review on the charge storage mechanisms in other aqueous systems is carried out, since this could aid the understanding of the Zn system.

In acidic electrolytes, the behaviour for charge storage is consistent with pseudocapacitance (redox) mechanisms. Lukatskaya et al. used in-situ X-ray adsorption spectroscopy and X-ray absorption near edge structure spectroscopy (XANES) to follow the oxidation state of Ti in  $\text{Ti}_3\text{C}_2$  during cycling in  $\text{H}_2\text{SO}_4$ .<sup>121</sup> They found a clear change in Ti oxidation state corresponding to an average change of 2.33 to 2.43 (i.e., by  $\approx 0.1 \text{ e}^-$  per Ti atom) over a 0.7 V window. This gave capacitance values similar to the experimentally measured ones. This shows the origin of capacitance in  $\text{Ti}_3\text{C}_2$  is from redox processes on the Ti, when in an acidic electrolyte. Simulations by Zhan et al. support this conclusion, but also find evidence of EDL capacitance occurring alongside the redox mechanism, with the balance between the two being voltage dependant.<sup>158</sup>

Hu et al. used in-situ Raman spectroscopy to study the charge storage mechanism of  $\text{Ti}_3\text{C}_2$  as the positive and negative electrode in  $\text{H}_2\text{SO}_4$ ,  $\text{MgSO}_4$  and  $(\text{NH}_3)_2\text{SO}_4$ .<sup>75</sup> It revealed that the  $-\text{O}$  terminal groups react directly with  $\text{H}^+$  in  $\text{H}_2\text{SO}_4$ , confirming this as the charge storage mechanism when  $\text{Ti}_3\text{C}_2$  is used as the negative electrode in acidic media. When used as the positive electrode, the charge storage mechanism is given only by EDL capacitance based on  $\text{SO}_4^{2-}$  adsorption. In  $\text{MgSO}_4$  and  $(\text{NH}_3)_2\text{SO}_4$  the charge storage was only given by EDL capacitance, regardless of whether the MXene was used as the positive or negative electrode, which the authors attributed, at least in part, to the smaller ion size of  $\text{H}^+$  ( $\text{H}_3\text{O}^+$ ), allowing it to access deep redox centres. In addition, the ion migration mechanisms also differed, with ion exchange dominating in the  $\text{H}_2\text{SO}_4$  negative electrode. In all other cases counter ion adsorption dominated.

Lin et al. also studied the mechanism of the same materials (also HF etched) using a mixture of XRD and electrochemical characterisation (impedance spectroscopy and galvanostatic measurements).<sup>159</sup> They used a KOH electrolyte, finding charge storage through the intercalation of  $\text{K}^+$ , without phase changes. They also found that the high electrical conductivity and layered structure of the MXene allowed ion intercalation even at high mass loadings.

Levi et al. used electrochemical quartz-crystal admittance and in-situ electronic conductance measurements to investigate the mechanism of charging in MXenes ( $\text{Ti}_3\text{C}_2$ , 50% HF etching).<sup>160</sup> They looked at a variety of cations intercalated between the layers, noting that the rates are superior to batteries, and give higher energy densities than typically seen for capacitors, supporting MXenes' suitability for metal-ion capacitor applications. They found that cationic insertion is accompanied by significant deformation of the MXene particles, but that it occurs so rapidly so as to resemble 2D ion adsorption at solid-liquid interfaces. This explains this intermediate behaviour, and makes these materials particularly promising for metal-ion capacitors. They also noted that the process is helped by the presence of interlayer water molecules, which is known to occur with HCl-LiF etching.

Li et al. studied  $\text{Ti}_3\text{C}_2$  in  $\text{Li}_2\text{SO}_4$  and  $\text{Na}_2\text{SO}_4$  for aqueous capacitor applications.<sup>161</sup> CV analysis showed rectangular voltammograms, with very broad peaks that were only a slight deviation from a rectangle. Kinetic analysis showed that the current was almost entirely capacitive, suggesting that the charge storage could be a mixture of pseudocapacitive and EDL capacitive mechanisms, though the oxidation states were not studied.

This shows that in aqueous electrolytes, charge storage has significant contributions from faradaic charge transfer reactions, including intercalation pseudocapacitive charge storage, but this strongly depends on the electrolyte used. Apart from initial expansions resulting from electrolyte penetration between the MXene layers, no

phase changes are reported, which supports capacitive-type charge storage. The surface chemistry is found to play an important role for electrolytes where charge storage is faradaic such as  $\text{H}_2\text{SO}_4$ , since the Ti-O groups are reported to actively bind with cations such as  $\text{H}^+$ . This helps explain the superior performance of HCl-LiF etched compared to HF etched  $\text{Ti}_3\text{C}_2$ , since the former contains a higher proportion of active Ti-O groups. Multivalent redox reactions were not found for  $\text{MgSO}_4$ , where the  $\text{Mg}^{2+}$  ions (which like  $\text{Zn}^{2+}$  are divalent) appeared to only be stored via EDL capacitance.

#### **2.4.2.1.6 Intercalation Hybrid Metal-ion Supercapacitors**

There have been some reports of papers on testing promising high-rate MXene materials in full-cell metal-ion capacitor systems, a selection of which are briefly discussed in this section to demonstrate that MXenes show promise in full metal-ion capacitor cells.

Several reports have been found using MXene electrodes in Li-ion capacitors (LIC). Come et al. tested a (HF etched)  $\text{Ti}_2\text{C}$ /activated carbon asymmetric cell between 1-3.5 V with a 1M  $\text{LiPF}_6$  in ethylene carbonate (EC) and dimethyl carbonate (DMC) 1:1 electrolyte. They found good capacity retention during 1,000 cycles at high rates up to 10C (6 min discharge time), showing the potential of this MXene for high rate LIC applications. The MXene showed a capacity of  $65 \text{ mAh g}^{-1}$  at 10C, with a maximum energy density of  $30 \text{ Wh kg}^{-1}$  at  $930 \text{ W kg}^{-1}$  showing the hybrid properties of a LIC.

Byeon et al. investigated HF etched  $\text{Nb}_2\text{CT}_x$ -CNT (carbon nanotube) composites as electrodes in LICs.<sup>162</sup> Three configurations were studied, a symmetric cell, and two asymmetric cells with graphite and  $\text{LiFePO}_4$  as the other electrodes respectively. The symmetric cell had the highest volumetric energy density ( $50\text{--}70 \text{ Wh dm}^{-3}$ ) across a 3 V window. Capacities up to  $43 \text{ mAhg}^{-1}$  were achieved (per weight of the two electrodes,  $86 \text{ mAh g}^{-1}$  per electrode was the average capacity). The CNTs were added the MXene in DI water and mixed via sonication. The electrolyte was 1 M  $\text{LiPF}_6$  in a 1:1 mixture of ethylene carbonate (EC) and diethyl carbonate (DEC).

Sodium-ion capacitors (NIC) are considered to be cheaper alternatives to LIC, but offering similar properties of high power and energy densities.

$\text{Ti}_2\text{C}$  has been studied as a negative electrode for NICs, in a 1 M  $\text{NaPF}_6$ /EC-DEC electrolyte by Wang et al.<sup>146</sup> It was synthesised by HF etching and combined with a carbon conductive agent and a binder for the electrode material. They achieved capacities over  $100 \text{ mAhg}^{-1}$  for the full cell, with little capacity loss after the 1<sup>st</sup> cycle for a total of 100 cycles. Dall'Agnesse et al. investigated HF etched  $\text{V}_2\text{C}$  as a positive electrode for a NIC. They tested the capacitance of the material in a half cell and then contrasted a full cell with a hard carbon negative electrode.<sup>96</sup> This showed reasonable performance with  $100 \text{ F g}^{-1}$  at  $0.2 \text{ mVs}^{-1}$  for the half cell and a capacity 50

mAh g<sup>-1</sup> with a maximum voltage of 3.5 V for the full cell. Clear sodiation peaks were seen on the cyclic voltammograms, but disappeared at rates above 2 mVs<sup>-1</sup>, suggesting the redox process is unable to occur due to a diffusion limitation at these higher rates.

Overall MXenes show much early promise in electrochemical energy storage systems, though further work is required to improve the understanding and performance of these materials in electrochemical energy storage systems.

#### 2.4.2.2 Porous MXene Electrodes

This section focuses on selected reports of porous MXenes with altered structures, and their use in organic Li- and Na-ion systems and as well some aqueous systems, with a focus on materials with the highest surface areas and / or electrochemical performance reported.

Amine-assisted delamination was studied on Nb<sub>2</sub>C by Mashtalir et al.<sup>131</sup> They found that due to restacking of the delaminated layers, the capacities were actually lower than the multi-layered material. The addition of CNTs (10 wt.%) as interlayer separates however increased the capacities to around 430 mAh g<sup>-1</sup>, which was recorded after 300 cycles. It should be noted that the capacity increased over these 300 cycles, thought to be because the structure was being opened up, which suggests that the spacer did not fully expand the structure initially. The electrochemical behaviour of these materials was more capacitive-like than battery-like, and therefore the materials were also tested as capacitors vs. a carbon electrode, giving capacitance of 165 F g<sup>-1</sup> and 325 F cm<sup>-3</sup>. This performance was better than Ti<sub>3</sub>C<sub>2</sub> studied by the same group.

Carbon nanotubes (CNTs) and reduced graphene oxide (rGO) have been common additives to create porous MXene structures, which have been found to inhibit restacking of the nanosheets and increase conductivity. Dall'Agnes et al. also reported that addition of the CNTs increased the surface area (23 to 70 m<sup>2</sup>g<sup>-1</sup>, measured using N<sub>2</sub> BET).<sup>163</sup> The resulting MXene was found to have improved capacitance with good stability upon addition of CNTs compared to the bare MXene in an electrolyte of 1 M EMITFSI solution in acetonitrile. The large EMI cation was found to intercalate but with diffusion-limited kinetics.<sup>163</sup>

Zhao et al. studied a variety of carbon additives in delaminated Ti<sub>3</sub>C<sub>2</sub>. They looked at different types of CNTs and rGO in slightly different configurations. They found that all additives increased the interlayer spacing, while all but one increased the conductivity but only three showed increased volumetric capacitance. The highest capacitance was for a rGO composite. A 1 M MgSO<sub>4</sub> aqueous electrolyte was used. Song et al. created Ti<sub>3</sub>C<sub>2</sub>-rGO aerogels with surface areas up to 260 m<sup>2</sup> g<sup>-1</sup>.<sup>164</sup> The rGO content was 30%, and pure rGO had a BET surface area of 280 m<sup>2</sup> g<sup>-1</sup>, which shows

that it would have a significant contribution to the total aerogel surface area. Ma et al. created delaminated  $\text{Ti}_3\text{C}_2$ -rGO composites with surface areas up to  $73 \text{ m}^2 \text{ g}^{-1}$ .<sup>165</sup> When tested as a Li-ion negative electrode it had a discharge capacity of around  $300 \text{ mAh g}^{-1}$  at  $50 \text{ mA g}^{-1}$ , and  $175 \text{ mAh g}^{-1}$  at  $1 \text{ A g}^{-1}$ , almost twice as high as the non-porous MXene. The CV curves showed no sharp redox peaks, with kinetic analysis showing around half the current was due to surface-limited processes.

Zhu et al. used a heat treatment technique ( $500^\circ\text{C}$  for 4 h in vacuum) to grow  $\text{TiO}_2$  nanoparticles on  $\text{Ti}_3\text{C}_2$  (HF etched).<sup>166</sup> It was noticed that a small amount of graphite also formed in this process, which increased electrical conductivity. They used  $\text{N}_2$  BET to measure the surface area, seeing an increase from 8 to  $32 \text{ m}^2 \text{ g}^{-1}$  upon growing the  $\text{TiO}_2$  nanoparticles. They used a 6 M KOH electrolyte and obtained capacitances 1.5 times that of non-porous  $\text{Ti}_3\text{C}_2$ . Hu et al. studied  $\text{Ti}_3\text{C}_3$  with a Ni-foam and found an increase in BET surface area of  $32 \text{ m}^2 \text{ g}^{-1}$  vs.  $0.5 \text{ m}^2 \text{ g}^{-1}$  for the bare MXene and a high gravimetric capacitance of  $499 \text{ F g}^{-1}$  in 1 M  $\text{H}_2\text{SO}_4$ , one of the highest for an MXene electrode.<sup>167</sup> The Ni-foam was found to be electrochemically inactive with strictly structural benefits. However, Ni-foams are not currently considered a scalable method to make porous MXenes, and the surface areas obtained were still relatively low.

Ren et al. used a chemical etching technique to create a porous  $\text{Ti}_3\text{C}_2$  framework, which was then combined with CNTs to give a very high performing LIB negative electrode.<sup>168</sup> The BET surface area was improved from 19.6 to  $93.6 \text{ m}^2 \text{ g}^{-1}$ , as high as delaminated MXenes, with the porous nature preventing the restacking found in the delaminated samples. The pore sizes were shown to be 4-6 nm, reduced from 10s of nm for the pristine MXene. It was also found that this technique reduces the number of F terminations and increases the OH and O terminations, which is thought to be beneficial for battery performance. The composites were then tested as negative electrodes for LIBs, a high rate capacity of  $330 \text{ mAh g}^{-1}$  at 10C. However, this technique clearly damages the MXene nanosheets.

Xie et al. used CTAB grafted CNTs to act as spacers between delaminated  $\text{Ti}_3\text{C}_2$  nanosheets, which gave high BET surface areas up to  $185 \text{ m}^2 \text{ g}^{-1}$ .<sup>169</sup> As a Na-ion negative electrode it returned a second cycle capacity of around  $150 \text{ mAh g}^{-1}$ , with a first cycle coulombic efficiency of just 35%, likely as a result of the large proportion of exposed surface area. Over 100 cycles at  $20 \text{ mA g}^{-1}$  the capacity increased slightly to  $175 \text{ mAh g}^{-1}$  as the structure was further opened up (4.5 times the bare MXene). The coulombic efficiency increased over 60 cycles at around 99%. No clear redox peaks could be seen on the CV curves, analysis of which showed the current was mostly surface-controlled. Zhao et al. used Li, Na and K hydroxides to crumple  $\text{Ti}_3\text{C}_2$  nanosheets giving porous, and slightly oxidised structures, with BET surface areas up to  $71 \text{ m}^2 \text{ g}^{-1}$ .<sup>170</sup> As a Na-ion negative electrode, the NaOH material focused on in their

paper showed a reversible capacity of 150 mAh g<sup>-1</sup> after 10 cycles, with 175 mAh g<sup>-1</sup> being achieved after the second cycle. Bao et al. used a freeze-drying technique to make aerogels out of delaminated Ti<sub>3</sub>C<sub>2</sub>, which had a BET surface area of 293 m<sup>2</sup> g<sup>-1</sup>; the largest found in this review.<sup>171</sup> This showed increased capacitance for capacitive water desalination, which was attributed to the larger surface area and open structure.

This section showed that there is a clear need for the development of new procedures to create porous and stable MXene structures, which have already been shown to have superior electrochemical performance compared to the multilayered counterparts. Delaminating nanosheets is not sufficient, since the sheets restack, giving lower surface area and poorer performance than multilayered MXenes. Increasing the surface area and creating porous structures can effectively prevent restacking, giving superior capacities, rate capabilities and cycling stabilities to multilayered MXenes. This is often with an increased capacitive contribution shown by the loss of redox peaks on CV curves and by kinetic analysis. However, many of the strategies developed are complicated, use dilute solutions which would hinder scale-up, destroy the MXene structure or still give relatively low surface areas. Therefore, alternative procedures, such as pillaring should be developed.

## 2.5 Pillaring

Pillaring is a technique that has been developed over the last few decades to create porous structures out of layered materials, typically layered clays. It involves the insertion of a foreign species, typically an ion or molecule, in the interlayer between sheets. These species cause an increase in the interlayer distance, and, if they are stable in the structure, maintain the increased interlayer spacing for use in applications. In other words, they hold apart two layers in the material, acting as pillars, analogously to pillars in buildings (Figure 2.19). This leads to the creation of new or enlarged pores, which can be tuned by choice of pillar and pillaring conditions, and is typically accompanied by a significant increase in surface area. This generally leads to increased performance for a variety of applications such as catalysis and sensors, where a higher surface area increases the number of active sites available to reactants, and the regular pore structure improves the transport properties of reaction species to and from the active sites.<sup>172,173</sup> Whilst the electrical conductivity of typical pillared clays is too low for their use as electrodes in electrochemical energy storage systems, the structural characteristics of pillared clays match closely with the desirable characteristics of high rate electrode materials. In addition, MXenes themselves are often described as conductive clays, and have similar surface chemistries to typical layered clays (oxy- and hydroxyl-based groups), which suggests that the pillaring techniques developed for layered clays have promise for creating porous MXene structures with increased surface areas and

controlled pore sizes. This would be expected to lead to improved electrochemical performance for the pillared MXenes due to increased access to the charge storage sites, and creation of large regular channels for fast ion transport.

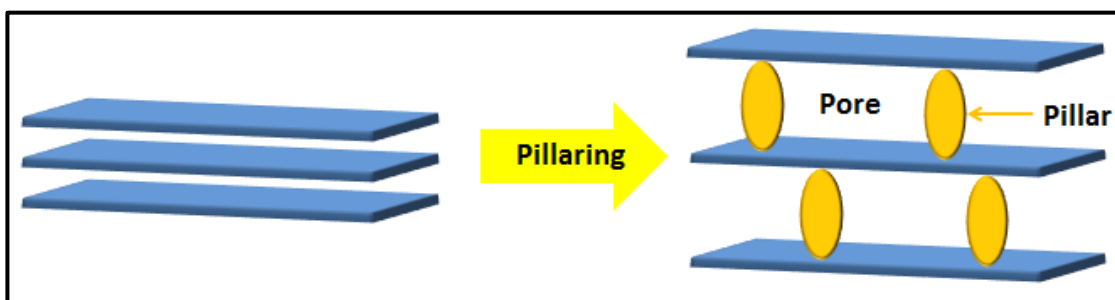


**Figure 2.19.** Schematic representation of the pillaring process, showing the insertion of pillars which separate the layers of a material creating new pores.

### 2.5.1 Pillars

A variety of species have been used as pillars in the creation of porous clays, though they can be classified into three main groups: oxides, ionic surfactants and molecular surfactants.

#### 2.5.1.1 Oxide pillars

Oxide pillars are typically synthesised by the intercalation of either an ionic or molecular (organometallic) precursor followed by a calcination or hydrothermal step to convert the precursor into the stable oxide.

Ionic precursors can be either single ion species dissolved in a solvent, such as the result of dissolving salts in solvents, or cage-like ions, which can consist of multiple metal atoms and can have high charges. For example, the  $\text{Al}_{13}^{7+}$  Keggin ion is a commonly used pillar which consists of oxy and hydroxy linkers between 12 octahedral Al sites and a central tetrahedral site. This gives pore diameters dictated by the size of the ion cage (e.g. around 1 nm in the case of  $\text{Al}_{13}$ ).<sup>172</sup> These are substantially higher than the sizes of single ion pillars, where the size will only be expanded by intercalation of the ion and / or solvent molecules, and any aggregation of the ions during heat treatment steps. Therefore, the majority of work on pillared clays which utilised ionic precursors for oxide pillars used cage ions as the pillar precursor. The chemistry of these cage ions is typically based around Al, Fe, Ga, V and Zr, with multi-element cages also known.<sup>172</sup> This class of pillar is generally limited by the need for multiple washing cycles, which require large amounts of water, and by low concentrations often being used.<sup>172</sup>

The use of molecular (organometallic) precursors has also been widely studied, with Si, Ti and Nb oxide pillars being reported. These pillaring techniques rely on the intercalation of the molecular precursor, followed by a hydrolysis reaction, which

then converted to a crystalline oxide during a calcination step. As for the cage-based pillars, multi-element pillars can also be created, for example Si-Ti mixed pillars using tetraethylorthosilicate (TEOS) and titanium isopropoxide. The size of the pillar is limited by the increase in the interlayer resulting from the intercalation of the molecule precursor and any solvent molecules. High surface areas can be achieved. For example Gallo et al. used niobium pentachloride to create a Nb-pillared montmorillonite with a BET surface area up to  $252 \text{ m}^2 \text{ g}^{-1}$ .<sup>174</sup>

### 2.5.1.2 Ionic Surfactants

Ionic surfactants are attractive as pillars because they typically have long carbon backbones and molecule lengths between 2-3 nm, which gives very large interlayer spacings up to the molecule length depending on the angle the surfactant is intercalated at. These interlayer distances are much larger than what can be achieved using oxide precursors, and can be tuned by the choice of surfactant and the angle of intercalation, which also gives a larger pore range than can be tuned by the typical oxide precursors.<sup>175</sup> Cationic surfactants, such as cetyltrimethylammonium bromide (CTAB, Figure 2.20), are generally used, since the surface of oxy and hydroxyl terminated clays tends to be slightly negatively charged, which allows the intercalation of the cationic surfactant via electrostatic attraction and ion exchange (if the clay already contains other ions in the interlayer, which is often the case).<sup>175</sup> This makes procedures using these types of pillars relatively simple compared to oxide based ones, but does not provide the functionality that non-carbon pillars often bring.

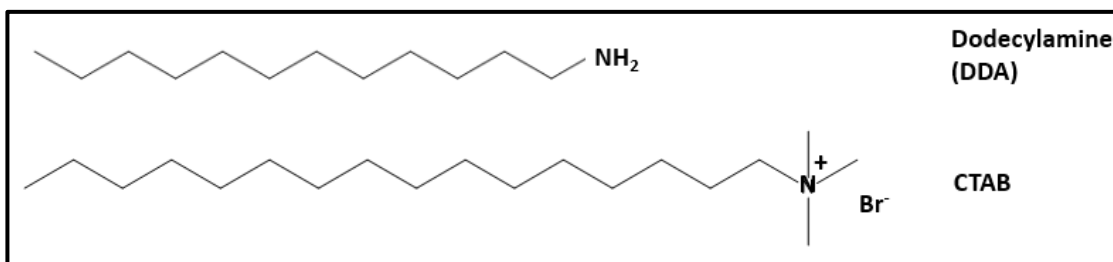


**Figure 2.20.** Illustration showing the chemical structure of a molecular surfactant (top, DDA) and ionic surfactant (bottom, CTAB), which are both used in this thesis.

### 2.5.1.3 Molecular Surfactants

Molecular surfactants, typically long chain amines (Figure 2.20), are also used in the same way that ionic surfactants are, and offer very similar advantages and disadvantages. The mechanism for intercalation is different however, since amines are not charged, electrostatic attraction is not strong enough. Instead, amines are thought to hydrogen-bond to certain surface groups such as OH groups, which then hold the pillars in place. Amines are also known to form bilayers, unlike cationic surfactants, which can give pore sizes twice that of the molecule chain length.

Consequently, interlayer distances over 3 nm are known, which is even larger than what cationic surfactants typically achieve.<sup>173</sup>

#### **2.5.1.4 Co-pillars**

The different advantages and disadvantages of the above types of pillars led to the development of co-pillaring strategies. Here the long chain surfactant pillars (cationic surfactants and amines) are used as co-pillars to expand the interlayer and act as templates for an oxide precursor. This can be done either by intercalating the surfactant in a separate pre-pillaring step followed by the oxide precursor intercalation or by adding the surfactant and oxide precursor simultaneously in a single step. The use of co-pillaring techniques allows for the advantages of the different classes of pillars to be combined: the pillared material should have the functional advantages provided by the oxide and the larger, and more tuneable, interlayer spacing afforded by the surfactant (which in turn can lead to higher loading of the functional oxide).<sup>173</sup> For example, Park et al. used an amine (dodecylamine, DDA) assisted pillaring method to intercalate TEOS between the layers of a titanosilicate. This created a porous silica pillared titanosilicate with a large gallery height of around 3 nm (d-spacing around (4 nm)) and a surface area as high as  $618 \text{ m}^2 \text{ g}^{-1}$ .<sup>176,177</sup> The DDA and TEOS co-intercalated in a 1 h room temperature step, which was followed by a short hydrolysis step and calcination step. Since titanosilicates have Ti-O and Ti-OH surface groups, which is the same as titanium-based MXenes, this work is especially significant for pillaring MXenes, and this method was applied to pillaring MXenes in this thesis.

#### **2.5.2 Pillaring of 2D Materials**

Since 2D materials are inherently layered in nature, there has been some interest in applying the pillaring methods which were developed for layered clays to 2D materials, such as graphene. The motivation for this research has been the tendency of 2D nanosheets to restack, which limits their performance in applications where access to the nanosheet surface is key to performance such as catalysis, gas separations and storage, water purification and electrochemical energy storage. This is as a result of these applications requiring access to active sites on the nanosheets' surface for reactions or binding. If these sites are not accessible then the reactions or binding cannot go ahead. As well as performance in applications, the fundamental properties of 2D materials are often dependant on the number of layers that are stacked together. For example, the optical and electrical properties of single layer graphene are different (often superior) to multi-layer graphene or graphite. For electrochemical energy storage applications, it is generally considered desirable to have relatively large interlayer spacings to allow for high amounts of charge storage with the maximum number of accessible ion storage sites, fast ion transport for high rate charging and stable interlayers to give long term cycling stability. All of these

characteristics could be achieved by pillaring. In addition, unlike some methods to create porous 2D materials such as creating holes in the nanosheets, pillaring keeps the nanosheets intact, preserving the underlying material.

Graphene has been the most studied 2D material, and the majority of work carried out on pillared graphene has utilised diaminoalkanes ( $\text{NH}_2(\text{CH}_2)_n\text{NH}_2$ , where  $n = 2, 6, 10$  etc.). Kim et al. had the earliest report found on this method, and found that the pillaring agent chain length and the annealing temperature affected the interlayer distance, which could be tuned to the nearest 0.1 nm up to 1 nm.<sup>178</sup>

This work has been followed up by several other studies, which have used this approach to study the effect of the small pore size ( $< 1$  nm) on ion sieving and performance in supercapacitors. For example, Yuan et al. demonstrated biphenyl-based pillars could increase the surface area of rGO from 11 to  $242 \text{ m}^2 \text{ g}^{-1}$  with an average pore size of 1 nm.<sup>179</sup> This led to the pillared rGO having a capacitance over twice that of the pristine rGO at all rates studied in 6 M KOH, which demonstrates the use of pillaring to improve the electrochemical performance of 2D materials. Banda et al. varied the concentration of diamine pillars in the rGO and found that reducing the concentration could improve the high rate performance of the electrode in an organic electrolyte, since the pillars themselves hindered ion transport at high rates.<sup>180</sup> However, their optimally pillared material had capacitance around twice that of the non-pillared rGO, which shows that pillaring is a viable strategy to improve electrochemical performance when the pillar concentration is not too high.

Hantel et al. used electrochemical pillaring to increase the spacing between rGO sheets, which were then tested as supercapacitor electrodes.<sup>181</sup> The emergence of these pillars caused an increase in the interlayer spacing from around 4 Å to around 13-14 Å, shown by in-situ XRD, which was maintained throughout future cycling. It was suggested that the pillars form during the first cycle are from reactions between the solvent and the O and OH groups on the rGO.

Paek et al. created a  $\text{TiO}_2$  pillared  $\text{MoS}_2$  material.<sup>182</sup> The interlayer distance was 1.03 nm, while the Langmuir specific surface area of the  $\text{TiO}_2$ -pillared  $\text{MoS}_2$  ( $186 \text{ m}^2 \text{ g}^{-1}$ ) was much larger than that of the restacked  $\text{MoS}_2$  ( $12 \text{ m}^2 \text{ g}^{-1}$ ). This showed that the  $\text{TiO}_2$  nanoparticles successfully prevent the restacking of the  $\text{MoS}_2$  nanosheets, creating a stable porous structure.

### 2.5.3 Pillared MXenes

Since MXenes and clays have several common characteristics such as similar surface chemistries and ability to intercalate and exchange cations, it is apparent that the pillaring techniques developed for clays also have promise for creating porous

MXenes. Some groups have reported studies which looked at pillared MXenes; these studies are reviewed in this section.

Shen et al. used tetramethylammonium hydroxide (TMAOH) to delaminate the MXene nanosheets and intercalate  $\text{TMA}^+$  between the layers in a pre-intercalation step (72 h).<sup>183</sup> Hexadecylamine hydrochloride (HEXCl) and dodecylamine hydrochloride (DDACl) were then used for ion-exchange reactions to intercalate  $\text{HEX}^+$  and  $\text{DDA}^+$  between the layers via electrostatic attraction (24 h). A heat treatment step was then used to carbonise the intercalated cations (6 h, Ar, 800 °C), which led to partial oxidation of the MXene surface. The interlayer spacing increased up to 2.83 nm, suggesting formation of tilted bilayers. The carbon-pillared  $\text{Ti}_3\text{C}_2$  was then tested for 1 M  $\text{H}_2\text{SO}_4$  supercapacitors and showed capacitance of  $365 \text{ F g}^{-1}$  at  $1 \text{ A g}^{-1}$ , five times that of the non-pillared MXene. This shows that pillaring can be effective at improving performance even in aqueous electrolytes with small ion sizes.

Zhang et al. created  $\text{Cu}_2\text{O-Ti}_2\text{C}$  hybrids and tested them as negative electrodes for a LIB.<sup>126</sup> The  $\text{Cu}_2\text{O}$  particles were introduced by mixing  $\text{Cu}(\text{CH}_3\text{COO})_2 \cdot \text{H}_2\text{O}$  and  $\text{Ti}_2\text{CT}_x$  powders in N-dimethylformamide (DMF) followed by solvothermal heating at 150 °C for 10 h. The weight ratio of  $\text{Cu}_2\text{O}$  and  $\text{Ti}_2\text{CT}_x$  in the composites was 25:100. Neither the interlayer spacing nor surface areas were reported, but from SEM images it could be seen that the  $\text{Cu}_2\text{O}$  particles attached in between MXene layers, as well as on the surface which suggests that this material was partially pillared. The electrochemical performance showed improved stability and high rate capacities while impedance spectroscopy confirmed that the Li-ion diffusion in the electrode was faster for the hybrid than for the bare materials. A discharge capacity of  $143 \text{ mAh g}^{-1}$  was obtained at a discharge current density of  $1 \text{ A g}^{-1}$ , much higher than the pristine MXene.

Lin et al. studied carbon nanofibers (CNFs) as conductive bridges between MXene particles, also proposing that they could fill some of the interlayer space therefore acting as pillars.<sup>184</sup> The CNFs were grown in-situ by CVD using a Co-based catalyst. While the BET surface area was modest ( $20 \text{ m}^2 \text{ g}^{-1}$ ), the CNF samples showed additional small pores, 3–16 nm in size, which were not found in the pristine samples. SEM images also showed that CNFs covered the outside of the MXene particles but were also found between MXene layers. Impedance spectroscopy showed reduced impedance for charge transfer in the CNF containing samples. It was also found that performance depended on CNF content, and that too much could damage the properties it is supposed to improve (surface area, conductivity). As a LIB electrode, capacities of  $320 \text{ mA h g}^{-1}$  were achieved, almost 3 times higher than the pristine MXene.

Zhang et al. used an ethanol: water solution to intercalate TEOS between  $\text{Ti}_3\text{C}_2$ , followed by a magnesiothermic-reduction to  $\text{Si-SiO}_x\text{-Ti}_3\text{C}_2$  composites. A direct

pyrolysis of the poly(methyl methacrylate) (PMMA) polymer on the surface of Si nanoparticles using urea as nitrogen source was then used to dope with N and create a carbon support. The final material had a slightly increased interlayer spacing (3 Å) and a large increase in BET surface area up to  $224 \text{ m}^2 \text{ g}^{-1}$  (from  $37 \text{ m}^2 \text{ g}^{-1}$ ) compared to bare  $\text{Ti}_3\text{C}_2$ .<sup>185</sup> The silicon content was up to 81 wt.%, which suggests that a large contribution to the surface area is likely from the Si-SiO<sub>x</sub> formation rather than the MXene, which made up as little as 10 wt.% of the composite. In addition, SEM images showed the MXene flakes were covered in particles, showing that a large amount of the Si-SiO<sub>x</sub> is external to the interlayer. The composite material had a reversible discharge capacity up to  $1,500 \text{ mAh g}^{-1}$  even after 200 cycles, based on the mass of Si in each electrode, as judged by XPS results. At a 10C rate,  $400 \text{ mAh g}^{-1}$  was retained. The specific capacities they report are higher than any other  $\text{Ti}_3\text{C}_2$  containing electrode found, but are slightly enhanced by only counting the Si mass, with a low mass loading of  $1 \text{ mg cm}^{-2}$ . Ex-situ XRD showed a significant shift in the (002) diffraction peak at low voltages, showing that the MXene expanded upon lithiation of Si, but only by about 10%, compared to 300% for pure Si. The load curves and CV plots matched well with previous Si reports, showing that in reality this material was a Si electrode, rather than an MXene one. Nevertheless, the performance was impressive, and shows the potential for Si-MXene based electrodes.

Some other reports also looked at  $\text{Ti}_3\text{C}_2$ -Si composites, but merely mixed Si nanoparticles and the MXene using ultrasonication. These materials had significantly worse electrochemical performance with capacities of  $188 \text{ mAh g}^{-1}$  after 200 cycles at  $0.2 \text{ A g}^{-1}$  and  $250 \text{ mAh g}^{-1}$  after 200 cycles at  $0.1 \text{ A g}^{-1}$  being reported by Kong et al. and Li et al. respectively.<sup>186,187</sup> This shows that simple mixing does not lead to as enhanced performance compared to method which increase the interlayer of the MXene. All these reports were really studying the performance of Si rather than the MXene, which was used as a conductive and flexible structural support.

Luo et al. used a polymer, PVP, and  $\text{Sn}^{4+}$  to pillar  $\text{Ti}_3\text{C}_2$  and tested it as a negative electrode for a LIB.<sup>188</sup> XRD showed an increase in the interlayer spacing upon  $\text{Sn}^{4+}$  loading, to 1.276 nm (from 0.95 nm), showing  $\text{Sn}^{4+}$  was successfully inserted between the layers. No surface area measurements were reported, but SEM images showed particles on and in between the MXene layers. High reversible capacities (around  $650 \text{ mAh g}^{-1}$ ) were reported, with good capacity retention over 200 cycles.

In 2017, Luo et al. used a CTAB-assisted pre-pillaring step to increase the interlayer spacing of  $\text{Ti}_3\text{C}_2$  up to 2.7 nm, followed by the intercalation  $\text{Sn}^{4+}$  using  $\text{SnCl}_4$ .<sup>189</sup> Both steps took 24 h. The interlayer spacing could be tuned by the CTAB intercalation temperature, time and concentration, as well as by the use of different cationic surfactants with different chain lengths. It was found that CTAB typically intercalated at an angle of  $30^\circ$ . When tested for a Li-ion capacitor electrode, the material showed

very high performance with  $765 \text{ mA g}^{-1}$  achieved at a rate of  $100 \text{ mA g}^{-1}$  and  $500 \text{ mAh g}^{-1}$  retained after 250 cycles at  $1 \text{ A g}^{-1}$ . The capacity of this material was boosted by the use of electrochemically active Sn, which is known to undergo alloy reactions with Li. The volume change which usually accompanies this alloying reaction appeared to be overcome by the small Sn particle size and the MXene host which could act as a buffer. CV analysis showed that the charge storage was almost entirely surface-limited (capacitive) in nature, which may have allowed the high capacities at fast rates.

A similar method was reported by Luo et al. in 2018, where  $\text{Sn}^{2+}$  was used with CTAB-assisted pillaring to create an electrode material for Na-ion system.<sup>190</sup> The interlayer spacings were the same as reported in their previous work. The pillared material retained 98.9% of its capacity over 500 cycles, which the authors attributed to allowing reversible Na plating on the MXene surface. The voltage window was 0.00-0.3 V to induce Na plating/ stripping and the load curves very different to typical  $\text{Ti}_3\text{C}_2$  load curves in Na-ion systems (in a 0.01-3 V window). The areal, rather than gravimetric capacities were given, making it difficult to directly compare to other studies.

A CTAB-assisted method has also been utilised for sulphur pillaring by Luo et al. in 2019.<sup>191</sup> Here CTAB was pre-intercalated before sulphur was added via sublimation followed by a heat treatment step to  $450 \text{ }^\circ\text{C}$  to create Ti-S bonds. The interlayer spacings were similar to what was previously reported for CTAB intercalation. The pillared material was tested in a Na-ion system and showed high capacities up to  $550 \text{ mAh g}^{-1}$  at  $0.1 \text{ A g}^{-1}$  and  $100 \text{ mAh g}^{-1}$  at a very high rate of  $15 \text{ A g}^{-1}$ . XPS showed the surface was covered with Ti-O and Ti-S groups. The capacities were greatly boosted by the sulphur content (12.2 wt.%), which can undergo conversion reactions with Na. Sulphur decorated  $\text{Ti}_3\text{C}_2$  also showed an improved performance compared to bare  $\text{Ti}_3\text{C}_2$ , as reported by Sun et al., who used  $\text{Na}_2\text{S}$  to pre-intercalate  $\text{Na}^+$  and support S on the MXene.<sup>192</sup> The Na-ion storage capacity was  $200 \text{ mAh g}^{-1}$ , twice that of the bare MXene, but less than reported by Luo et al. for S-pillared  $\text{Ti}_3\text{C}_2$ , which shows the importance of increasing the interlayer spacing and surface area to maximise the MXene performance.

Xie et al. delaminated  $\text{Ti}_3\text{C}_2$  nanosheets and introduced S to prevent re-stacking using a dilute solution of  $0.5 \text{ mg ml}^{-1}$  of MXene and a  $400 \text{ }^\circ\text{C}$  heat treatment under argon.<sup>193</sup> This gave a material with a BET surface area of  $84 \text{ m}^2 \text{ g}^{-1}$  and a reversible capacity as a Na-ion electrode of  $186 \text{ mAh g}^{-1}$ , with an initial coulombic efficiency of 30%. They also reported that without the S content, the delaminated sheets restacked to give a lower capacity than the multilayered MXene, showing the importance of keeping the sheets separated. The electrodes had a low mass loading of  $1 \text{ mg cm}^{-2}$ .

Luo et al. used a technique they described as cation pillaring to improve the performance of  $\text{Ti}_3\text{C}_2$  in a Na-ion system.<sup>149</sup> They used a Li, Na or K hydroxide to intercalate the metal-ion, remove  $-\text{F}$  groups in the alkali solution and partially oxidise the surface to create  $\text{TiO}_2$ , which was detected by XRD and XPS. A heat treatment at 450 or 700 °C was also used to remove more  $-\text{F}$  groups and some  $-\text{OH}$  groups. The sample treated with NaOH and heat treated at 450 °C showed the best performance with capacities of 175 mAh  $\text{g}^{-1}$  (170% of the bare material). The sample just intercalated with Na did not show any improvement in performance, and the interlayer spacings were only slightly increased compare to the bare material, which suggests that the improvement may have been a result of the change in the MXene surface chemistry, rather than any pillar effect. The initial coulombic efficiency of this material was 63%, whereas the materials with other metal-ions intercalated were all below 50%, which suggests that the Na pre-intercalation and changes in the surface chemistry were responsible for a significant reduction in the irreversible reactions on the first cycle.

Only one report has been found for this review on pillaring non-titanium based MXenes. Wang et al. used KOH to pre-intercalate  $\text{K}^+$  ions between  $\text{V}_2\text{C}$  layers, which were then exchanged for Co ions to create Co-pillared  $\text{V}_2\text{C}$ . This material only had a slightly increased interlayer spacing compared to the non-pillared material, but showed a significantly enhanced capacity of around 1,000 mAh  $\text{g}^{-1}$  (compared to around 650 mAh  $\text{g}^{-1}$  for bare  $\text{V}_2\text{C}$ ). This capacity was boosted by redox activity of the Co as well as the slight increase in interlayer spacing. Ex-situ XRD showed that the interlayer spacing varied slightly with charge and discharge due to the electrochemical activity of Co, which expanded the interlayer upon lithiation, allowing further Li to be intercalated between the layers. Despite the slight volume change, the cycling stability was high, with almost no capacity loss over 15,000 cycles at 8 A  $\text{g}^{-1}$ .

The results from this review show that pillaring is a promising method to increase the interlayer spacing to create porous MXenes, which in turn often show improved electrochemical performance across different metal-ion and electrolyte systems. In addition, the chemistry of the pillars can be varied, which expands the chemistries available for MXene-based materials. Cationic surfactant-assisted pillaring methods have been widely studied, as has the intercalation of metal-ions. However, the use of amine-assisted pillaring methods such as those developed for titanosilicates, has not been studied to date. The use of in-situ electrochemical pillars, where pillars can be intercalated within the electrochemical cell, such as those studied by Hantel et al. for graphene supercapacitors,<sup>181</sup> have also not been studied for MXenes. Cheaper pillaring elements such as silica-based pillars, have also been scarcely reported, despite the very high abundance of silica on Earth. Finally, whilst titanium-based MXenes have been well studied, there are not reports on molybdenum-based ones.

Therefore, these are the areas studied further in this thesis, with a focus on pillaring techniques based around the cationic surfactant CTAB and a co-pillaring technique using amine (dodecylamine, DDA) and TEOS are studied for MXenes.

## 2.6 Aims and objectives

As previously discussed, there is an urgent need for the development of new energy storage technologies to enable the global energy system to transition away from fossil fuel based energy sources to cleaner renewable-based energy sources. Electrochemical energy storage technologies, such as batteries and supercapacitors, are uniquely placed with potential applications in renewable energy grid storage and decarbonising the transport sector. However, current generations of devices suffer from limitations including a trade-off between high energy densities (batteries) or high power densities and long lifetime (supercapacitors), which is a result of the way the active materials in these devices store charge. Intercalation pseudocapacitance in nanomaterials has been suggested as a way of overcoming this trade-off in performance, potentially enabling devices with high energy densities, high power densities and low lifetime all in one device. In addition, there are concerns about the sustainability of certain elements (such as Co and Li) currently used in Li-ion batteries, which are the current leading technology for these applications. Therefore, ion systems beyond Li, such as Na and Zn are beginning to be explored, and the use of abundant elements in new electrode materials is becoming increasingly important.

Two-dimensional nanomaterials have been shown to be promising candidates for pseudocapacitive intercalation electrode materials. Among these, MXenes, a family of two-dimensional transition metal carbides and nitrides, have recently emerged as materials with high potential for electrochemical energy storage applications. However, their performance depends on the electrode architecture, with multilayered and delaminated MXenes not showing sufficient performance characteristics. This has led to an increasing research focus on developing porous MXenes with increased ion accessibility and stability towards long-term cycling. However, many of the methods developed to date have significant drawbacks such as destroying the MXene surface, use of low concentration dispersions and low final surface areas. Therefore, despite previously reported porous MXenes, including pillared MXenes, showing significantly enhanced energy storage performance compared to multilayered MXenes, there is still a need to develop new pillaring methods to create MXenes with higher surface areas, easy to control interlayer distances using abundant elements. In addition, the majority of work so far on porous MXenes has focused on  $\text{Ti}_3\text{C}_2$ , with porous structures of other MXenes rarely being reported, despite some promising electrochemical performances from these materials.

Therefore, the aim of this thesis is:

To create stable porous MXene structures using pillaring techniques previously developed for clays in order to improve the electrochemical performance of MXene electrodes in a variety of electrochemical energy storage systems.

To meet this aim, the following objectives have been set:

- Develop pillaring methods to create porous and stable MXene structures using earth abundant elements.
- Understand the pillaring processes; mechanisms and interplay between MXene surface chemistry, interlayer spacings and the pillaring reagents.
- Test these porous MXenes as electrodes for metal-ion capacitor applications, aiming to see increased performance in terms of increased capacity, stability and rate performance.
- Understand the effect of pillaring on the electrochemical performance (changes in chemistry, structure, mechanisms).
- Compare between different MXene chemistries, both in terms of the pillaring process and the electrochemical performance.
- Demonstrate MXene capacity in divalent zinc-ion systems, investigate the charge storage mechanism, and study the effect of pillaring.

# **Chapter Three**

## **Materials and Methods**

### 3.1 Introduction and Materials

This chapter introduces and outlines the materials and methods used to carry out the research reported in this thesis. This includes the synthesis methods used to make the MAX phase precursors, the MXenes and the pillaring techniques used. In addition, the characterisation techniques used to determine the structure and chemical composition of the synthesised materials such as x-ray diffraction (XRD), Raman spectroscopy, scanning and transmission electron microscopy (SEM and TEM), energy dispersive x-ray spectroscopy (EDS), x-ray photoelectron spectroscopy (XPS), nuclear magnetic resonance spectroscopy (NMR), BET analysis, thermal gravimetric analysis (TGA) and infrared (IR) spectroscopy. Finally, the electrochemical characterisation tests which were used to access and understand the electrochemical performance in different electrolyte systems, such as galvanostatic charge-discharge testing (GCD) and cyclic voltammetry (CV), are described.

The following materials were obtained and used without further purification: titanium powder (-325 mesh, 99% purity, Alfa Aesar), aluminium powder (-100+325 mesh, 99.5% purity, Alfa Aesar), titanium carbide powder (-325 mesh, 98% purity, Sigma Aldrich),  $\text{Ti}_3\text{AlC}_2$  powder (>85% purity, Carbon Ukraine Ltd.), molybdenum powder (-325 mesh, 98% purity, Sigma Aldrich), sodium fluoride (99% purity, Alfa Aesar), lithium fluoride (98% purity, Alfa Aesar), hydrochloric acid (37.5 wt.% Sigma Aldrich), tetraethylortho silicate (TEOS, 98% purity, Alfa Aesar), 1-dodecylamine (DDA, 97% purity, Alfa Aesar), n-octylamine (>98% purity, TCI Chemicals), hexadecyltrimethylammonium bromide (CTAB, Sigma Aldrich, >99% purity), octylamine (>98% purity, TCI Chemicals), Tetradecyltrimethylammonium bromide (TTAB, TCI Chemicals, >98% purity), sodium hydroxide (97% purity, pellets, Sigma Aldrich), N-methyl-2-pyrrolidone (NMP, 99.5% purity, Alfa Aesar), PVDF (99.0% purity, Alfa Aesar), Super P carbon black (99% purity, Alfa Aesar),  $\text{NaPF}_6$  (99% Alfa Aesar), diethyl carbonate (DEC) and ethylene carbonate (EC) (1:1 w/w%, 99% purity Gotion), 1 M  $\text{LiPF}_6$  in 1:1 wt DEC:EC (Sigma Aldrich), zinc sulphate heptahydrate (>99%, Sigma Aldrich), acetonitrile (ACN, anhydrous, 99.8% Alfa Aesar), aluminium foil (Tob New Energy), copper foil (Tob New Energy), zinc foil (Tob New Energy) and titanium foil (Tob New Energy, 100  $\mu\text{m}$ ). Where deionised (DI) water was used, it was obtained from an Elga Purelab Flex deioniser, Model PF3XXXXM1, with a resistivity of 18.2 M $\Omega$ .

## 3.2 Methods

### 3.2.1 Materials synthesis

#### 3.2.1.1 $\text{Ti}_3\text{C}_2$ MXenes

$\text{Ti}_3\text{AlC}_2$  MAX phase powder was synthesised based on the reports outlined in the background chapter (Section 2.4.1). Ti, Al and TiC powders were mixed in a pestle and mortar in a 1:1.2:1.9 molar ratio. The mixture was then heated in a tube furnace under argon at 1,350 °C for 2 h, with a heating rate of 5 °C min<sup>-1</sup>. The resulting lightly sintered block was then crushed with a pestle and mortar and ground to give a fine grey powder. This is used in Chapter 4 in this thesis. For Chapter 6, commercial  $\text{Ti}_3\text{AlC}_2$  acquired from Carbon Ukraine Ltd. was used.

To obtain the  $\text{Ti}_3\text{C}_2$  MXene, the fluoride salt-HCl etching method first reported by Ghidui et al. was adapted,<sup>114</sup> since this is significantly less hazardous than handling concentrated HF solutions, and gives a product with increased -O terminations. These are thought to be beneficial to electrochemical energy storage applications, as described in Section 2.4.2 of Chapter 2. For the etching, 3 g of the as-synthesised  $\text{Ti}_3\text{AlC}_2$  were sieved through a -400 mesh sieve (pore size of 38 µm) and added over 10 min to a 6 M HCl solution with pre-dissolved NaF (7.5:1 F to Al ratio). This mixture was heated to 40 °C and left to etch for 48 h with magnetic stirring using the set-up shown in Figure 3.1 The acidic fluoride solution was then vacuum filtered through borosilicate glass microfiber filter paper (pore size 45 µm, Cole-Parmer) to collect the black solid, which was dried overnight at 60 °C. NaF was chosen as the etching salt due to its significantly higher abundance and lower cost, which is more in keeping with the aims of Na and Zn-ion systems research than using LiF, which still requires the use of expensive lithium resources.

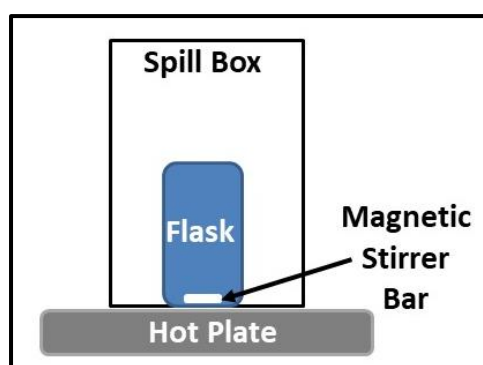


**Figure 3.1.** Schematic representation of the etching set-up for MXene synthesis.

In Chapter 4, a study was carried out to investigate the effect of different surface terminations on the pillaring procedure. Previous reports have shown how the surface groups of  $\text{Ti}_3\text{C}_2$  can be changed by different chemical treatment, with alkali treatments leading to a higher proportion of -O terminal groups compared to acid-

treated ones.<sup>194,195</sup> Therefore, two different washes were used to give two MXenes with different surface groups.

To obtain the MXene with a greater number of -O terminations, denoted  $\text{Ti}_3\text{C}_2\text{-O}$ , the dried  $\text{Ti}_3\text{C}_2$  powder was immersed in 1 M NaOH at room temperature for 4 h. The powder was then recovered by vacuum filtration and washed with DI water. The resulting black powder was dried overnight at 60 °C. For the MXene with the higher number of OH surface groups, denoted  $\text{Ti}_3\text{C}_2\text{-OH}$ , the NaOH treated MXene ( $\text{Ti}_3\text{C}_2\text{-O}$ ) was further treated by placing it in 1 M HCl at room temperature for 4 h. This was filtered, washed and dried in the same way as  $\text{Ti}_3\text{C}_2\text{-O}$ . These materials were used in Chapter 4.

### 3.2.1.2 $\text{Mo}_2\text{TiC}_2$ MXene

The  $\text{Mo}_2\text{TiAlC}_2$  MAX phase is not commercially available, and so was synthesised following literature methods.<sup>100,113</sup> Elemental powders of Mo, Ti, Al and C in a 2:1:1.2:2 molar ratio were sieved through a 38  $\mu\text{m}$  sieve (-400 mesh), first mixed in a pestle and mortar, and then mixed in a planetary mixer for 1 h hour with zirconia balls. The recovered powder was heated for 4 h at 1,600 °C under argon, using a heating and cooling rate of 5 °C  $\text{min}^{-1}$ . The calcined material (light grey) was then gently ground in a pestle and mortar to give a fine powder.

To avoid the handling of HF, the synthesis of  $\text{Mo}_2\text{TiC}_2$  was attempted using the LiF-HCl method which has been successfully used for the titanium-based MXenes. Typically, 3 g of  $\text{Mo}_2\text{TiAlC}_2$  was slowly added to 30 ml of 9 M HCl with 3 g of LiF pre-dissolved. The mixture was heated to 60 °C and stirred for 5 days. After this the acidic solution was diluted with DI water and centrifuged to recover the powder. This was then redispersed in a fresh etching solution, using the same quantities as used in the first etching stage. After four more days of etching, the solid was collected via centrifuging, and washed with water over repeated centrifuging cycles until the pH was around 6 (measured with pH paper). The reasons for this two-stage etching procedure are discussed in more detail in the results in Chapter 5.

## 3.2.2 Pillaring Experiments

### 3.2.2.1 Amine-assisted Pillaring

Chapters 4 and 5 investigate the use of an amine-assisted pillaring method based on the work described in Section 2.5 of Chapter 2 to develop silica-pillared titanosilicates. This method was chosen for a number of reasons:

- Silica is cheap and highly abundant, and the hydrolysis of TEOS (Figure 3.2) is well studied.

- The pillaring steps are fast (much less than 24 h) and carried out at room temperature.
- The surface areas and interlayer distances achieved for pillared clay using this method are amongst the highest, and can be tuned by the use of different amines and calcination conditions.
- The surface chemistry of titanosilicates is very similar to titanium-based MXenes.
- Amines have already been shown to intercalate into MXenes.

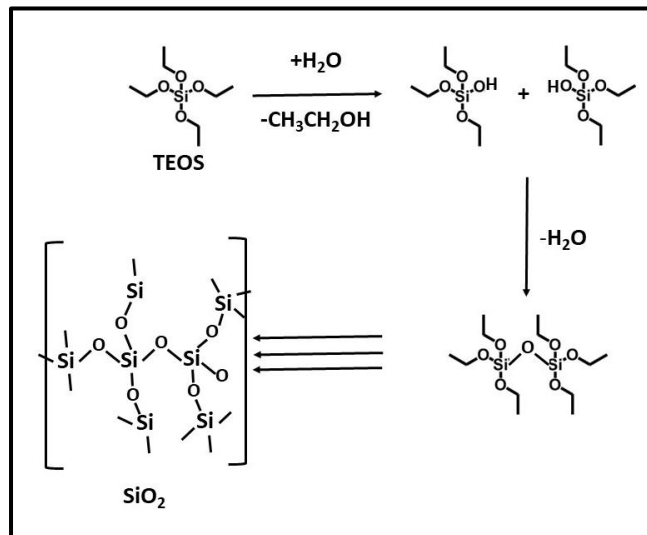


**Figure 3.2.** Diagram illustrating the TEOS hydrolysis reaction pathway to form the SiO<sub>2</sub> pillars.

A schematic outlining the pillaring method is shown in Figure 3.3.

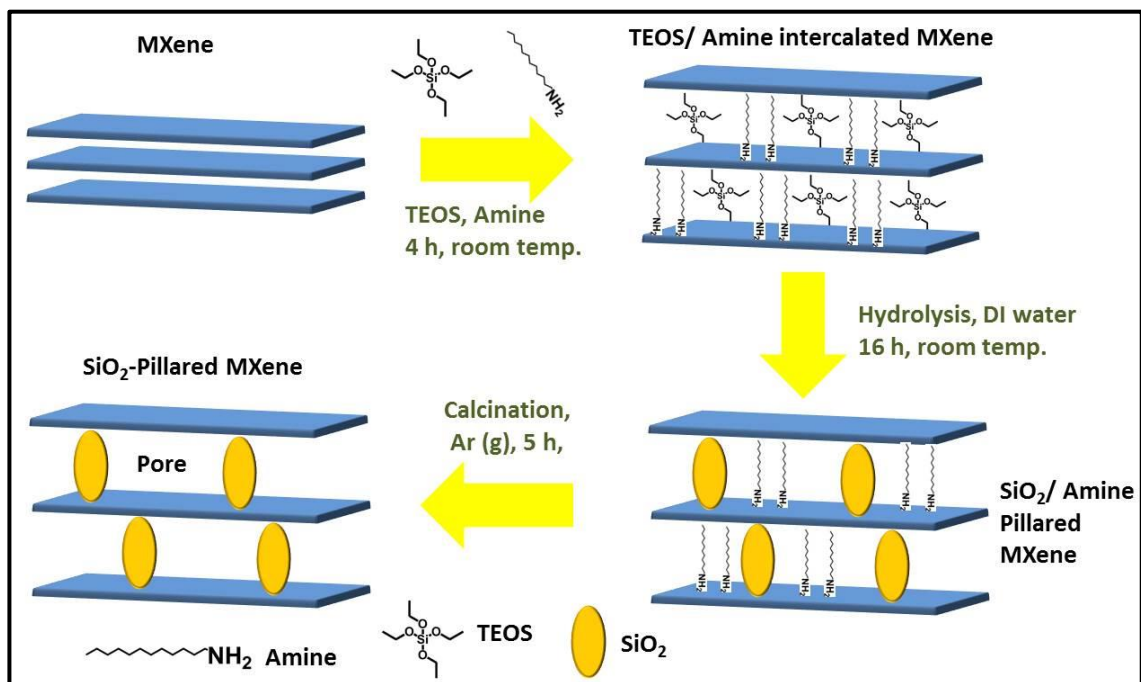


**Figure 3.3.** Schematic illustrating the amine-assisted pillaring method.

### 3.2.2.2 Pillaring of $Ti_3C_2$

For the pillaring experiments, 0.5 g of the NaOH or HCl-treated MXene were added to a solution of dodecylamine (DDA) dissolved in TEOS in a MXene:DDA:TEOS molar ratio of 1:6-10:15-20 under argon. This was stirred in a sealed glass vial under argon at room temperature for 4 h. The black powder was then recovered by vacuum filtration, dried on the filter paper under vacuum before being re-dispersed in DI water (25 ml) overnight at room temperature (18 h). The intercalated product (Figure 3.4) was then recovered by vacuum filtration and dried overnight at 60 °C. These samples were then calcined at either 300, 400 or 500 °C for 2 h under argon with a heating rate of 5 °C min<sup>-1</sup>. Argon was used for the heat treatment steps instead of air (which would be expected to give more complete removal of the carbon template) to minimise the oxidation of the MXene.

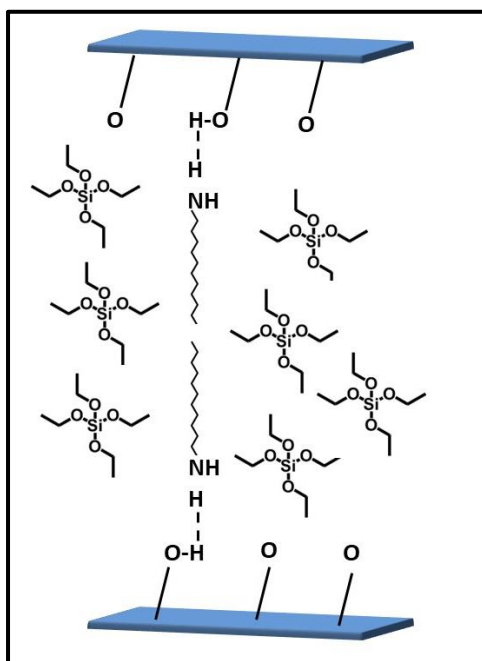


**Figure 3.4.** Schematic illustration of the arrangement of the co-pillars in the intercalated materials.

For the pillaring using octylamine as the co-pillar, the same procedure was followed, using a molar ratio of MXene: OA: TEOS of 1:10:20. For the experiment using only TEOS for intercalation, the same procedure as described for the DDA assisted method was used, with a MXene: TEOS molar ratio of 1:20 used.

### 3.2.2.3 Pillaring of $Mo_2TiC_2$

For the pillaring of  $Mo_2TiC_2$ , the procedure was the same as used for the  $Ti_3C_2$  MXene. A molar ratio of 1:10:20 of MXene: DDA: TEOS was stirred for 4 h at room temperature under argon. The intercalated material was recovered by vacuum filtration and dried under vacuum on the filter paper (under argon). This was then re-

dispersed in DI water for 16 h at room temperature, before being recovered again by vacuum filtration. The recovered material was dried at 60 °C for 24 h. A calcination step under argon was then carried out at 400 °C for 5 h using a heating rate of 5 °C min<sup>-1</sup>.

#### **3.2.2.4 CTAB Pillaring**

In Chapter 6, which focuses on MXenes in zinc-ion systems, CTAB pillaring methods were also studied for Ti<sub>3</sub>C<sub>2</sub>, in addition to the amine-assisted pillaring method. In-situ and ex-situ methods were compared. CTAB pillaring had previously been shown to be effective for MXene pillaring, due to the positive charge of the cation, CTA<sup>+</sup>, which easily intercalates, as discussed in Section 2.5.3 of Chapter 2.

#### **3.2.2.5 Ex-situ CTAB Pillaring**

For CTA<sup>+</sup> intercalation, 200 mg of Ti<sub>3</sub>C<sub>2</sub> was dispersed in a solution of DI water (30 ml) and CTAB (100 mg). The dispersion was stirred for 24 h at 40 °C. The pillared MXene was then recovered by vacuum filtration and dried at 60 °C overnight. This was based on the work of Luo et al. who studied CTA<sup>+</sup> intercalation in detail.<sup>189</sup>

#### **3.2.2.6 In-situ CTAB Pillaring**

For the in-situ pillaring, 0.1 wt.% of CTAB was added to the 0.1 M ZnSO<sub>4</sub> electrolyte used in the coin cell tests, to intercalate CTA<sup>+</sup> during cycling within the cell. The purpose of this study was to investigate the feasibility of CTA<sup>+</sup> pillaring within the cell (in-situ), avoiding the need for the extra time consuming steps used in traditional ex-situ methods. Further details on the electrochemical characterisation are provided in Section 3.2.3.11.

### **3.2.3 Characterisation**

#### **3.2.3.1 X-ray Powder Diffraction**

X-ray powder diffraction (XRD), is a widely used technique to study the crystal structure of solid crystalline materials. It utilises the wave-particle duality of X-rays, which diffract when passing through slits which match the size of the wavelength, which is approximately 1 Å; the length of a typical chemical bond. While the majority of x-rays are simply reflected randomly (scattered) by the electron of atoms in the crystals, at certain orientations the scattered x-rays interact with each constructively, resulting an increased signal at these orientations, which corresponds to diffracting x-rays. This is represented by the Bragg equation (Equation 3.1).

$$n\lambda = 2d \sin\theta \quad \text{Equation 3.1}$$

Here  $n$  is the order of the scattered x-ray (positive integer),  $\lambda$  is the wavelength of the incident x-ray,  $d$  is the distance between two planes of atoms which the x-ray is

scattering off and  $\theta$  is the angle between the incident x-ray and the plane of atoms. This is illustrated by Figure 3.5. During a typical x-ray diffraction experiment, the wavelength of the incident x-rays is fixed by using a monochromatic x-ray source,  $n$  is typically one since the proportion of x-rays which undergo multiple scattering events is very low and the angle of diffraction,  $\theta$ , is varied, either by moving the sample or the source and detector. Therefore, the distance,  $d$ , between different planes of atoms can be calculated. This allows the structure of the solid being probed to be determined by using the distance between each plane of atoms to build up the overall crystal structure which contains all the planes of atoms detected in the diffraction pattern. Diffraction patterns are typically plots of intensity of detected x-rays against angle (as  $2\theta$ ), with peaks corresponding to different  $d$ -values between planes.

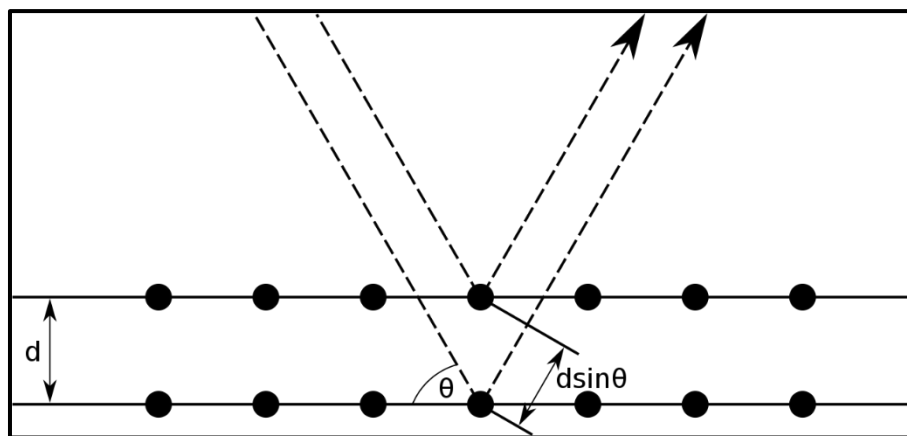


**Figure 3.5.** Schematic illustration of diffraction according to the Bragg equation. The dashed lines and arrows represent two in-phase X-rays which are scattered by two different places of atoms. They interact constructively to give a diffraction signal when the incident x-rays have a  $\theta$  angle which fulfils the Bragg equation.

To identify the planes of atoms,  $(hkl)$  nomenclature is used, which relates the atomic planes to the unit cell of the crystal. A unit cell is the smallest repeating unit needed to build up the total crystal structure. Three cell axis labels are used,  $a$ ,  $b$ , and  $c$ , which relate to the  $h$ ,  $k$  and  $l$  planes introduced above. These planes intersect the unit cell, with the point of intersection given by the integer value assigned to  $h$ ,  $k$  or  $l$ , which corresponds to the number of times the plane intersects the unit cell in the  $a$ ,  $b$  or  $c$  axis, respectively. The unit cell for  $Ti_3C_2$ , with the intersections highlighted by the  $(002)$  plane (i.e.,  $h = 0$ ,  $k = 0$  and  $l = 2$ ) is given in Figure 3.3 as an example. This means that the plane which gives rise to the  $(002)$  diffraction peak does not cross the  $a$  or  $b$  axis (there is no intersection, hence  $h$  and  $k = 0$ ), but the  $c$ -axis is intersected twice (therefore  $l = 2$ ). As can be seen by Figure 3.6, the unit cell of  $Ti_3C_2$  consists of three (partial)  $Ti_3C_2$  layers, as a result of the different stacking of atoms within each  $Ti_3C_2$  block. This means that the inter-plane distance,  $d$ , for the  $(002)$  reflection corresponds to the interlayer spacing between each  $Ti_3C_2$  layer.

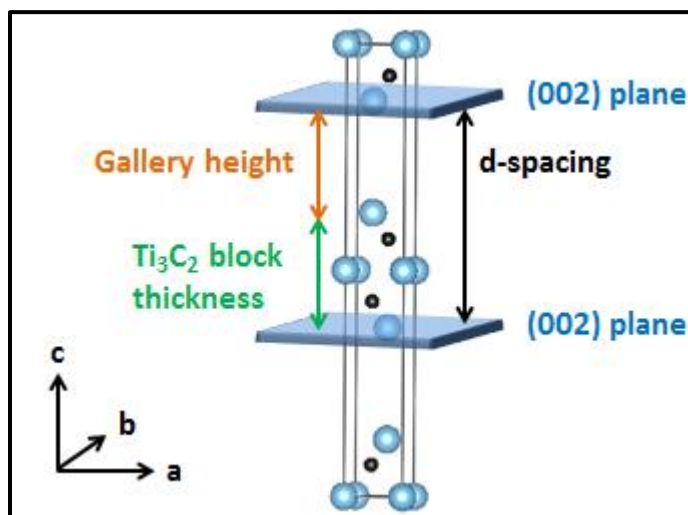


**Figure 3.6.** Diagram showing the unit cell of  $\text{Ti}_3\text{C}_2$  and demonstrating the use of the (002) plane to calculate the interlayer spacing and gallery height.

This allows the interlayer distance between MXene sheets to be calculated by solving the Bragg equation for the (002) peak, which has been widely reported in the literature to be highly useful to study the intercalation and pillaring of MXenes, as was shown in Section 2.5.3. Consequently, this method is used in this thesis to follow changes in the interlayer distance of the MXenes during intercalation and pillaring processes, and during electrochemical cycling by ex-situ XRD experiments. A shift to lower  $2\theta$  values corresponds to an increase in interlayer spacing, which would suggest successful intercalation of species between the layers, which have expanded to accommodate that species.

In addition to the location of the diffraction peaks on the  $2\theta$  axis, powder XRD peaks also contain information on the crystallinity of the material (from the peak width) and the atomic arrangement in the plane (from the peak intensity). A sharper peak corresponds to a material with a higher degree of crystallinity than a broader peak, which signifies a more disordered material. This is because a disordered material will have a wider range of  $d$ -values for each plane, since the distance between each plane varies throughout the sample. A perfectly ordered crystal would have just one  $d$ -value for each set of atomic planes, therefore the peak would in theory be infinitely sharp. Amorphous materials have such a large range of  $d$ -values for each plane that peaks are very broad (can be over  $5^\circ$   $2\theta$  wide), if they can even be distinguished from the background. Therefore powder XRD is only suitable for crystalline solids.

Powder XRD has a number of advantages including simple sample preparation, data collection and analysis, which makes it widely used for structure determination. In addition, it is a bulk technique, which means that the structure of the entire sample can be characterised, not just the sample near the surface.

In this thesis, powder XRD was used to identify the phases of synthesised material by comparing the collected patterns with those reported in the literature and for monitoring the interlayer spacing after intercalation and pillaring experiments, and during electrochemical cycling by ex-situ XRD experiments. Samples were characterised in a Smartlab diffractometer (Rigaku, Tokyo, Japan) using Cu K $\alpha$  radiation as the x-ray source ( $\lambda = 1.54 \text{ \AA}$ ) operating in reflection mode with Bragg-Brentano geometry to investigate the crystal structure. In other words, the sample was flat and stationary during measurements, and the x-ray source and detector were moved to obtain the desired range of  $\theta$  angles. Following the typical diffraction ranges found in the literature, the  $2\theta$  range of  $5\text{-}50^\circ$  with a scan rate of  $3^\circ \text{ min}^{-1}$  was used, apart from for the study of the amine-assisted pillared materials where the very large interlayer distances meant that a lower range of  $1.8$  to  $10^\circ 2\theta$ , with a slower scan rate of  $0.5^\circ \text{ min}^{-1}$  was used.

Prior to XRD characterisation, all samples were dried in an oven for 18 h at  $80^\circ \text{C}$ . The black powders were then ground and placed on a silica sample holder and pressed flat with a glass slide. For ex-situ studies (Chapter 6), cells were disassembled at the desired state-of-charge, the electrode was extracted and placed immediately, while wet, on a flat stage for diffraction analysis. This was to ensure that the material had not dried out, which gives an environment closer to that in the cycling cell.

### **3.2.3.2 Raman Spectroscopy**

Raman spectroscopy also provides information on the structure of materials, and, like XRD, is used for structure identification. It is a vibrational spectroscopy technique which uses energy changes in inelastically scattered photons to study bonds in solids, liquids and gases. Visible light (radiation) of a fixed wavelength (and therefore energy) is focused through a microscope onto the sample. This excites the vibrational modes of the atoms in the material (called phonons in a solid), which move, via so-called virtual states, to a state of higher energy, absorbing some of the energy of the radiation (for Stokes Raman scattering).<sup>196</sup> This changes the energy (wavelength) of the photons by the amount of energy absorbed by the transition. This change in energy is called a Raman shift. The difference in energy between the ground state and excited state (which corresponds to a peak in a Raman spectrum) is different for each vibrational mode for each material, which allows for the vibrations and the material to be identified by analysis of a Raman spectrum. It is also possible for a scattered photon to gain energy from transitions in the vibrational modes (anti-Stokes scattering), though this signal is often weaker than the Stokes scattered signal, so is rarely used. Scattered photons which do not undergo any change in energy (elastic scattered photons) are called Rayleigh scattered photons. These make up the bulk of the scattered photons, but are filtered out within the spectrometer to

allow the detection of the photons which underwent a Raman shift. The Raman process is illustrated in Figure 3.7.

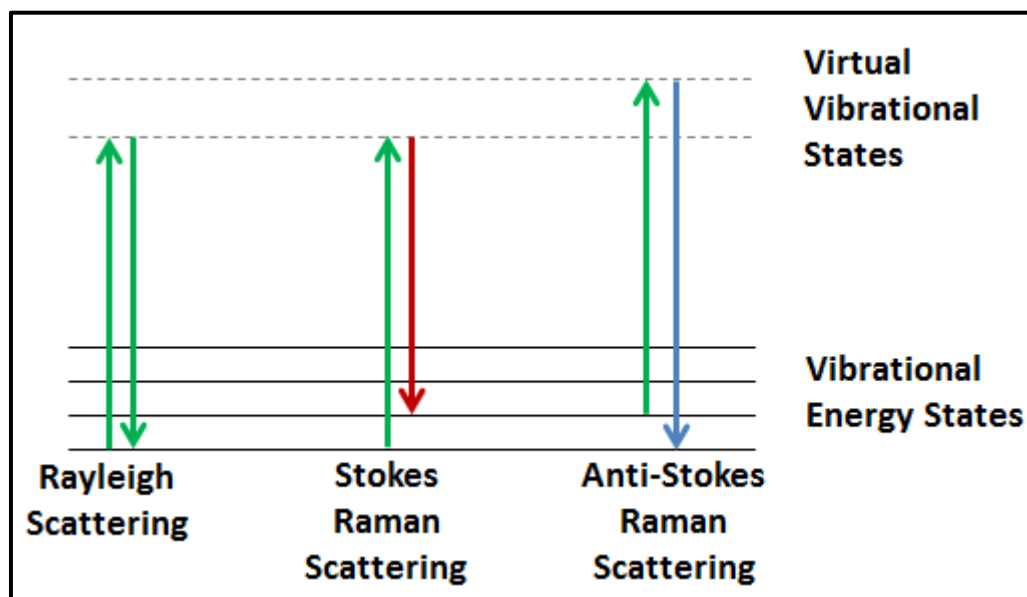


**Figure 3.7.** Schematic illustrating the Raman Effect in terms of the changes in energy levels which occur when visible light scatters from a material.

A Raman spectrum consists of the Raman shift plotted on the  $x$ -axis and the intensity (of detected photons) on the  $y$ -axis. The Raman shift is plotted relative to the energy of the incident photons, in units of wavenumbers,  $\text{cm}^{-1}$ , which is the number of waves per cm. Therefore a larger wavenumber corresponds to a smaller wavelength, and a larger energy change in the Raman scattered photon. As for XRD, the width of the Raman peaks can give information about the degree of crystallinity of the material, with sharper peaks suggesting a more crystalline material.<sup>196</sup> Unlike XRD, Raman spectroscopy is a more localised technique, with the laser used as the light source usually focussed to a spot size microns in size. This means that the Raman spectrum will consist of only information from that spot, rather than the entire sample.

As well as phase identification, for  $\text{Ti}_3\text{C}_2$  MXene Raman spectroscopy has been used to study the surface groups. Hu et al. discovered that the location of the peaks (the magnitude of the Raman shift) was highly sensitive to the surface groups terminating the MXene.<sup>197</sup> In particular, the Ti-O and Ti-OH peaks can easily be distinguished. Figure 3.5 illustrates the vibrational modes predicted to occur for  $\text{Ti}_3\text{C}_2$  terminated with -OH and -O groups respectively, with the modes most useful for experimental Raman studies highlighted.<sup>197,198</sup> The labels  $E_g$  and  $A_{1g}$  shown in Figure 3.8 describe the nature of the vibrational mode.  $E$  corresponds to a doubly degenerate mode,  $A$  to a singly degenerate mode and  $g$  shows that the wavefunction used to describe the mode is even (gerade), i.e. that an inversion through the centre of symmetry gives the same result as before the inversion.<sup>197</sup> It should be noted that -F terminations

tend to result in peaks which overlap closely with peaks from –OH and –O groups, and therefore are not studied using Raman spectroscopy in this work. For Mo<sub>2</sub>TiC<sub>2</sub>, only Mo-O surface groups have been assigned in the literature to date, with vibrations from the Mo and C planes also being identified. This is discussed more in Chapter 5.

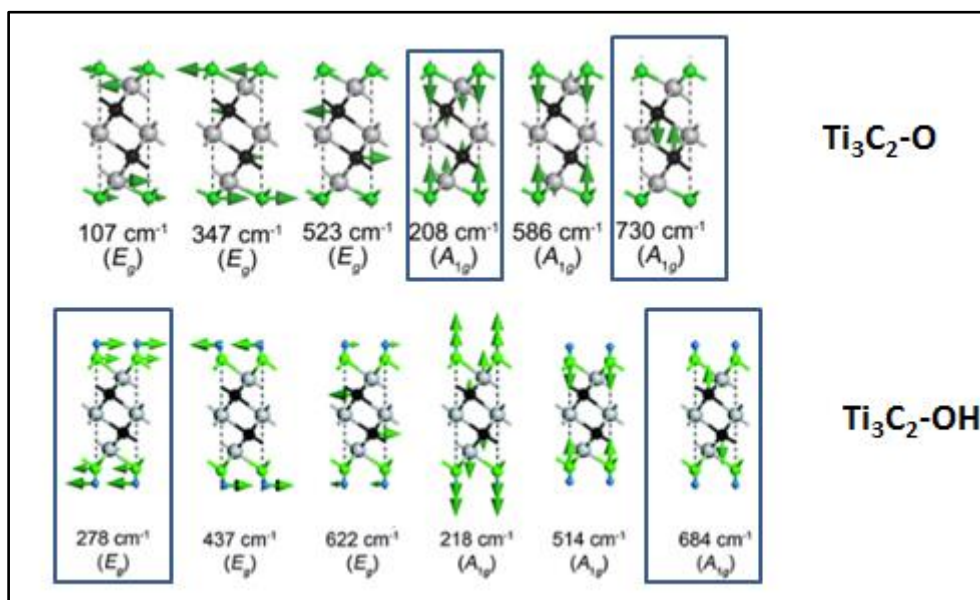


**Figure 3.8.** Illustration of the vibrational modes predicted to occur for Ti<sub>3</sub>C<sub>2</sub> terminated with –OH and –O groups respectively, with the modes most useful for experimental Raman studies highlighted (blue rectangles). Adapted from Hu et al. with permission.<sup>197</sup>

Therefore Raman spectroscopy is used in this thesis for confirming the MXene phase after synthesis and studying changes in the surface chemistry. Raman spectroscopy was carried out on a Horiba Lab Raman Spectrometer (Horiba, Minami-ku Kyoto, Japan) with an EM-cooled Synapse camera. For taking spectra, a 100x, 0.90 NA microscope objective was used. The dried powder was sandwiched between two glass microscope slides which were pressed together to give flat MXene particles. One of these slides was then discarded, with the other slide placed flat under the diode laser (532 nm, 200 μW) for measurements.

For ex-situ studies (Chapter 6), the electrode was extracted from the cell at the desired state-of-charge, washed five times with DI water (the electrolyte solvent) to remove any surface salts from the electrolyte, dried overnight at 60°C and placed flat on a glass microscopy slide under the microscope.

### 3.2.3.3 Infrared (IR) Spectroscopy

Like Raman Spectroscopy, IR Spectroscopy is an optical vibrational technique. It is complementary to Raman spectroscopy, in that modes which are inactive to Raman spectroscopy tend to be active for IR spectroscopy. Therefore, slightly different bonding information can be determined by IR spectroscopy. Instead of visible light,

infrared light is used as the incident radiation. This causes excitations in vibrational states for certain bonds in a material, which show up as peaks in an IR spectrum. To be IR active, a vibrational mode must undergo a change in the dipole moment (seen by a change in symmetry) of the mode upon the excitation. It is widely used for detecting C-H bonds in organic materials, and Si-O bonds, as present in silica-type materials also show up clearly. Therefore it is used in this thesis to confirm the presence of the amine and TEOS in the intercalated and pillared Ti<sub>3</sub>C<sub>2</sub> materials.

#### 3.2.3.4 Scanning Electron Microscopy (SEM)

Scanning electron microscopy uses an electron beam to collect images, analogously to visible light beams being used in optical microscopes, which is focused through a series of lenses into the sample. It is used as an alternative to optical microscopes to study features below 200 nm, which is the typical resolution limit of optical microscopes. The microscope resolution is given by Equation 3.2.

$$\delta = \frac{0.61\lambda}{n \sin\alpha} \quad \text{Equation 3.2}$$

Here,  $\delta$  is the microscope resolution, 0.61 is a constant,  $\lambda$  is the wavelength of the probing beam,  $n$  is the refractive index of the medium between the sample and the lens (around 1 for air and a vacuum), and  $\alpha$  is the angle of collection of the magnifying lens.<sup>199</sup> Therefore, it can be seen that by changing the wavelength of the probing beam, the resolution can greatly increase. Optical microscopes use visible light as the probing beam, which has a wavelength greater than 390 nm.<sup>199</sup> On the other hand, electrons have significantly shorter wavelengths, for example, 0.0123 nm in a 10 kV beam.<sup>199</sup> This allows electron microscopes to have significantly improved resolutions compared to optical microscopes, and SEM can reach resolutions below 1 nm, though 1-20 nm is more typical.<sup>199</sup> This is the main motivation for using electron microscopy instead of optical microscopes; the huge improvement in resolution allows features on the order of a few nm to be visualised, which is crucial for the study of nanomaterials such as MXenes.

One disadvantage of electron microscopes is that the imaging has to be carried out under vacuum, unlike optical microscopes. In addition, the material being imaged must be electrically conductive, to allow the electron beam to interact with the electron beam without becoming trapped, which leads to sample charging and a loss of resolution. The electrons must be able to enter the sample, interact with it, and leave the sample to reach the detector to achieve good resolution in the final image.

When the electron beam interacts with the sample there are a number of different processes which can give rise to multiple types of electrons and types of matter being generated, each of which can provide different information about the sample. A selection of these which are relevant to this thesis are shown in Figure 3.9. For SEM

imaging, backscattered electrons were detected and used to create the SEM images shown in this thesis. Backscattered electrons are electrons from the incident beam which have penetrated, interacted with, and left the sample at the same side as the incident beam enters them. These are then collected by a detector the signals from which are converted into the images. If the vacuum is not sufficient, then the backscattered electrons could be further scattered or altered by particles in the atmosphere, which would mean that the image collected on the detector would not only include information from the sample, resulting in a loss of resolution. This is why SEM is carried out under high vacuum conditions.

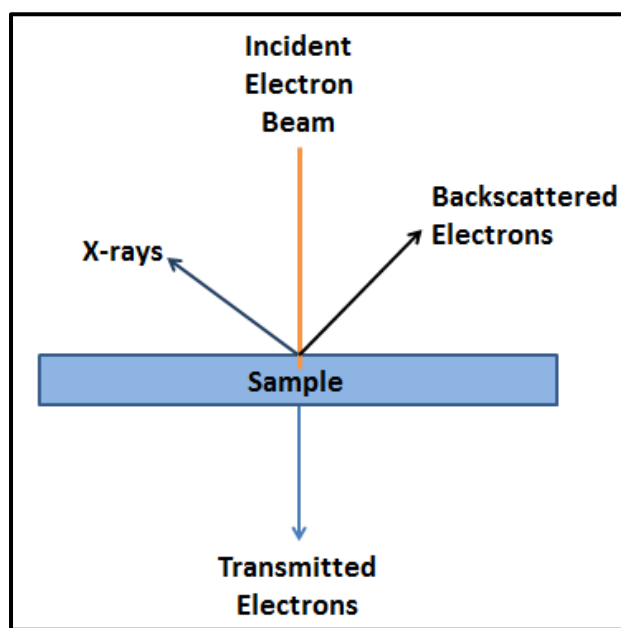


**Figure 3.9.** Schematic representation of some of the effects of the interaction of the focused electron beam with the sample.

In this thesis, SEM was used to study the morphology of the MXene particles after synthesis and intercalation and pillaring experiments. SEM was carried out in a JEOL JSM-7800F (JEOL, Tokyo, Japan), using an accelerating voltage of 10 kV and a working distance of 10 mm. The dried powder samples were dry cast onto a conductive carbon tape support, which was placed on to a copper stub for analysis.

### 3.2.3.5 Transmission Electron Microscopy (TEM)

Like SEM, TEM is a high resolution microscopy technique which uses electron beams to collect images. In this case, however, instead of the detector being placed on the same side of the sample to the incident electron beam, it is placed on the opposite site, behind the sample. This allows for transmitted electrons, which have travelled all the way through the sample (Figure 3.6), to be detected.<sup>199</sup> This means that there is an extra requirement for samples to be imaged by TEM techniques, in addition to the requirements for SEM imaging. The sample must be electrically conductive enough and thin enough to allow for the electrons to pass through the sample so

that they can reach the detector. This can lead to some extra sample preparation steps to make the sample thin enough so that the electrons can pass through. The resulting image is a 2D projection of the area of the sample that the electrons passed through. Scanning TEM (STEM) is a variation of TEM where the electrons are focused into a beam, as in SEM, but only the transmitted electrons are detected. Imaging in high-angle annular dark field (HAADF)-STEM mode gives high resolution images with up to atomic resolution, where the sample is observed as pale features on a black background, which gives the images high contrast, making features easier to observe. In addition, this technique is sensitive to the atomic mass,  $Z$ , of the elements in the sample, which can allow for the identification of individual atoms in the image.<sup>200</sup>

In this thesis, STEM was used to image the interlayer distances of the as-made, intercalated and pillared  $\text{Ti}_3\text{C}_2$ , as a complementary technique to the XRD analysis. The higher resolution of the TEM allowed for this to be imaged, which could not be achieved in the SEM. For STEM characterisation each specimen was crushed using a mortar and pestle, dispersed in methanol and drop-cast onto holey carbon grids to ensure single thin flakes were isolated, which would allow for the electrons to pass through the sample. They were then loaded into an FEI Tecnai TF30 (FEI-Thermo Fisher Scientific, Hillsboro, US) and imaged in HAADF-STEM mode. The microscope was operated at 300 kV, with a beam current of 200 pA and dwell time of 32  $\mu\text{s}$ .

### 3.2.3.6 Energy Dispersive X-ray Spectroscopy (EDS)

EDS can be used alongside either SEM or TEM techniques to provide information on the elemental composition of the sample being imaged. Figure 3.6 showed that x-rays can be generated by the electron beam in an electron microscope when it interacts with a sample. These x-rays are detected and analysed for EDS. The electron beam excites atoms in the sample, which can lead to the ejection of electrons from the inside shells of the atom (e.g.  $n = 1$ ,  $K$  shell, the orbitals closest to the nucleus). This leaves a vacancy in this shell, which can then be filled by an electron in an outer (and higher energy) shell, (e.g.  $n = 2$ ,  $L$  shell), which has now moved into a lower energy state (Figure 3.10). Following the requirement of thermodynamics for the conservation of mass and energy, the energy difference between the two shells that the electron has moved between is emitted as radiation. This radiation has a wavelength (energy) which places it in the x-ray part of the electromagnetic spectrum. The exact energy of the x-ray depends on the difference in energy between the two shells the electron which emitted it transitioned between, which is unique to each element. This allows these x-rays to act as a fingerprint which can be used to identify each element present in the sample.<sup>201</sup> The exceptions are H and He, which have no occupied higher energy electron shells, and Li and Be, which have too few electrons to generate sufficient x-rays for detection.<sup>201</sup>

Since each x-ray corresponds directly to a single transition event, EDS can be used to quantify the elements in the sample.<sup>201</sup> In addition, since the electron beam can be finely controlled for imaging, EDS maps can be build up over a chosen area, showing variation in the elemental composition of a sample.

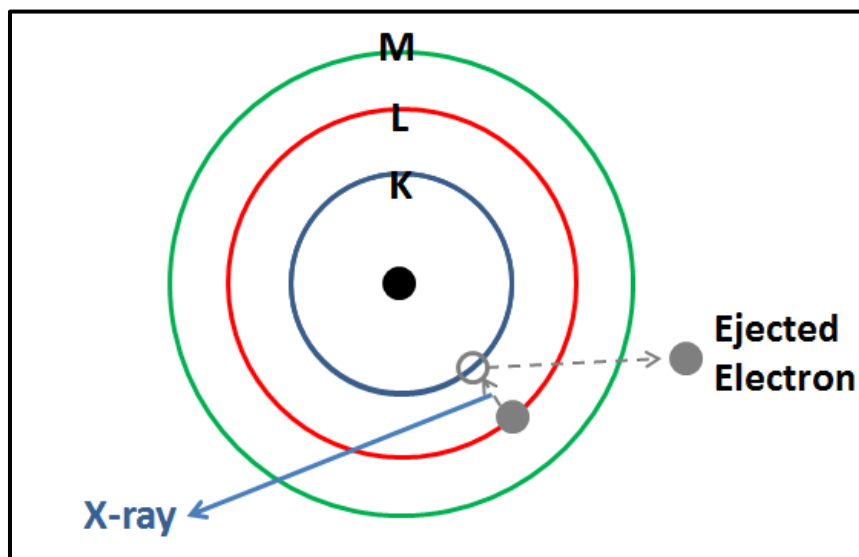


**Figure 3.10.** Schematic diagram of the generation of an x-ray for EDS analysis.

However, care should be taken when using EDS quantitatively with powdered samples, since rough surfaces present in powders can cause shadows or changes in x-ray interactions which can lead to inaccurate results.<sup>201</sup> In addition, the escape depth of electrons for EDS is typically in the range of a few microns, so it is a relatively surface sensitive technique which may not give an accurate representation of the elemental composition of the entire sample. Nevertheless, it is a useful technique to identify and semi-quantify elements present in samples, even when in powdered form.

SEM-EDS was performed in a X-Max50 (Oxford Instruments, Abingdon, UK) using an accelerating voltage of 10 kV and a working distance of 10 mm, which was used to study the elemental composition. For ex-situ EDS studies (Chapter 6), the electrodes were extracted from the cell at the desired state-of-charge, washed five times with DI water (the electrolyte solvent) to remove any surface salts from the electrolyte, dried overnight at 60°C before being attached to a Cu stub by a carbon tape. The use of Cu instead of Al stubs was to ensure that any Al signal originated from the sample, not the stub, since this is an important measure of MXene purity. Maps on flat looking flake surfaces were taken to reduce the error in the measurements.

### 3.2.3.7 X-ray Photoelectron Spectroscopy (XPS)

XPS is also a technique used to analyse the elemental composition of a sample. In XPS, an incident x-ray ejects an electron from an atom (Figure 3.11).<sup>202</sup> The ejected electron is then detected by the spectrometer, which measures the kinetic energy of the electron. The kinetic energy then allows the binding energy to be calculated by Equation 3.3.

$$BE = hv - (KE + \phi) \quad \text{Equation 3.3}$$

Here  $BE$  is the binding energy between the ejected electron and the nucleus,  $hv$  is the energy of the x-ray photon,  $KE$  is the kinetic energy of the electron and  $\phi$  is a workfunction correction for the sample being analysed.<sup>202</sup> Therefore the binding energy of the ejected electron can be determined, since the energy of the x-ray is fixed and known. The binding energy depends on the element the electron was ejected from, the orbital the electron was ejected from and the chemical environment the atom it was ejected from was in.<sup>202</sup> Therefore, it can be used to identify elements present in a sample, the oxidation state of the element and its chemical environment. This makes XPS very useful for electrochemical materials, where the oxidation state of elements plays an important role in electrochemistry. Ex-situ XPS can be used on electrodes at various states of charge to investigate how the oxidation state of elements changes with cycling, which gives important information on the charge storage mechanisms of materials.

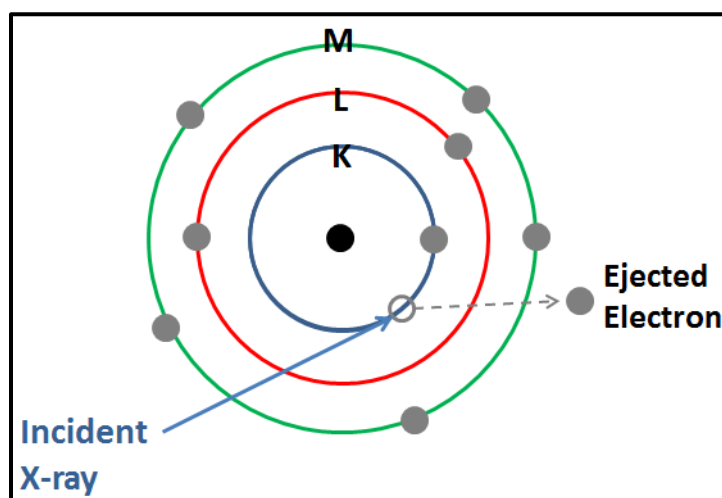


**Figure 3.11.** Schematic diagram showing the ejection of a photoelectron by an x-ray which can then be analysed by XPS.

Photoelectrons ejected by XPS have a very shallow escape depth within the sample, often between 0.3-4 nm depending on the KE of the electron and the energy of the x-ray beam. This means that it is a very surface sensitive technique, and does not detect the bulk of the sample.<sup>202</sup> This also means that care should be taken when preparing samples for XPS, in particular to minimise any surface contamination which

would cover the sample signals. XPS is carried out under vacuum, since particles between the sample and the detector could interact with the electron photoelectron and change the KE, which would also lead to inaccurate results.

XPS is used in this thesis to identify the elements present within samples, and the oxidation states of potentially electrochemically active elements before cycling and at varying stages of charge (ex-situ analysis) to understand the charge storage mechanisms occurring. XPS was performed on a Thermo Fisher Scientific NEXSA spectrometer. Samples were analysed using a micro-focused monochromatic Al x-ray source (19.2 W) over an area of approximately 100 microns. Data were recorded at pass energies of 150 eV for survey scans and 40 eV for high resolution scan with 1 eV and 0.1 eV step sizes respectively. Charge neutralisation of the sample was achieved using a combination of both low energy electrons and argon ions. To remove any surface contaminants, cluster cleaning was performed with 2 keV energy at 0.5 x 0.5 mm area for 60s. For ex-situ studies, the electrodes were extracted from the cell at the desired state of charge, washed five times with the electrolyte solvent to remove surface salts, dried at room temperature under vacuum, and packed under argon before testing. For electrodes which had been cycled in organic electrolytes, the above electrode extraction and washing was carried out in an argon filled glovebox ( $O_2 < 0.1$  ppm,  $H_2O < 0.1$  ppm) to try and prevent elements reacting after cycling, and a polypropylene membrane separator (Celgard) was used instead of a microfiber glass separator to minimise surface contamination from fibres. For electrodes cycled in aqueous electrolytes, only after washing and drying were the samples transferred to a glovebox, since water could not be allowed to contaminate the glovebox. A hydrophilic surfactant-coated polypropylene membrane (Celgard) was used as the separator in this case.

### **3.2.3.8 Nuclear Magnetic Resonance (NMR) Spectroscopy**

NMR is a technique that, like XPS, gives information on the chemical environment of atoms, which can allow the structure to be determined. To run an NMR experiment, the sample (which contains a magnetic moment) is placed in a magnetic field in a rotor. A radio frequency pulse is applied, which aligns the nuclear spins of the nuclei being investigated with the magnetic field. Once the pulse has stopped, the spins relax back to their original state, which results in a free induction decay signal being detected in the radio frequency signal. This relaxation results in different time constants (of relaxation) depending on the chemical environment of the nuclei being studied, which is contained in the radio signal, and converted to a chemical shift (relative to a standard reference), to give an NMR spectrum.<sup>203</sup> The frequency of the applied radio signal in the magnetic field is specific to the nuclei for each element. Therefore different elements can be identified and studied using different frequencies (Larmor frequencies) in NMR experiments.

In an NMR spectrum, peaks are observed relative to a standard (chemical shift). The magnitude of the chemical shift provides information on the chemical environment of those nuclei, and can act as fingerprint for known environments and compounds. The intensity of the peaks is directly proportional the number of nuclei in that environment. Therefore the area under each peak can be compared to determine the relative population of nuclei in each environment. Peak width contains information on the degree of freedom of the nuclear spins in the sample, since the orientation of the spin with respect to the magnetic field affects the relaxation time. Liquids, where nuclei are constantly tumbling, have very sharp peaks since the tumbling motions occur on a much faster timescale than the NMR measurement, which means that a single average spin is all that is observed. This makes it relatively easy to identify and separate out individual chemical environments in liquid NMR. In solids, nuclei are highly restricted, and have strong interactions with each other, since strong covalent bonds keep the atoms in place. This means that there is a variety of orientations of spins which can be detected in the NMR experiment, even for the same chemical environment.<sup>203</sup> This can easily lead to very broad peaks which are either undetectable or merge, making it difficult to identify specific environments. Disorder in a solid can also lead to peak broadening, since this will lead to a range of slightly different chemical environments for a given atomic site.

To overcome the broad nature of the peaks in solid-state NMR, magic-angle-spinning is used. Here, the sample is rotated at an angle of  $54.74^\circ$  relative to the applied magnetic field, which removes the effects of the nuclei being restricted in movement and some of the interactions between neighbouring nuclei.<sup>203</sup> This can give much sharper peaks and allow different chemical environments to be detected. The use of very high rotation speeds can also help reduce peak width, and is commonly used in solid-state NMR experiments.

In Chapter 4, solid-state NMR studies were carried out to investigate the changes in  $\text{Ti}_3\text{C}_2$  upon intercalation and pillaring.  $^1\text{H}$ ,  $^{19}\text{F}$ ,  $^{13}\text{C}$ , and  $^{29}\text{Si}$  solid-state NMR spectra were obtained at 16.4 T on a Bruker Advance 700 MHz spectrometer (Bruker Biospin Corporation, Massachusetts, USA) operating at Larmor frequencies of 700.1, 658.8, 176.0, and 139.0 MHz, respectively. Powdered samples were packed into 2.5 mm MAS rotors, and rotated at a MAS rate of 30 kHz for most of the experiments. The exact details used for NMR data collection are shown in Table 3.1.

**Table 3.1.** Experimental parameters used for MAS solid-state NMR experiments.

Sample	MAS rate / kHz	<sup>1</sup> H		<sup>19</sup> F		<sup>13</sup> C		<sup>29</sup> Si	
		Recycle delay / s	Number of transients	Recycle delay / s	Number of transients	Recycle delay / s	Number of transients	Recycle delay / s	Number of transients
Ti <sub>3</sub> C <sub>2</sub> -O	30	15	80	120	96	10	6352	NA	NA
Ti <sub>3</sub> C <sub>2</sub> -OH	29	15	160	120	96	10	14720	NA	NA
Ti <sub>3</sub> C <sub>2</sub> -OH-Si	30	15	48	120	96	10	6400	60	1424
Ti <sub>3</sub> C <sub>2</sub> -OH-Si-400	30	15	80	120	96	10	6464	60	1440
Reference materials		L-Alanine (NH <sub>3</sub> $\bar{\nu}_{iso}$ 8.5 ppm)		PTFE ( $\bar{\nu}_{iso}$ -122 ppm)		L-Alanine (CH <sub>3</sub> $\bar{\nu}_{iso}$ 20.5 ppm)		Kaolinite ( $\bar{\nu}_{iso}$ -91.2 ppm)	

### 3.2.3.9 Gas Sorption

Gas adsorption experiments have become the standard method for calculating specific surface areas of materials. A gas, typically nitrogen, is allowed to enter the experimental chamber in controlled quantities to be adsorbed onto the surface of the solid, until equilibrium is reached (i.e. no more gas can be adsorbed, and surface coverage is complete). This is carried out at a constant temperature, 77 K for N<sub>2</sub>, just above its boiling point, to give a sorption isotherm. The amount of gas adsorbed in a monolayer is then calculated, and converted to a specific surface area using the Brunauer-Emmett-Teller (BET) formula by using the amount of gas adsorbed at multiple pressure points.<sup>204–206</sup> This allows for the comparison of the degree of porosity across different materials. Pore size distributions (PSD) can then be estimated with a variety of methods based on the adsorption isotherm. One common method is non-local density functional theory (NLDFT), which is a common method for nanoscale-resolution pore size distributions. The NLDFT method calculates the sorption isotherm using a classical fluid density functional theory and ideal pore geometries (e.g., N<sub>2</sub> adsorption in the slit-pore model at 77 K). The PSD result can be obtained by solving an adsorption integral equation.<sup>207</sup>

Gas sorption isotherms were measured on a Micromeritics ASAP 2020Plus gas sorption analyser 2020 (Micromeritics Instrument Corporation, Georgia, USA) using high purity nitrogen gas at 77 K. BET surface areas were calculated over a relative pressure range of 0.05-0.15 P/P<sub>0</sub>. The BET method was used to determine the specific surface area of the materials. Pore size distributions were calculated using the NL-DFT method using a slit pore model.

### 3.2.3.10 Thermogravimetric Analysis (TGA)

TGA is a technique which monitors the mass change of a sample as it is heated. This can be done in different atmospheres, (N<sub>2</sub>, air etc), and at different rates to monitor the thermal stability of materials in different environments. In addition, differential scanning calorimetry (DSC) can be coupled with TGA to track phase changes during the temperature changes, which can add extra information on the changes occurring during heating.

In this thesis, TGA was used to investigate the thermal stability of MXenes, and to estimate the quantity of CTAB intercalated into Ti<sub>3</sub>C<sub>2</sub> in Chapter 6. TGA was done in a STA 449 F3 Jupiter (Netzsch, Selb, Germany) to look at the effect of heat treatments on the intercalated and pillared sample. Small amounts of the dried MXene (20 to 30 mg) were placed into alumina crucibles which were then placed directly into the heated chamber of the TGA. Samples were then heated at a rate of 1 °C min<sup>-1</sup> from 25 °C to 700 °C under air or nitrogen.

### 3.2.3.11 Electrochemical Characterisation

To test the effect of the pillaring process on the electrochemical behaviour, the pillared and un-pillared materials were tested in half-cell configurations in CR2032 coin cells. The coin cells consisted of two outer cases, the MXene (working) electrode, a separator (Whatman micro glass fibre paper) wetted with the electrolyte, the counter and reference electrode and a metal spacer and spring, which are used to ensure good contact throughout the cell (Figure 3.12). These were sealed using a coin cell crimper (Tob New Energy), which ensured good sealing of the cells at a consistent pressure. Coin cells for testing MXenes in organic electrolytes were assembled and sealed in an argon filled glovebox (O<sub>2</sub> and H<sub>2</sub>O levels < 0.1 ppm), while cells using aqueous electrolytes were assembled in the open atmosphere.



**Figure 3.12.** Photo of coin cell parts used in this thesis for the electrochemical characterisation. Note that a metal foil would also be added between the spacer and separator as the counter and reference electrode.

To prepare the working electrodes, slurries were made by mixing the MXene with carbon black (super P, company) as a conductive additive and PVDF as a binder in a 75:15:10 weight ratio respectively. These were added to NMP, and left to stir for 24 h

at room temperature. The slurry was then manually casted onto the metal foil current collector using a doctor blade (set at a distance of 25  $\mu\text{m}$ ), and circular disk electrodes were then cut. The active mass was around 3  $\text{mg cm}^{-2}$  for all electrodes studied. Four different metal-ion systems were tested: organic Li-ion, organic Na-ion, organic Zn-ion and aqueous Zn-ion. The electrolytes and current collectors used in each system are shown in Table 3.2.

**Table 3.2.** Components used in test cells for different electrochemical systems.

System	Counter / Reference Electrode	Electrolyte	Current Collector
Organic Li-ion	Li metal disks	1 M $\text{LiPF}_6$ in EC/DEC (1:1 weight ratio)	Cu
Organic Na-ion	Na metal disks	1 M $\text{NaPF}_6$ in EC/DEC (1:1 weight ratio)	Al
Organic Zn-ion	Zn metal disks	1 M $\text{Zn(TFSI)}_2$ in ACN	Ti
Aqueous Zn-ion	Zn metal disks	0.1 M $\text{ZnSO}_4$ in DI water	Ti

### 3.2.3.12 Galvanostatic charge-discharge (GCD) Testing

GCD testing is used to study the electrochemical performance of a potential electrochemical energy storage material. A constant current is applied to the cell, and the change in voltage is recorded along with the charge stored by the material. This can then be plotted with the voltage on the y-axis and charge (as specific capacity) on the x-axis, to give a load curve. In an electrochemically active material, the voltage will change as charge is stored, and will either increase or decrease until it reaches a cut-off voltage set by the user. The current will then reverse, and the voltage will change in the opposite direction as the charge storage process is reversed, until a second cut-off limit is reached. This is the end of one charge-discharge cycle. This process can then be repeated for as many cycles as the user desires. In addition, the rate of cycling can be investigated by changing the magnitude of the applied current.

Therefore, GCD testing can quantify several key parameters which determine the promise of potential electrochemical energy storage materials. The total amount of charge stored (capacity) can be determined by the amount of current which has passed by the end of each charge or discharge. This is usually normalised by mass of the active material to allow for fair comparison between different experiments ( $\text{mAh g}^{-1}$ ); in this thesis all capacities are normalised to the mass of the MXene material, including any pillaring species and residues, in the electrode. The long-term stability and electrode degradation can be determined by comparing the capacity across multiple cycles, and the rate capability (how the electrode responds to fast charging

or discharging times) can be investigated by changing the current and recording how the capacity changes. Coulombic efficiency can also be determined from the GCD testing. This is calculated by dividing the charge capacity by the discharge capacity, and reveals the extent of any irreversible or side-reactions occurring within the cell. If a coulombic efficiency is less than 100%, then some charge carrying ions are being consumed or trapped via an irreversible process. This means that those ions are no longer available to reversibly store charge, leading to lower capacities on the subsequent charge and following cycles. The initial coulombic efficiency (for the first cycle) is often very low for MXenes, partly due to SEI formation and partly due to irreversible side-reactions. This could cause issues in a full cell, where the positive electrode is often the ion source, and so would need to be oversized to counter the ion loss, which reduces the overall energy density of the cell. If the coulombic efficiency is greater than 100%, then side-reactions are occurring, potentially between the electrode and electrolyte, which are providing extra irreversible capacity, as is as undesirable as low coulombic efficiency.

In addition, the voltage profile in the load curve provides key information on the mechanism of charge storage and identifies whether a material should be considered as a positive electrode or a negative electrode. To be classed as a negative electrode, the average voltage of the material should be as low as possible (but above the metal plating potential for the ion system being studied), typically below 1.5 V for organic Li and Na-ion systems. For positive electrodes, the average voltage should be as high as possible, typically well above 3 V for organic Li- and Na-ion systems. For aqueous systems, the voltage window is typically limited by the electrolysis of water, to around 1.23 V. As seen in the Background chapter (Chapter 2), MXenes have voltages which best suit applications as negative electrode materials.

The shape of the voltage profile contains information on the mechanism of charge-storage. If the slope of the profile is linear, then the charge-storage mechanism does not involve any phase changes in the active material. Instead the original phase is maintained through cycling, suggesting that a solid solution or surface charge storage mechanism is present. On the other hand, if a plateau is observed on the load curve, then the charge storage in that region involves two phases, with the initial phase being changed into a new product phase. Typically, battery materials display significant plateaus in their voltage profiles, which give batteries their relatively constant working voltages and contribute to higher energy densities than supercapacitors. A linear profile is typically seen in capacitive materials, where the lack of phase changes allows for improved cycling stability since there is no (or minimal) lattice mismatch in the electrode. If a profile contains no clear plateaus but is not truly linear, than there is likely a mixed charge storage mechanism involving multiple processes occurring. The different load curve types are shown in Figure 3.13 as examples.

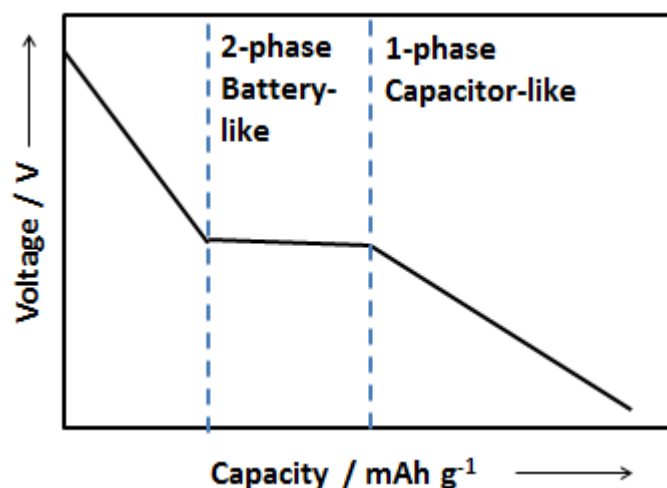


**Figure 3.13.** Load curve diagram illustrating the two main types of load curve features observed for electrochemical energy storage materials.

The galvanostatic charge-discharge tests were carried out on a Neware battery cycler (Neware battery system, China) at a current density of  $20 \text{ mA g}^{-1}$  in the voltage range of 0.01-3 V for 100 cycles. For rate capability tests, the cells were cycled at a current density of  $20 \text{ mA g}^{-1}$  for 1 cycle to stabilise the cell before five cycles at each current density of 20, 50, 200, 500 and  $1,000 \text{ mA g}^{-1}$  were run before returning to  $20 \text{ mA g}^{-1}$ .

### 3.2.3.13 Cyclic Voltammetry (CV)

Cyclic voltammetry (CV) is a technique which can also study the electrochemical reactions of an energy storage material. In cyclic voltammetry experiments, the voltage is varied at a constant scan rate between two cut-off voltages, and the current produced is measured. A CV plot consists of the current,  $i$ , plotted on the  $y$ -axis against voltage,  $V$ , on the  $x$ -axis. As the voltage is decreased, the potential becomes more reductive (cathodic sweep) and as the voltage is increased the potential becomes more oxidative (anodic sweep).<sup>208</sup> CV can give information on the number, reversibility, kinetics and voltage of electrochemical reactions. For electrochemical energy storage systems, there are two main shapes of CV curves: rectangular, with no clear peaks and significant current across the voltage window and those with clear, sharp redox peaks with limited current away from those peaks. These correspond to capacitive-like and battery-like charge storage mechanisms respectively. Pseudocapacitive materials display features from both types of mechanism, with significant current generated across the voltage window and broad redox peaks which should have minimum voltage separation between the cathodic and anodic scans, corresponding to the fast charge transfer kinetics. Battery-like materials with slower kinetics than pseudocapacitive materials display larger separation between the peaks on the cathodic and anodic scans.<sup>209</sup> The different shapes of CV curves and the corresponding charge storage mechanism are shown alongside the GCD curves in Figure 3.14.

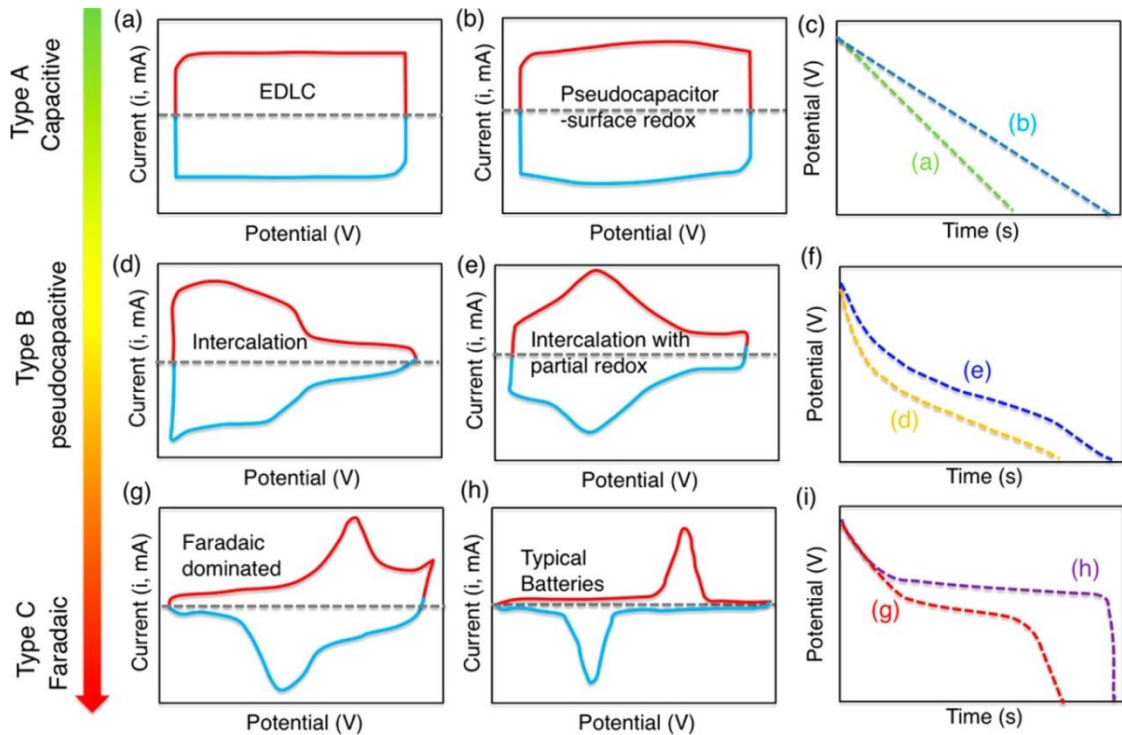


**Figure 3.14.** “(a, b, d, e, g, h) Schematic cyclic voltammograms and (c, f, i) corresponding galvanostatic discharge curves for various kinds of energy-storage materials. A pseudocapacitive material will generally have the electrochemical characteristics of one, or a combination, of the following categories: (b) surface redox materials (e.g.,  $\text{MnO}_2$  in neutral, aqueous media), (d) intercalation-type materials (e.g., lithium insertion in  $\text{Nb}_2\text{O}_5$  in organic electrolytes), or (e) intercalation-type materials showing broad but electrochemically reversible redox peaks (e.g.,  $\text{Ti}_3\text{C}_2$  in acidic, aqueous electrolytes). Electrochemical responses in (g–i) correspond to battery-like materials.” Reprinted with permission from ACS Nano, 2018, 12, 3, 2081-2083.<sup>209</sup> Copyright 2018 American Chemical Society.

In addition to analysing the shape of the CV curves (and GCD curve), the kinetics of the charge storage mechanism can be studied by varying the scan rate of the CV experiment and analysing the variation of the current response. It is known that the charge storage of capacitive and capacitive-like mechanisms is surface-controlled. Therefore, the current-scan rate relationship is linear, as shown by Equation 3.4.<sup>210</sup>

$$i = vCA \quad \text{Equation 3.4}$$

Here  $i$  is the current response,  $v$  is the scan rate,  $C$  is the capacitance and  $A$  is the surface area of the electrode. For battery-like processes, charge storage is diffusion-limited and the current-scan rate relationship varies with the square root of the scan rate, as shown by Equation 3.5.<sup>210</sup>

$$i = nFAC * D^{1/2}v^{1/2}(\alpha nF/RT)^{1/2}\pi^{1/2}\chi(bt) \quad \text{Equation 3.5}$$

Here, in addition to the variables for capacitive storage,  $n$  is the number of electrons involved in the redox reaction,  $F$  is the Faraday constant,  $C^*$  is the surface concentration of the material,  $D$  is the diffusion co-efficient,  $\alpha$  is the charge transfer

co-efficient,  $R$  is the molar gas constant,  $T$  is the temperature and  $\chi(bt)$  is a function which represents the normalised current. Therefore, the dependence of current on scan rate can be written as a power law (Equation 3.6).<sup>209,210</sup>

$$i = av^b \quad \text{Equation 3.6}$$

Here  $a$  and  $b$  are adjustable parameters. The value of  $b$  can vary between the surface-limited case ( $b = 1$ ), which indicates that the current is completely surface-controlled and therefore fully capacitive (EDL or ideal pseudo capacitors), or the diffusion-limited case ( $b = 0.5$ ), where the current is completely diffusion-limited as is the case for typical battery materials. Values of  $b$  between these two end points signify a mixed charge-storage mechanism with both surface-limited (capacitive) and diffusion-limited (battery-like) processes contributing to the overall charge storage. If the  $b$ -value is closer to 1 then the current is predominantly capacitive in nature, and vice versa. Therefore, calculating the  $b$ -value allows for the proportion of the diffusion-limited and surface-limited contribution to the total charge storage to be determined. Typically, this is done by taking logs of the current and scan rate, a plot of which should give a linear fit with a gradient of  $b$ . Whilst typically just peak currents are used, this can be done at different voltages within the window, to give a more detailed analysis of how the mechanism changes with voltage, which can be particularly useful for pseudocapacitive materials, such as MXenes. This  $b$ -value analysis is used in this thesis to analyse the charge storage mechanisms in the MXenes, including after pillaring.

CV measurements were conducted using an Ivium potentiostat (Ivium Technologies BV, The Netherlands) with a scan rate of  $0.2 \text{ mV s}^{-1}$  for five cycles, followed by further cycles at  $0.5$ ,  $2$  and  $5 \text{ mV s}^{-1}$  sweep rates in the voltage range of  $0.01$ - $3\text{V}$ .

### 3.2.3.14 Summary

Overall, this chapter described the synthesis methods used to make the MAX phase precursors, the multilayered MXenes and the pillared MXenes. In addition, the structural and chemical characterisation techniques used in this thesis were outlined. XRD is used to identify the MAX and MXene phases and to study the effect of pillaring and electrochemical cycling on the interlayer spacing. Raman, IR, NMR and x-ray photoelectron spectroscopies are used to investigate the surface groups and pillaring species present in the MXenes before and after pillaring, and can also provide information on bonding changes after cycling. Electron microscopy techniques, such as SEM and TEM are used to study the morphology of the MXene materials, and can be matched with chemical information when combined with EDS. This can help to confirm material purity and the presence of pillaring elements within the samples. Gas adsorption experiments using the BET method can determine the specific surface area of a material, which would show if the pillaring methods had

successfully created porous MXenes. TGA experiments allow the thermal stability of the MXene before and after intercalation to be studied, which can help determine appropriate calcination conditions for the pillaring process. Electrochemical characterisation techniques, such as GCD testing and CV, using half-cells allow the electrochemical performance of the MXene materials to be assessed, and provide important mechanistic information on the charge storage processes.

To determine whether or not a material is storing charge in a battery-like or capacitive-like way is becoming increasingly important in the development of materials for electrochemical energy storage, particularly where energy storage is concerned. As mentioned previously, MXenes typically display mixed mechanisms with both capacitive and battery-like features. These can be identified by analysing the load curves obtained by GCD testing and by detailed kinetic (*b*-value) analysis using CV. To complement these techniques, ex-situ studies such as XRD, XPS and Raman spectroscopy are used to identify any new phases (battery-like) or changes in bonding/ valence states (battery-like or pseudocapacitive) as a result of electrochemical reactions, which would also help to classify the charge storage mechanism.

# **Chapter Four**

## **SiO<sub>2</sub>-Pillared Ti<sub>3</sub>C<sub>2</sub>**

## 4.1 Introduction

As discussed in the background chapter (Chapter 2), a common difficulty with the practical application of MXenes is creating stable architectures which maintain the properties and performance of the 2D nanosheets without layers restacking.<sup>211</sup> The surface areas of MXenes ( $4\text{-}20\text{ m}^2\text{ g}^{-1}$ )<sup>140,184,212</sup> are significantly smaller than those of other 2D materials ( $300\text{-}2,000\text{ m}^2\text{ g}^{-1}$  have been reported for graphene / graphene oxide materials)<sup>37,213,214</sup> which is a key property for high performance in a variety of applications such as energy storage, catalysis and gas capture and storage, as discussed in the introduction chapter. Even when fully delaminated, the reported surface areas are no greater than  $98\text{ m}^2\text{ g}^{-1}$ .<sup>130</sup> In addition, delaminated nanosheets restack over time, leading to reduced performance e.g. in a lithium-ion battery.<sup>130</sup> Therefore, porous and stable MXene structures need to be developed.

To date, a number of different strategies have been reported, including the use of nanocarbon spacers,<sup>124,133</sup> deliberate oxidation of the MXene surface,<sup>212</sup> or insertion of metal ions.<sup>194,215,216</sup> While these methods all increased the interlayer spacing of the MXene material, they have several drawbacks, including partial destruction of the MXene structure, and poor control over the final interlayer distances. As discussed in Section 2.4.2.2, the surface areas of porous MXenes typically do not exceed  $100\text{ m}^2\text{ g}^{-1}$ , and only one case has been found of a surface area over  $200\text{ m}^2\text{ g}^{-1}$ , which was obtained by freeze-drying.<sup>217</sup>

This chapter focuses on the development of a pillaring method adapted from clay engineering, where it had been used to produce materials with surface areas as high as of  $618\text{ m}^2\text{ g}^{-1}$ , which were investigated as heterogeneous catalysts. The focus was on pillaring methods previously demonstrated on titanosilicates, since these have titanium layers covered with OH functional groups,<sup>176</sup> and thus are very similar to the surface chemistry of Ti-based MXenes. This led to the development of a  $\text{SiO}_2$ -pillared  $\text{Ti}_3\text{C}_2$  material, which was synthesised using amines (dodecylamine - DDA and octylamine - OA) as co-pillars with the organometallic precursor tetraethylortho silicate (TEOS). Silica is comprised of the two most abundant elements in the Earth's crust,<sup>218</sup> and therefore meets the demand for affordable and sustainable materials. The amines intercalated at the same time as TEOS, removing the need for a pre-pillaring step. In addition, the amines also act as catalysts to the hydrolysis of TEOS, speeding up the reaction. The intercalation and hydrolysis are carried out at room temperature, with a calcination step employed to give further control over the interlayer spacing over a range of  $0.75\text{-}3.2\text{ nm}$  and to remove the amine template.

The intercalation mechanism was studied to understand the pillaring process, using acid (HCl) and alkali (NaOH) treatments to carry out a detailed study on the effect of surface chemistry on the pillaring process and used this understanding to show the

functional groups can be tailored to optimise the pillaring process (illustrated in Figure 4.1).

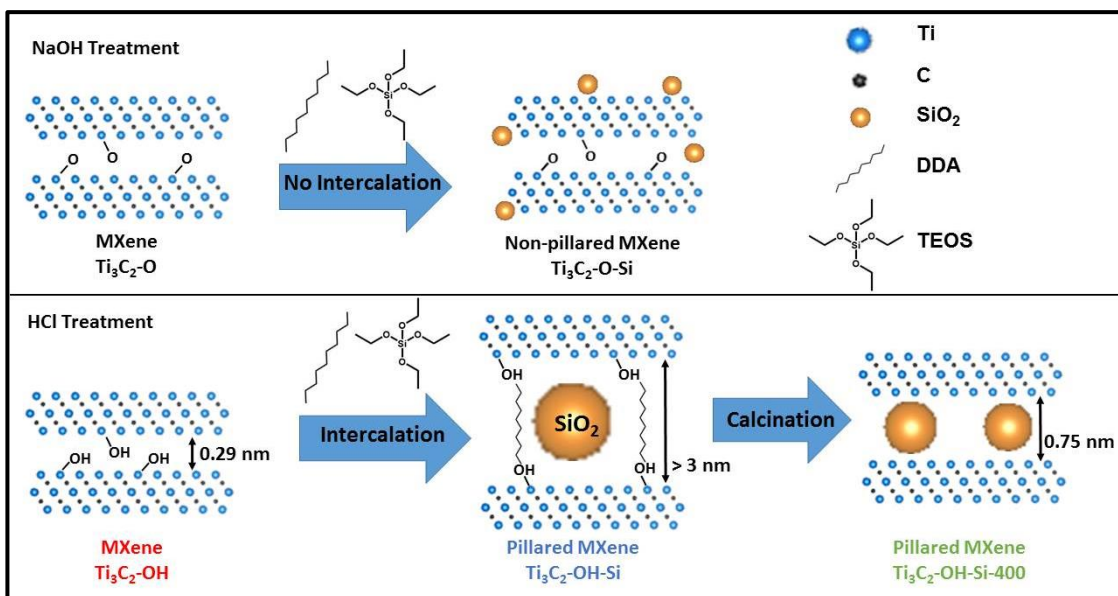
The resulting pillared MXenes were then tested as negative electrodes in organic Na-ion and Li-ion systems since large interlayer spacings in the pillared material should allow for improved cycling stability and rate performance, overcoming some of the drawbacks of this technology.

It was found that the amine-assisted silica pillaring method successfully created porous MXenes, with surface areas being amongst the highest reported (up to  $235 \text{ m}^2 \text{ g}^{-1}$ ). The intercalation and pillaring mechanism was investigated using XRD, SEM, TEM, EDS, Raman spectroscopy,  $^1\text{H}$ ,  $^{13}\text{C}$ ,  $^{19}\text{F}$  and  $^{29}\text{Si}$  solid-state NMR to determine the structure of the pillared product and the role of the MXene surface groups. The electrochemical performance was then investigated by GCD testing in Na and Li-ion systems and compared to the non-pillared material. Rate capability tests were carried out at currents up to  $1 \text{ A g}^{-1}$  to investigate how pillaring affects the high rate performance. It was shown that the pillared MXenes had superior capacities, cycling stabilities, coulombic efficiencies and rate capabilities in both systems. CV analysis was also used to study the kinetics of the systems and to identify the redox reactions occurring. Ex-situ XPS was used to investigate the electrochemical activity of the  $\text{SiO}_2$  pillars in the Na-ion system.

## 4.2 Results and Discussion

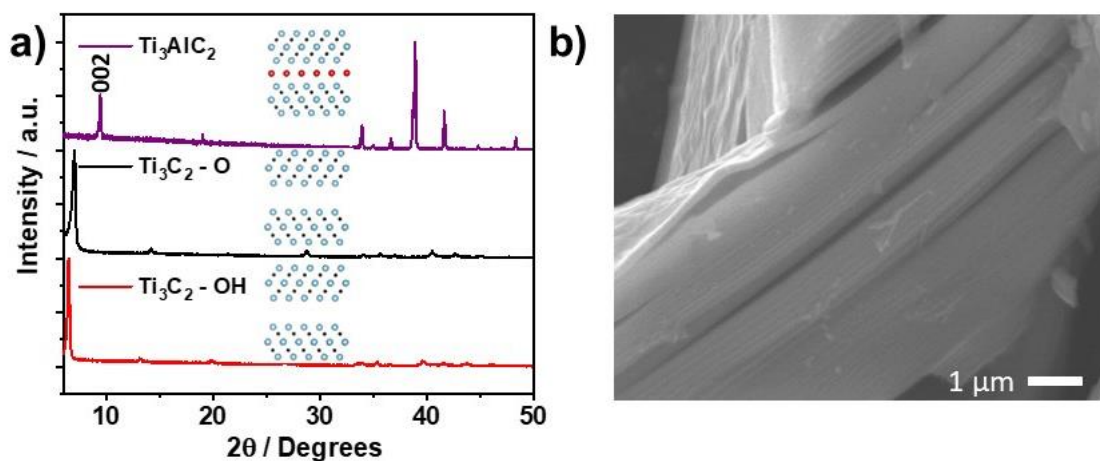
### 4.2.1 Controlling the MXene Surface Chemistry

The  $\text{Ti}_3\text{AlC}_2$  MAX phase was synthesised and etched to give the as-made MXene, using a modified version of the HCl and fluoride salt-based method first reported by Ghidui et al.<sup>114</sup> Samples were treated with 1 M NaOH or HCl and are referred to as  $\text{Ti}_3\text{C}_2\text{-O}$  and  $\text{Ti}_3\text{C}_2\text{-OH}$  respectively, due to the presence of -O or -OH functional groups associated with these samples. The treated MXenes were then mixed with DDA and TEOS to intercalate Si between the  $\text{Ti}_3\text{C}_2$  layers; these materials are referred to as  $\text{Ti}_3\text{C}_2\text{-O-Si}$  and  $\text{Ti}_3\text{C}_2\text{-OH-Si}$ . Finally, the intercalated materials were calcined under argon at 300, 400 or 500 °C which is shown by appending the calcination temperature onto the above sample names (Figure 4.1).



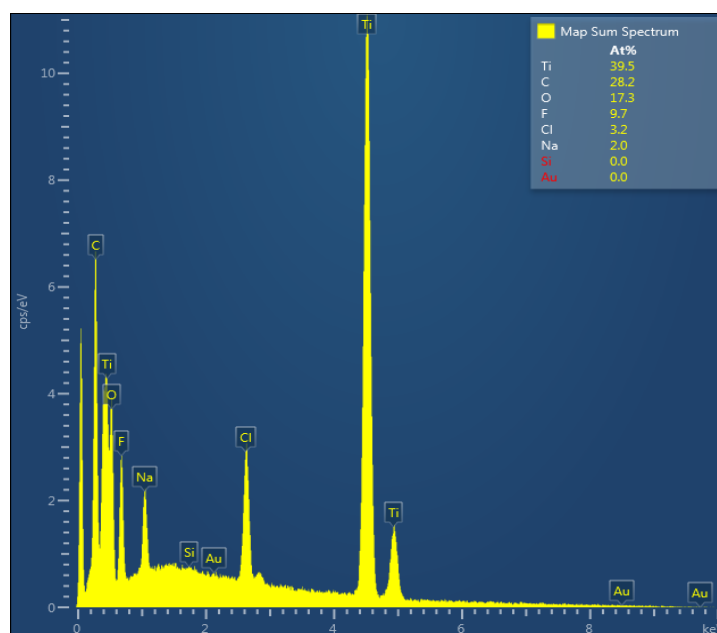
**Figure 4.1.** Schematic illustrating the pillaring process.

Figure 4.2 shows the successful synthesis of the  $\text{Ti}_3\text{AlC}_2$  MAX phase, with the diffraction peaks matching those previously reported.<sup>219</sup> The  $\text{Ti}_3\text{C}_2$  was then successfully etched from the sieved  $\text{Ti}_3\text{AlC}_2$ , with the  $\text{Ti}_3\text{C}_2$  X-ray diffraction (XRD) patterns showing only typical MXene reflections. In particular, the (002) diffraction peak<sup>219</sup> has shifted to lower angles, corresponding to the enlarged interlayer spacing in the MXene compared to the MAX phase. This is accompanied by the loss of the typical  $\text{Ti}_3\text{AlC}_2$  diffraction peaks.<sup>219</sup> Scanning electron microscopy (SEM) shows the open layered morphology which is typical of MXenes (Figure 4.2b).<sup>86,114</sup> Both the HCl and NaOH treatments maintain the MXene crystal structure but the (002) diffraction peak for OH-functionalised MXene ( $\text{Ti}_3\text{C}_2\text{-OH}$ ) has shifted to a lower angle relative to  $\text{Ti}_3\text{C}_2\text{-O}$  (Figure 4.2a). This indicates that the acid treatment results in a small increase in interlayer spacing, possibly due to the re-arrangement of hydrogen-bonded water between the layers (see NMR results in Section 4.2.2.3).



**Figure 4.2.** a) XRD patterns of the as made  $\text{Ti}_3\text{AlC}_2$ ,  $\text{Ti}_3\text{C}_2$  after NaOH treatment ( $\text{Ti}_3\text{C}_2\text{-O}$ ) and after HCl treatment ( $\text{Ti}_3\text{C}_2\text{-OH}$ ). (002) diffraction peak was indexed according to Peng et al.<sup>219</sup> b) SEM micrograph of the as-made  $\text{Ti}_3\text{C}_2$ .

In addition, Energy dispersive spectroscopy (EDS, Figure 4.3) shows no Al content, confirming complete etching. The EDS results also show that the majority of surface groups are -O based terminations, with the levels of F (9%) and Cl (3%) being low.



**Figure 4.3.** EDS spectra of the as-etched  $\text{Ti}_3\text{C}_2$ , confirming the selective removal of the Al layer.

Raman spectroscopy has previously been used to study  $\text{Ti}_3\text{C}_2\text{-OH}$  and  $\text{-O}$  terminations, which are not easily distinguished using other techniques, as described in Section 3.2.3.2.<sup>220</sup> Figure 4.4 shows the results from Raman spectroscopy for the samples with the NaOH ( $\text{Ti}_3\text{C}_2\text{-O}$ ) and HCl treatments ( $\text{Ti}_3\text{C}_2\text{-OH}$ ), and for the pillared ( $\text{Ti}_3\text{C}_2\text{-OH-Si}$ ) and calcined samples ( $\text{Ti}_3\text{C}_2\text{-OH-Si-400}$ ). A table listing the peak analysis and assignments can be found in the appendix (Table A.1)

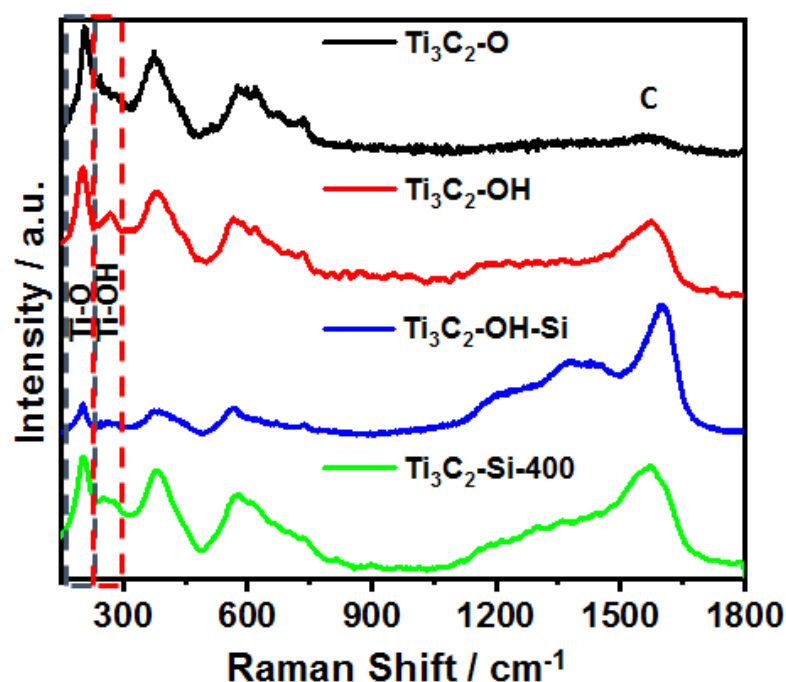


**Figure 4.4.** Raman spectra of the alkali (black,  $\text{Ti}_3\text{C}_2\text{-O}$ ) and acid (red,  $\text{Ti}_3\text{C}_2\text{-OH}$ ) treated MXene, and the acid treated intercalated (blue,  $\text{Ti}_3\text{C}_2\text{-OH-Si}$ ) and calcined at 400 °C (green,  $\text{Ti}_3\text{C}_2\text{-Si-400}$ ) pillared MXene, with columns highlighting the key peaks corresponding to Ti-O (grey) and Ti-OH (orange) functional groups.

The NaOH treated sample ( $\text{Ti}_3\text{C}_2\text{-O}$ ) shows a distinctive peak at  $207\text{ cm}^{-1}$  corresponding to Ti-O terminations, with a shoulder sloping to  $300\text{ cm}^{-1}$  resulting from Ti-O-Na groups, which have previously been reported to form after NaOH treatments.<sup>221</sup> Following HCl treatment ( $\text{Ti}_3\text{C}_2\text{-OH}$ ), the Ti-O peak ( $207\text{ cm}^{-1}$ ) sharpens, with no shoulder visible. In addition, a new peak appears at around  $270\text{ cm}^{-1}$  resulting from Ti-OH vibrations, i.e. protonated Ti-O groups.<sup>75</sup> This demonstrates how the surface chemistry of  $\text{Ti}_3\text{C}_2$  can be controlled by changing the pH of  $\text{Ti}_3\text{C}_2$  solvents, which is further supported by NMR results (Section 4.2.2.3). The other peaks present up to  $1,000\text{ cm}^{-1}$  are known to be formed by the overlap of Ti-X vibrations (where X is any of the known termination groups) and are therefore not useful here for the study of the surface chemistry.<sup>220</sup> The -F terminations are studied using NMR and discussed in a later section. The broad peak at around  $1,570\text{ cm}^{-1}$  shows that there is a small amount of amorphous carbon present in the treated MXenes, suggesting slight over-etching of  $\text{Ti}_3\text{AlC}_2$ .

## 4.2.2 DDA-TEOS Pillaring

### 4.2.2.1 Synthesis and characterisation

Both the  $\text{Ti}_3\text{C}_2\text{-OH}$  and the  $\text{Ti}_3\text{C}_2\text{-O}$  samples were treated using the same intercalation process to compare the effect of surface chemistry on the pillaring process (denoted  $\text{Ti}_3\text{C}_2\text{-OH-Si}$  and the  $\text{Ti}_3\text{C}_2\text{-O-Si}$  respectively). 0.5 g  $\text{Ti}_3\text{C}_2$  were added to a DDA-TEOS

solution in a 1:10:20 molar ratio under argon and stirred for 4 h at room temperature. The solid product was then recovered by vacuum filtration, dried under vacuum and dispersed in DI water (100 ml) for 16 h for hydrolysis. Vacuum filtration was then used again to recover the product, which was dried at 60 °C overnight. Figure 4.5 shows the XRD results from the acid and alkali-treated samples after the pillaring experiments. The  $\text{Ti}_3\text{C}_2\text{-O-Si}$  sample shows no sign of an increase in interlayer spacing, with no MXene diffraction peaks visible (note that the small peaks at 2.1 and 3° 2 $\theta$  in  $\text{Ti}_3\text{C}_2\text{-O-Si}$  are from the sample holder). This suggests that the pillaring was unsuccessful for the MXene functionalised with –O groups.

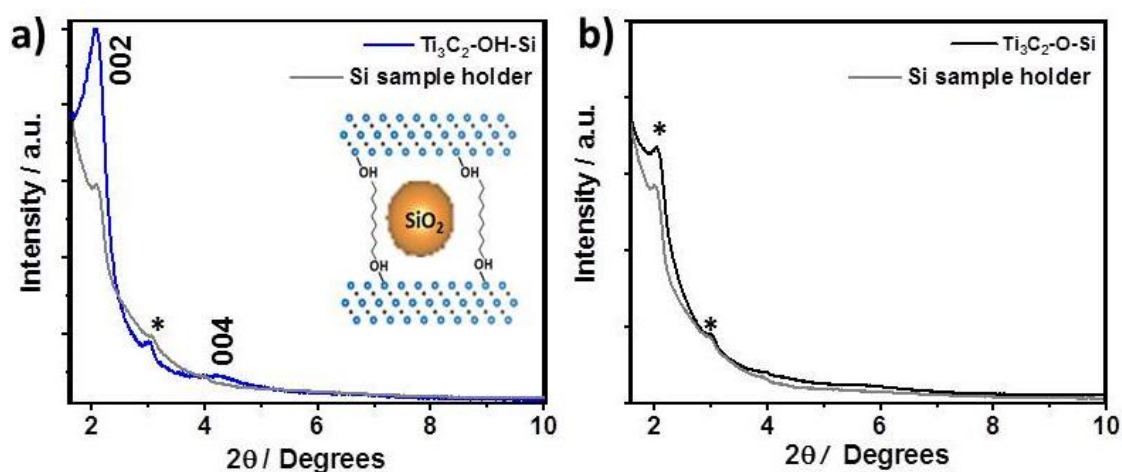


**Figure 4.5.** Low angle XRD of the a) acid (blue,  $\text{Ti}_3\text{C}_2\text{-OH-Si}$ ) and b) alkali (black,  $\text{Ti}_3\text{C}_2\text{-O-Si}$ ) treated MXenes after the intercalation experiments. The sample holder (grey) is also shown for reference. The asterisks highlight peaks corresponding to the glass sample holder.

In contrast, the HCl treated material ( $\text{Ti}_3\text{C}_2\text{-OH-Si}$ ) shows a clear and relatively sharp peak at 2.1° 2 $\theta$ , which corresponds to an expanded  $d$ -spacing of 4.2 nm. This diffraction peak is much more intense than the small peak seen in the sample holder diffractogram and the alkali treated sample, confirming that it corresponds to the (002) diffraction peak from the MXene. It has previously been reported that the thickness of a single  $\text{Ti}_3\text{C}_2$  sheet is 0.95 nm,<sup>189</sup> which gives a gallery height of 3.25 nm for the pillared MXene, around 10 times that of the starting MXene; a clear sign of successful pillaring. This is larger than any interlayer distance found in the literature review for an MXene and is also one of the largest for any 2D material, which are rarely above 2 nm.<sup>179,180,222–228</sup> STEM analysis (Figure 4.6) also confirms the large increase in interlayer spacing, from an average of around 1 nm to 2.7 nm (Figure 4.6 b-c). This is slightly lower than the spacing calculated by XRD, perhaps due to electron beam induced specimen damage or the movement / partial removal of the intercalated molecules within the TEM vacuum. Differences may also result from the sampling volumes between the two methods – XRD is a bulk method, whereas the STEM measurements are very localised. The STEM measurements were manually carried out on 70 interlayer spacings for each sample and suggest that the standard

deviation of interlayer distances increases with pillaring, suggesting that the pillars have some variation in size or concentration across the sample. This is also supported by pore size distribution results which are discussed later in this section.

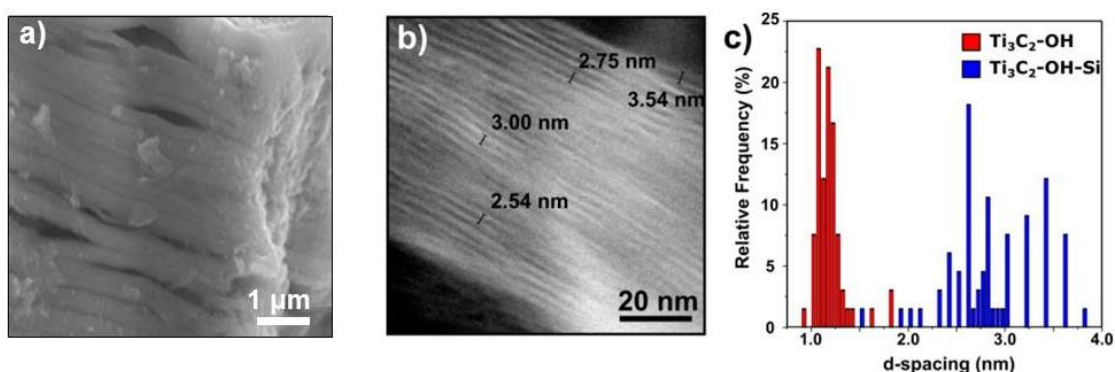


**Figure 4.6.** Microscopy studies of the intercalated MXene. a) SEM micrograph of the intercalated MXene ( $\text{Ti}_3\text{C}_2\text{-OH-Si}$ ) b) STEM cross sectional image of atomic planes of  $\text{Ti}_3\text{C}_2\text{-OH-Si}$ , with example  $d$ -spacings labelled. c) Graph showing the results of the (002) interlayer distances measured using STEM.

EDS results (Figure 4.7a) confirm that this increase in interlayer spacing is correlated with the presence of Si in the sample (3.1 wt.%), and SEM shows no sign of  $\text{SiO}_2$  particles external to the MXene (Figure 4.7b). This suggests the successful intercalation of TEOS into the interlayer of  $\text{Ti}_3\text{C}_2\text{-OH}$  (after acid treatment). The presence of Si is further confirmed by NMR spectroscopy (Section 4.2.2.3). Additionally, three new Raman peaks appear between  $1,100\text{-}1,700\text{ cm}^{-1}$  corresponding to the presence of DDA and TEOS hydrolysis products (Figure 4.4). There is an increase in carbon content in the EDS, from 28.2 wt.% (Figure 4.3) to 33 wt.% (Figure 4.9a) and which is also seen in the NMR results (Section 4.2.2.3). (Note that although C content measurements with EDS will contain some C content from the carbon tape used to secure the sample, the measurements were done on thick particles ( $1\text{-}10\text{ }\mu\text{m}$ ) to minimise this contribution, and the higher levels in the intercalated material were seen across multiple particles). Taken together, these results confirm the successful co-intercalation of DDA and TEOS into the acid treated  $\text{Ti}_3\text{C}_2$ .

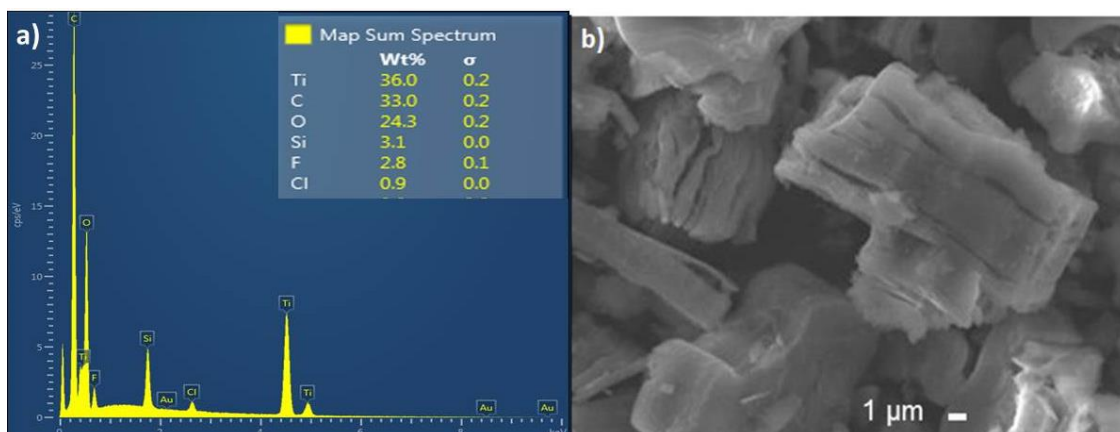


**Figure 4.7.** SEM-EDS analysis of  $\text{Ti}_3\text{C}_2\text{-OH-Si}$ . a) EDS spectra of  $\text{Ti}_3\text{C}_2\text{-OH-Si}$ , confirming the presence of Si in the material (3.1 wt.%). b) SEM micrograph of sample.

IR spectroscopy also supports these findings (Figure 4.8), with peaks at 2,916 and 2,849  $\text{cm}^{-1}$  corresponding to C-H vibrations from the intercalated DDA. The small peak at 1,050  $\text{cm}^{-1}$  is from Si-O vibrations, suggesting that the intercalated Si is still bound to oxygen atoms. The peaks at 2,337 and, 2,089, 2,117 and 1,996  $\text{cm}^{-1}$  are found in all samples studied and are therefore assigned as MXene vibrations.

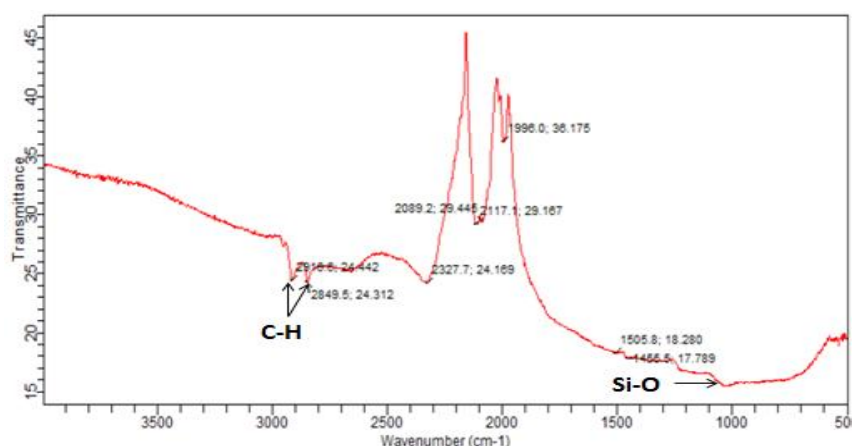


**Figure 4.8.** IR spectroscopy results of  $\text{Ti}_3\text{C}_2\text{-OH-Si}$  recorded between 500-4,000  $\text{cm}^{-1}$ .

When  $\text{Ti}_3\text{C}_2$  is dispersed in just TEOS at room temperature for 4 h and recovered by vacuum filtration before being dried at 60 °C for 16 h (following the same procedure used for the amine-assisted pillaring but without adding DDA), there is no sign of intercalation (Figure 4.9). The SEM image in Figure 4.9a shows the formation of  $\text{SiO}_2$  particles on the MXene outer surface confirming while the EDS (Figure 4.9b) shows some Si content in the sample (1.4 wt.%), this Si is not in the interlayer. This is further confirmed by XRD which shows that the (002) diffraction peak has shifted from  $6.5^\circ 2\theta$  to  $8.5^\circ 2\theta$ , corresponding to a decrease rather than an increase in the interlayer spacing. This confirms that the TEOS does not intercalate without assistance from DDA, and suggests that instead previously intercalated water molecules (which are shown by NMR to be present in  $\text{Ti}_3\text{C}_2$ ) are lost from between the nanosheets.

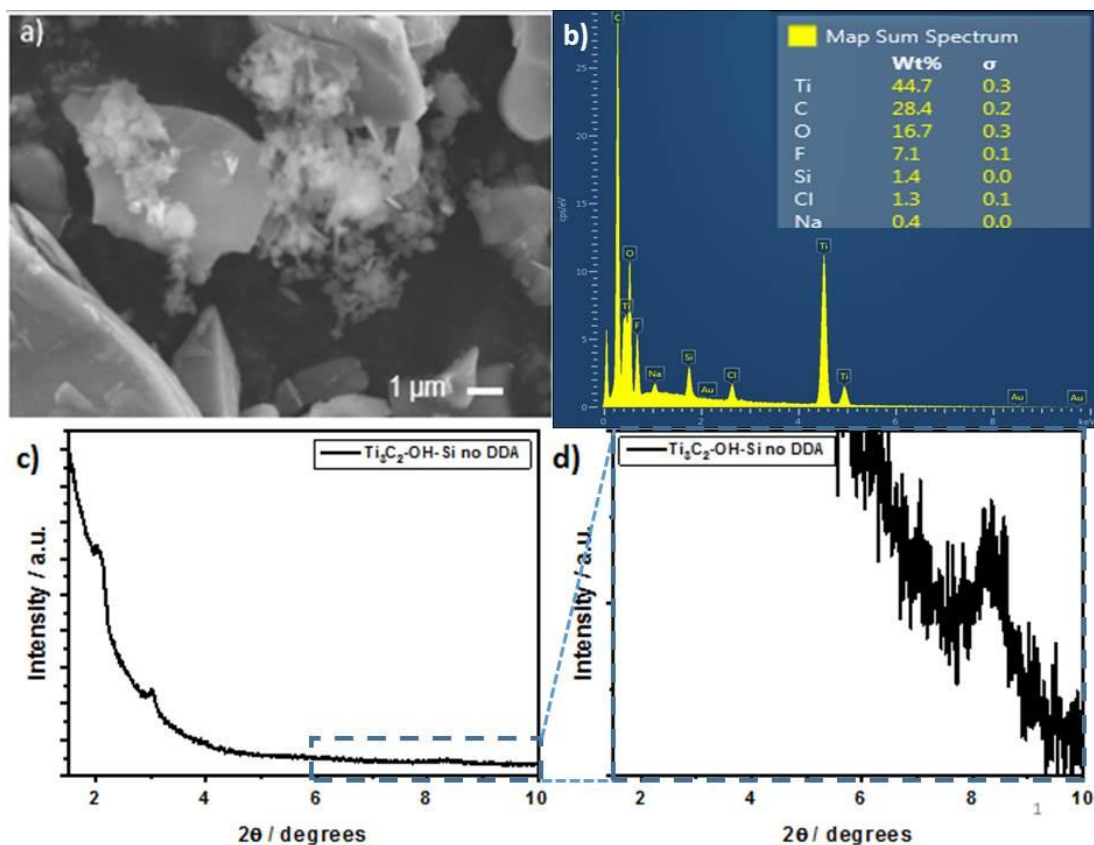


**Figure 4.9.** Analysis of  $\text{Ti}_3\text{C}_2\text{-OH}$  dispersed in TEOS at room temperature for 4 h and recovered by vacuum filtration before being dried at 60 °C. a) SEM image, b) EDS spectrum and c-d) XRD plot of  $\text{Ti}_3\text{C}_2\text{-OH}$  after dispersing in just TEOS. d) Expanded view of the (002) diffraction peak, highlighted by the dashed blue box in c).

After calcination, the (002) diffraction peak broadens and shifts to higher angles, suggesting a shrinkage of the interlayer spacings (Figure 4.10). This, combined with the TGA analysis which shows a continuous loss of mass during increasing temperatures (Figure 4.11), implies that this method can be used to create materials with a range in interlayer spacings. By 500 °C, the (002) diffraction peak is no longer visible, suggesting a loss of the ordered pillared structure. This is likely to be due to the continual removal of the DDA template as the temperature increases.

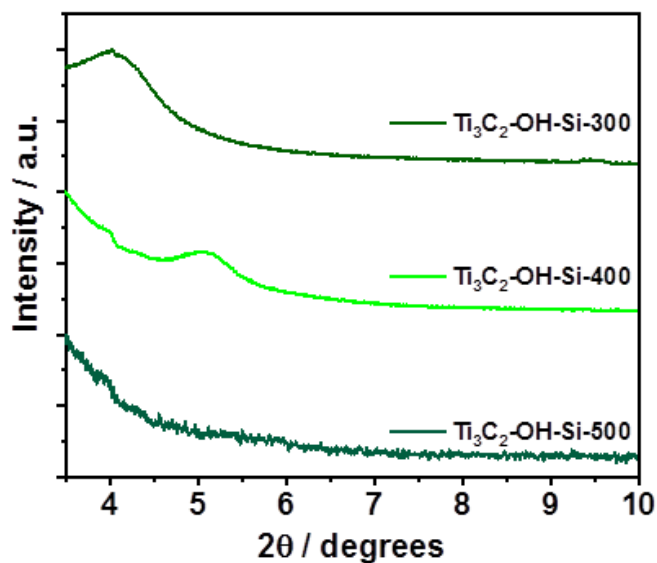


**Figure 4.10.** XRD results showing the shift in the (002) diffraction peak when calcined at 300, 400 and 500 °C.

TGA results of the intercalated  $\text{Ti}_3\text{C}_2$  (Figure 4.11) support the loss of the carbon template, with a constant mass loss through this temperature range. Between 25 and 200 °C, there is a gradual mass loss which is likely to be due to some water content in the sample (the material was not dried directly before placing in the TGA). The small increase in mass between 200-250 °C shows that something from the atmosphere used ( $\text{N}_2$ ) has been taken up by the sample, either as part of a decomposition reaction of the DDA, or via partial oxidation from any  $\text{O}_2$  present in the gas stream (99.99% purity  $\text{N}_2$  was used, but this could still contain traces of  $\text{O}$ ). Between 250 and 550 °C there is a steady loss of mass corresponding to around 30% of the sample's mass. This corresponds to the loss of the intercalated amine template and its decomposition products from the material. The overall mass of template in the sample could be higher than 30%, if the process leading to mass gain is also occurring simultaneously at these temperatures. The DSC curve shows two large peaks at 240 and 310 °C corresponding to transitions in the DDA which were not present in the non-intercalated sample, further confirming that DDA is present in the material.

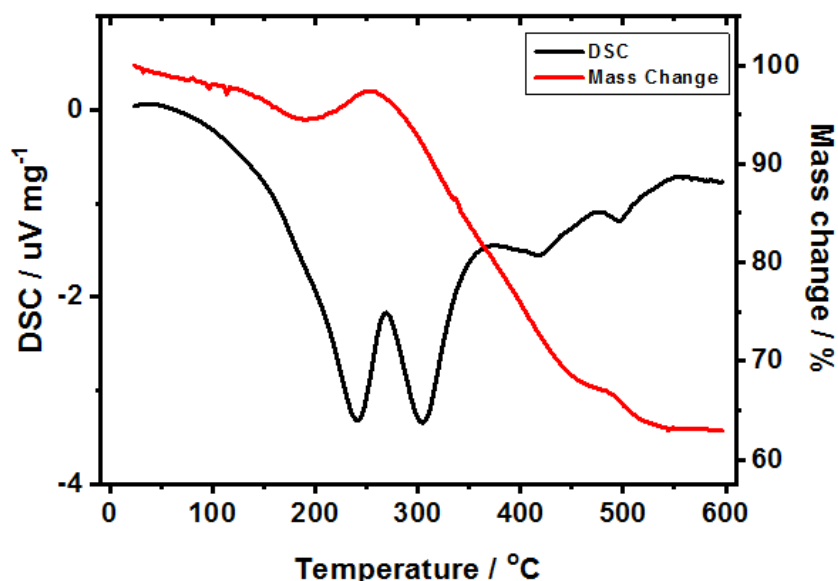


**Figure 4.11.** TGA and DSC plot from the heating of  $\text{Ti}_3\text{C}_2\text{-OH-Si}$  to 600 °C under  $\text{N}_2$ .

In addition, EDS results for the sample calcined at 400 °C (Figure 4.12a) show that the carbon content is decreased after calcination (12.1 wt.% after calcination compared to 33.0 wt.% before calcination), which also has the effect of increasing the relative Si content in the sample (up to 6.3 wt.%). There is uncertainty in the C content measured in the EDS, since the MXene was deposited on carbon tape as a conductive support for measurement. To minimise the contribution to the readings from the carbon tape, measurements were taken on flat sides of thick particles. The decomposition and removal of the amine is also confirmed by the broadening and decrease in intensity of peaks between 1,100-1,700  $\text{cm}^{-1}$  in the Raman spectrum (Section 4.2.1) and the loss of C-H vibrations in the IR spectrum (Figure 4.12b). The IR spectrum also showed that the Si-O vibration had sharpened and increased in intensity compared to the pre-calcination material.

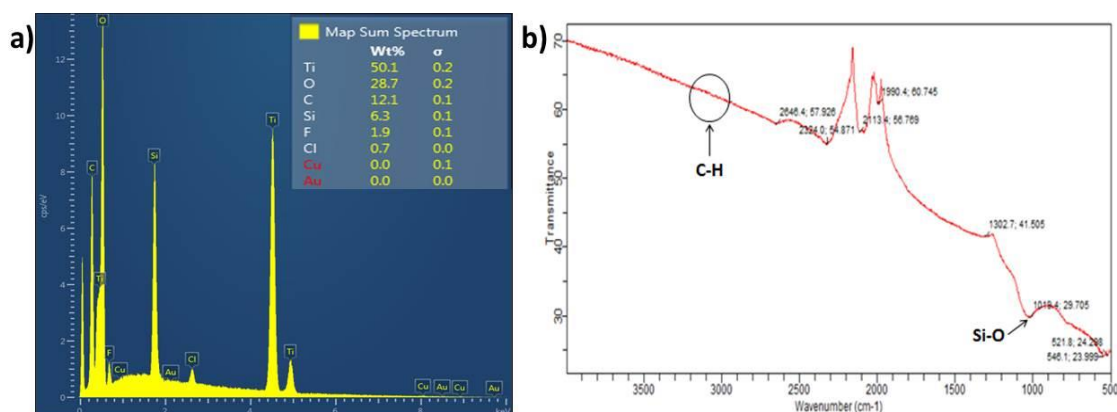


**Figure 4.12.** a) EDS of  $\text{Ti}_3\text{C}_2\text{-OH-Si-400}$ . b) IR spectroscopy results of  $\text{Ti}_3\text{C}_2\text{-OH-Si-400}$  after calcination under argon. The peaks corresponding to the C-H vibrations are no longer visible, supporting the breakdown of the DDA.

TEM-EDS maps (Figure 4.13) confirm the nanoscale layered nature of Ti and Si in the calcined sample ( $\text{Ti}_3\text{C}_2\text{-OH-Si-400}$ ) is retained after the heat treatment, with alternating bands of Ti and Si clearly visible. This matches features seen on EDS maps previously reported for MXene pillaring, offering further support for the Si based pillaring.<sup>149,189</sup> Importantly, this rules out the Si content occurring as a result of the formation of large isolated particles. In addition, STEM measurements of the interlayer distances gives an average  $d$ -spacing of 1.6 nm, which matches well with the XRD results.

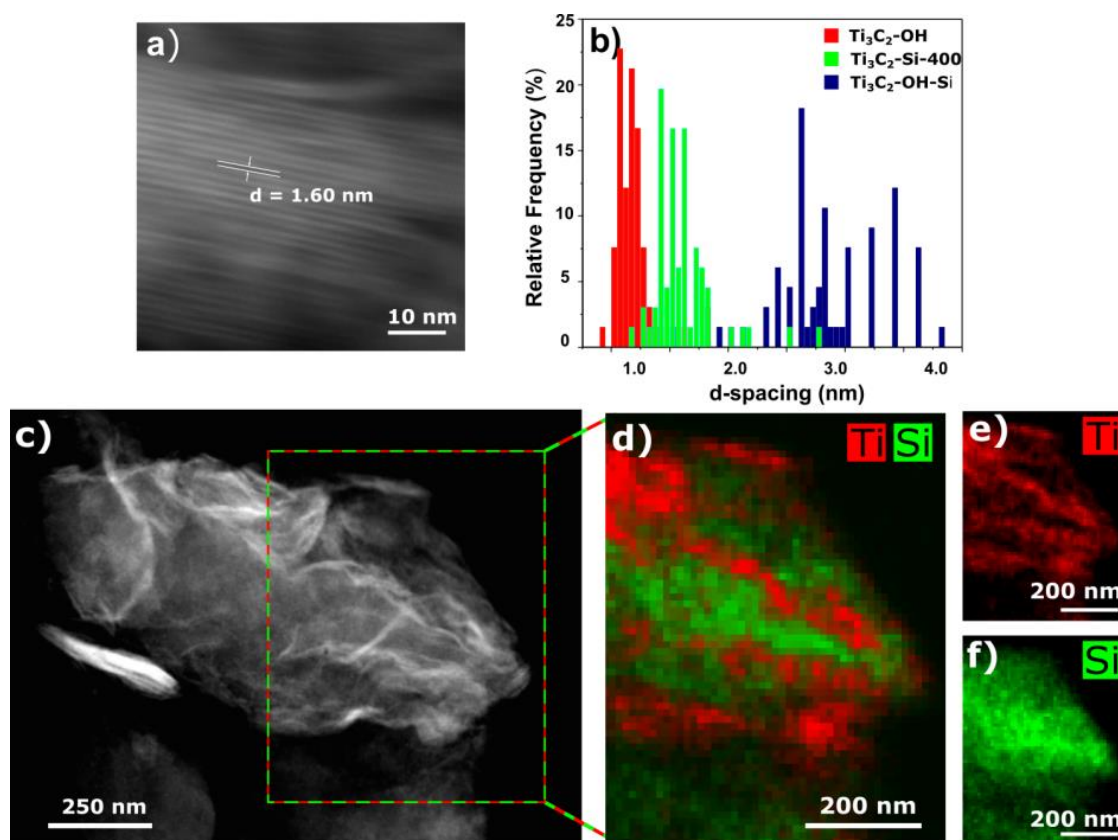


**Figure 4.13.** TEM and EDS studies of the pillared MXene post calcination ( $\text{Ti}_3\text{C}_2\text{-OH-Si-400}$ ). a) STEM cross sectional image of atomic planes of  $\text{Ti}_3\text{C}_2\text{-OH-Si-400}$ , with an example  $d$ -spacing labelled, b) Histogram showing the results of the (002) interlayer distances measured using STEM, c) TEM image of  $\text{Ti}_3\text{C}_2\text{-OH-Si-400}$ , d) overlaid TEM-EDS maps of the Ti and Si content in the area highlighted in c), e) EDS map of Ti content f) EDS map of Si content.

Neither XRD (Figure 4.14) nor Raman (Section 4.2.1, Figure 4.4) results show peaks relating to  $\text{TiO}_2$  content, showing that the MXene was not oxidised during calcination.  $\text{TiO}_2$  anatase and rutile have strong diffraction peaks at 25 and 27° 2 $\theta$  respectively, neither of which are present in this XRD.<sup>229</sup>  $\text{TiO}_2$  also has known strong vibrations at 150  $\text{cm}^{-1}$  which are also not present in Section 4.2.1, Figure 4.4.<sup>230</sup> Therefore, calcination at 400 °C ( $\text{Ti}_3\text{C}_2\text{-OH-Si-400}$ ) was taken as the optimum temperature due to retaining the ordered structure while removing maximum template and used for further characterisation.

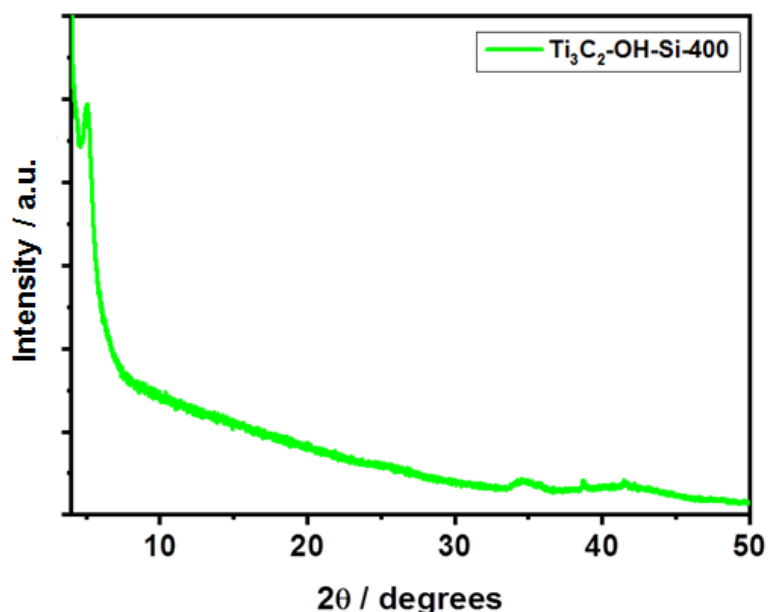


**Figure 4.14.** XRD plot of  $\text{Ti}_3\text{C}_2\text{-OH-Si-400}$  sample between 4 and  $50^\circ$   $2\theta$ .

To study the effect of the pillaring process on the surface area and porosity of the MXene in more detail,  $\text{N}_2$  adsorption-desorption experiments were carried out. BET analysis done on the nitrogen isotherms (Figure 4.15) shows that the non-pillared alkali and acid treated MXenes had very low surface areas of 15 and  $4 \text{ m}^2 \text{ g}^{-1}$  respectively. The lower surface area for the acid treated MXene compared to the alkali treated one (despite the XRD in Section 4.2.1 showing that the acid treated MXene has a larger interlayer spacing) is likely to be due the de-gassing procedure carried out before the gas sorption experiments were carried out, which will have removed most, if not all, of the interlayer water present in the samples. The alkali treated material will have retained the  $\text{Na}^+$  cations which intercalated from the NaOH (as shown by the Raman results, Section 4.2.1), which led to this material having a slightly enlarged interlayer spacing, and therefore surface area. These surface areas are typical for multi-stacked MXenes, and match those previously reported.<sup>124</sup> After the intercalation experiments, there is a large increase in the surface area, from  $4 \text{ m}^2 \text{ g}^{-1}$  after acid treatment to  $235 \text{ m}^2 \text{ g}^{-1}$ , which is almost a 60-fold increase. This is comparable to, and in many cases larger than, that of many pillared graphene-based materials, which have typically reported specific surface areas between 130 and  $330 \text{ m}^2 \text{ g}^{-1}$ , and pillared  $\text{MoS}_2$  ( $186 \text{ m}^2 \text{ g}^{-1}$ ).<sup>179,180,182,226,228</sup> The average pore width determined from Non-Local Density Functional Theory (NL DFT) also increased from 0.82 nm to 3 nm after intercalation, (Figure 4.16), which further confirms the high interlayer spacings seen in the XRD and TEM. This is higher than any surface area for an MXene using an intercalation-based pillaring method found in the literature review and proves the creation of a new porous material. The only comparable surface area for MXene based materials was  $293 \text{ m}^2 \text{ g}^{-1}$ , which was achieved by engineering a 3D structure via freeze-drying and is compared below.<sup>171</sup>

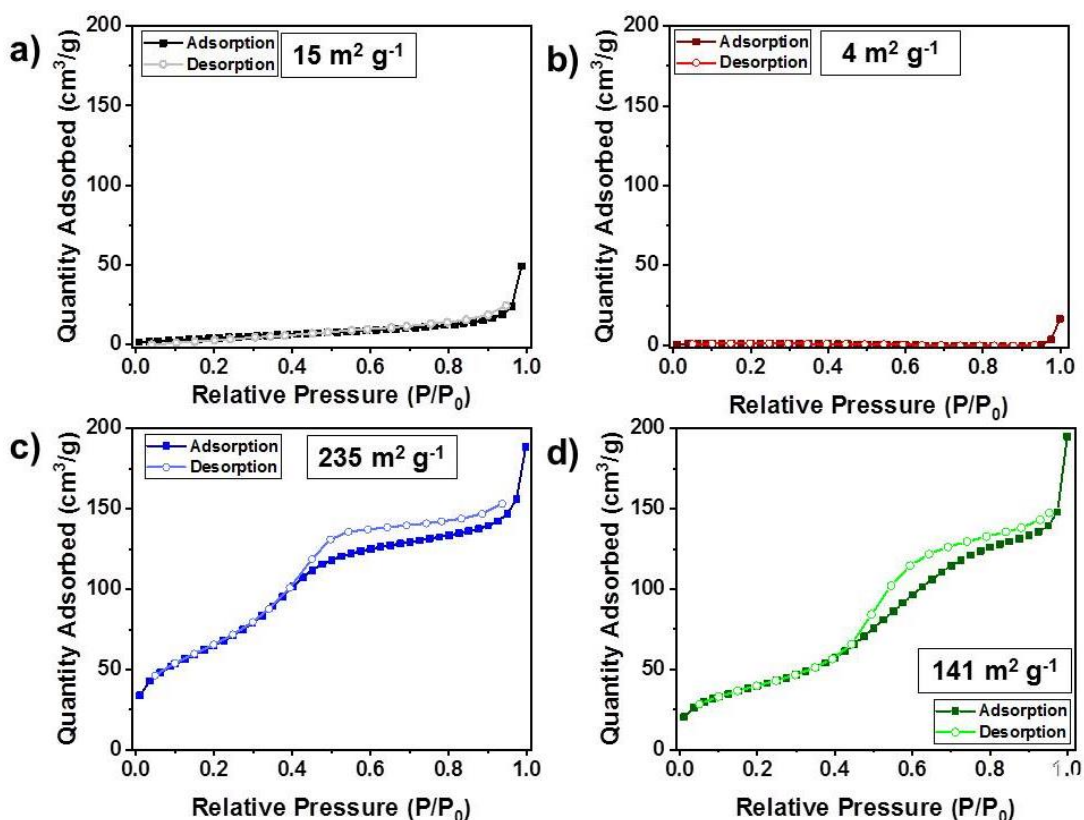


**Figure 4.15.** Adsorption isotherms from  $N_2$  adsorption-desorption experiments. The BET surface area is also given in each panel. a)  $Ti_3C_2-O$ , b)  $Ti_3C_2-OH$ , c)  $Ti_3C_2-OH-Si$ , and d)  $Ti_3C_2-OH-Si-400$ .

The adsorption isotherms (Type IV according to the IUPAC classification guide, suggesting a mesoporous material)<sup>231</sup> match those found in  $N_2$  adsorption studies of freeze-dried MXenes, with a small, but significant, hysteresis observed above 0.5  $P/P_0$  partial pressures.<sup>171</sup> These results confirm successful pillaring, with a subsequent substantial increase in the surface area and interlayer pore sizes. Unlike the report on freeze-dried MXenes, there was only minimal formation of larger mesopores above 10 nm in diameter, suggesting that the increase in surface area is mostly due to the expansion of the interlayer of multistacked  $Ti_3C_2$ , by the incorporation of pillars, and not the delamination and re-stacking of nanosheets. This methodology also leads to a much more uniform pore size than those obtained in the freeze-dried MXene, as can be observed in Figure 4.16. Potentially, 3D structuring methods could be combined with the amine-assisted pillaring approach, and could create even larger surface area MXene materials, with hierarchically ordered architectures.

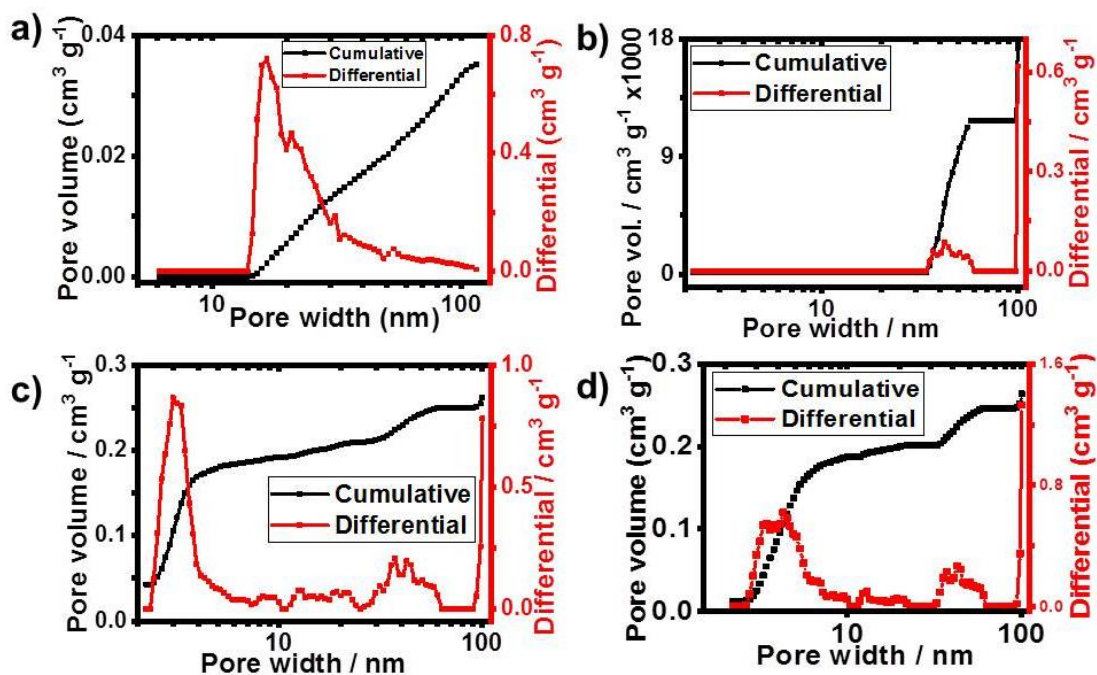


**Figure 4.16.** Pore size distributions derived from the isotherms using the NL DFT method a)  $\text{Ti}_3\text{C}_2\text{-O}$ , b)  $\text{Ti}_3\text{C}_2\text{-OH}$ , c)  $\text{Ti}_3\text{C}_2\text{-OH-Si}$ , and d)  $\text{Ti}_3\text{C}_2\text{-OH-Si-400}$ .

BET surface area measurements on the calcined sample show a decrease in surface area from  $235 \text{ m}^2 \text{ g}^{-1}$  in the pre-calcination material to  $141 \text{ m}^2 \text{ g}^{-1}$  (Figure 4.15), with an average pore width of around 4 nm, with a wider pore size distribution than the one observed before calcination. The increase in average pore distribution is consistent with the XRD results (Section 4.2.2.1), where the (002) diffraction peak broadens after calcination, suggesting a wider range of interlayer distances. The XRD results do not cover the region that would detect a 4 nm pore ( $d$ -spacing  $\sim 5$  nm hence  $2\theta < 1.5^\circ$ ), so cannot study this pore size. The XRD does show a (002) peak at around 1.75 nm  $d$ -spacing, consistent with TEM, which suggests the 4 nm pores may be caused by restacking of the sheets rather than interlayer spacings. Importantly the surface area of the calcined  $\text{Ti}_3\text{C}_2\text{-OH-Si-400}$  material is still  $\sim 30$  times larger than the initial MXene, confirming that post-calcination the MXene maintains its porosity and consists of well-defined pores between the  $\text{Ti}_3\text{C}_2$  nanosheets and the  $\text{SiO}_2$  pillars. The overall decrease in surface area after calcination is likely to be due to the removal of the DDA template, which props the structure up above the level the Si pillars can hold, but it is still substantially increased compared to the initial MXene. This confirms that the post-calcination MXene maintains its porosity and creates a structure with well-defined pores between the  $\text{Ti}_3\text{C}_2$  nanosheets and the  $\text{SiO}_2$  pillars. It is worth noting that the adsorption measurements were carried out 10 months after the pillaring experiments, confirming that the pillars can prevent the nanosheets re-stacking long-term.

Overall these results show the importance of the calcination step in creating a well-ordered strongly bonded pillared MXene with a controllable and well-defined pore size.

#### 4.2.2.2 Effect of Starting Material Ratios

Figure 4.17 shows that the starting ratios of  $\text{Ti}_3\text{C}_2\text{-OH}$ , DDA and TEOS has a significant effect on the pillaring process. Here the same intercalation procedure was followed for each sample, only varying the ratio of the starting materials. When the molar ratio of DDA was lowered to 1:2:20 ( $\text{Ti}_3\text{C}_2\text{:DDA:TEOS}$ ), the XRD shows a broad peak with low intensity between 2 and 3 degrees. However, the intensity was very low, suggesting that the material was very disordered, and that a well-defined porous material was not obtained.

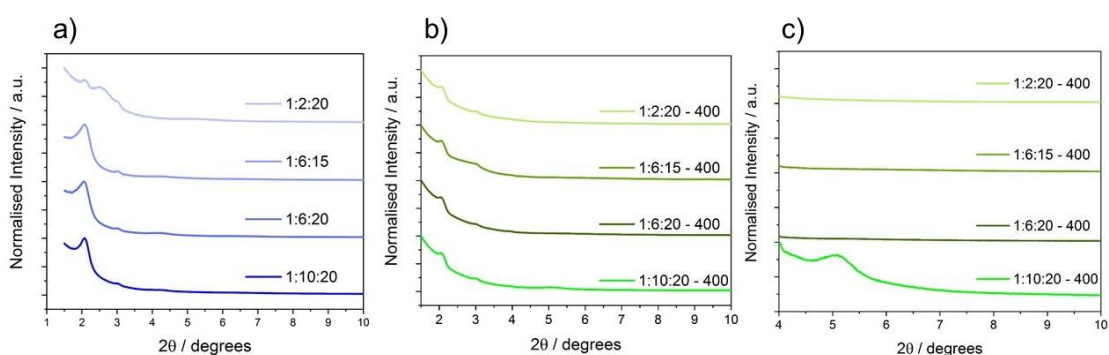


**Figure 4.17.** XRD analysis of the effect of the starting ratios for pillaring. a) TEOS intercalated into  $\text{Ti}_3\text{C}_2\text{-OH}$  with different starting ratios of the reactants used. b and c) The same samples after calcination, with expansion in c).

In contrast, when the used ratios for  $\text{Ti}_3\text{C}_2\text{: DDA: TEOS}$  were 1:6:15, 1:6:20 and 1:10:20, a clear peak at 2.1 degrees was obtained, suggesting successful intercalation and an ordered pillared material. These results highlight the importance of the interaction between the DDA, TEOS and the  $\text{Ti}_3\text{C}_2$ . When insufficient DDA is used, there is not enough amine to bring the TEOS into the interlayer space to form uniform pillars. There appears to be little difference between the three successful ratios at the intercalation stage. However, after calcination at 400 °C, only the 1:10:20 still had a clear XRD peak showing the retention of an ordered layered structure, as shown in Figure 4.17c. This is explained by insufficient DDA to aid the intercalation of the TEOS into the interlayer in the 1:6:20 sample, but enough DDA to prop open the structure itself, until it is subsequently removed in the calcination step. In addition, it is also necessary to have enough TEOS in the starting ratio; when the DDA:TEOS ratio is too high, there is also insufficient TEOS brought in between the layers, as seen in the case of the 1:6:15. Here the DDA still intercalates, giving a large interlayer spacing initially, but this then collapses after calcination when the DDA is

removed and there is also too little Si content to prop the layers up. These results confirm that starting ratio of 1:10:20 was optimum out of those studied.

#### 4.2.2.3 Intercalation Mechanism

The results presented so far indicate that the surface chemistry of the MXene has a significant influence on the pillaring process. The acid-treated MXene ( $\text{Ti}_3\text{C}_2\text{-OH}$ ) successfully intercalates DDA and TEOS, unlike the alkali-treated material ( $\text{Ti}_3\text{C}_2\text{-O}$ ), which strongly suggests that -OH surface groups are actively involved in the pillaring process. Furthermore, Raman spectroscopy (Section 4.2.1), shows that the Ti-OH peak ( $270\text{ cm}^{-1}$ ) has broadened to between  $220\text{ cm}^{-1}$  and  $300\text{ cm}^{-1}$  and lowered significantly in intensity in both the intercalated ( $\text{Ti}_3\text{C}_2\text{-OH-Si}$ ) and calcined ( $\text{Ti}_3\text{C}_2\text{-OH-Si-400}$ ) materials (FWHM increased from 23 to 48 and  $45\text{ cm}^{-1}$  respectively). In addition, there is no change in the vibrations linked to Ti-O ( $205\text{ cm}^{-1}$ ) upon intercalation, supporting the -O functional groups being inactive.

Solid-state nuclear magnetic resonance (NMR) was used to gain further information on the surface functional groups and pillaring species present in the MXene samples (Figure 4.18). Hope et al. had previously used solid-state NMR to study the surface groups of  $\text{Ti}_3\text{C}_2$ , as was discussed in Section 2.4.1.4, and is used to identify the surface groups here.<sup>120</sup> There are three main H environments expected for the protons in the MXene samples (Ti-OH,  $\text{H}_2\text{O}$ , and amine). The  $^1\text{H}$  spectra for the four samples are different (Figure 18a), indicating differences in surface species, water content, and H-bonding. The  $^1\text{H}$  spectrum for  $\text{Ti}_3\text{C}_2\text{-O}$  is dominated by a peak at 4.2 ppm, which can be assigned to water present in the sample. A similar peak is observed in the calcined-pillared sample ( $\text{Ti}_3\text{C}_2\text{-OH-Si-400}$ ), but is absent in the  $^1\text{H}$  spectra for  $\text{Ti}_3\text{C}_2\text{-OH}$  and  $\text{Ti}_3\text{C}_2\text{-OH-Si}$ . The  $^1\text{H}$  spectrum for  $\text{Ti}_3\text{C}_2\text{-OH}$  has broad peaks at 13 and 7 ppm, the former can be assigned to Ti-OH,<sup>120</sup> and is not observed in the  $^1\text{H}$  spectra for the pillared materials, supporting the Raman results (Section 4.2.1). The broad peaks around 7-9 ppm in the samples may correspond to Ti-OH and/or water, with different H-bonding to those discussed above. This suggests that OH surface functional groups are actively involved in the pillaring process. The absence of a peak corresponding to Ti-OH in the alkali-treated sample ( $\text{Ti}_3\text{C}_2\text{-O}$ ) is consistent with the Raman spectra (Section 4.2.1). There are additional peaks between 0-2 ppm, which are as yet unidentified in the literature<sup>120</sup> and are not considered further here. In addition, the  $\text{Ti}_3\text{C}_2\text{-OH-Si}$  sample shows sharp peaks between 1 and 2 ppm corresponding to the DDA, further confirming that this is present in the sample.

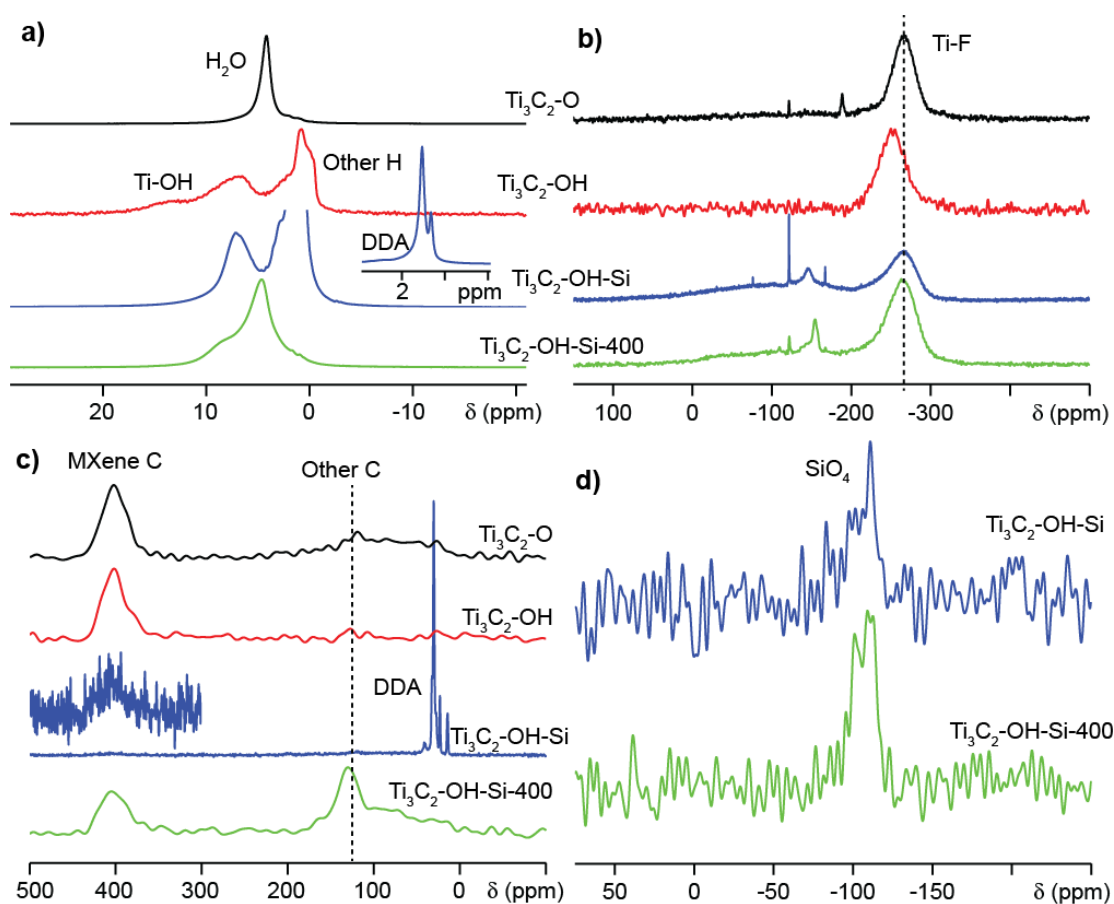


**Figure 4.18.** Solid-state NMR spectra (16.4 T, 29-30 kHz Magic Angle Spinning (MAS)) of  $\text{Ti}_3\text{C}_2\text{-O}$ ,  $\text{Ti}_3\text{C}_2\text{-OH}$ ,  $\text{Ti}_3\text{C}_2\text{-OH-Si}$  and  $\text{Ti}_3\text{C}_2\text{-OH-Si-400}$ . a)  $^1\text{H}$  MAS NMR spectra, where the inset shows the DDA peaks at full intensity, b)  $^{19}\text{F}$  MAS NMR spectra c)  $^{13}\text{C}$  MAS NMR spectra, where the inset in  $\text{Ti}_3\text{C}_2\text{-OH-Si}$  is a magnification of the MXene C peak, and d)  $^{29}\text{Si}$  MAS NMR spectra of the Si containing samples.

After calcination, a peak corresponding to interlayer water appears at 4.7 ppm, which was not present in  $\text{Ti}_3\text{C}_2\text{-OH-Si}$  (pre-calcination). This implies the adsorption of water from the atmosphere occurs between the calcination and the measurement, (the time between calcination and the NMR measurements was around 3 months), since the calcination was done under an argon atmosphere, and the high temperatures would not be compatible with additional water accumulating between the sheets during the calcination process. Both the pre- and post-calcination samples were stored in the same conditions for the same time, which suggests that the DDA repels any atmospheric water encountered during this time. It is possible, due to the hydrophobic nature of the DDA, that during the pillaring process, the DDA repels water molecules as it intercalates between the layers, and any remaining water molecules react with the TEOS to form the  $\text{SiO}_2$  hydrolysis product. Once the hydrolysis reaction is complete, no further water enters the interlayer due to repulsion by the DDA. The use of hydrophobic intercalants to keep the interlayer free of water could be important for applications where water would be harmful to performance. In addition, it could be a useful way of preventing the oxidation of

MXenes over time, since water has been shown to be a key contributor to the oxidation of  $\text{Ti}_3\text{C}_2$ .<sup>232</sup> It is also possible that the  $^1\text{H}$  NMR signal from the amine, which has very high intensity, is masking the signal corresponding to the interlayer water. Importantly, the post-calcination material ( $\text{Ti}_3\text{C}_2\text{-OH-Si-400}$ ) shows that water can re-enter the interlayer after the amine has decomposed, suggesting that the MXene surface has been returned to its original hydrophilic state. The  $^1\text{H}$  NMR results for the calcined sample also show that the DDA has completely decomposed during the heat treatment, since the peaks relating to the DDA are no longer present.

The  $^{19}\text{F}$  NMR spectra (Figure 4.18b) show a main peak centred around -275 ppm for most of the samples, but shifted for the  $\text{Ti}_3\text{C}_2\text{-OH}$  sample, which is assigned to  $-\text{F}$  terminations. There were challenges in spinning the  $\text{Ti}_3\text{C}_2\text{-OH}$  sample, indicating some difference in behaviour of this sample. Generally, the similar shift for the other samples suggests that the  $-\text{F}$  surface groups are inactive with respect to the pillaring process, further emphasising the importance of  $-\text{OH}$  groups and surface chemistry in general for the intercalating and pillaring of MXenes. This also suggests that the amount of Si intercalated may be tuneable by carefully controlling the amounts of  $-\text{F}$ ,  $-\text{O}$  and  $-\text{OH}$  groups. This means that this pillaring method could be used to study the effect of pillar concentration on ion diffusion, and subsequent rate capability of devices, as has been done in amine pillared graphene.<sup>180,228</sup> The  $^{19}\text{F}$  NMR results also show the presence of F containing impurities, likely to be from the etching process, as have been reported in other studies.<sup>120,233</sup> These impurities are likely to be very low in quantity, since they do not show up in the XRD data (Figures 4.2 and 4.14).

The  $^{13}\text{C}$  NMR spectra (Figure 4.18c) shows the C layer in the MXene with a broad peak at 400 ppm present in all samples, which is consistent with the results from Hope et al.<sup>120</sup> The spectrum for the intercalated sample further confirms the presence of DDA in that sample with peaks between 20-50 ppm, matching the other results which indicate this (note that the spectrum for the  $^{13}\text{C}$  NMR for the  $\text{Ti}_3\text{C}_2\text{-OH-Si}$  sample appears noisy due to the high intensity of the DDA signals). After calcination, these peaks are no longer present, which shows that the DDA has completely decomposed, in agreement with the  $^1\text{H}$  NMR results. However, a peak at around 125 ppm can be distinguished from the background C (0-200 ppm). This corresponds to the amorphous graphitic C as observed in the Raman (Section 4.2.1, Figure 4.4) and EDS (Section 4.2.2.1, Figure 4.12), and is the remains of the DDA template that had not been removed during the calcination step. It is possible that this carbon content could help improve the electrical conductivity of the pillared MXene, which is particularly important for high rate electrochemical applications.<sup>234,235</sup>

The  $^{29}\text{Si}$  NMR spectra (Figure 4.18d) show that there are tetrahedral Si environments ( $\text{SiO}_4$ ) in the samples, with a broad peak between -100 and -120 ppm,<sup>211</sup> confirming

the successful DDA-catalysed hydrolysis of TEOS to silica, revealing SiO<sub>2</sub> as the final pillar. There is no noticeable shift resulting from the calcination step, suggesting that this does not alter the Si environment.

Overall, these results suggest the intercalation mechanism relies directly on the Ti-OH termination groups. The -OH groups hydrogen-bond to the N-H groups of the amine (DDA), which intercalates between the MXene layers with the TEOS solvent, thus allowing the pillaring of the MXene with Si-based pillars. Neither the -F or -O are active towards the intercalation and hydrolysis process, which is accompanied by the removal of water molecules from the interlayer. Upon calcination, the hydrocarbon templates are decomposed and largely removed from the pillared MXene, giving a highly conductive and stable porous material.

Other amines also assist the intercalation of TEOS into Ti<sub>3</sub>C<sub>2</sub>, as shown by the XRD of Ti<sub>3</sub>C<sub>2</sub>-OH intercalated with octylamine and TEOS in Figure 4.19, which followed the same procedure as DDA-assisted pillaring. The (002) Ti<sub>3</sub>C<sub>2</sub> diffraction peak shifts to 5.9° 2θ, corresponding to a *d*-spacing of 1.5 nm and a gallery height of 0.55 nm respectively. This gives a different interlayer spacing to using dodecylamine, showing the potential for this technique to give a range of pore sizes. The spacing achieved here is larger than those achieved by cationic surfactant pillaring of molecules of the same chain size.<sup>189</sup> This shows that the orientation of the molecules in the interlayer is very different, with cationic surfactants thought to lay at an angle of around 30 degrees,<sup>189</sup> whereas these amines are clearly more vertically aligned. In fact, DDA in clay pillaring is thought to form bilayers in the interlayer, giving gallery heights of two times that of the chain length.<sup>176,236</sup> This is important for future work on the pillaring of MXenes, since it shows that consideration of the chain size of the pillar alone is not enough, as the interactions between the pillaring molecules and MXene surface groups must be well understood for controlled pillaring.

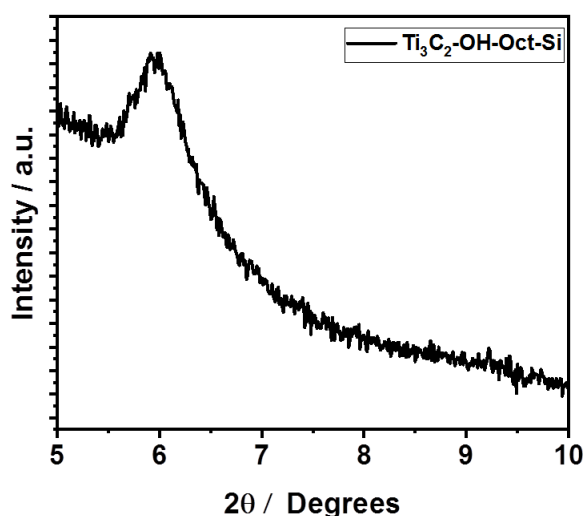


**Figure 4.19.** XRD of Ti<sub>3</sub>C<sub>2</sub>-OH intercalated with octylamine and TEOS.

### 4.2.3 Electrochemical performance

#### 4.2.3.1 Sodium-ion system

To investigate the effect of the pillaring process on the electrochemical performance, the pillared and non-pillared materials were tested against Na as counter and reference electrode in the voltage range of 0.01–3 V for 100 cycles at 20 mA g<sup>-1</sup>. Figure 4.20 (a-b) shows the load curves for the non-pillared and pillared MXene respectively. The pillared material shows a higher capacity on the second cycle (155 mAh g<sup>-1</sup> compared to 132 mAh g<sup>-1</sup> for the non-pillared material) and significantly better cycling stability. By the 100<sup>th</sup> cycle, the pillared material showed a capacity 1.7 times that of the non-pillared material (131 compared to 76 mAh g<sup>-1</sup> for the pillared and non-pillared material respectively). Between the 40<sup>th</sup> and 100<sup>th</sup> cycles, the pillared MXene retains 98.5% of its capacity, whereas the as-made MXene only retains 89%. This highlights the potential for the pillared MXene as a long life electrode for Na-ion batteries and confirms that pillaring is an effective approach to improve the cycling stability. This is particularly important for Na-ion batteries, where the large Na<sup>+</sup> ion has made it difficult to identify electrode materials that can accommodate repeated cycling without significant fading. In addition, the potential low cost of Na-ion batteries has led to grid storage being considered a likely application, which would require very long life batteries to be viable. The pillared material also shows better coulombic efficiency than the non-pillared MXene (after the first cycle). It takes only 14 cycles for Ti<sub>3</sub>C<sub>2</sub>-OH-Si-400 to reach efficiencies greater than 99%, whereas the as-made MXene takes over 40 cycles.

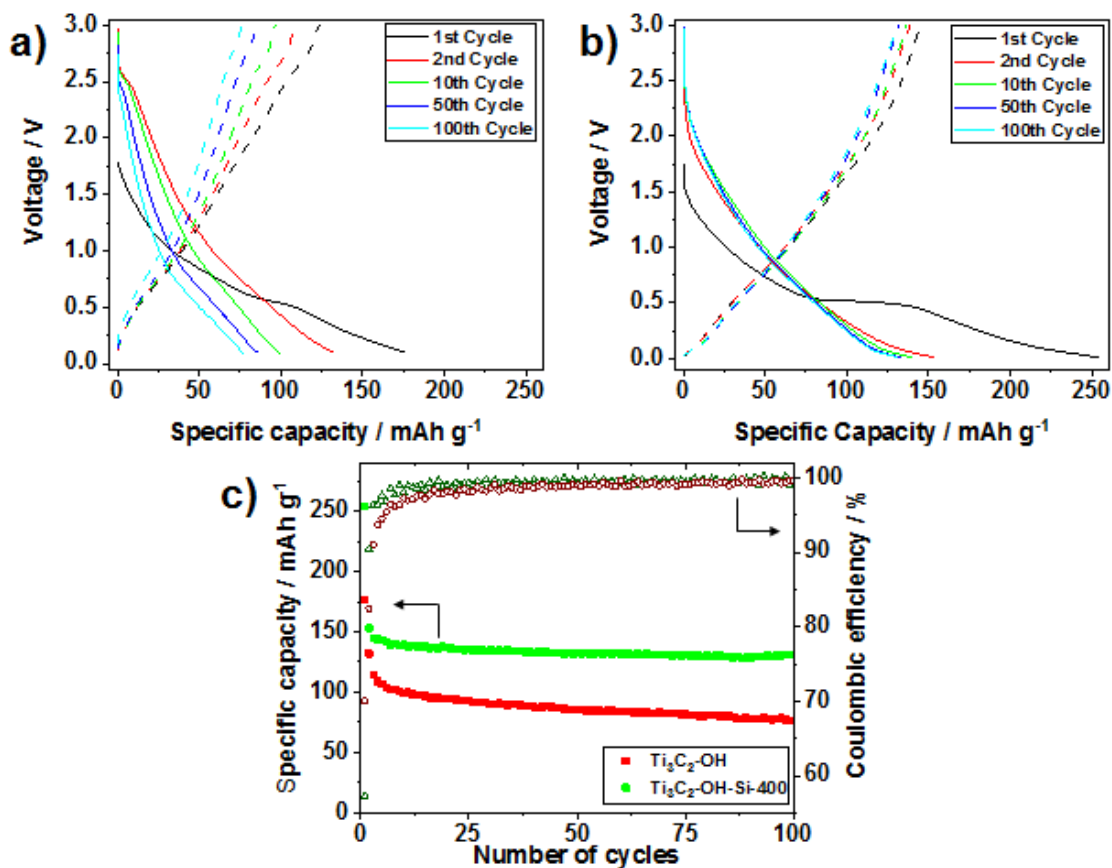


**Figure 4.20.** Galvanostatic data from half-cell tests against Na metal at  $20 \text{ mA g}^{-1}$  in the voltage range 0.01-3 V using 1 M  $\text{NaPF}_6$  in DEC:EC (1:1 wt. ratio) as the electrolyte. a) Load curves for selected cycles for a)  $\text{Ti}_3\text{C}_2\text{-OH}$  and b)  $\text{Ti}_3\text{C}_2\text{-OH-Si-400}$ , c) Coulombic efficiency and discharge capacities of the pillared and non-pillared samples over 100 cycles.

Both materials showed a significantly increased capacity on the first discharge compared to subsequent cycles, which is likely due to SEI (solid-electrolyte interphase) formation and irreversible reactions with the MXene functional groups.<sup>148</sup> This is further supported by the CV data (Figure 4.21), which shows several peaks corresponding to irreversible processes on the first cycle. This is discussed in more detail below. It is important to note that the pillared material reaches a stable capacity from the 2<sup>nd</sup> cycle onwards, whereas the non-pillared one takes around five cycles to stop seeing rapid decreases between cycles (Figure 4.20c).

The significantly higher initial capacity in the pillared MXene may be due to the irreversible reactions of Na or the electrolyte with the MXene surface groups, since more of the MXene surface will be accessible to the Na and electrolyte immediately. That the pillared  $\text{Ti}_3\text{C}_2$  reached stable cycling after just one cycle is consistent with the structure being already expanded, and fully wetted with the electrolyte on the first cycle. On the other hand, fresh surface of the non-pillared MXene could be getting exposed to the electrolyte due to expansion of the structure during the first few cycles. This large initial irreversible capacity led to a low initial coulombic

efficiency for the pillared material compared to the non-pillared one (57% to 70% respectively). Importantly, 40-60% initial coulombic efficiencies are typical for  $\text{Ti}_3\text{C}_2$  and Li and Na systems, so the pillared material is still amongst the highest reported.<sup>237</sup> The improved coulombic efficiency over subsequent cycles in the pillared MXene is likely to be due to the enlarged interlayer spacing allowing for improved ion transport in and out of the structure, thus avoiding the trapping of  $\text{Na}^+$  which is seen in multilayer MXenes.

To study the electrochemical performance in more detail, cyclic voltammetry experiments were conducted. Figure 4.21 shows the cyclic voltammograms at a scan rate of  $0.2 \text{ mV s}^{-1}$  in the voltage range of 0.01-3 V vs.  $\text{Na}^+/\text{Na}$ . The non-pillared MXene shows clear sodiation peaks at 2.1 and 0.3 V on the first cycle, with a small peak at 0.8 V. These have previously been assigned to  $\text{Na}^+$  intercalation, SEI formation and irreversible reactions between the MXene,  $\text{Na}^+$  and/or the electrolyte and do not appear on subsequent cycles. For the pillared MXene, sodiation peaks are observed at 0.8 and 0.3 V, also corresponding to irreversible reactions and SEI formation. No peak is present above 2 V. Over cycles 2-5, the non-pillared MXene displays clear redox peaks at 2.4 / 2.6 V (which has shifted from 2.1 V on the 1<sup>st</sup> cycle) and 0.6 / 0.65 V (sodiation / desodiation). These have previously been assigned as  $\text{Na}^+$  (de)-intercalation peaks, and equivalent peaks for  $\text{Li}^+$  intercalation are also reported.<sup>148,238</sup> There is a noticeable decrease in current across these cycles below 0.6 V, which matches the loss of capacity seen in the load curves (Figure 4.20). For the pillared MXene, no redox peaks are seen above 2 V.

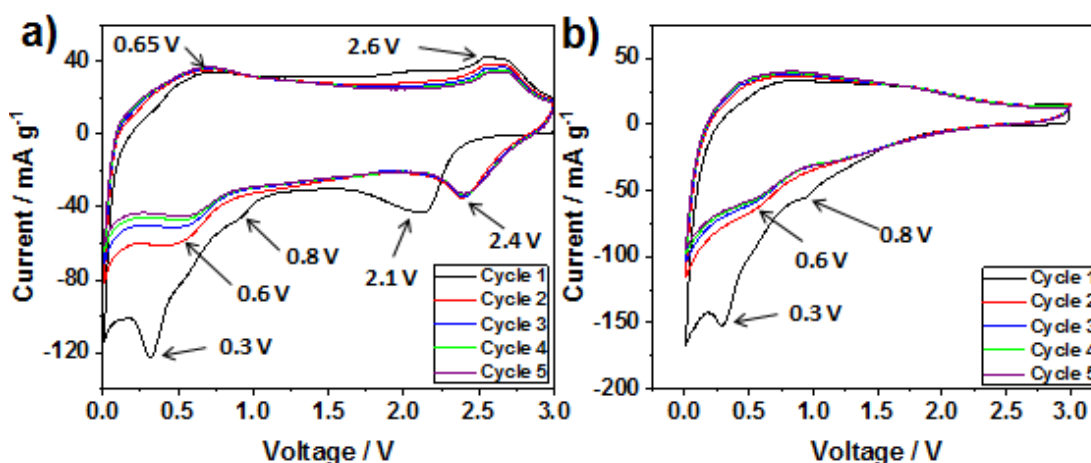


**Figure 4.21.** Cyclic voltammograms at 0.01-3 V vs. Na metal using 1 M  $\text{NaPF}_6$  in DEC:EC (1:1 wt. ratio) as the electrolyte at a scan rate of  $0.2 \text{ mV s}^{-1}$  for the a) non-pillared and b) pillared MXene.

In a report on the mechanism of  $\text{Ti}_3\text{C}_2$  in lithium-ion batteries, Cheng et al. showed that increasing the interlayer spacing of the MXene with  $\text{NH}_4$  also caused the loss of the equivalent high voltage peak, which they linked to intercalation in narrow

interlayer sites.<sup>238</sup> This suggests that the loss of this peak is directly due to the enlarged interlayer spacing present in the pillared material. The lack of high voltage redox peaks contributes to the majority of current being below 1 V in the pillared material, which lowers the average potential of this electrode compared to the non-pillared material. A lower voltage is ideal for negative electrodes when used in a full cell since this maximises the overall cell energy density. This change is also reflected in the load curves (Figures 4.20 a-b) where the pillared MXene has a greater proportion of the capacity occurring under 1 V compared to the non-pillared MXene (which shows a more linear relationship between capacity and current, suggesting a more capacitive-like behaviour). The CV results also support the improved stability and capacity of the pillared MXene (Figure 4.20), with less fade over cycles 2-4 and higher currents than the non-pillared material showed.

Further CV experiments were run at increasing rates from 0.2-5 mV s<sup>-1</sup> to study the kinetics in both systems (Figure 4.22). For the non-pillared material the previously sharp redox peaks shift and broaden, giving a fairly rectangular (capacitive) shape at 5 mV s<sup>-1</sup>, suggesting poor kinetics of the intercalation at high rates. However, the low voltage peak was still clearly visible. The pillared material keeps its shape well at all rates but sees a shift in the 0.6 V peak to 1.5 V by 5 mV s<sup>-1</sup> (shown by the arrow in Figure 4.22b).

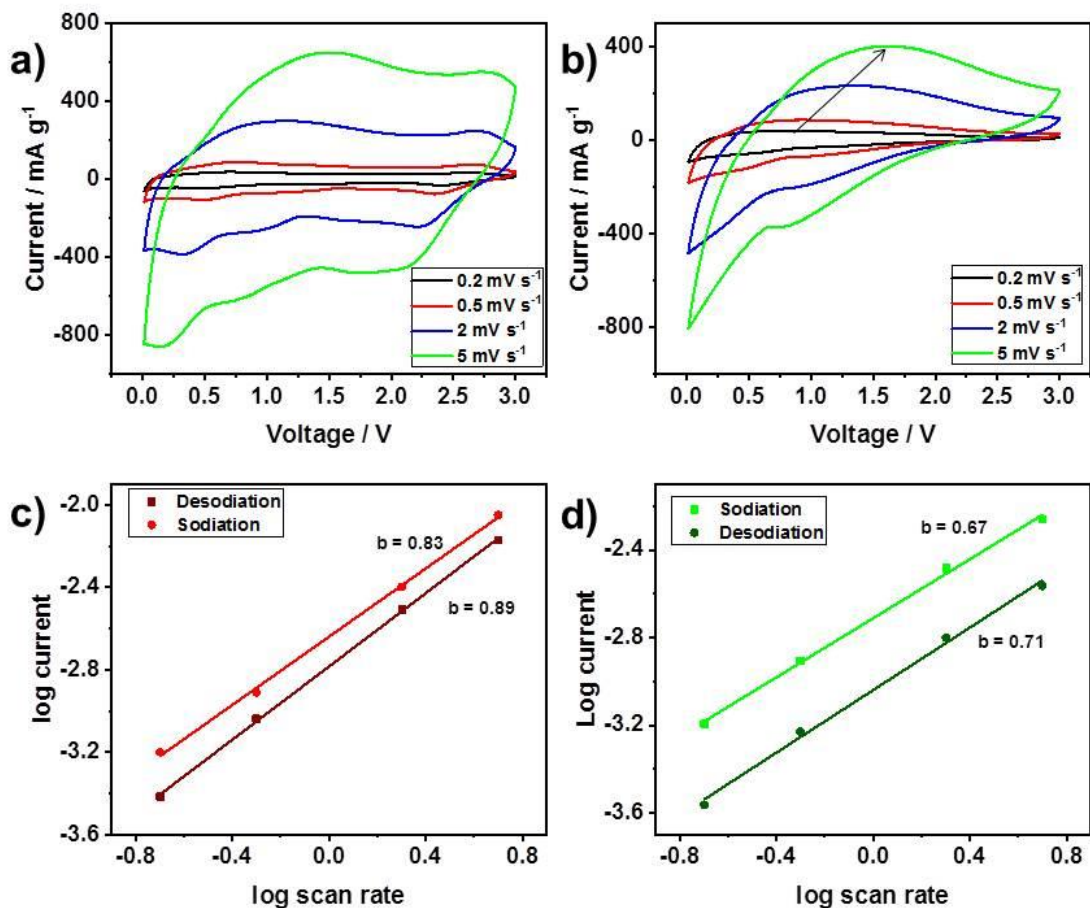


**Figure 4.22.** CV analysis at different scan rates. a) CV plots for  $\text{Ti}_3\text{C}_2\text{-OH}$  at scan rates of 0.2, 0.5, 2 and  $5 \text{ mV s}^{-1}$  in the voltage window 0.01-3 V vs.  $\text{Na}^+ / \text{Na}$ . b) CV plots for  $\text{Ti}_3\text{C}_2\text{-OH-Si-400}$  at scan rates of 0.2, 0.5, 2 and  $5 \text{ mV s}^{-1}$  between 0.01-3 V vs. Na metal. The arrow highlights the shift in the cathodic peak from 0.6 V to 1.5 V as the cycle rate increases. c-d) Log plot showing  $b$ -values for c)  $\text{Ti}_3\text{C}_2\text{-OH}$  and d)  $\text{Ti}_3\text{C}_2\text{-OH-Si-400}$  calculated from the peak currents from the CV plots in a) and b).

As described in Section 3.2.3.13, the relationship between the current ( $i$ ) and scan rate ( $v$ ) is given by Equation 4.1:

$$i = av^b \quad \text{Equation 4.1}$$

where  $a$  and  $b$  are fitting parameters.<sup>239</sup> Importantly, a  $b$ -value of 0.5 corresponds to a diffusion-limited battery-like charge storage process and a  $b$ -value of 1 indicates a capacitive, surface-controlled process. A plot of  $\log(i)$  against  $\log(v)$  gives a straight line with a slope of  $b$ . Following this analysis, the non-pillared material shows a  $b$ -value of 0.83 on the sodiation and 0.89 on desodiation (Figure 4.22). The pillared MXene has  $b$ -values of 0.67 (sodiation) and 0.71 (desodiation). This shows that for both materials charge storage occurs via a combination of mechanisms with contributions from both diffusion-limited and surface-limited processes. The pillared material shows significantly more current from battery-like processes than the non-pillared material, possibly due to increased exposure of redox active sites which

explains the higher capacity seen in this material. Rate capability testing (Figure 4.23) shows that the pillared MXene maintains a superior capacity at all rates tested (current densities of 20, 50, 200, 500, 1,000 mA g<sup>-1</sup>). For example, the pillared material shows capacities of 96 mAh g<sup>-1</sup> at 200 mA g<sup>-1</sup> and 64 mAh g<sup>-1</sup> at 500 mA g<sup>-1</sup>. In comparison, the non-pillared MXene has capacities of just 67 mAh g<sup>-1</sup> at 200 mA g<sup>-1</sup> and 49 mA g<sup>-1</sup> at 500 mA g<sup>-1</sup>. This suggests that the faradic processes are fast, likely owing to easy ion transport within the pillared structure. This implies that the SiO<sub>2</sub> pillars are not impeding the diffusion of Na<sup>+</sup> ions within the electrode structure. Importantly, the capacity recovers to 144 mAh g<sup>-1</sup> when the rate is returned to 20 mA g<sup>-1</sup>, showing that the structure is not damaged by the high cycling rates.

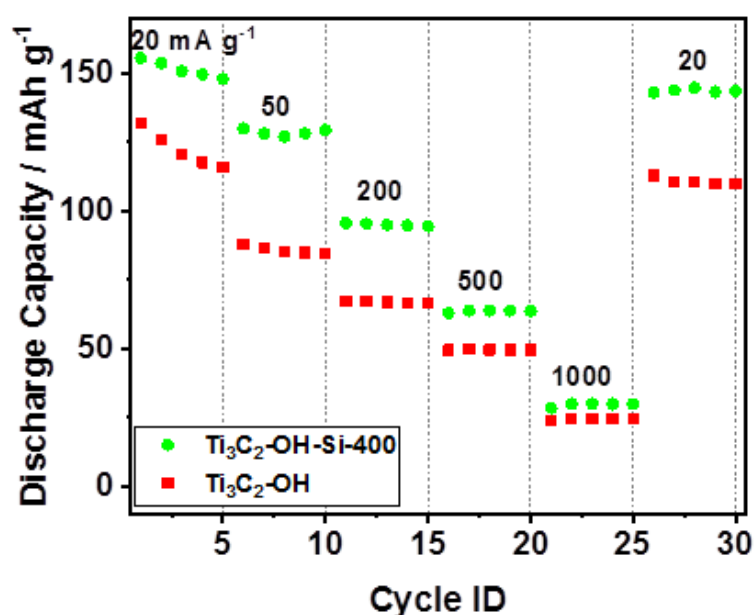


**Figure 4.223.** Rate capability tests for the pillared and non-pillared MXene at rates of 20, 50, 200, 500 and 1,000 mA g<sup>-1</sup>. Five cycles are shown for each rate (one additional initial cycle at 20 mA g<sup>-1</sup> was conducted to ensure SEI formation).

It is possible that the increase in diffusion limited charge storage and change in the CV profiles in the pillared material could be due to redox activity from the SiO<sub>2</sub>. SiO<sub>2</sub> has not been reported previously to be active to Na<sup>+</sup> ion storage, with the literature review only finding reports on Si and SiO<sub>x</sub> (which contain metallic Si) electrodes for Na-ion storage. This could open up SiO<sub>2</sub>, a very cheap and sustainable material, as a potential electrode material for Na-ion batteries, although the capacities are expected to be lower than for Si-based materials in Li-ion systems and other alloying materials such as Sn, S, and P for Na-ion systems.

To further investigate the role of the silica pillars in the sample, ex-situ Si 2p XPS was carried out at OCV, after discharge to 0.01 V and after charge to 3 V (Figure 4.24, with peak fitting data available in the appendix, Table A.2). It can be seen that in each case just one component was required to fit each peak, suggesting just one environment was present in each sample. Significantly, there is no noticeable shift

between the sample at OCV and at 0.01 V (peak for both samples is 102.3 eV), suggesting that the Si is not reduced during sodiation. In addition, no peaks corresponding to metallic Si were detected, which would be an expected product if sodiation of SiO<sub>2</sub> occurs in the same way as lithiation.<sup>240–242</sup> It should be noted that the peaks are slightly shifted to lower binding energies than would be expected for SiO<sub>2</sub>, which potentially could be as a result of Si interacting with electrolyte in the samples if this was not fully removed during drying. Upon charging to 3 V, the Si 2p shifts slightly to 103.8 eV, which is the typical binding energy for O 1s in SiO<sub>2</sub>.<sup>240</sup> An alternative explanation could be that the discharge products of any sodiation of silica could be unstable, and relaxed during the time between the cycling and XPS measurement. Si 2p XPS peaks for Si in sodium silicates can vary in the range of 103–101 eV,<sup>243,244</sup> which would match the OCV and 0.01 V samples here, however, silica would not react spontaneously with Na just by being placed in the electrolyte. Further work would be required to fully investigate any sodiation of silica, but no evidence of such a reaction has been found here, which suggests that the increase in capacity is only due to the increase in interlayer spacing.

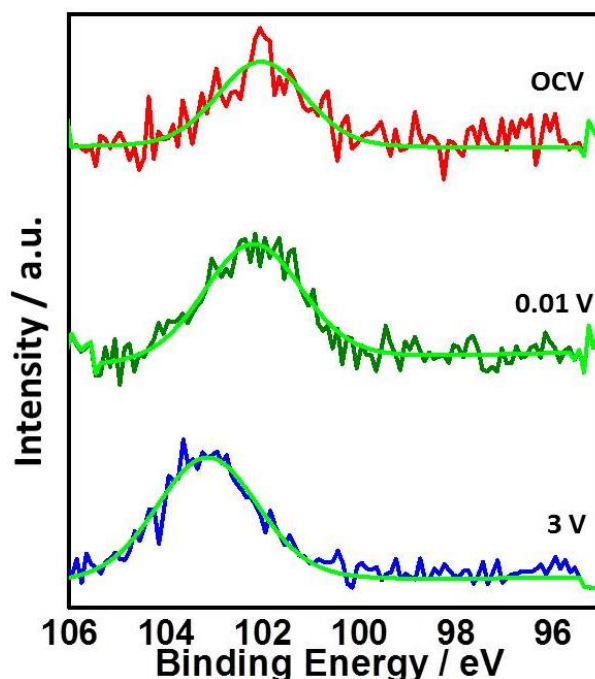


**Figure 4.24.** Ex-situ XPS Si 2p spectra for Ti<sub>3</sub>C<sub>2</sub>-OH-Si-400 at OCV, after discharge to 0.01 V and charging to 3 V. The green line shows the peak fit in each case.

To investigate the effect of the calcination step on the electrochemical performance, half-cell tests were also carried out on the intercalated material, Ti<sub>3</sub>C<sub>2</sub>-OH-Si, with no calcination treatment. The electrodes were cycled at 20 mA g<sup>-1</sup> for 100 cycles between 0.01–3V against Na/ Na<sup>+</sup>. The results are shown in Figure 4.25. The load curves show a similar profile to that seen for the non-pillared and calcined samples, suggesting similar processes in the electrochemical behaviour. There is however a

slight plateau at just over 0.01 V on the discharge on cycles 2 and 10, which is not seen in the other two samples, and is not as distinguishable in the 50<sup>th</sup> and 100<sup>th</sup> cycles. An equivalent feature is not seen on the charging cycles, suggesting this is an irreversible process. The first cycle discharge capacity is higher than either the non-pillared or the calcined samples at 282 mAh g<sup>-1</sup> (this compares to 252 mAh g<sup>-1</sup> for the calcined material and 176 mAh g<sup>-1</sup> for the non-pillared material). This is explained by this sample having the largest surface area and interlayer spacing, which allows the electrolyte to access a large amount of the surface of the electrode. However, only 58 mAh g<sup>-1</sup> is recovered upon the subsequent charge, giving a coulombic efficiency of 21%. This is much lower than what was achieved for the calcined (57%) and non-pillared (70%) materials. This shows that the majority of the first discharge capacity is irreversible, which could result from the formation of an SEI layer on a larger electrode surface. In addition, the interlayer of this electrode still contains a large amount of DDA template, which could block the removal of Na<sup>+</sup> when the cell is charged. The coulombic efficiency of the electrode does increase, over subsequent cycles, but is still low, reaching only 81% after 10 cycles and even after 100 cycles is still only 98%. This suggests the packed interlayer is constantly trapping Na<sup>+</sup> ions, leading to a much lower coulombic efficiency than the other two materials across the 100 cycles.

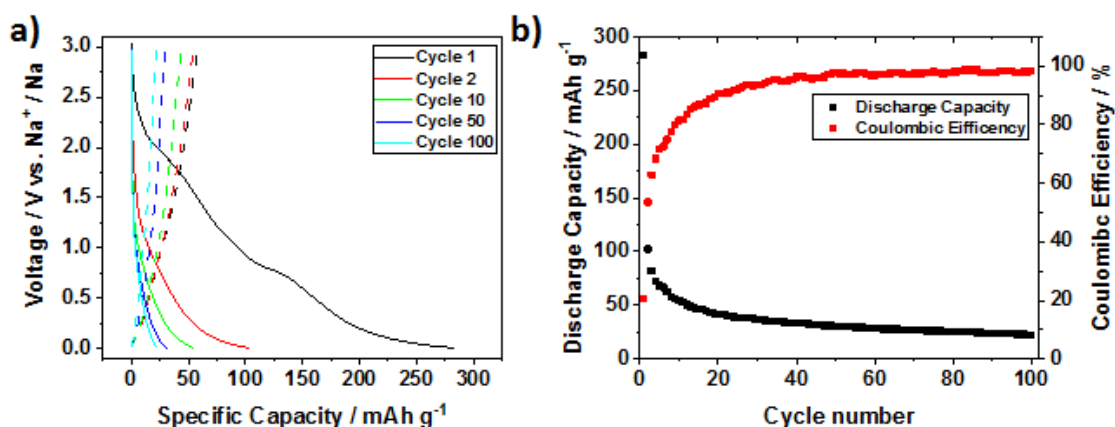


**Figure 4.25.** Galvanostatic charge-discharge tests for the non-calcined pillared MXene, Ti<sub>3</sub>C<sub>2</sub>-OH-Si. The electrodes were cycled at 20 mA g<sup>-1</sup> for 100 cycles between 0.01-3V against Na<sup>+</sup>/Na. a) Load curves for the 1<sup>st</sup>, 2<sup>nd</sup>, 10<sup>th</sup>, 50<sup>th</sup> and 100<sup>th</sup> cycles. b) Discharge capacity and coulombic efficiency over 100 cycles.

Both the load curves and the cycling stability data show that the non-calcined pillared material suffered from severe capacity fade over the 100 cycles. Despite the first cycle capacity being the highest of the three samples, the second cycle has a capacity of just 102 mAh g<sup>-1</sup>, which is lower than the other two samples (155 mAh g<sup>-1</sup> for the calcined material and 132 mAh g<sup>-1</sup> for the non-pillared MXene). This rapid fade continued upon further cycling, so that by the 4<sup>th</sup> cycle a discharge capacity of only 72 mAh g<sup>-1</sup> was returned, lower than the other two materials showed after 100

cycles (the calcined MXene had a discharge capacity of 131 mAh g<sup>-1</sup> and the non-pillared material had a capacity of 76 mAh g<sup>-1</sup> after 100 cycles). By the 100<sup>th</sup> cycle, the non-calcined MXene had a discharge capacity of only 22 mAh g<sup>-1</sup>, which corresponds to a capacity retention between the 2<sup>nd</sup> and 100<sup>th</sup> cycles of just 21%.

The low capacity and large fade for the non-calcined intercalated material can be due to a few factors. Firstly, the DDA is soluble in the organic electrolyte used in the cell, which can easily lead to the removal of the amine from the interlayer, and in the process, this could wash out the SiO<sub>2</sub> pillars, which seem to be smaller than the interlayer achieved via the amine (this is implied in the shrinking interlayer upon calcination and DDA removal in the XRD data, Figure 4.10). This would lead to a collapse of the structure and subsequent restacking of the Ti<sub>3</sub>C<sub>2</sub> nanosheet layers, blocking the active sites for Na<sup>+</sup> storage. Secondly, the low coulombic efficiency shows that many of the Na<sup>+</sup> are being trapped in the material, either by reacting with the DDA, being blocked by the DDA, or trapped by the collapsing structure. These are then not available for further charge storage. Finally, since the DDA template is inactive electrochemically, and makes up at least 45 wt.% of the sample according to the TGA data (Figure 4.11), the specific capacity will be lowered by accounting for the dead weight of the amine in the electrode.

These results highlight the importance of the calcination step in creating a pillared material with open pores for easy ion diffusion and charge storage and which is stable in the cell environment. In particular, these results demonstrate that an electrode with the largest interlayer spacing and surface area will not necessarily show improved electrochemical performance.

Overall, these results show that correctly pillared Ti<sub>3</sub>C<sub>2</sub> MXene is well suited to Na-ion battery applications where low cost, long life and high power are essential.

#### 4.2.3.2 Li-ion System

Since the SiO<sub>2</sub>-pillared Ti<sub>3</sub>C<sub>2</sub> sample showed promising performance for the Na-ion system, it was also tested for the Li-ion system using Li metal as the reference and counter electrode, Cu as the current collector for the MXene and LiPF<sub>6</sub> in EC:DEC (1:1 wt. ratio) as the electrolyte. Galvanostatic charge-discharge testing was carried out at 20 mA g<sup>-1</sup> in a voltage window of 0.01-3 V vs. Li<sup>+</sup> / Li, and the results are shown in Figure 4.26. The shapes of the load curves for the non-pillared and pillared MXenes on discharge are similar, with predominantly linear profiles between 3 and around 0.3 V. Between 0.03 and 0.01 V there is a slightly curved profile feature, showing a different process is occurring at voltages below 0.3 V compared to those above. As discussed in Chapter 2 (Section 2.4.2.1.2), it is thought that the lithiation of Ti<sub>3</sub>C<sub>2</sub> occurs via a two-stage process. The first stage is the intercalation of Li<sup>+</sup> between the Ti<sub>3</sub>C<sub>2</sub> sheets to form Li<sub>2</sub>Ti<sub>3</sub>C<sub>2</sub>T<sub>x</sub>, while the second stage consists of Li<sup>+</sup> adsorption on

top of the intercalated Li layer. This would explain the two-stage mechanism observed on the load curves here. The first discharge displayed a very different shape, with a short plateau around 0.7 V in both samples. This is likely to be a result of the formation of an SEI layer, as well as possible irreversible reactions between Li and the MXene surface group, as has previously been reported. The charge profiles are also fairly linear, but with a small plateau-like feature around 1.5 V, which could correspond to the de-intercalation of Li. This feature is much more prominent in the load curves for the pillared  $\text{Ti}_3\text{C}_2$  than the non-pillared material, where it is barely distinguishable, but does seem to feature a slight deviation from linearity at 1.5 V.

The first discharge capacity of the pillared MXene ( $536 \text{ mAh g}^{-1}$ ) is much larger than the non-pillared material ( $289 \text{ mAh g}^{-1}$ ). However in both cases, as was observed for the Na-ion system, and has been reported several times previously, there is a large irreversible capacity loss on the first cycle. This leads to initial coulombic efficiencies of 58% for pillared  $\text{Ti}_3\text{C}_2\text{-Si-400}$  and only 43% for non-pillared  $\text{Ti}_3\text{C}_2$ . As was discussed in Chapter 2 (Section 2.4.2.1.2), 58% is among the highest initial coulombic efficiencies reported for  $\text{Ti}_3\text{C}_2$  in an organic Li-ion system, and is likely to be a result of surface groups (-OH) having already reacted during the pillaring process, which reduces the irreversible reactions with  $\text{Li}^+$ . In addition, the larger interlayer spacings should provide for clear open delithiation pathways, preventing Li trapping. The second cycle discharge capacities are still significantly larger for the pillared MXene ( $314 \text{ mAh g}^{-1}$ ) compared to the non-pillared material ( $142 \text{ mAh g}^{-1}$ ), which is greater than a 2.2-fold increase. This increase in capacity is likely to be a result of the larger interlayer spacing giving greater ion accessibility to the redox sites on the MXene surface. Since a greater number of layers of Li ions (up to four) have been shown to be stable on  $\text{Ti}_3\text{C}_2$  compared to Na (up to two), the increase in capacity is much greater than was observed for the Na-ion system, which saturates with lower ion coverage and therefore has no further gains from the large interlayer spacing present.

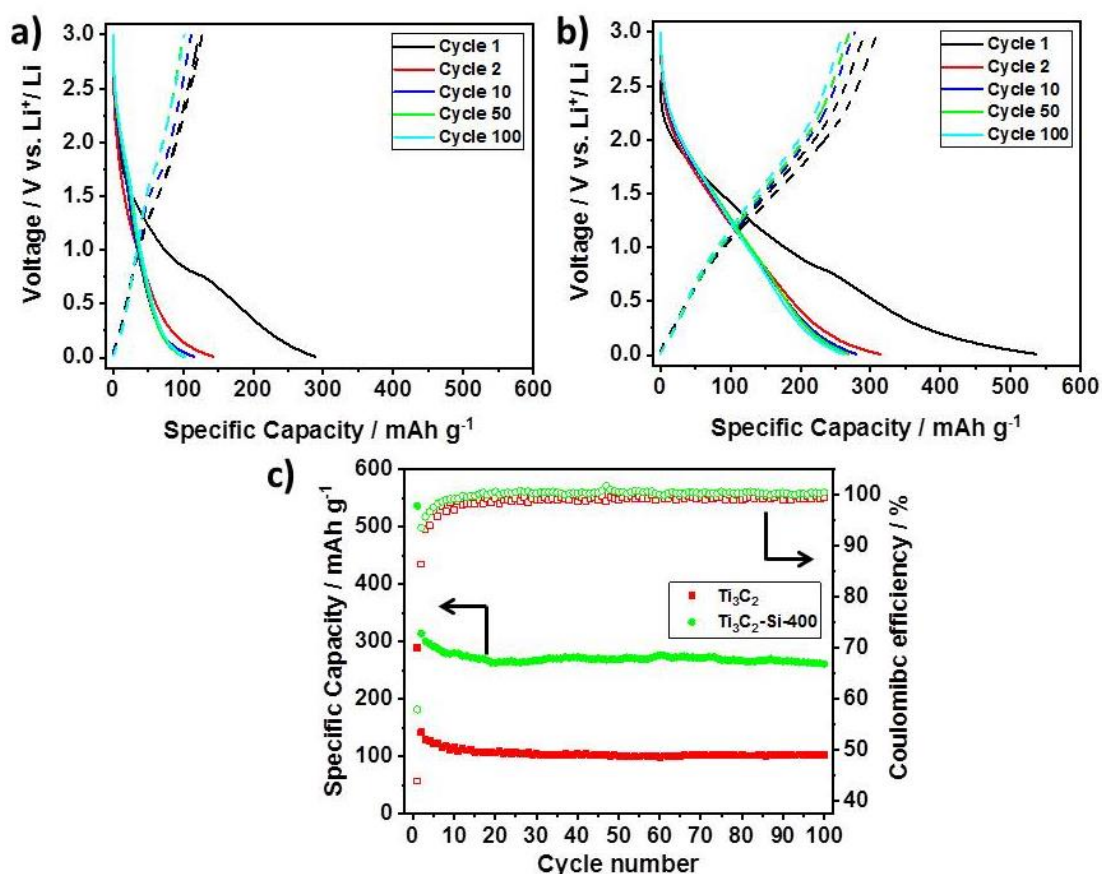


**Figure 4.26.** Galvanostatic data from half-cell tests against Li metal at  $20 \text{ mA g}^{-1}$  in the voltage range 0.01-3 V using 1 M  $\text{LiPF}_6$  in EC:DEC (1:1 wt. ratio) as the electrolyte. a) Load curves for selected cycles for a)  $\text{Ti}_3\text{C}_2\text{-OH}$  and b)  $\text{Ti}_3\text{C}_2\text{-OH-Si-400}$ , c) coulombic efficiency and discharge capacities of the pillared and non-pillared samples over 100 cycles.

The superior capacity and coulombic efficiency of the  $\text{SiO}_2$ -pillared MXene is maintained across all cycles. By the 100<sup>th</sup> cycle, pillared  $\text{Ti}_3\text{C}_2$  shows a discharge capacity of  $262 \text{ mAh g}^{-1}$ , compared to  $101 \text{ mAh g}^{-1}$  for the non-pillared  $\text{Ti}_3\text{C}_2$ . This corresponds to a capacity retention of 83% and 72% respectively, showing that the  $\text{SiO}_2$  pillars succeed in creating an electrode material with increased stability. The majority of the capacity fade occurs over the first 15 cycles, with capacity retentions of 96% and 91% respectively between the 15<sup>th</sup> and 100<sup>th</sup> cycles. It should be noted that the capacity for the  $\text{SiO}_2$ -pillared  $\text{Ti}_3\text{C}_2$  increases slightly between the 30<sup>th</sup> and 40<sup>th</sup> cycles. It has previously been reported that  $\text{SiO}_2$  can undergo activation over early cycles when used as a negative electrode for Li-ion batteries, as a result of formation of metallic Si, which could be occurring here and helping to maintain stable capacities. However, no extra features are distinguishable on the load curves to support this.

To investigate the high rate performance of the pillared MXene, which is essential for Li-ion capacitor applications, rate capability tests were carried out with five cycles at each rate of 20, 50, 200, 500, 1,000 and  $20 \text{ mA g}^{-1}$  (Figure 2.27). At all rates the

pillared MXene shows superior performance compared to the non-pillared material, with discharge capacities of 307, 260, 206, 173, 147 and 285 mAh g<sup>-1</sup> at the respective rate compared to 113, 104, 82, 55, 35 and 109 respectively for the non-pillared Ti<sub>3</sub>C<sub>2</sub>. Significantly, the relative performance of the pillared MXene is larger at higher rates than lower ones. At 1,000 mA g<sup>-1</sup> (which corresponded to an 8 min charge), the capacity of the pillared material is over 4.2 times that of the non-pillared one, compared to just 2.7 times at 20 mA g<sup>-1</sup>. This shows that the high rate performance particularly benefits from the pillaring process, and suggests that the increase in the interlayer spacing creates channels which allows for fast Li<sup>+</sup> ion diffusion in and out of the structure. This also demonstrates that the pillars do not impede the ion transport, which can occur if the concentration of pillars is too high.<sup>180</sup> The capacities of the pillared material at 1 A g<sup>-1</sup> are comparable to high rate lithium negative electrodes such as lithium titanate and niobium oxides (discussed in Section 2.3.1 in the background chapter), while at low rates the capacity is much greater than even the theoretical capacities of the oxides (less than 200 mAh g<sup>-1</sup>), suggesting that this material is competitive as a high power Li-ion battery or capacitor electrode.

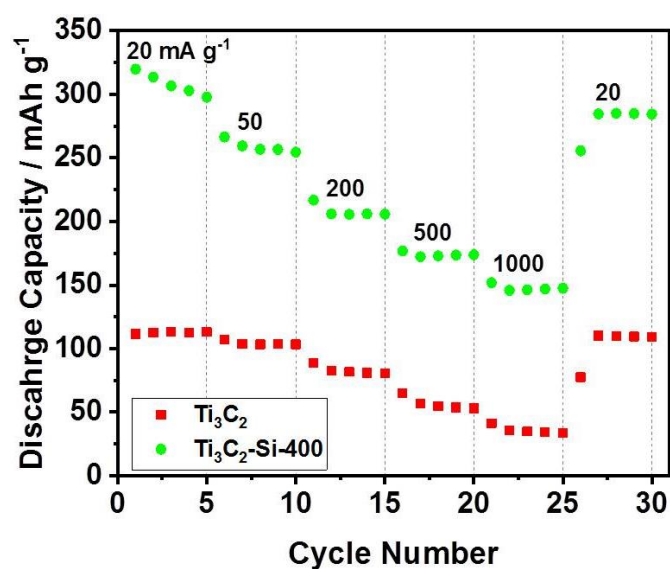


**Figure 2.27.** Rate capability tests for the pillared and non-pillared MXene at rates of 20, 50, 200, 500 and 1,000 mA g<sup>-1</sup>. Five cycles are shown for each rate (one additional initial cycle at 20 mA g<sup>-1</sup> was conducted to ensure SEI formation).

To further test the high rate performance of the SiO<sub>2</sub>-pillared Ti<sub>3</sub>C<sub>2</sub>, it was cycled at a rate of 1 A g<sup>-1</sup> for 500 further cycles after the rate capability test (Figure 4.28). The first cycle upon returning to 1 A g<sup>-1</sup> resulted in a discharge capacity of 151 mAh g<sup>-1</sup>, with the 500<sup>th</sup> cycle showing a capacity of 107 mAh g<sup>-1</sup>, which corresponds to a capacity retention of 71% over 500 cycles, showing that the structure was fairly stable at high rates. The average coulombic efficiency across these cycles was greater than 99.9%, showing efficient Li transport within the pillared structure.

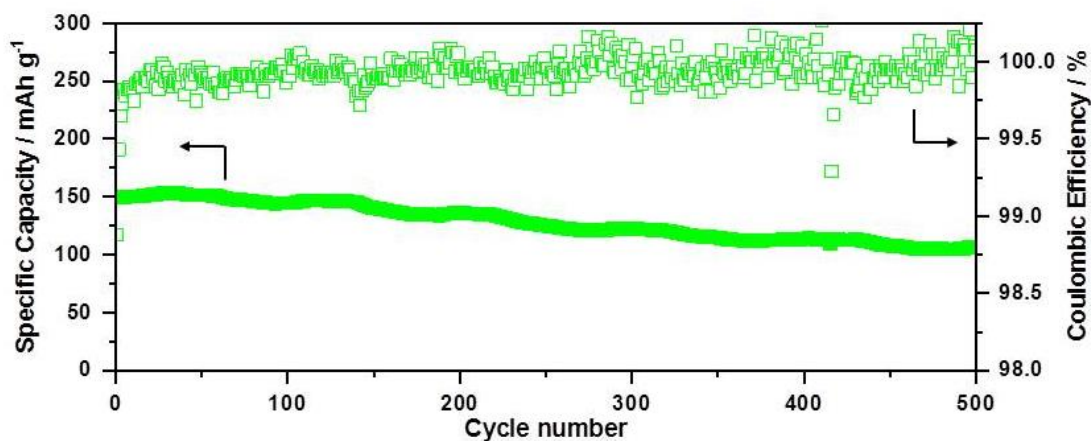


**Figure 4.28.** Galvanostatic charge-discharge data for SiO<sub>2</sub>-pillared Ti<sub>3</sub>C<sub>2</sub> in a Li-ion half-cell tested for 500 cycles at a rate of 1 A g<sup>-1</sup> in a voltage window of 0.01-3 V vs. Li<sup>+</sup>/Li.

These results show that the amine-assisted pillaring method is an effective way of improving the performance of Ti<sub>3</sub>C<sub>2</sub> MXene in a Li-ion system as well as the Na-ion system, especially at high rates.

To study the electrochemical reactions and kinetics of the system in more detail, cyclic voltammetry experiments were carried out on the pillared MXene (Figure 4.29), using the same scan rates as were used for the Na-ion system. Figure 4.29a shows the cyclic voltammograms for the first five cycles at a scan rate of 0.2 mV s<sup>-1</sup>. The first lithiation sweep shows a slightly different shape to the following cycles, with an extra peak at 0.6 V. This is as a result of the irreversible relations including SEI formation as was observed for the Na-ion system, and as has previously been reported. The following cycles are all very similar in shape, showing stable cycling performance which matches the GCD results. The overall shape of the CV curves is fairly rectangular, with broad peaks at around 1.5 V on the lithiation and delithiation sweeps, which matches well with the short plateaus seen on the charging voltage profile. These broad peaks look like they actually consist of two broad peaks each, centred on around 1.2 and 1.7 V on both the charge and discharge sweeps. This suggests predominantly pseudocapacitive behaviour, which is also implied by there being minimal offset between the peaks at lithiation and delithiation. The shape of this curve also closely matches with the shape reported by Cheng et al.,<sup>238</sup> when they had used NH<sub>4</sub><sup>+</sup> to expand the interlayer distance which removed sharper redox peaks that they assigned to narrow interlayer sites. This implies that the pillaring has successfully removed the narrow charge storage sites, as would be expected. It also shows that the electrochemical reactions are very similar to those observed by Cheng et al., which suggests minimal contribution from the SiO<sub>2</sub> pillars.

As the scan rate increases, the peaks shift, and the peak separation on lithiation and delithiation increases to around 500 mV, suggesting that the intercalation is not purely pseudocapacitive. The two contributions to the main broad peaks are now

more easily distinguished, especially on lithiation (Figure 4.29b). To investigate the charge storage mechanism in more detail,  $b$ -value analysis was carried out at selected voltages. At all voltages tested, the charge storage has significant contributions from both diffusion-limited (battery-like) and surface-limited (capacitive-like) processes, since the  $b$ -values are between 0.5 and 1. At low voltages, (below 0.5 V) the charge storage is predominantly diffusion-limited, which could be as a result of battery-like redox processes occurring. Since this peak lines up with voltages which have been reported to correspond to multi-layer adsorption of Li, it is also possible that the diffusion limitation is a result of high lithium content between the layers impeding further Li diffusion. This implies the performance could be further improved by increasing the interlayer spacing even more. At voltages above 0.5 V, (with the exception of at 1 V on the delithiation sweep), the  $b$ -values corresponding to redox peaks are at 0.85 or above, suggesting that the peaks correspond to processes that are predominantly capacitive in nature. The significant proportion of capacitive contributions to the charge storage explains the impressive rate performance observed in this material.

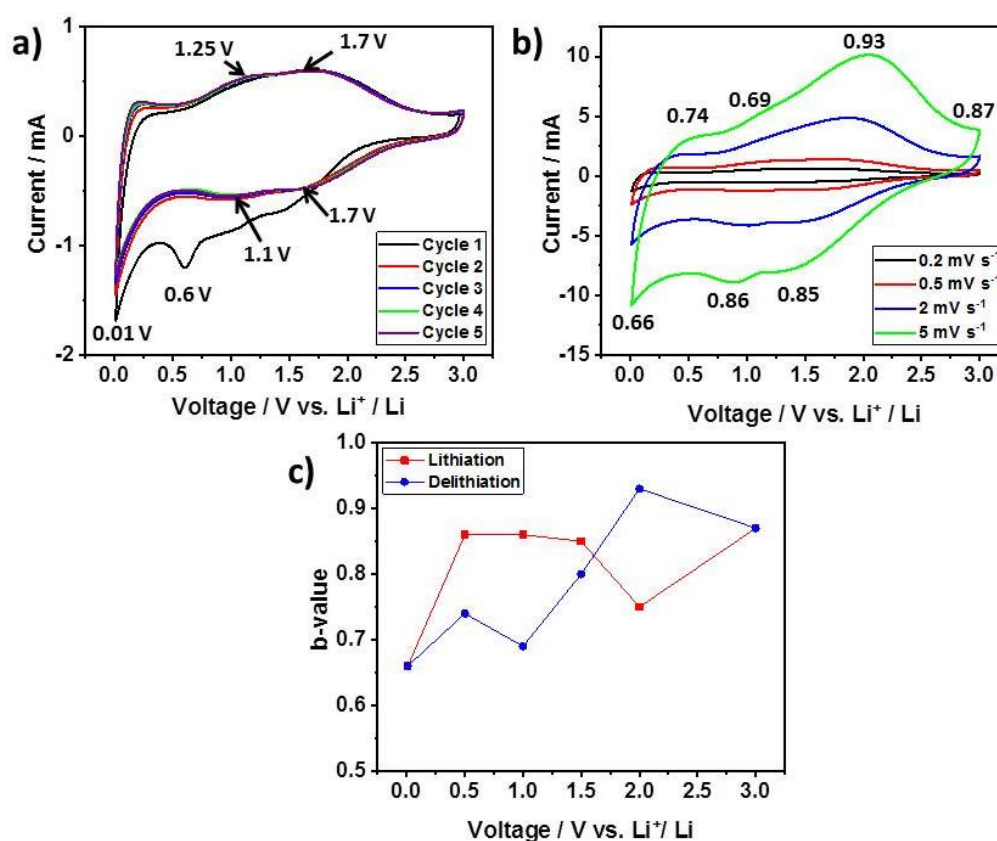


**Figure 4.29.** CV data from  $\text{Ti}_3\text{C}_2\text{-Si-400}$  in the  $\text{Li}$ -ion system. Cells were run in a voltage window of 0.01-3 V vs.  $\text{Li}^+ / \text{Li}$  using 1 M  $\text{LiPF}_6$  in EC:DEC (1:1 wt. ratio) as the electrolyte. a) First five cycles at a scan rate of  $0.2 \text{ mV s}^{-1}$ . The numbers and arrows highlight reaction peaks. b) Cyclic voltammograms when cycled at increasing rates of 0.2, 0.5, 2 and  $5 \text{ mV s}^{-1}$  in a voltage window of 0.01-3 V vs.  $\text{Li}^+ / \text{Li}$ . Two cycles were carried out at each rate, with the second cycle being used for analysis. The numbers show selected  $b$ -values for reaction peaks. c) Calculated  $b$ -values at selected voltages for the data in b).

### 4.3 Conclusions

In conclusion, the successful pillaring of  $\text{Ti}_3\text{C}_2$  with earth-abundant silica-based pillars through an amine-assisted synthesis procedure has been demonstrated. To the best of the author's knowledge, this is the first report of silica-MXene composites. In addition, this was achieved without a pre-pillaring step, in contrast to previous reports of surfactant-assisted pillaring in MXenes (which were discussed in Section 2.5.3). It was shown that the choice of amine co-pillar and calcination temperature could be used to control the interlayer spacing from 0.2 nm to 3.2 nm, the latter of which is larger than a 10-fold increase over the initial distance. This represents the largest interlayer spacing reported to date for any MXene, and one of the largest reported for any two-dimensional material. The pillaring also led to a substantial increase in BET surface areas (around 60 times larger than the non-pillared material), with the intercalated MXene showing a surface area of  $235 \text{ m}^2 \text{ g}^{-1}$ , which is the highest surface area obtained for an MXene using an intercalation-based method. The detailed characterisation of the surface chemistry revealed the pillaring mechanism and provided insight into the interactions between the MXene surface termination groups, the amine co-pillar and the TEOS silica precursor, showing that the  $-\text{O}$  termination groups were inactive in the pillaring process, while the  $-\text{OH}$  groups formed a hydrogen-bonding interaction with the amine groups, enabling the co-intercalation of TEOS and large increases in interlayer spacings. This understanding can guide the optimisation of the surface chemistry for the reported pillaring method. This methodology also provides a guide for the development and understanding of future techniques for the intercalation and pillaring of MXenes, and more widely on 2D materials.

The pillared MXene was tested electrochemically as the negative electrode for a Na-ion battery system, and demonstrated superior capacity, rate capability and stability compared with the non-pillared version. This is likely to result from the more open structure, with the pillars preventing the re-stacking of the MXene sheets. Crucially, for sodium-ion batteries, the material was extremely stable towards the reversible (de)intercalation of the large  $\text{Na}^+$  ion, retaining 98.5% capacity between the 40<sup>th</sup> and 100<sup>th</sup> cycles. Further work is required to fully understand the effect of the pillars on the electrochemical performance, which is discussed in Chapter 7. In a Li-ion system, the pillared MXene also outperformed the non-pillared material, with capacities over 4.2 times those of the non-pillared material at high rates of  $1 \text{ A g}^{-1}$  (8 min charge), which suggests that the pillared material could be worthy of further development for high rate Li-ion applications. CV analysis showed that the charge storage had significant contributions from capacitive surface-controlled processes, which explains the good rate performance.

**Chapter Five**

**SiO<sub>2</sub>-Pillared Mo<sub>2</sub>TiC<sub>2</sub> for Li and Na-ion  
systems**

## 5.1 Introduction

In this chapter the amine-assisted pillaring method developed for the  $\text{Ti}_3\text{C}_2$  MXene is applied to the out-of-plane ordered double transition metal Mo-based MXene  $\text{Mo}_2\text{TiC}_2$ . This MXene is analogous to the  $\text{Ti}_3\text{C}_2$  MXene studied in the previous chapter, with the outer M layers comprised of Mo atoms rather than Ti, which is only found in the central M layer.

This is as a result of the different preferred environment of the different elements within the MAX phase structure. Mo elements have been shown to be unstable in a face centred cubic arrangement with the C atoms, which is the case in  $\text{Mo}_3\text{C}_2$ .<sup>100</sup> Instead, Mo is more stable in a hexagonal environment. Therefore, if Mo exists only on the surface M layers, it can achieve its preferred environment and avoid the face centred cubic arrangement with the C atoms. Ti, which is perfectly stable in the face centred cubic sites, then occupies the central M layer to stabilise the structure, giving rise to the ordered double transition metal MAX phases and the corresponding MXenes.<sup>100,113</sup>

This type of MXene was first predicted to be stable by Anasori et al., who used DFT to screen a variety of possible chemistries to discover stable materials.<sup>100</sup> They found that over 20 different ordered double transition metal MXenes were predicted to be stable, using M elements of Ti, V, Nb, Ta, Cr or Mo. In all cases C was the X element. They then synthesised  $\text{Mo}_2\text{TiC}_2$ ,  $\text{Mo}_2\text{Ti}_2\text{C}_3$  and  $\text{Cr}_2\text{TiC}_2$ . Of these,  $\text{Mo}_2\text{TiC}_2$  is the most studied, though there are only a few reports on this MXene.<sup>100,245–248</sup> The ordered nature of this MXene offers the opportunity to study the effect of changing the surface M elements on the properties and applications of MXenes, since this surface M layer is the only difference between  $\text{Mo}_2\text{TiC}_2$  and  $\text{Ti}_3\text{C}_2$ . The  $\text{Mo}_3\text{C}_2$  is unstable and has not been synthesised, and therefore cannot be used for this comparison. The synthesis of  $\text{Mo}_2\text{C}$  MXene has also been reported in the literature, but from a  $\text{Mo}_2\text{Ga}_2\text{C}$  precursor.<sup>127,249</sup> The high cost of gallium meant that synthesis of this MXene was not studied here.

$\text{Mo}_2\text{TiC}_2$  has been studied for lithium-ion battery applications in both its multilayered and delaminated form, with delaminated  $\text{Mo}_2\text{TiC}_2$  showing a capacity of up to 260  $\text{mAh g}^{-1}$ , retaining 92% after 25 cycles.<sup>100</sup> The performance had several promising features which make it worthy for further investigation. For example, the first cycle capacity loss was only 14%, which is much lower than for other MXenes, making it promising for full cells. In addition, 85% of the total capacity was obtained below 1 V, which would lead to higher energy densities in a full cell. Unlike the fairly linear voltage profile observed for other MXenes, the load curve for  $\text{Mo}_2\text{TiC}_2$  displayed a plateau below 0.6 V, suggesting a phase change and charge storage mechanism clearly different to other MXenes. Computational studies suggested that this plateau

was as a result of a conversion reaction between the lithiated Mo-O surface groups and the Li as shown by Reaction 5.1.



Therefore, the lithiation of  $\text{Mo}_2\text{TiC}_2$  is a two-stage mechanism. In the first stage, Li is intercalated on to the MXene surface, in a similar mechanism to the  $\text{Ti}_3\text{C}_2$  MXene. In the second stage, the lithiated MXene reacts further to form  $\text{Li}_2\text{O}$ , which gives a large boost to capacity. The theoretical capacity of the intercalated MXene is just  $150 \text{ mAh g}^{-1}$ , whereas when the conversion reaction is included this increases to  $356 \text{ mAh g}^{-1}$ . If more than one layer of Li can intercalate, the theoretical capacity could increase further.

The proposed conversion reaction is similar to the lithiation mechanism of Mo oxides, where it is known to be accompanied by large volume changes which cause significant capacity fade.<sup>57</sup> This could explain the relatively high fade seen in the initial  $\text{Mo}_2\text{TiC}_2$  study, where 8% of the capacity was lost over just 25 cycles.

There have been no reports to date on ways to improve the electrode architecture of  $\text{Mo}_2\text{TiC}_2$  for electrochemical applications, despite the clear promise for this material. Therefore, this chapter tests the pillared  $\text{Mo}_2\text{TiC}_2$  MXene materials as electrodes for Li and Na-ion systems, and compares this to the un-pillared material. The pillared material is characterised by XRD, Raman spectroscopy, SEM-EDS, XPS and BET to investigate the effect of the pillaring process on this different MXene. In addition, ex-situ XPS on the Li-ion system was carried out, which supported the formation of  $\text{Li}_2\text{O}$  upon discharge which disappeared upon subsequent charging. This would seem to support the previously proposed mechanism which had not been experimentally probed until now.

## 5.2 Results and Discussion

### 5.2.1 MAX Phase and MXene Synthesis

The  $\text{Mo}_2\text{TiAlC}_2$  MAX phase is not commercially available, and so was synthesised following literature methods.<sup>100,113</sup> Elemental powders of Mo, Ti, Al and C in a 2:1:1.2:2 molar ratio were sieved through a  $38 \mu\text{m}$  sieve (-400 mesh) first mixed in a pestle and mortar, and then mixed in a planetary mixer for 1 h hour with zirconia balls. The recovered powder was heated for 4 h at  $1,600 \text{ }^\circ\text{C}$  under argon, using a heating and cooling rate of  $5 \text{ }^\circ\text{C min}^{-1}$ . The calcined material (light grey) was then gently ground in a pestle and mortar to give a fine powder. XRD results show a diffraction pattern which matches previous reports, showing the successful synthesis of  $\text{Mo}_2\text{TiAlC}_2$  (Figure 5.1).<sup>100</sup>

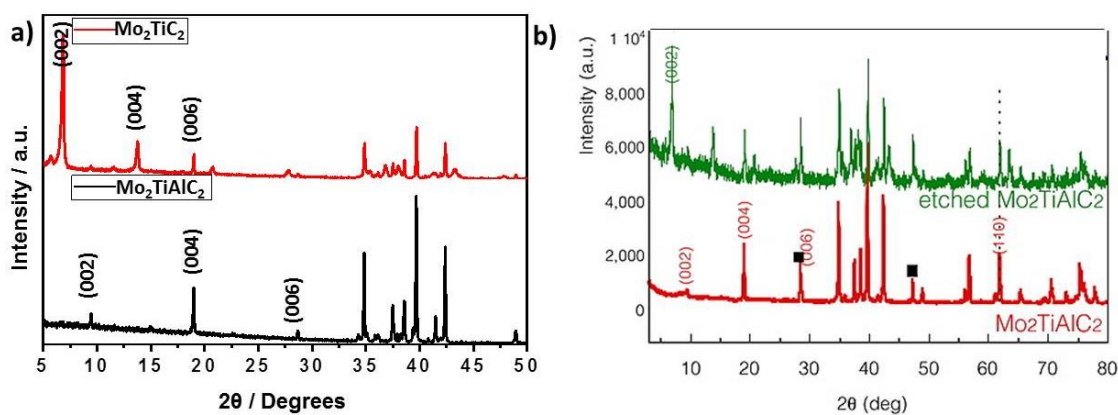


**Figure 5.1.** XRD patterns of  $\text{Mo}_2\text{TiAlC}_2$  MAX phase (bottom) and  $\text{Mo}_2\text{TiC}_2$  MXene (top). a) XRD patterns obtained for this thesis. b) Previously reported XRD patterns reproduced from Anasori et al., <https://pubs.acs.org/doi/10.1021/acsnano.5b03591>, with permission.<sup>100</sup> Further permissions related to the material reproduced should be directed to the ACS.

To avoid the handling of HF, the synthesis of  $\text{Mo}_2\text{TiC}_2$  was attempted using the LiF-HCl method which has been successfully used for the titanium-based MXenes. Typically, 3 g of  $\text{Mo}_2\text{TiAlC}_2$  were slowly added to 30 ml of 9 M HCl with 3 g of LiF pre-dissolved. The mixture was heated to 60 °C and stirred for 5 days. At this point the powder was recovered by centrifuging cycles, with DI water added after each cycle until the pH was around 6. The sample was then analysed by XRD, which showed that significant amounts of unetched MAX phase remained in the sample. Therefore, the partially etched sample was re-dispersed in a fresh etching solution using the same volumes and concentrations used previously. After four more days etching, the solid was collected via centrifuging, using the same protocol as described above. This time, XRD analysis showed minimal MAX phase content, although a small peak at 9.5° 2 $\theta$  clearly corresponds to the (002) diffraction peak of  $\text{Mo}_2\text{TiAlC}_2$  showing that some MAX phase remains. In addition, there are a large number of peaks between 35 and 45° 2 $\theta$  which could easily mask MAX phase reflections, as well as other impurities. Nevertheless, this XRD pattern matches well with those previously reported for  $\text{Mo}_2\text{TiC}_2$ , and shows that the  $\text{Mo}_2\text{TiAlC}_2$  MXene was successfully etched using the described method.<sup>100</sup> Most significantly, the (002) diffraction peak has clearly shifted to a lower angle (around 7° 2 $\theta$ ) which is accompanied by a large increase in intensity. This matches the behaviour typically seen when etching MAX phases to make MXenes, and is a clear sign of successful etching.

Interestingly, leaving the MAX phase to etch for nine consecutive days with no replenishing on the etching solution does not provide a well etched material, even when 12 M HCl is used with 6 g of LiF (the total amount used when the solution is replenished). Only when a two stage etching process was used was a well etched material recovered. The long etching times mean that this etching method is unlikely to be used for large scale  $\text{Mo}_2\text{TiC}_2$  synthesis, but provides an option for lab studies

where users would rather avoid the use of HF solutions. The significantly longer etching times needed when using the HCl-LiF method compared to the HF method (48 h at 55 °C) is a much larger difference than that seen for the Ti-based MXenes, but matches differences reported for the Mo<sub>2</sub>C synthesis, (where HCl-LiF etching was reported to take 1 week).<sup>127</sup> A washing step where the powder was dispersed in 1 M HCl for 3 h at room temperature was used to remove any salt impurities resulting from the etching step. A NaOH washing step was also tried, but this caused the dissolution of the majority of the powder in just half an hour, with a small amount of pale material remaining, showing that the Mo<sub>2</sub>TiC<sub>2</sub> material is not stable in alkali conditions, in contrast to Ti<sub>3</sub>C<sub>2</sub>.

In addition to the XRD analysis, SEM and EDS studies were also carried out to further confirm the formation of Mo<sub>2</sub>TiC<sub>2</sub> MXene. SEM micrographs show that the etched material has a layered morphology typical of an MXene, and some opening up between the layers is also visible (Figure 5.2). The flakes appear to be in the range of 1-10 μm, which is similar to that of other MXenes reported, including for Mo<sub>2</sub>TiC<sub>2</sub>.<sup>100</sup> EDS analysis shows that the MXene-like flakes contain no Al, demonstrating successful etching of the MAX phase (Figure 5.3).

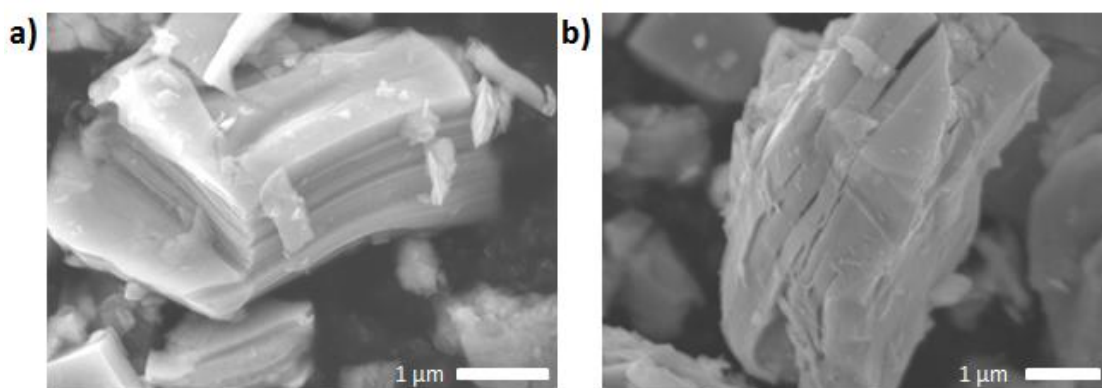


**Figure 5.2.** SEM micrographs of as-synthesised Mo<sub>2</sub>TiC<sub>2</sub> flakes.

Figure 5.3 shows an example EDS spectrum which demonstrates that like the Ti<sub>3</sub>C<sub>2</sub> MXene, Mo<sub>2</sub>TiC<sub>2</sub> is also terminated with –O and / or –OH groups (9.3 wt.%) and –F groups (1.5 wt.%). This is similar to what is observed for HCl-LiF etched titanium-based MXenes, where O-based surface groups make up a much higher proportion of the termination groups than the –F groups. Unlike Ti<sub>3</sub>C<sub>2</sub> etched using HCl mixtures, no Cl content was detected in the EDS, suggesting that any –Cl terminations are present in very low amounts. Overall, the EDS analysis suggests that the MXene has a formula of Mo<sub>2</sub>TiC<sub>2</sub>O<sub>1.75</sub>F<sub>0.25</sub>, which shows that only one in eight terminations are –F groups. Oxygen-based groups account for seven in eight, which will dominate the surface properties of the MXene. Anasori et al. also found via EDS analysis that by far the majority of the surface groups in Mo<sub>2</sub>TiC<sub>2</sub> were –O based terminations when HF etching was used.<sup>100</sup>

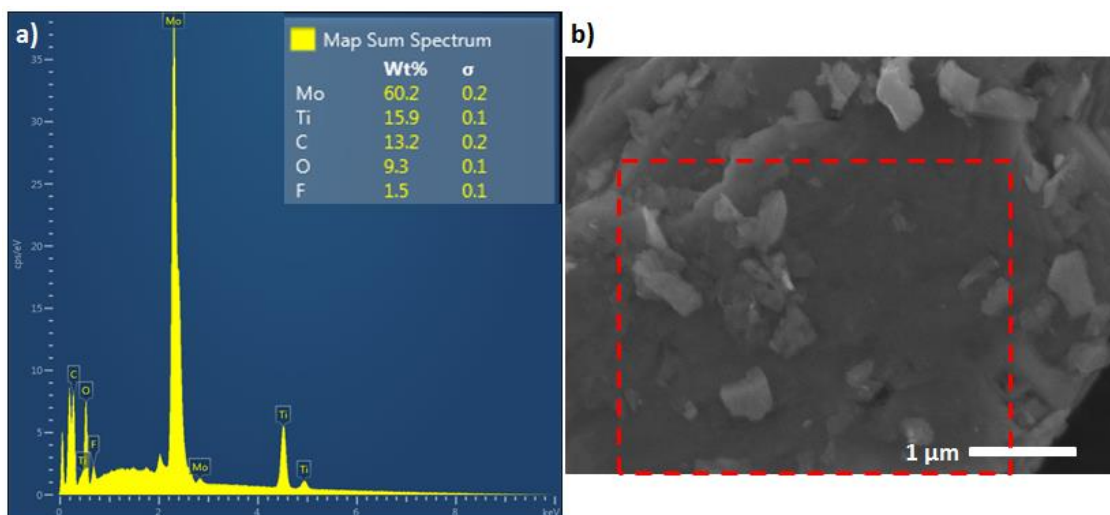


**Figure 5.3.** EDS analysis of as-etched  $\text{Mo}_2\text{TiC}_2$ . a) EDS spectrum of area highlighted in b), which is the corresponding SEM image.

The thermal stability of the MXene was investigated using TGA analysis since this is directly relevant to the pillaring process, and the thermal stability of  $\text{Mo}_2\text{TiC}_2$  had not yet been reported in the literature. Mass change data was collected between 25 and 700  $^{\circ}\text{C}$  in air, with a heating rate of 1  $^{\circ}\text{C min}^{-1}$ . The results are shown in Figure 5.4. It can clearly be seen that the mass changes very little up to around 350  $^{\circ}\text{C}$ , at which point there is a rapid increase in mass. Between 350-400  $^{\circ}\text{C}$ , 2.5 mg is gained by the sample. Between 400 and 600  $^{\circ}\text{C}$  the mass gain plot has a lower gradient, but still sees an increase of 2.5 mg. Between 600 and 700  $^{\circ}\text{C}$ , there is a very rapid increase in the mass gain, with 15 mg extra added to the mass. These results suggest that above 350  $^{\circ}\text{C}$  the MXene undergoes oxidation in a similar way the titanium based MXenes, likely resulting in the formation of Mo and Ti oxides. Unlike for the Ti-based MXenes, no mass loss associated with the loss of oxidised carbon as  $\text{CO}_2$  is seen, which could be due to the ability of Mo to obtain higher oxidation states than Ti through further oxidation. Ti is fully oxidised as titanium dioxide, whereas Mo can form  $\text{MoO}_3$ . Indeed, by 700  $^{\circ}\text{C}$ , the mass change (gain) is still continuing, suggesting that the material is still being oxidised. To fully characterise the thermal stability of  $\text{Mo}_2\text{TiC}_2$ , XRD studies at different temperatures combined with mass spectrometry or IR spectroscopy on the TGA exhaust would be interesting to show the phase changes and behaviour of the surface groups, but is beyond the scope of this study. For the purpose of this study, the TGA results show that the material is unstable in temperatures exceeding 350  $^{\circ}\text{C}$ , so the calcination step used in the pillaring process (400  $^{\circ}\text{C}$ ) described in the previous chapter was done under argon as for the  $\text{Ti}_3\text{C}_2$  MXene.

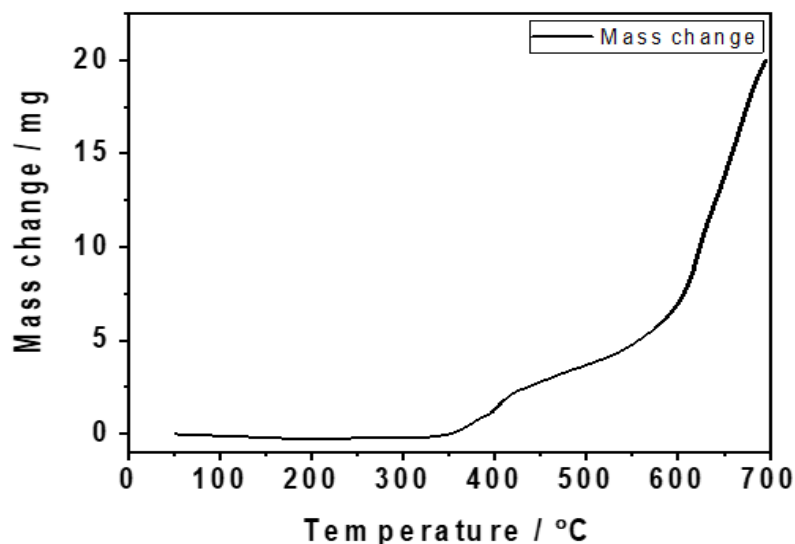
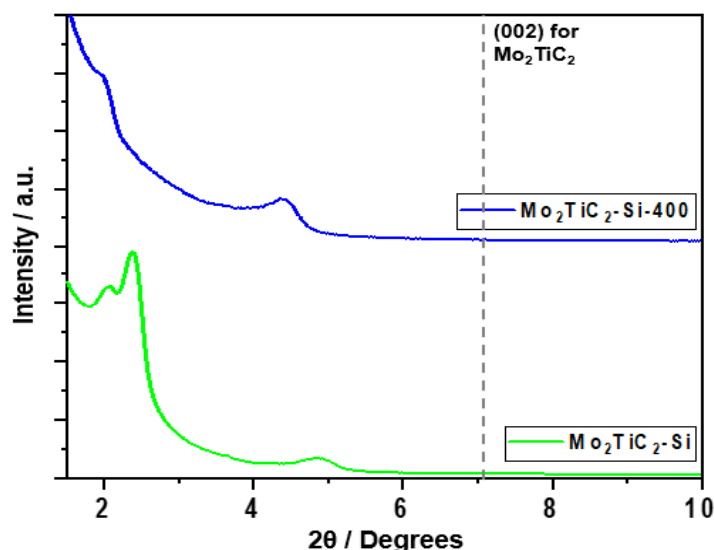


Figure 5.4. TGA plot of mass loss (mg) against temperature.

### 5.2.2 Pillaring of $\text{Mo}_2\text{TiC}_2$

Having characterised the as-synthesised  $\text{Mo}_2\text{TiC}_2$  MXene, the application of the previously discussed amine-assisted pillaring method was then investigated. The procedure was the same as used for the  $\text{Ti}_3\text{C}_2$  MXene. A molar ratio of 1:10:20 of MXene: DDA: TEOS was stirred for 4 h at room temperature under argon. The intercalated material was recovered by vacuum filtration and dried under vacuum on the filter paper (under argon). This was then re-dispersed in DI water for 16 h at room temperature, before being recovered again by vacuum filtration. The recovered material was dried at 60 °C for 24 h. A calcination step under argon was then carried out at 400 °C for 5 h using a heating rate of 5 °C min<sup>-1</sup>.

XRD was carried out on the material for signs of intercalation (Figure 5.5). There is a clear shift in the split (002) diffraction peak to 2.2° 2θ, which is similar to the intercalated  $\text{Ti}_3\text{C}_2$  MXene, showing clear evidence of successful intercalation. This gives a similar *d*-spacing of around 4 nm, corresponding to a gallery height of around 3 nm, very similar to intercalated  $\text{Ti}_3\text{C}_2$ . In addition to the peaks at around 2.2° 2θ, a small diffraction peak at 4.9° 2θ is also visible. This corresponds to a *d*-spacing of 1.8 nm. This could be due to (002) diffraction from layers that have differently aligned DDA/ TEOS between the layers (which would give a gallery height of 0.8-0.9 nm), or it could be the (004) diffraction peak shifted from 14° 2θ in the non-pillared  $\text{Mo}_2\text{TiC}_2$ . Since the *d*-spacing is about half that of the (002) diffraction peak, it fits well with it being assigned as the (004) reflection. In addition, the peak at 4.9° 2θ has not split, unlike the (002) diffraction peak after etching and at 2.2° 2θ. A shift in the (004) diffraction peak after intercalation and delamination with DMSO has previously been reported, which further supports this assignment.



**Figure 5.5.** Low angle XRD diffraction pattern of the intercalated,  $\text{Mo}_2\text{TiC}_2\text{-Si}$ , and calcined,  $\text{Mo}_2\text{TiC}_2\text{-Si-400}$  samples. The dashed grey line highlights the location of the (002) diffraction peak in the non-pillared MXene.

After calcination, the (002) diffraction peak shifts to a higher angle to  $4.5^\circ$   $2\theta$  (Figure 5.6), matching the effect of calcination seen for the calcined  $\text{Ti}_3\text{C}_2$  material (Section 4.2.1). The  $d$ -spacing is around 2 nm, which gives a gallery height of around 1 nm, slightly larger than the corresponding height of the calcined  $\text{SiO}_2$ -pillared  $\text{Ti}_3\text{C}_2$ . The shift suggests that the DDA template is successfully removed, and shows that the layered structure of the MXene is retained after intercalation and calcination at  $400^\circ\text{C}$ , as was the case for  $\text{Ti}_3\text{C}_2$ . This implies that the amine-assisted pillaring method is unaffected by the change in the surface M layer in the MXene, and is directly applicable to Mo-based MXenes. This implies that this pillaring method may in fact be able to be applied to any MXene, so long as  $-\text{OH}$  surface groups are present.

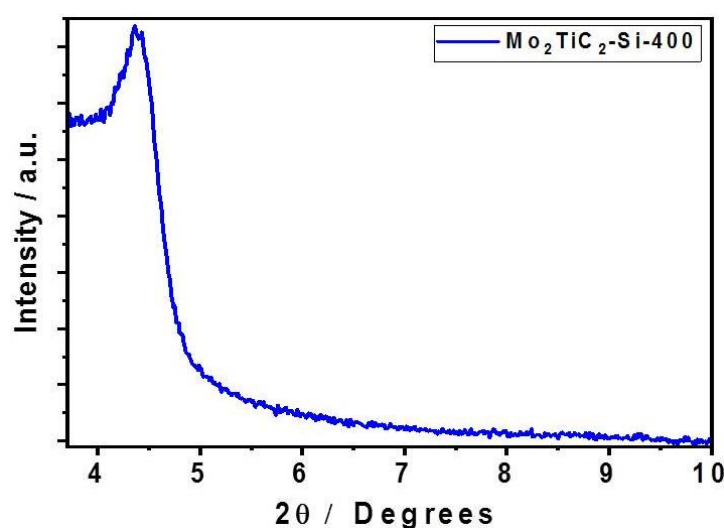


**Figure 5.6.** Low angle XRD pattern showing the (002) diffraction peak in the pillared  $\text{Mo}_2\text{TiC}_2$  after calcination at  $400^\circ\text{C}$ . No other peaks are visible.

SEM and EDS analysis was then carried out to further study the  $\text{Mo}_2\text{TiC}_2$  material intercalated with DDA and TEOS (Figure 5.7). The SEM image (Figure 5.7a) shows that the flakes retain the layered morphology on the micron scale after the intercalation, and there is no sign of  $\text{SiO}_2$  flakes forming outside the interlayer as was observed when the alkali treatment was used on  $\text{Ti}_3\text{C}_2$ . However, the nature of the layers does look slightly different compared to the pre-intercalated MXene. In fact, the images look similar to what is seen when MXenes are delaminated, and then restack. When centrifuging the as-made  $\text{Mo}_2\text{TiC}_2$  samples, it was noticed that some material stayed in suspension even after 30 min at 13,000 rpm, especially after a short sonication step, which implies the delamination of  $\text{Mo}_2\text{TiC}_2$  into few-layered nanosheets. This is much easier delamination than was achieved for the  $\text{Ti}_3\text{C}_2$  MXene. Therefore, it is possible that the  $\text{Mo}_2\text{TiC}_2$  delaminates during the intercalation process (where the interlayer is significantly enlarged) as a result of the stirring motion combined with the expanded interlayer, which can be expected to weaken the interlayer bonding. Upon vacuum filtration, these sheets then restack slightly, separated by the  $\text{SiO}_2$  pillars.

EDS mapping was then carried out to investigate the elemental composition of the flakes, and the distribution of the Si content throughout the flakes. A typical spectrum and map are shown in Figure 5.7. The carbon content has noticeably increased from 13.2 wt.% in the as-made material to 34.4 wt.% in the intercalated material (note that this is not reliable for an absolute measurement due to the sample being prepared on a carbon tape), which implies the intercalation of the DDA. Additionally, there is now significant Si content, with 3.1 wt.% being detected, which confirms the increase in interlayer spacing is correlated with the introduction of Si into the sample, implying successful  $\text{SiO}_2$  intercalation and pillaring. There is also an increase in oxygen content (9.3 to 10.7 wt.%, despite the large increase in C content), which further supports the  $\text{SiO}_2$  intercalation. Figure 5.7 c and d show an SEM image of the top of a flake, and the corresponding EDS map respectively. This shows that the Si is evenly dispersed throughout the sample, as would be expected for a pillared material. There is no sign of  $\text{SiO}_2$  particles on the surface of the MXene flake, or from the Si EDS map, suggesting that the Si content is coming from intercalated Si.

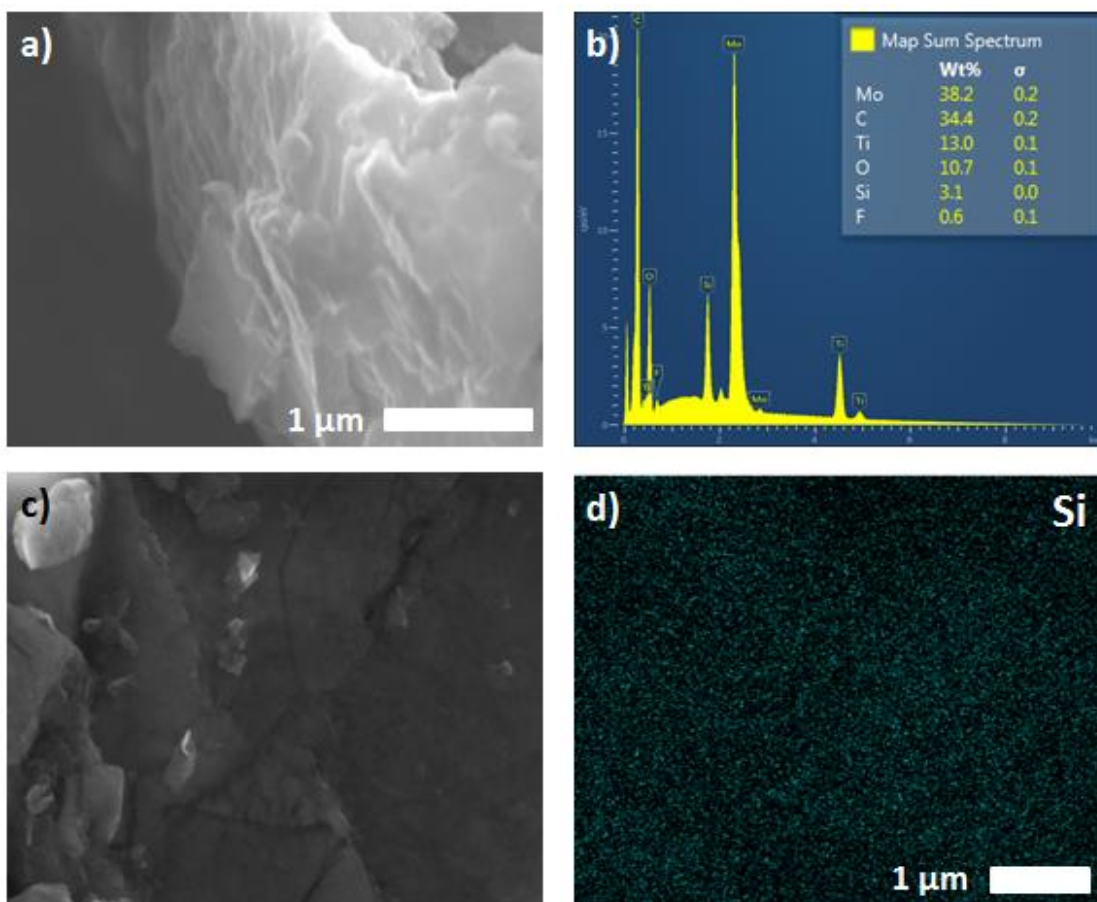


**Figure 5.7.** SEM-EDS studies of the Si intercalated  $\text{Mo}_2\text{TiC}_2$  MXene. a) SEM micrograph showing the layers on the side of a typical intercalated flake. b) EDS spectrum of intercalated  $\text{Mo}_2\text{TiC}_2$  flake. c) The corresponding SEM image for the EDS spectrum in b) and the map in d). The analysis was carried out over the entire area in the image. d) EDS map showing the distribution of the Si content in the  $\text{Mo}_2\text{TiC}_2$  material intercalated with DDA and TEOS.

After calcination at 400 °C under argon, SEM images (Figure 5.8) show that the layered morphology is still retained, which supports the XRD results (Figure 5.6). The flakes still look slightly different to the pre-pillared material, which could be due to the proposed delamination of the nanosheets during intercalation. A higher magnification micrograph (Figure 5.8b) shows what appear to be separated nanosheets stacked on top of each other, which make up the larger flakes. The morphology of the calcined material looks very similar to the intercalated material, showing that the flakes are not damaged by the calcination step. Importantly, there is no sign of  $\text{SiO}_2$  crystals on the surface of the flakes, suggesting that the Si content observed in the SEM-EDS analysis (Figures 5.7 and 5.9) is in between the layers, not on the surface of the MXene.

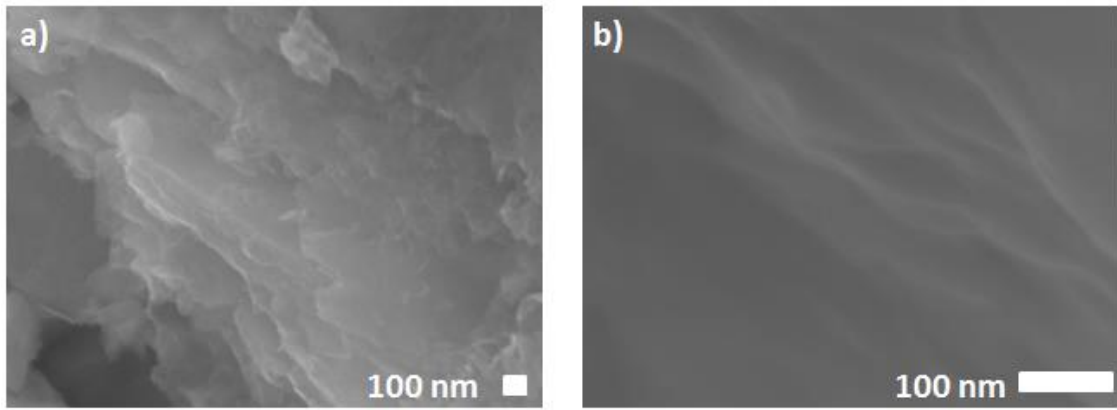


**Figure 5.8.** SEM micrographs of the SiO<sub>2</sub> pillared Mo<sub>2</sub>TiC<sub>2</sub> MXene after calcination at 400 °C for 5 h under argon.

SEM-EDS mapping was then carried out to study the Si content in the calcined sample (Figure 5.9). It can be seen that the Si content (around 3.2 wt.%) is uniformly distributed across the flake, suggesting that the calcination process has not resulted in large SiO<sub>2</sub> particles agglomerating. There does appear to be a slight increase in the concentration of the Si content where the layers are most open (Figure 5.9c), while the Ti signal is slightly weaker in this region. This would support SiO<sub>2</sub> forming in the interlayer spacing of the MXene, as suggested by the XRD results (Figure 5.6) and as seen for the pillared Ti<sub>3</sub>C<sub>2</sub> MXene in the Chapter 4.

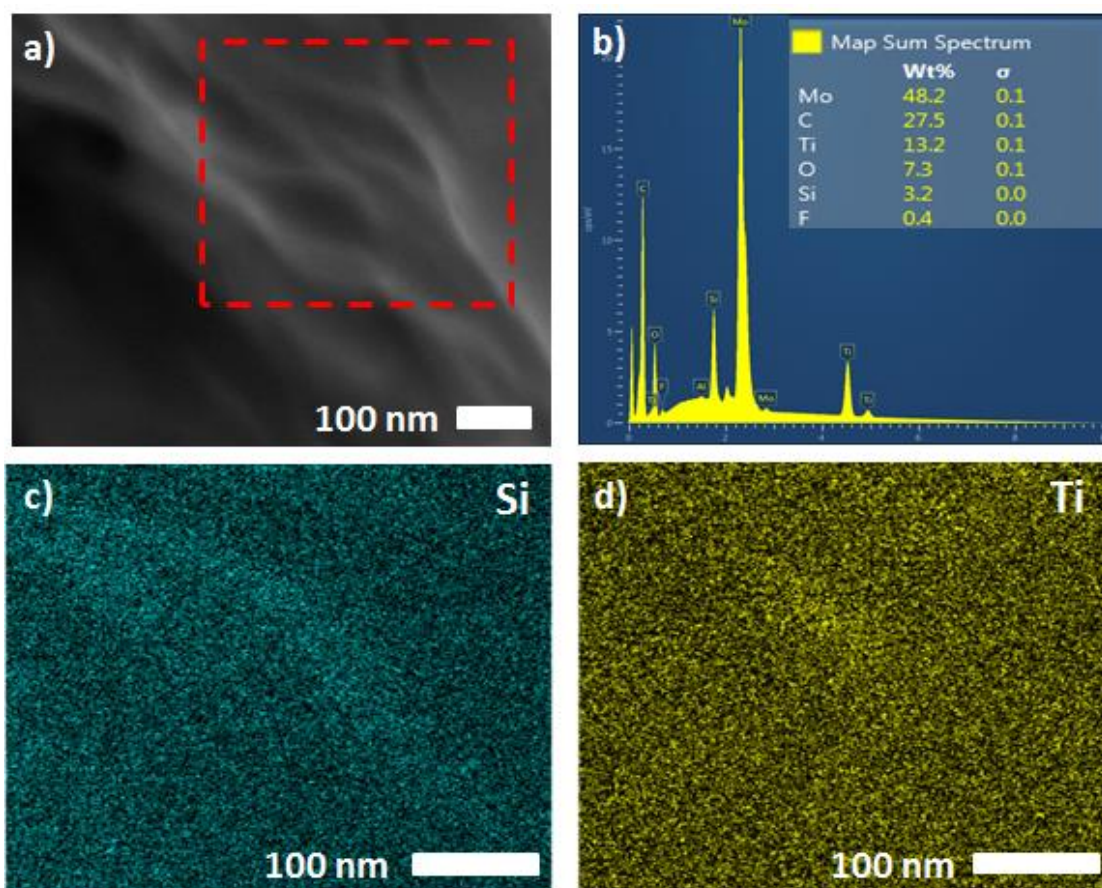


**Figure 5.9.** SEM-EDS studies of the SiO<sub>2</sub> pillared Mo<sub>2</sub>TiC<sub>2</sub> MXene after calcination at 400 °C for 5 h under argon. a) SEM micrograph showing the layers on the side of a typical calcined flake, with the dashed red box highlighting the area used for mapping. b) EDS spectrum of the calcined Mo<sub>2</sub>TiC<sub>2</sub> flake. c) The corresponding EDS map for the Si content. d) The corresponding EDS map for the Ti content.

Raman spectroscopy was then used to study the bonding in the non-pillared (Mo<sub>2</sub>TiC<sub>2</sub>), intercalated pillared (Mo<sub>2</sub>TiC<sub>2</sub>-Si) and calcined pillared (Mo<sub>2</sub>TiC<sub>2</sub>-Si-400) MXene materials (Figure 5.10). Peaks can be observed at around 170, 240, 310, 450, 650 and 775 cm<sup>-1</sup> in all samples, and do not appear to shift or change significantly as a result of the pillaring process. These peaks closely match previous reports on the Raman spectra of Mo<sub>2</sub>TiC<sub>2</sub>, giving further evidence to the successful synthesis of Mo<sub>2</sub>TiC<sub>2</sub>.<sup>246,247</sup> It has been reported that the peak around 170 cm<sup>-1</sup> results from the *Eg* vibration of both Mo and Ti atoms in -O terminated Mo<sub>2</sub>TiC<sub>2</sub>.<sup>246</sup> The peak at around 240 cm<sup>-1</sup> corresponds directly to the *Eg* vibration of the O atoms.<sup>246</sup> This supports the EDS results which suggested the presence of Mo-O in this MXene. The peaks at 310, 450 and 650 and 750 cm<sup>-1</sup> are all thought to mostly originate from the vibrations of C atoms in the MXene.<sup>246,247</sup> It should be noted that there are some differences in assignment in the literature, with Chen et al. assigning the 450 cm<sup>-1</sup> peak to C vibrations, while Kim et al. assign it to O surface O vibrations.<sup>246,247</sup>

In addition to the above peaks, the intercalated pillared material also shows extra peaks between 1,000 and 1,700  $\text{cm}^{-1}$  which are much more intense than the MXene peaks. These broad peaks correspond to DDA vibrations, and match the peaks seen in the intercalated  $\text{Ti}_3\text{C}_2$  Raman spectra in the previous chapter, suggesting that DDA has been successfully intercalated. These peaks are significantly reduced in the calcined material with only very small broad peaks at 1,170, 1,300 and 1,600  $\text{cm}^{-1}$  distinguishable, which shows that the majority of the carbon template has been removed after calcination as was the case for the  $\text{Ti}_3\text{C}_2$  MXene. However, a small amount of graphitic carbon remains in the structure.

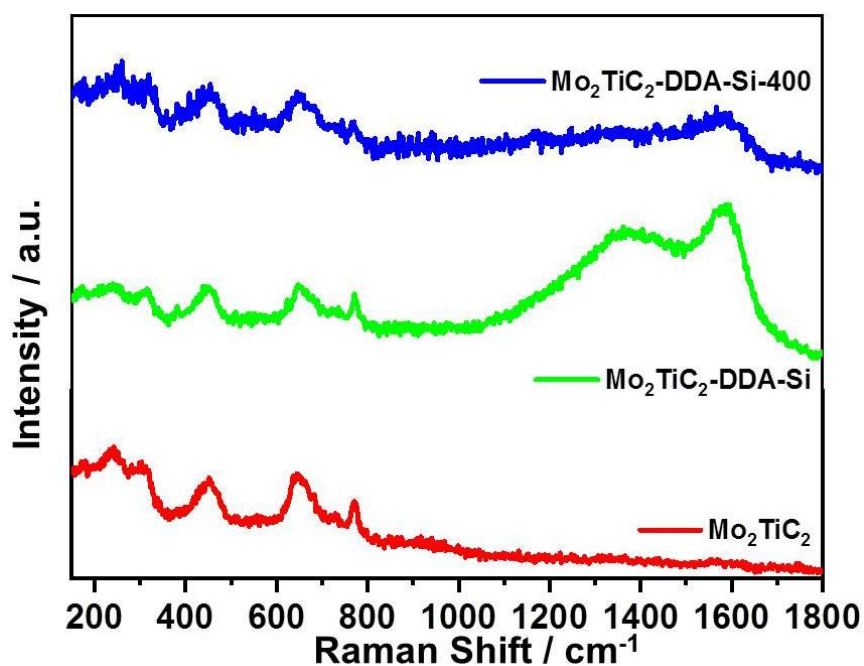


**Figure 5.10.** Raman spectroscopy of the non-pillared ( $\text{Mo}_2\text{TiC}_2$ , red), intercalated pillared ( $\text{Mo}_2\text{TiC}_2\text{-Si}$ , green) and calcined pillared ( $\text{Mo}_2\text{TiC}_2\text{-Si-400}$ , blue) MXene materials.

To further investigate the structure of the synthesised  $\text{Mo}_2\text{TiC}_2$  and the effect of the pillaring process on the MXene, XPS was used to study the Mo, Ti and O states in the as-made and pillared MXene, while Si was also studied in the pillared material.

Figure 5.11 shows the Mo 3d XPS for the non-pillared and pillared  $\text{Mo}_2\text{TiC}_2$ . There are three main peaks visible in both samples centred at 229.8, 233.0 and 236.0 eV for  $\text{Mo}_2\text{TiC}_2$  and 229.7, 232.9 and 236.1 eV for  $\text{Mo}_2\text{TiC}_2\text{-Si-400}$ . These peaks are in good agreement with a previous report on  $\text{Mo}_2\text{TiC}_2$  Mo 3d XPS.<sup>245</sup> It is known that the large peaks at around 229.8 and 233.0 eV correspond to the 3d 5/2 and 3d 3/2 electrons for the expected MXene Mo environment (Mo-C), which indicates that  $\text{Mo}^{4+}$  is the dominant oxidation state. This further confirms the successful synthesis of  $\text{Mo}_2\text{TiC}_2$ , and the preservation of the MXene structure after pillaring and calcination. The small peak at 236.0 eV corresponds to surface Mo oxides, ( $\text{Mo}^{6+}$ , 3d 3/2 electrons) showing that like titanium-based MXenes,  $\text{Mo}_2\text{TiC}_2$  also undergoes

some slight surface oxidation either in the etching process or when exposed to ambient conditions. The  $\text{Mo}^{6+}$ , 3d 5/2 electrons contribute to the peak centred around 233.0, with an expected binding energy of 232.7 eV. The presence of a small amount of these surface oxides has also been reported previously for  $\text{Mo}_2\text{TiC}_2$ , where HF etching was used.<sup>250</sup> The surface oxide peaks do not appear to grow after pillaring and calcination, suggesting that the Ar atmosphere used in the tube furnace was sufficient to avoid extra MXene oxidation.

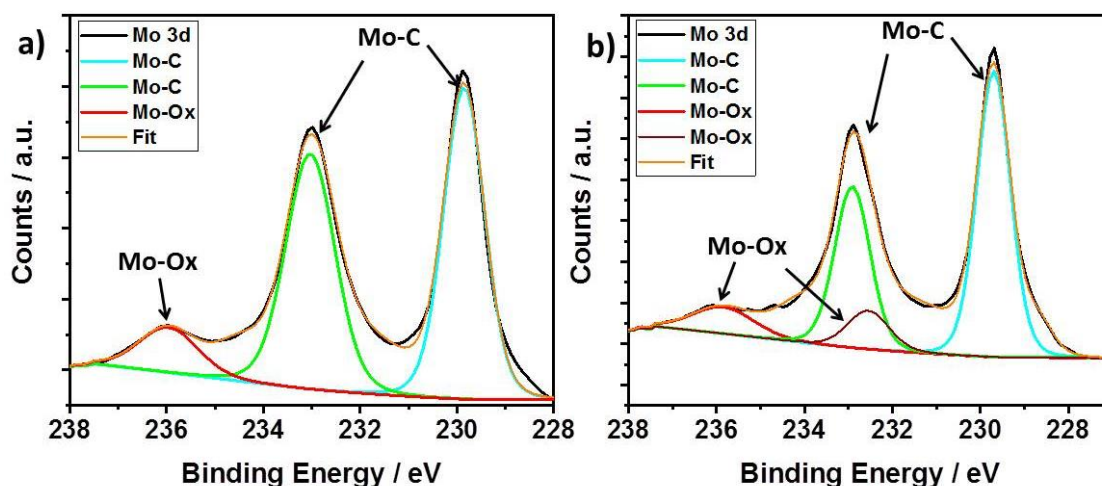


**Figure 5.11.** Mo 3d XPS spectra for a) non-pillared  $\text{Mo}_2\text{TiC}_2$  and b)  $\text{SiO}_2$ -pillared  $\text{Mo}_2\text{TiC}_2$  after calcination at 400 °C,  $\text{Mo}_2\text{TiC}_2$ -Si-400.

The XPS spectra for Ti 3d (Figure 5.12) show a similar pattern, with peaks corresponding to both Ti-C groups and Ti-O oxide groups visible. Both the non-pillared and pillared MXenes have similar peaks at 456.1, 458.8, 461.8 and 465.0 eV for  $\text{Mo}_2\text{TiC}_2$  and 456.0, 459.2, 461.8 and 464.7 eV for  $\text{Mo}_2\text{TiC}_2$ -Si-400. These peaks also match those previously reported, which showed that the peaks at around 456 eV and 461.8 eV correspond to MXene Ti-C bonds while the peaks around 459 and 465 eV relate to Ti-O surface oxides.<sup>245</sup> These surface oxides likely form from the MAX phase synthesis not being completely phase pure (so not all Ti atoms are below the surface) or from over-etching of the MXene. Peak assignments and fitting data for Figures 5.11 and 5.12 can be found in the Appendix in Tables A3-A6.

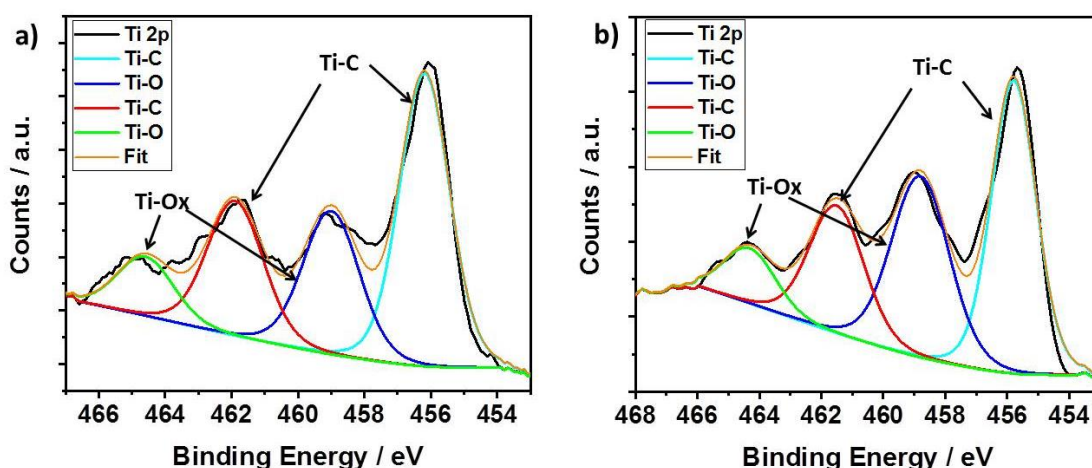


**Figure 5.12.** Ti 2p XPS spectra for a) non-pillared  $\text{Mo}_2\text{TiC}_2$  and b)  $\text{SiO}_2$ -pillared  $\text{Mo}_2\text{TiC}_2$  after calcination at  $400\text{ }^\circ\text{C}$ ,  $\text{Mo}_2\text{TiC}_2\text{-Si-400}$ .

XPS results for the O 1s scans are shown in Figure 5.13. This time there are some clear differences between the non-pillared and pillared  $\text{Mo}_2\text{TiC}_2$ . The non-pillared  $\text{Mo}_2\text{TiC}_2$  MXene looks similar to the previous reported results and shows a very broad asymmetric peak which is comprised of a variety of components as a result of multiple oxygen containing species being present in the sample.<sup>245</sup> A component centred around 530.5 eV corresponds to the formation of Mo and Ti oxides, which supports the Mo 3d and Ti 2p spectra. At 531 eV is a component corresponding to Mo-O groups, while a peak around 532 eV reveals the presence of Mo-OH termination groups. At 534 eV there is a small component which corresponds to surface-bound  $\text{H}_2\text{O}$  molecules. After pillaring and calcination, there is a significant new broad peak centred around 533.2 eV, which is a result of oxygen in silica; the pillar. In addition, there is a substantial decrease in the component relating to -OH surface groups. Before pillaring the -OH: O ratio is approximately 2:1, but decreases significantly to 1:1 after pillaring. This shows their direct involvement in the pillaring process, as was observed for  $\text{Ti}_3\text{C}_2$  pillaring in the previous chapter. Finally the Si 2p XPS spectrum for  $\text{Mo}_2\text{TiC}_2\text{-Si-400}$  shows a broad peak at 103.9 eV, which is consistent with  $\text{SiO}_2$  being the pillar.<sup>240</sup>

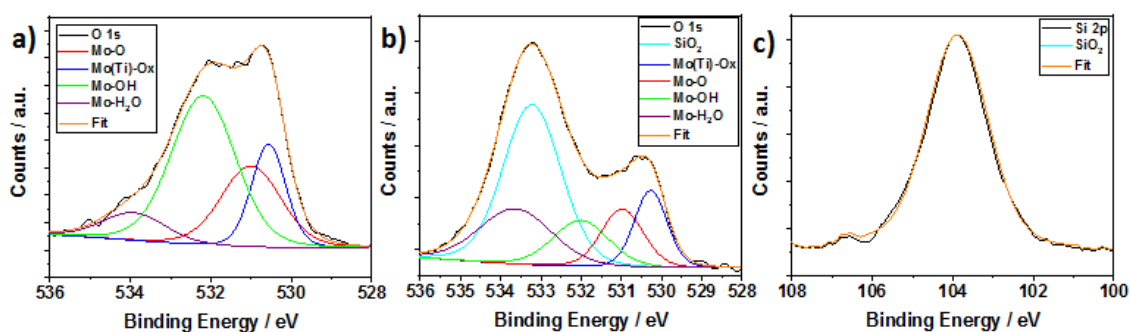


**Figure 5.13.** XPS analysis of a) O 1s spectrum of non-pillared  $\text{Mo}_2\text{TiC}_2$  b) O 1s spectrum of the pillared MXene  $\text{Mo}_2\text{TiC}_2\text{-Si-400}$  and c) Si 2p spectrum of the pillared MXene  $\text{Mo}_2\text{TiC}_2\text{-Si-400}$ .

### 5.2.3 Electrochemical Testing

Having confirmed that  $\text{Mo}_2\text{TiC}_2$  had successfully been pillared with  $\text{SiO}_2$ , the material was then tested as an electrode material in lithium and sodium half-cells to determine its promise for Li- and Na-ion battery applications. Its performance was compared to the un-pillared  $\text{Mo}_2\text{TiC}_2$  MXene.

#### 5.2.3.1 Lithium-ion System

Figure 5.14 shows the performance of the non-pillared and pillared  $\text{Mo}_2\text{TiC}_2$  MXene in Li-ion half cells at a current density of  $20 \text{ mA g}^{-1}$  in a voltage window of 0.01-3 V vs.  $\text{Li}^+/\text{Li}$ . The load curve for the non-pillared  $\text{Mo}_2\text{TiC}_2$  looks very different to the load curve of  $\text{Ti}_3\text{C}_2$ , with a linear part between 3 and 0.6 V, indicating capacitive type behaviour in this region, and a long sloping plateau between 0.6 and 0.01 V, which suggests a type of phase transition in this region, and a battery-like charge storage mechanism. This matches the load curves previously reported for  $\text{Mo}_2\text{TiC}_2$  in Li-ion battery systems, showing that the HCl-LiF etching method does not lead to significant changes to the electrochemical behaviour.<sup>100</sup> The load curve on the first discharge shows slightly different features, with short plateaus at 1.7 V and 0.7 V in addition to the two main features previously outlined. These short plateaus do not appear on the subsequent discharge nor on the following discharge cycles. This suggests that they arise from irreversible processes which are likely to result from irreversible reactions with the MXene surface groups and SEI formation, as has been reported for other MXenes.<sup>251</sup> The charge profiles show a short plateau between 1 and 1.5 V, with linear capacitive-like profiles outside this region.

The 1<sup>st</sup> cycle discharge capacity is  $344 \text{ mAh g}^{-1}$ , higher than the 311 and  $268 \text{ mAh g}^{-1}$  previously reported (which used rates of 25 and  $100 \text{ mA g}^{-1}$  respectively).<sup>100,246</sup> Of this,  $219 \text{ mAh g}^{-1}$  was recovered on subsequent charge, which compares to 269 and  $134 \text{ mAh g}^{-1}$  in other reports. This shows that there is a significant capacity loss on the first cycle, with an initial coulombic efficiency of 63%. This is higher than the majority of MXenes (40-60%) and sits in between the two reports so far on  $\text{Mo}_2\text{TiC}_2$  in Li-ion systems (50% and 86%).<sup>100,246</sup> The variation in reported initial capacities and coulombic efficiencies could be due to differing surface groups or the accessibility of the electrode surface due to differences in electrode architecture, but is yet to be studied. The electrolytes were the same in all cases. The coulombic efficiency increases to 90% on the second cycle, and is greater than 99% after the 25<sup>th</sup> cycle. As for previous work on low rates, there is significant capacity fade upon cycling, with  $125 \text{ mAh g}^{-1}$  being retained after 100 cycles (56% compared to the second discharge capacity). Chen et al. reported only  $52 \text{ mAh g}^{-1}$  being retained after 100 cycles, while Anasori et al. only ran a limited number of cycles (25) at low rates.<sup>100,246</sup> Overall, the use of the HCl-LiF etching method gives an MXene with comparable performance to previous works which use concentrated HF solutions.

Anasori et al. explained the low voltage plateau (<0.6 V) present in the load curves being the result of a conversion reaction between Mo-O groups on lithiated  $\text{Mo}_2\text{TiC}_2\text{O}_x$  (formed by Li intercalation between 3 and 0.6 V) and further Li to give  $\text{Li}_2\text{O}$ .<sup>100</sup>  $\text{Li}_2\text{O}$  is known to be a poor electrical conductor, and it is possible that its formation (which in transition metal oxide electrodes is often accompanied by a large volume change) is the main cause of the capacity fade seen in these electrodes. A pillared structure with large open pores could lead to improved cyclability of this material by providing free space for the reversible formation of  $\text{Li}_2\text{O}$  as well as improved access to the active sites for the  $\text{Li}^+$  ions.

The load curves for the  $\text{SiO}_2$  pillared MXene are shown in Figure 5.14b. There are similar features to the non-pillared material, with a sloping low voltage plateau below 0.6 V on the discharge profile, and a short plateau (albeit longer than in the non-pillared material) in the charge profile. On the first discharge profile, the short plateau at around 1.7 V which was present in the non-pillared material is no longer visible, which shows that this unidentified process (potentially trapping of Li ions with surface groups) is no longer occurring. Further work is needed to identify this process. The short plateau at around 0.7 V is still present, and slightly elongated, implying that it is linked to the exposure of the electrode surface, and could be due to SEI formation or another trapping process of Li ions.

The first cycle capacities are 473 and 314  $\text{mAh g}^{-1}$  on the discharge and charge respectively, which are larger for than the non-pillared material etched using HCl-LiF and HF etched  $\text{Mo}_2\text{TiC}_2$  reported elsewhere, including the delaminated MXene.<sup>100,246</sup> This gives an initial coulombic efficiency of 66%, a slight increase compared to the non-pillared material. The second cycle coulombic efficiency is 94% and reaches around 99% after 18 cycles, which is also an improvement on the non-pillared MXene. Around 80% capacity is retained between the 2<sup>nd</sup> (316  $\text{mAh g}^{-1}$ ) and 100<sup>th</sup> (250  $\text{mAh g}^{-1}$ ) cycles, compared to 54% for the as-made  $\text{Mo}_2\text{TiC}_2$ . This shows that the pillaring process has improved the capacity of  $\text{Mo}_2\text{TiC}_2$ , which is likely as a result of improved access for the Li ions to the electrode. In addition, the presence of the pillars seems to be successfully preventing nanosheets from restacking, and provides adequate space for the reversible formation of  $\text{Li}_2\text{O}$ , which results in improved cycling stability. This can be seen by the plateau in the load curves for the pillared MXene clearly being more stable during cycling. Anasori et al. predicted that the theoretical capacity of  $\text{Mo}_2\text{TiC}_2$  in a Li-ion system is 356  $\text{mAh g}^{-1}$ ,<sup>100</sup> which the 2<sup>nd</sup> discharge capacity of 316  $\text{mAh g}^{-1}$  is very close to (89% of the theoretical capacity), especially when it is considered that the pillared  $\text{Mo}_2\text{TiC}_2$  contains  $\text{SiO}_2$  and amine derived carbon which are included in the active mass for the specific capacity. The theoretical calculation assumed only one layer of  $\text{Li}^+$  was intercalated, which would seem to be the case here despite the large interlayer spacing of the pillared MXene, since the discharge capacities are not larger than the theoretical values.

It should be noted that SiO<sub>2</sub> has been investigated as an electrode material for Li storage itself, and has been shown to have significant capacity when nanosized,<sup>241,242,252</sup> as is in the case here. Therefore, is it possible that some of the gains in capacity could be as a result of alloying reactions involving the pillars, rather than just improved ion access to the MXene surface. However, the load curves for the pillared and non-pillared materials have the same features, which suggests that there is not significant contribution here from the SiO<sub>2</sub>. The Mo<sub>2</sub>TiC<sub>2</sub> and Ti<sub>3</sub>C<sub>2</sub> load curves reported in the previous chapter also look very different, suggesting that the MXenes are the active material. In addition, SiO<sub>2</sub> electrodes suffer from very low initial coulombic efficiencies (typically around 20-40%),<sup>241</sup> which seems incompatible with the improvement in coulombic efficiency reported here.

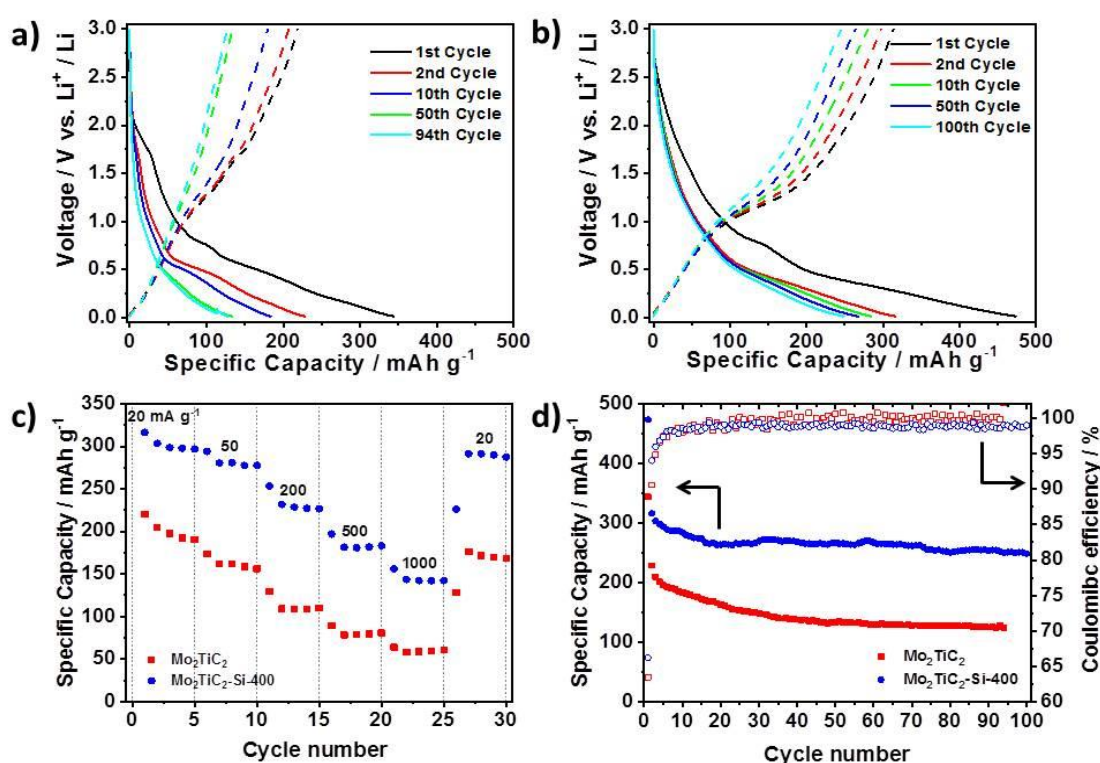


**Figure 5.14.** Galvanostatic charge-discharge testing of Mo<sub>2</sub>TiC<sub>2</sub> samples in Li-ion half cells. a) Load curves for selected cycles of Mo<sub>2</sub>TiC<sub>2</sub>. b) Load curves for selected cycles of Mo<sub>2</sub>TiC<sub>2</sub>-Si-400 c) Rate capability testing at 20, 50, 200, 500, 1,000 mA g<sup>-1</sup> for 5 cycles at each rate for the pillared (blue) and non-pillared (red) samples. (One initial cycle at 20 mA g<sup>-1</sup> was conducted to ensure SEI formation, which is not shown). d) Cycling stability data and coulombic efficiencies across 100 cycles for the pillared (blue) and 94 cycles for non-pillared (red) samples.

Rate capability tests were then carried out at increasing rates of 20, 50, 200, 500, and 1,000 mA h g<sup>-1</sup> to compare the high rate performance of the materials (Figure 5.14c). The pillared material shows improved performance at all rates, delivering discharge capacities of 312, 281, 229, 182 and 143 mA h g<sup>-1</sup> respectively. When the current was returned to 20 mA g<sup>-1</sup>, the capacity recovered to 292 mA h g<sup>-1</sup>, showing that the electrode was not severely damaged by the high rates used. In comparison, the non-

pillared  $\text{Mo}_2\text{TiC}_2$  material delivered capacities of 205, 162, 108, 79 and 59  $\text{mAh g}^{-1}$  at the respective rates, with 172  $\text{mAh g}^{-1}$  recovered at 20  $\text{mA g}^{-1}$ .

Since the pillared electrode showed significant capacity at high rates, its cycling stability at high rates was then tested by continuous cycling at 1  $\text{A g}^{-1}$  after the rate capability test, which corresponded to a charging time of about 8 min. Five stabilisation cycles were given to allow the electrode to adjust to the new current, before cycling for 500 charge-discharge cycles. After 500 cycles at 1  $\text{A g}^{-1}$ , it retained a capacity of 108  $\text{mAh g}^{-1}$ , a capacity retention of 80% compared to the 1<sup>st</sup> cycle (135  $\text{mAh g}^{-1}$ ), as shown in Figure 5.15. The average coulombic efficiency over these cycles was 99.9%, indicating highly reversible charge storage at this rate. This shows that after an initial stabilisation phase when beginning high rate cycling, the pillared  $\text{Mo}_2\text{TiC}_2$  material is a very stable electrode which makes it very suitable for high rate and long-life batteries. It is also worth noting that these results were obtained with a mass loading of 3.2  $\text{mg cm}^{-2}$ , higher than many reports on high rate electrode materials. For example,  $\text{Mo}_2\text{C}$  MXene had an exceptional high rate performance of 250  $\text{mAh g}^{-1}$  at a rate of 5  $\text{A g}^{-1}$ , but the mass loading was only 0.9  $\text{mg cm}^{-2}$  in this case.<sup>127</sup> These results suggest it would be a promising material to develop for lithium-ion capacitors, since it shows superior high rate capacities to graphite and a lower voltage with comparable capacities to lithium titanate.

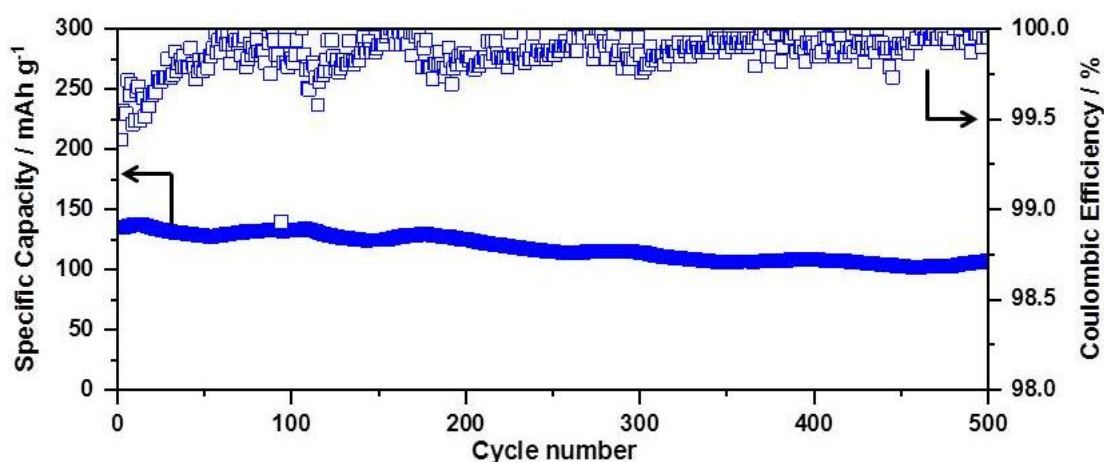


**Figure 5.15.** Discharge capacity and coulombic efficiency of  $\text{Mo}_2\text{TiC}_2\text{-Si-400}$  for 500 cycles at a rate of 1  $\text{A g}^{-1}$  in a voltage window of 0.01-3 V vs.  $\text{Li}^+/\text{Li}$ .

Cyclic voltammetry was then used to investigate the reactions and kinetics of the system in more detail. Figure 5.16 shows the cyclic voltammograms for five cycles collected at a scan rate of 0.2  $\text{mV s}^{-1}$  between 0.01-3 V vs.  $\text{Li}^+/\text{Li}$ . On the first discharge cycle, there are redox peaks at 1.7 V, 0.7 V, 0.8 V and a large broad peak between 0.6-0.01 V. This matches the plateaus observed on the first discharge on seen in the load curves in Figure 5.14. On the first charging sweep, there is a small broad peak at around 0.1-0.4 V, which shows that there is some reversibility for the process occurring below 0.6 V on the discharge. There is a further broad redox peak

at around 1.3 V, which matches the short plateau seen on the load curve and could be the reversal of the 0.8 V discharge process. A redox peak at 1.8 V is also visible on the first charge, with very little offset compared to the corresponding discharge peak, suggesting that the 1.7 V process is reversible.

On the 2<sup>nd</sup>-5<sup>th</sup> cycles, the discharge peak at 0.7 V is no longer visible, confirming that this results from an irreversible process which contributes to the initial capacity loss on the first cycle. In addition, the peak at 1.7 V is much lower in intensity in the subsequent cycles, which also links this to a partially irreversible process. The other features of the first cycle CV plots are still present in further cycles, showing good reversibility, although the peak between 0.6-0.01 V sees a significant decrease in current, which matches the capacity loss observed in the galvanostatic charge-discharge testing. As discussed previously, this is likely to be from a combination of SEI formation, Li<sup>+</sup> trapping, and poor reversibility of Li<sub>2</sub>O formation.

The CV plots show that current is produced across the entire voltage range studied, suggesting a capacitive contribution to the charge storage, with the area between 0.6-3 V being fairly rectangular in shape. In addition, it can clearly be seen that the majority of the discharge current occurs below 0.6 V, which matches well with the load curves in Figure 5.14.

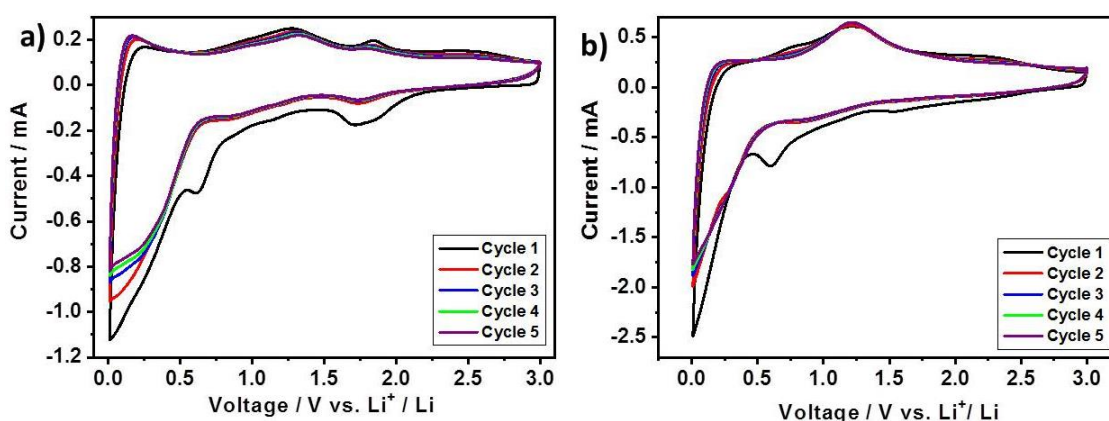


**Figure 5.16.** Cyclic Voltammograms for the a) non-pillared and b) pillared Mo<sub>2</sub>TiC<sub>2</sub> MXene materials. In both cases scan rates of 0.2 mV s<sup>-1</sup> were used in a voltage window of 0.01-3 V vs. Li<sup>+</sup>/Li. The first five cycles are shown.

For the pillared Mo<sub>2</sub>TiC<sub>2</sub> MXene, the shape of CV curves look very similar to the non-pillared material. The first discharge cycle has a small irreversible peak at 1.6 V, which is significantly reduced compared to the non-pillared MXene, and matches the corresponding plateau on the load curves. This partially explains the improved coulombic efficiency in the pillared material; this irreversible process is significantly reduced after pillaring, which suggests the process could be linked to the trapping of Li<sup>+</sup> ions. A second irreversible peak can be seen at 0.7 V, and there is a large peak between 0.5-0.01 V which is significantly reduced in intensity on the following cycles,

matching what was seen for the non-pillared material. On the charging cycles, there is a broad peak at 1.3 V, which is more distinctive than the corresponding peak in the non-pillared MXene. This matches what was observed in the load curves, and suggests that the reversibility of this process was improved by pillaring. The corresponding discharge peak can be distinguished at 0.8 V on cycles 2-5, but was obscured by the irreversible 0.6 V peak on the first discharge. Cycles 2-5 are very stable, and even the 0.5-0.01 V discharge peak shows very little fade, which matches the improved capacity retention observed in the galvanostatic charge-discharge testing. In contrast to the non-pillared material, there is no noticeable peak at around 1.7 V after the first discharge sweep, suggesting that this process no longer occurs in the pillared MXene. This could be analogous to the loss of high voltage redox peaks seen in the pillared  $\text{Ti}_3\text{C}_2$  experiments, but further work is needed to identify the origin of the redox peaks here. Anasori et al. proposed that the intercalation of Li into  $\text{Mo}_2\text{TiC}_2$  should occur mostly around 1.6 V vs.  $\text{Li}^+/\text{Li}$ , so the loss of this peak is likely to be the result of a change in the intercalation process as a result of the increase in interlayer spacing, possibly relating to differences in the solvation/desolvation of Li ions.<sup>100</sup>

Overall these CV redox peaks match well with the galvanostatic charge discharge testing, with the pillared material showing improved reversibility which explains its superior cycling stability. However, further work is required to identify the specific processes leading to each redox peak. Finally, the fact that the CV plots for the pillared and non-pillared material show very similar features suggest that the electrochemistry is the same in both cases; i.e. the majority of the current comes from the  $\text{Mo}_2\text{TiC}_2$  MXene, rather from the  $\text{SiO}_2$  pillars being redox active. In addition, both CV curves match the previous report by Anasori et al. for  $\text{Mo}_2\text{TiC}_2$  in a lithium-ion system,<sup>100</sup> and the  $\text{SiO}_2$ -pillared  $\text{Ti}_3\text{C}_2$  in Chapter 4 looked very different, which further supports the MXene being the redox active component. However, the majority of current from a  $\text{SiO}_2$  electrode would be expected to occur below 1 V, and the low voltage peak in the  $\text{Mo}_2\text{TiC}_2$  CV plots does change slightly after pillaring (becomes sharper with less contribution at higher voltages), so a small  $\text{SiO}_2$  contribution cannot be completely ruled out.

To investigate the kinetics of the system in more detail, the cells were then cycled at increasing scan rates of 0.5, 2 and 5  $\text{mV s}^{-1}$  (Figure 5.17). The pillared material shows similar shaped CV plots at all rates, suggesting reasonably fast kinetics of the system, though there are small changes as the rate increases. The discharge peak at around 0.8 V broadens and becomes more prominent at higher rates, although there is almost no shift (around 50 mV) in the peak position. The broad discharge peak between 0.6-0.01 V sharpens as the rate increases, with a lower contribution of current at the higher voltage side of the peak. On the charging sweeps, the 0.1 V peak shifts the higher voltages (around 0.5 V at a scan rate of 5  $\text{mV s}^{-1}$ ), moving it

considerably closer to the 1.2 V peak. The rectangular part of the plot at voltages above 2 V seems to distort, with a possible broad peak now distinguishable centred around 1.5 V at 5 mV s<sup>-1</sup>.

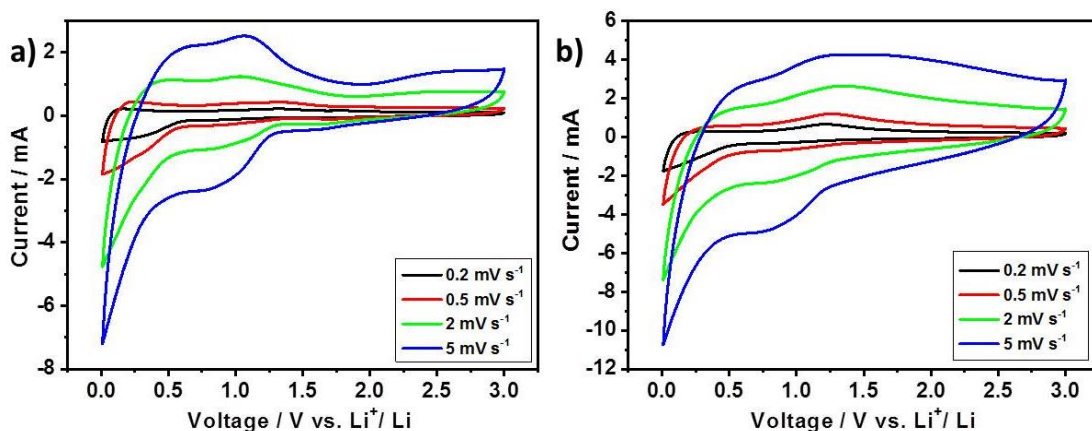


**Figure 5.17.** Cyclic voltammograms for the a) non-pillared and b) pillared Mo<sub>2</sub>TiC<sub>2</sub> MXene materials. In both cases increasing scan rates of 0.2, 0.5, 2 and 5 mV s<sup>-1</sup> were used in a voltage window of 0.01-3 V vs. Li<sup>+</sup>/Li.

The CV plots for the pillared Mo<sub>2</sub>TiC<sub>2</sub> MXene show more significant changes at higher scan rates, with the overall shape of the plot becoming much more rectangular at 5 mV s<sup>-1</sup>, indicative of an increased contribution of capacitive processes to the charge storage. This could explain the improved rate capability (Figure 5.14c) of the pillared MXene compared to as-made Mo<sub>2</sub>TiC<sub>2</sub> MXene. The pillared material has an increased interlayer spacing and specific surface area, which allows for faster Li<sup>+</sup> ion migration and therefore increased capacitive charge storage compared to the non-pillared MXene, which doesn't have this high rate contribution. The redox peaks at 0.8 V (discharge) and 1.3 V (charge) are however still present at 5 mV s<sup>-1</sup>, although they are significantly broader than at lower scan rates. The sharper peak between 0.5-0.01 V is also still clearly present. This shows that these peaks originate from fast redox processes, which further explains the high rate performance, and shows that, as for the non-pillared material, there is a mixture of mechanisms contributing to the charge storage.

As has been previously discussed, plotting the log of the current against the log of the scan rate gives a straight line with a gradient of *b*. When *b* = 0.5, the current derives solely from battery-like diffusion limited faradic processes, whereas a *b*-value of 1 indicates a purely surface controlled capacitive reaction (either pseudocapacitance or EDL capacitance). A value in between these end points indicates to a charge storage mechanism which is a mix of diffusion-limited and surface-limited processes. When this analysis is carried out at different voltages, the relative contribution of these processes can be studied across the voltage window on the charge and discharge sweeps.

Figure 5.18 shows plots of the  $b$ -values against the voltage for the pillared and non-pillared  $\text{Mo}_2\text{TiC}_2$ . In both cases there is significant variation in the  $b$ -value across the voltage range covered. For the non-pillared MXene, the current at 3 V at the start of the lithiation (discharge) sweep gives a  $b$ -value of 0.84, which suggests a mixed charge storage mechanism is contributions from both diffusion-limited (battery-like) and surface-controlled (capacitive) processes, but with the majority of the current originating from capacitive-like processes at this voltage. At 2 V, the  $b$ -value decreases to 0.62, showing that at this voltage a diffusion-limited battery-like process occurs, which matches with the small broad redox peak at 1.8 V (Figure 5.16). At 1 V the  $b$ -value increases again to 0.88, showing capacitive processes contribute mostly to the current again, which matches the CV shape at this voltage. At 0.5 and 0.01 V the  $b$ -values decrease to 0.64 and 0.68 showing the battery-like diffusion limited processes dominate at these voltages, which corresponds to the large peak observed in the CV plot below 0.6 V (likely to result from a conversion reaction to form  $\text{Li}_2\text{O}$ ). On the delithiation (charging) sweep, the  $b$ -values increase to 0.80 and 0.82, showing that the reverse of the  $\text{Li}_2\text{O}$  formation is mostly surface-controlled, with less diffusion limitation compared to the  $\text{Li}_2\text{O}$  formation. The  $b$ -values at 2 and 3 V closely match those on the lithiation sweep (0.61 and 0.84 respectively), corresponding to the reverse of the discharge processes. These values also match the shape of the CV plots with a redox peak at 1.9 V and no peak at 3 V.

For the  $\text{SiO}_2$  pillared  $\text{Mo}_2\text{TiC}_2$  MXene the initial  $b$ -value at 3 V is 0.86, slightly larger than the non-pillared material (0.84). At 2 V the pillared MXene shows a  $b$ -value of 0.83, which is significantly larger than the non-pillared material (0.62), showing that the current here a predominantly from surface-controlled processes. This matches the CV plots, since the small 1.8 V redox peak present in the non-pillared MXene is not observed for the pillared material. At 1 V, the  $b$ -value is 0.83, similar to the non-pillared material (0.88), suggesting similar processes occur here. As was seen for the non-pillared material, the  $b$ -values at 0.5 and 0.01 V decrease to 0.74 and 0.56 respectively, which matches the large redox peak at 0.5-0.01 V on the CV plot. The value of 0.56 shows the vast majority of the current here originates from battery-like processes, which suggests that pillaring aids the conversion reaction, which explains the increased capacity shown by this material. On the charging sweeps, the  $b$ -values at 0.5 and 1 V remain low (0.65 for both voltages), which are on the edge of the very broad CV peak which centres on 1.5 V (Figure 5.16). This likely corresponds to the reverse of the  $\text{Li}_2\text{O}$  conversion reaction, and since the  $b$ -values are much lower than for the non-pillared material at these voltages, implies that the reversibility of this reaction has significantly increased, causing the increased contribution from battery-like diffusion-limited processes. At 2 and 3 V the  $b$ -values (0.83 and 0.86) are identical to the discharge values, showing a return to mostly capacitive processes, as implied by the CV curves.

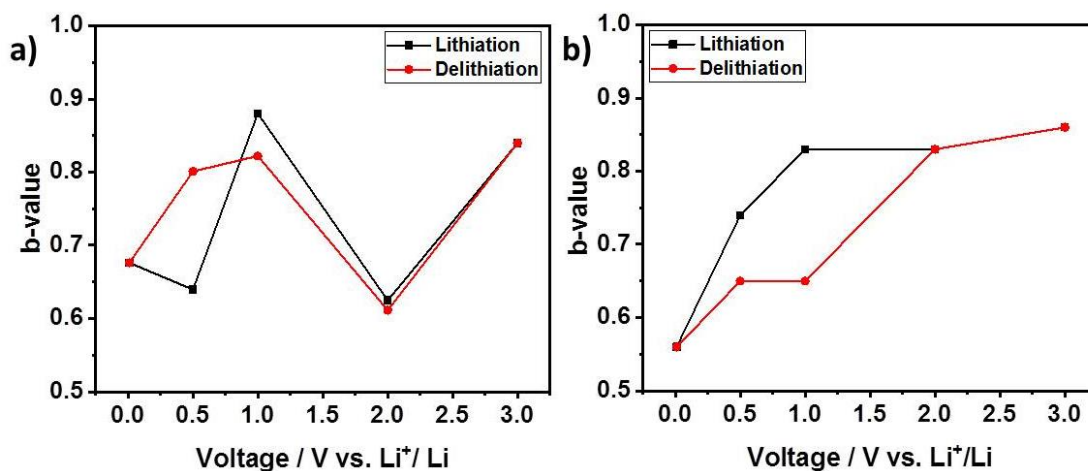


**Figure 5.18.** Plot of  $b$ -values against voltage vs. Li<sup>+</sup>/Li. a) Non-Pillared Mo<sub>2</sub>TiC<sub>2</sub> b) Pillared-Mo<sub>2</sub>TiC<sub>2</sub>.

Ex-situ XPS analysis was then carried out to investigate the proposed mechanism of reversible Li<sub>2</sub>O formation in Mo<sub>2</sub>TiC<sub>2</sub>, which had not been experimentally studied so far. Mo<sub>2</sub>TiC<sub>2</sub>-Si-400 electrodes were extracted from cells which were at OCV, discharged to 0.01 V and charged to 3 V, washed with DMC and dried under vacuum in the antechamber of the argon filled glovebox before sealing the vial and posting for measurements. The O 1s results are shown in Figure 5.19, while data on the peak fittings can be found in the appendix, Table A.7. At OCV there is just one broad peak visible, which is centred on 532 eV. Deconvolution reveals that there are two main components to this peak at 531.7 eV (assigned as organic carbonate oxygen) and 530.6 eV (which matches the Mo-Ox environment found in the powdered samples in Figure 5.13). This implies that electrolyte remains in the material, since oxygen in an organic environment such as the carbonate-based electrolyte solvents used here is known to give a broad peak centering on 532 eV,<sup>253</sup> and SEI formation would not be expected without applying current. There is little change in these two peaks upon charging and discharging, with the shifts varying less than 0.2 eV for both environments at all states-of-charge. However, the spectrum for the electrode discharged to 0.01 V shows a new peak at 528.6 eV, which matches well with Li<sub>2</sub>O.<sup>240</sup> Upon charging to 3 V, this peak disappears, confirming that Li<sub>2</sub>O is indeed reversibly formed and removed upon lithiation (discharging) and delithiation (charging) respectively.

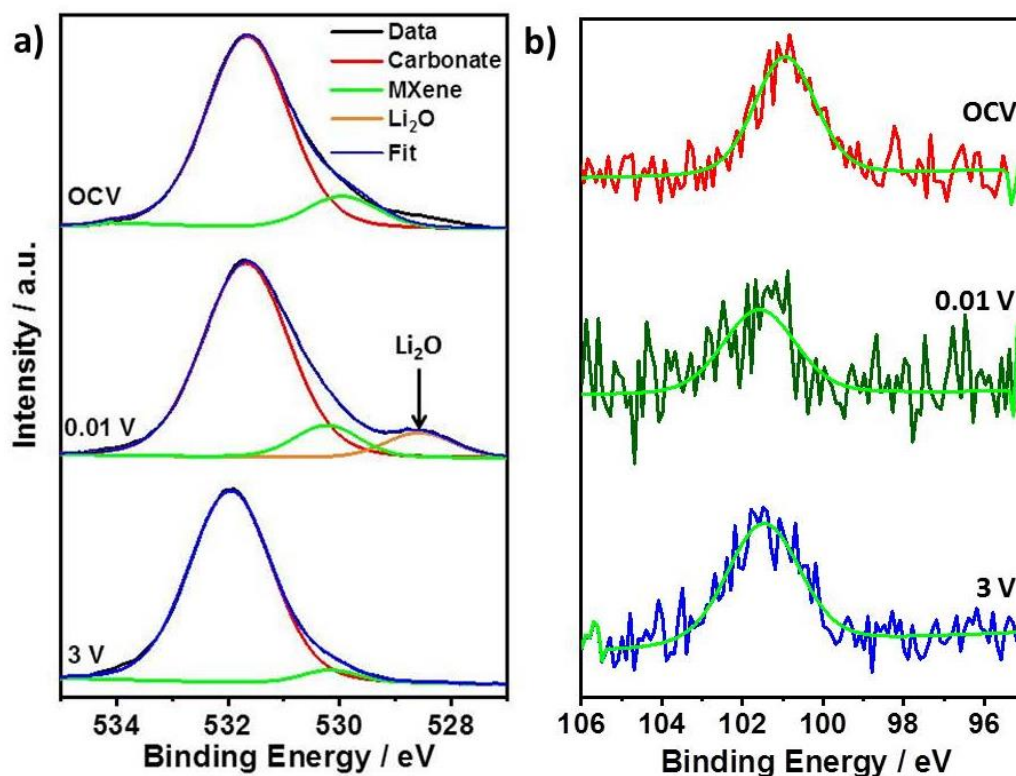


**Figure 5.19.** Ex-situ XPS of SiO<sub>2</sub>-pillared Mo<sub>2</sub>TiC<sub>2</sub>. a) Ex-situ O 1s XPS of Mo<sub>2</sub>TiC<sub>2</sub>-Si-400 at OCV (top), after discharge to 0.01 V (middle) and after charging to 3 V (bottom). b) Ex-situ Si 2p XPS of Mo<sub>2</sub>TiC<sub>2</sub>-Si at OCV (top), after discharging to 0.01 V (middle) and after charging to 3 V (bottom).

XPS results for Si 2p are shown in Figure 5.19, with peak fitting data in Table A.8 in the appendix. It can be seen that the Si peak has shifted from 103.9 eV in the synthesised pillared MXene to 100.9 eV in the OCV electrode. The reason for this shift is unclear, since SiO<sub>2</sub> does not spontaneously react with Li ions, and was for many years thought to be inactive for Li-ion battery applications.<sup>240,241</sup> Potentially, it could result from interactions between the Si pillars and the organic electrolyte, which the O 1s spectra suggest remains in the sample. A similar binding energy was also observed for the pillared Ti<sub>3</sub>C<sub>2</sub> material in the Na-ion system in Chapter 4. Interestingly, there is no shift in the Si 2p peak for the electrode discharged to 0.01 V, suggesting that the SiO<sub>2</sub> is not contributing to the charge stored here. In addition, no peaks relating to metallic Si (99.5 eV) or Li<sub>x</sub>Si alloys (96.0–97.3 eV) are observed. This is significant because the expected lithiated mechanism of SiO<sub>2</sub> is based on the Reactions 5.2-5.4.<sup>240-242</sup>



Reactions 5.2 and 5.3 are considered irreversible, giving SiO<sub>2</sub> electrodes low initial coulombic efficiencies, and form metallic Si which then acts as the lithiation host via the formation of Li<sub>x</sub>Si. Reaction 5.2 could give an alternative explanation for the formation of Li<sub>2</sub>O other than reaction with the Mo-O groups. However, since neither Si nor Li<sub>x</sub>Si is detected in the XPS, these are unlikely to be the Li<sub>2</sub>O source here. In addition, Reaction 5.2 is expected to be irreversible, so Li<sub>2</sub>O should remain in the structure upon charging, which is not the case here. Recently, alternative reactions have been proposed, as shown in Reactions 5.5 and 5.6.<sup>240</sup>



These reactions have recently been proposed as alternative reversible lithiation pathways via the formation of lithium silicates as Li is inserted into the SiO<sub>2</sub> structure, and give an alternative mechanism for charge storage in SiO<sub>2</sub> without the formation of Li<sub>x</sub>Si alloys. However, these reactions also result in the formation of metallic Si, which has not been detected in the XPS results presented in Figure 5.19. Therefore it seems unlikely that the SiO<sub>2</sub> pillars are contributing significantly to the charge storage of the pillared MXene, although further characterisation such as in-situ XANES and / or NMR could provide more insight into the charge storage mechanism. These would overcome some of the limitations of ex-situ XPS such as the available time for charge/ discharge products to relax between cycling and measurement and the surface nature of XPS, which may be affecting the results presented here. Nevertheless, due to the limited shift in the Si 2p peak after discharge and charge and the lack of Si or Li<sub>x</sub>Si species being present, no evidence has been found so far to support electrochemical activity from the SiO<sub>2</sub> pillars. If the SiO<sub>2</sub> pillars are in fact active, the currently accepted irreversibility of Reaction 5.2 (Li<sub>2</sub>O formation) would not appear to stand here. Therefore, Mo<sub>2</sub>TiC<sub>2</sub> is the likely source of the Li<sub>2</sub>O detected, supporting the previously reported mechanism for this MXene.

Overall the analysis shown in this section suggests that the effect of pillaring is two-fold. Firstly, it allows increased contribution to the capacity from the Li<sub>2</sub>O conversion reaction (likely due to increased access to the MXene surface for the Li<sup>+</sup> ions), and improves its reversibility (due to free space Li<sub>2</sub>O to form and be held in without damaging the overall structure). Secondly, at voltages where the conversion reaction does not occur, the contribution of capacitive current is greater for the pillared than non-pillared MXene, which can be explained by a reduction in the diffusion limitation arising from the increased interlayer spacing. These results help explain the increased capacity, rate capability and cycling stability of the pillared Mo<sub>2</sub>TiC<sub>2</sub> compared to the non-pillared material.

### 5.2.3.2 Sodium-ion System

Following the promising performance of the  $\text{Mo}_2\text{TiC}_2$  MXene in a Li-ion system the non-pillared and pillared materials were then tested as Na-ion electrodes to investigate their behaviour in this system, which has not previously been reported.

Figure 5.20 shows the load curves and cycling stability results from galvanostatic testing in a Na-ion half-cell at a rate of  $20 \text{ mA g}^{-1}$  in a voltage window of 0.01-3 V vs.  $\text{Na}^+/\text{Na}$ . In both cases the load curves show very similar shapes, although the pillared material has a smoother load curve. There is little capacity between 3 and 0.8 V, and the voltage decreases rapidly across this range. Between 0.8 and 0.01 V the load curves enter a different region, with the majority of the capacity occurring here. The load curve for the pillared material is slightly smoother than the non-pillared MXene, which shows more abrupt changes in gradient as the voltage drops. However neither material shows significant plateaus (apart from on the first discharge cycle, where a sloping plateau between 0.8 to 0.5 V can be observed, which likely relates to SEI formation). This suggests that the charge storage mechanism is more capacitive based than for the Li-ion system, at least without major phase changes. Whilst the majority of the discharge capacity for both systems occurs at low voltages, the Li-system shows distinctive plateau features on both charge (1.2 V) and discharge (0.6-0.01 V) which are not present in the Na-ion system, suggesting different charge storage mechanisms.

The pillared MXene shows significantly improved performance compared to the as-etched  $\text{Mo}_2\text{TiC}_2$ , with a second cycle discharge capacity of  $109 \text{ mAh g}^{-1}$  compared to  $74 \text{ mAh g}^{-1}$  for the non-pillared material. By the 80<sup>th</sup> cycle, the non-pillared MXene had retained a capacity of just  $48 \text{ mAh g}^{-1}$  (65% capacity retention) compared to  $82 \text{ mAh g}^{-1}$  for the pillared MXene (75% capacity retention). Both materials showed significant capacity loss between the 1<sup>st</sup> and 2<sup>nd</sup> cycles, with the pillared  $\text{Mo}_2\text{TiC}_2$  demonstrating a 1<sup>st</sup> cycle discharge capacity of  $205 \text{ mAh g}^{-1}$  and the non-pillared  $\text{Mo}_2\text{TiC}_2$  giving a 1<sup>st</sup> cycle capacity of  $151 \text{ mAh g}^{-1}$ . These capacities are significantly lower than the capacities obtained for the Li-ion system, and the  $\text{Ti}_3\text{C}_2$ -based materials in the same Na-ion system reported in the previous chapter. However, both materials do reversibly store  $\text{Na}^+$  ions in a voltage window suitable for the negative electrode of a Na-ion battery.

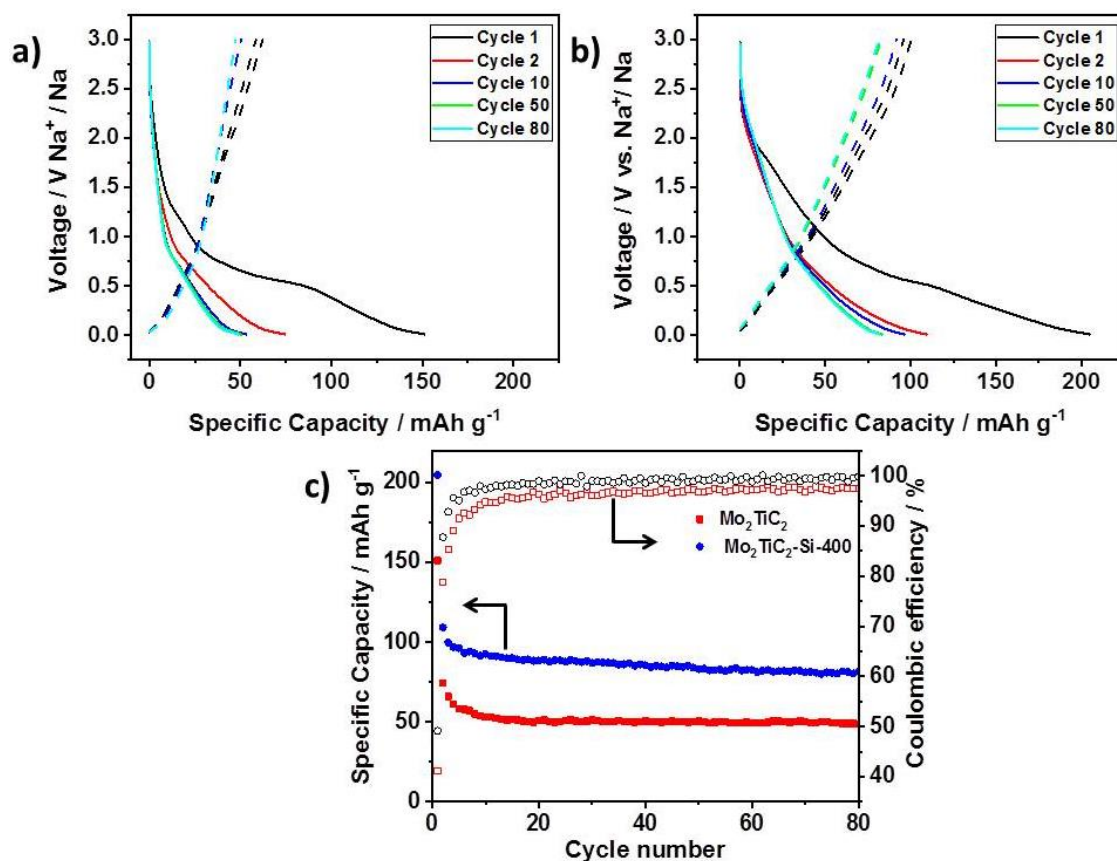


**Figure 5.20.** Galvanostatic charge-discharge testing of Mo<sub>2</sub>TiC<sub>2</sub> samples in Na-ion half cells at 20 mA g<sup>-1</sup> in a voltage window of 0.01-3 V vs. Na<sup>+</sup>/Na. a) Load curves for selected cycles of Mo<sub>2</sub>TiC<sub>2</sub>. b) Load curves for selected cycles of Mo<sub>2</sub>TiC<sub>2</sub>-Si-400. c) Cycling stability data and coulombic efficiencies across 80 cycles for the pillared (blue) and non-pillared (red) samples.

The pillared Mo<sub>2</sub>TiC<sub>2</sub> showed an initial coulombic efficiency of 49%, slightly higher than the non-pillared material (41%). In both cases this is significantly lower than the values for the Li-ion system. The coulombic efficiency then rapidly increased for the pillared material reaching 96% on the 4<sup>th</sup> cycle (compared to 89% for the non-pillared MXene) and achieving 99% on the 23<sup>rd</sup> cycle. In contrast, the highest coulombic efficiency for the non-pillared Mo<sub>2</sub>TiC<sub>2</sub> was 98%. The superior coulombic efficiency of the pillared material compared to the non-pillared MXene is further confirmed by the average coulombic efficiencies between the 2<sup>nd</sup> and 80<sup>th</sup> cycle of 99% and 95% respectively. This suggests that the pillaring has aided in preventing the trapping of Na<sup>+</sup> between intercalation and de-intercalation.

Rate capability tests were then carried out at increasing rates of 20, 50, 200, 500 and 1,000 mA h g<sup>-1</sup> (Figure 5.21). The pillared material shows superior performance at all rates tested, with discharge capacities of 103, 88, 66, 52 and 40 mA h g<sup>-1</sup> respectively, compared to capacities of 70, 42, 29, 23 and 18 mA h g<sup>-1</sup>. In addition, when the rate returns to 20 mA g<sup>-1</sup> the capacity recovers to 95 mA h g<sup>-1</sup>, showing that the structure is not damaged by the high rate cycling. For comparison, the non-pillared MXene only recovers to 50 mA h g<sup>-1</sup> on the change to 20 mA g<sup>-1</sup>. This shows that as for the

other pillared MXene results in this thesis, the pillars do not hinder the ion transport, which is in fact enhanced due to the enlarged interlayer spacing. Interestingly, the capacity for the SiO<sub>2</sub>-pillared Mo<sub>2</sub>TiC<sub>2</sub> at 1 A g<sup>-1</sup> (40 mAh g<sup>-1</sup>) is higher than the one that was obtained for the SiO<sub>2</sub>-pillared Ti<sub>3</sub>C<sub>2</sub> material in the previous chapter (30 mAh g<sup>-1</sup>), which could be due to a lower concentration of SiO<sub>2</sub> pillars in the sample (3.2 wt.% compared to 6.3 wt.% according to the EDS results), resulting in less blocking from the pillars. Alternatively, this could be as a result of the diffusion barriers of the MXene materials themselves.

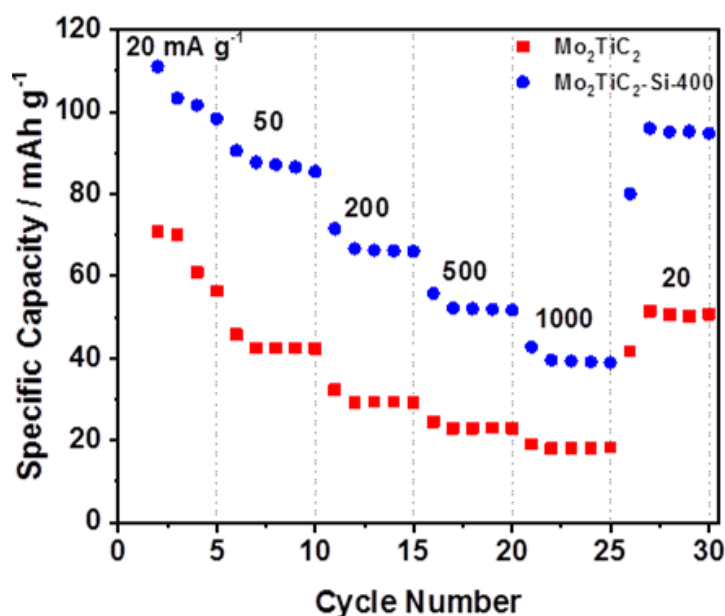


**Figure 5.21.** Rate capability testing at 20, 50, 200, 500, 1,000 mA g<sup>-1</sup> for five cycles at each rate for the pillared (blue) and non-pillared (red) samples. (One initial cycle at 20 mA g<sup>-1</sup> was conducted to ensure SEI formation, which is not shown).

These results demonstrate that the pillared MXene shows significantly improved performance compared to the non-pillared material, but the charge storage mechanism in a Na-ion systems appears to be different to the behaviour in the Li-system. In their computational study, Anasori et al. reported that the conversion reaction which contributes significant capacity at low voltages in Li-ion systems (up to 200 mAh g<sup>-1</sup>) does not occur in Na-ion systems.<sup>100</sup> The conversion reaction has two main effects; it increases the capacity of the electrode but lowers the cycling stability. Since Mo<sub>2</sub>TiC<sub>2</sub> has significantly lower capacities but increased stability in the Na-ion electrolyte compared to the Li-ion system, even when pillared, these results seem to support the computational study by Anasori et al. This suggests that Na<sup>+</sup> intercalation/ deintercalation is the major source of capacity in Na-ion systems for Mo<sub>2</sub>TiC<sub>2</sub>. It is worth noting that Anasori et al. also claimed that K<sup>+</sup> systems should behave the same as Na<sup>+</sup>, but Mg<sup>2+</sup> and Al<sup>3+</sup> should show similar behaviour to Li<sup>+</sup> and undergo a viable conversion reaction to gain extra capacity.<sup>100</sup> This suggests that the pillared Mo<sub>2</sub>TiC<sub>2</sub> MXene could be promising for these battery systems.

Cyclic voltammetry studies were then carried out to further investigate the electrochemical behaviour. Figure 5.22 shows that the non-pillared  $\text{Mo}_2\text{TiC}_2$  material has a narrow rectangular CV plot between the voltages of 0.8 and 3 V, suggesting a capacitive-like charge storage mechanism in this voltage range which matches the load curves (Figure 5.20). On the 1<sup>st</sup> discharge sweep, there is a broad peak which centres on 0.4 V which does not appear on the charging sweep and is significantly reduced on subsequent cycles, which is likely to correspond to SEI formation and matches the short plateau observed on the 1<sup>st</sup> discharge on the load curve (Figure 5.20). On the first charge sweep there is a broad peak between 0.01 and 0.8 V, before the rectangular region mentioned earlier begins. On the second discharge sweep, there is a very broad peak centred around 0.5 V which continues to the cut-off voltage (0.01 V). On the 2<sup>nd</sup> charge sweep, there is a relatively sharp peak at 0.1 V which is followed by a very broad peak to 0.8 V. These peaks likely correspond to the intercalation (discharge) and deintercalation (charge) of  $\text{Na}^+$  ions between the  $\text{Mo}_2\text{TiC}_2$ . As was observed for the load curves, whilst there is some capacity across the whole voltage window studied, the majority of the charge storage reactions occur below 0.8 V.

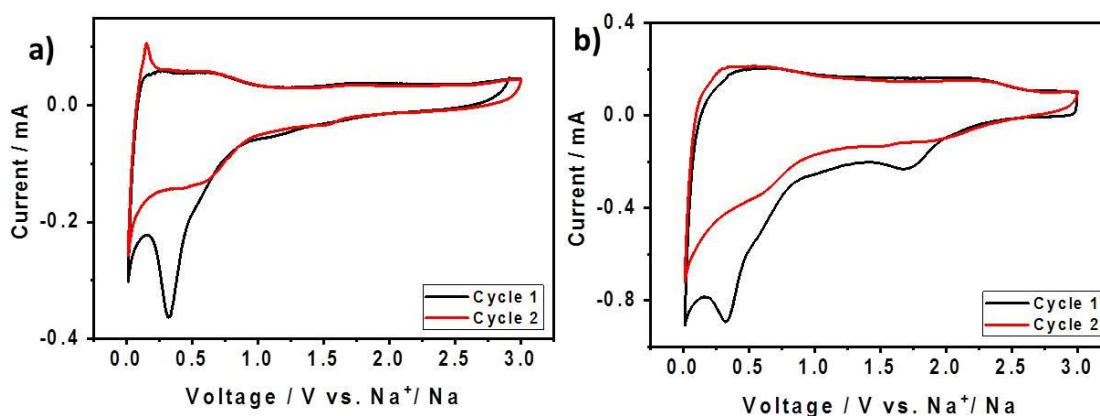


**Figure 5.22.** Cyclic voltammograms collected at a scan rate of  $0.2 \text{ mV s}^{-1}$  in a voltage window between 0.01-3 V vs.  $\text{Na}^+/\text{Na}$  for a) the non-pillared  $\text{Mo}_2\text{TiC}_2$  and b) pillared  $\text{Mo}_2\text{TiC}_2\text{-Si-400}$ .

The pillared material has a similar shaped CV curve to the non-pillared MXene, but there are a few differences. For example, on the first discharge, there is an extra irreversible redox peak at 1.8 V, which was not present on the non-pillared material. This suggests an extra, unidentified process occurs on the first discharge for the pillared  $\text{Mo}_2\text{TiC}_2$ . On the second charge, the redox peak at 0.2 V on the non-pillared material is not present for the pillared MXene, suggesting that this process no longer occurs. This could be linked to the enlarged interlayer spacing as was discussed in the previous chapter for pillared  $\text{Ti}_3\text{C}_2$ . The other CV features are seen in both pillared and non-pillared MXenes, suggesting similar overall electrochemical behaviour.

To probe the kinetics of the system, CVs were collected at increasing sweep rates 0.2, 0.5, 2 and  $5 \text{ mV s}^{-1}$  (Figure 5.23). The general shape of the CV plots is maintained at

all rates, though the discharge peak at 0.5 V broadens and appears to shift to lower voltages, with the CV plot collected at 5 mV s<sup>-1</sup> featuring a main discharge peak at 0.01-0.3 V (however a small shoulder at 0.6 V can be seen). The charging peak corresponding to the reverse of this process shifts from 0.1 V at 0.2 mV s<sup>-1</sup> to 0.5 V at 5 mV s<sup>-1</sup>. The capacitive region between 0.8 and 3 V remains the same at all rates. For the pillared material, there is also a broadening and shifting of the redox peaks to higher voltages. The CV at 5 mV s<sup>-1</sup> has a much more rectangular shape across the entire voltage range, suggesting increased capacitive contribution at this scan rate, which is likely to be a result of the higher surface area in the pillared material. This would explain the superior rate performance of the pillared MXene compared to the non-pillared Mo<sub>2</sub>TiC<sub>2</sub>.

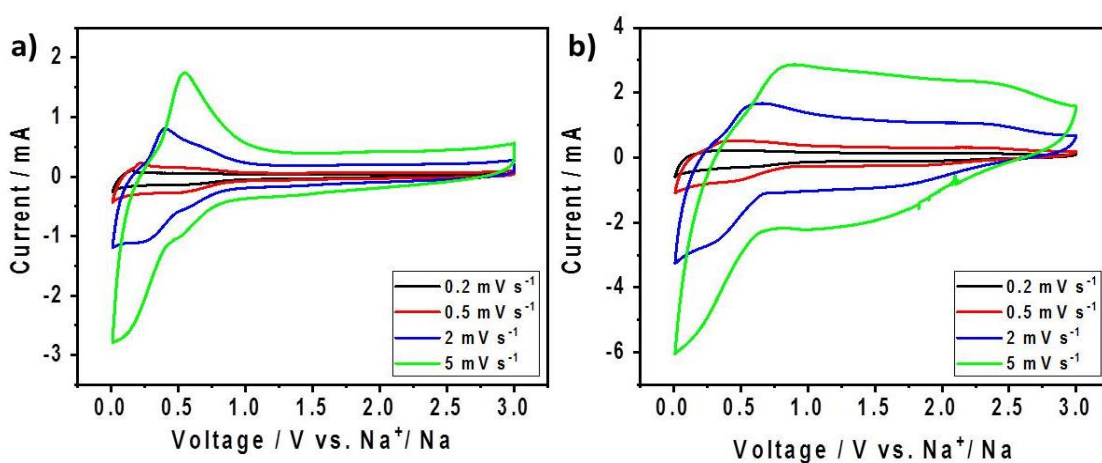


**Figure 5.23.** Cyclic voltammograms collected at increasing scan rates of 0.2, 0.5, 2 and 5 mV s<sup>-1</sup> in a voltage window of 0.01-3 V vs. Na<sup>+</sup>/Na for a) the non-pillared Mo<sub>2</sub>TiC<sub>2</sub> and b) pillared Mo<sub>2</sub>TiC<sub>2</sub>-Si-400.

The CV data was then used to carry out the *b*-value-voltage analysis previously discussed (Figure 5.24). As has been observed for the other MXene studies in this thesis, the charge storage mechanism has contributions from surface- and diffusion-limited processes at all voltages studied.

For the SiO<sub>2</sub>-pillared material, the *b*-values are generally slightly larger than the non-pillared material, but a similar pattern of increased surface-limited (capacitive) current at high voltages and increased contribution from diffusion-limited (battery-like) processes at lower voltages is still followed. At 3 V, the *b*-value was 0.85, slightly larger than the non-pillared material (0.81) showing that even more of the current is capacitive-like at the voltage. At 2 V, the proportion of diffusion-limited current is greater than the surface-controlled current, as shown by a *b*-value of 0.72. This corresponds to a redox peak observed in the CV plots, which is not clearly visible for the non-pillared material (Figure 5.24), which had a *b*-value of 0.79 at 2 V. At 1 V, the pillared material had a *b*-value of 0.87, showing that current is predominately surface-controlled, which is in contrast to the non-pillared material where the *b*-

value was 0.62, showing very different behaviour at this voltage. At 0.01 V, the  $b$ -value was 0.73 (0.74 for the non-pillared MXene), showing a diffusion-limited battery-like process now contributes the majority of the current. On desodiation, the  $b$ -values are 0.89, 0.88 and 0.88 at 1, 2 and 3 V respectively, showing that the majority of the current is surface-controlled, which matches the rectangular shaped CV plot in this region. These  $b$ -values are all higher than the corresponding values for the non-pillared material (0.87, 0.79, 0.79 respectively).

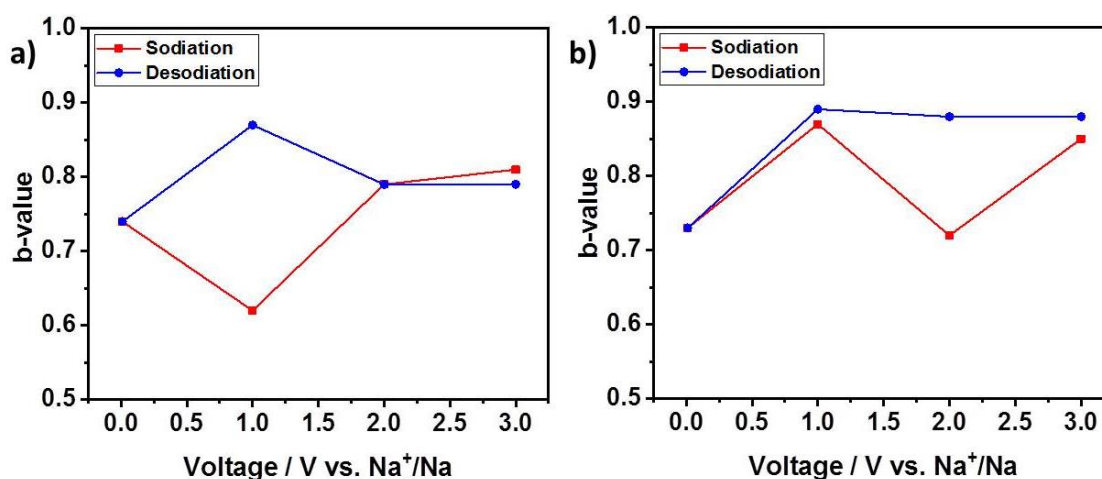


**Figure 5.24.** Plot of  $b$ -values against voltage vs.  $\text{Na}^+/\text{Na}$ . a) Non-pillared  $\text{Mo}_2\text{TiC}_2$ , b) pillared- $\text{Mo}_2\text{TiC}_2$ .

This shows that, as for other systems, the majority of the current originates from capacitive-like processes at higher voltages while the proportion of battery-like diffusion limited processes increases at lower voltages for both the pillared and non-pillared  $\text{Mo}_2\text{TiC}_2$  in the Na-ion system. The enlarged interlayer spacing and higher surface area causes an increase in the proportion of current from capacitive-like processes, as was implied from the more rectangular shape of the high rate CV (Figure 5.23). This helps explain the superior rate performance of the pillared material.

The  $b$ -values for  $\text{Mo}_2\text{TiC}_2$  in the Na-ion system are higher than in the Li-ion system, which is especially apparent at 0.01 V (SiO<sub>2</sub>-pillared  $\text{Mo}_2\text{TiC}_2$  has a  $b$ -value of 0.73 in the Na-ion system, but 0.56 in the Li-ion system). This supports work by Anasori et al., which predicted that the conversion reaction to form  $\text{Na}_2\text{O}$  does not occur for Na, with the charge storage instead relying on  $\text{Na}^+$  intercalation/ adsorption on the MXene surface,<sup>100</sup> which also explains the substantially lower capacities obtained for the Na-ion system.

### 5.3 Conclusions

This chapter has shown that the HCl-LiF method, which avoids the direct handling of concentrated HF solutions, can be applied to  $\text{Mo}_2\text{TiAlC}_2$  to synthesise  $\text{Mo}_2\text{TiC}_2$ , although two etching steps were required to achieve this, and the reaction times (nine days) were much longer than the reported HF method (two days).

In addition, the amine-assisted pillaring method developed for  $\text{Ti}_3\text{C}_2$  MXene in Chapter 4 can be applied directly to the Mo-based MXene  $\text{Mo}_2\text{TiC}_2$ . As was seen for the  $\text{Ti}_3\text{C}_2$  MXene, this leads to a large increase in interlayer spacing, with a *d*-spacing of 4.2 nm achieved. This corresponds to a gallery height of around 3 nm, which is by far the largest for a Mo-based MXene, and larger than any reports found for other Mo-based layered materials such as  $\text{MoS}_2$ . This suggests that the amine-assisted silica pillaring method could be applied to a wide range of MXenes, and perhaps other layered materials, so long as there are sufficient –OH groups present on the surface to bind to the amine. Switching from Ti to Mo on the surface seemed to have little effect on the pillaring process, with similar interlayer distances obtained both before and after calcination for the two MXene compositions. This led to the creation of a new porous material based on Mo surface chemistry, which has very different properties, including electrochemically, than the  $\text{Ti}_3\text{C}_2$  MXene.

When tested as the negative electrode in a lithium-ion battery, the non-pillared material had comparable performance to previous reports on  $\text{Mo}_2\text{TiC}_2$  electrodes, showing that the HCl-LiF etching method does not produce an MXene with inferior electrochemical properties. The pillared material showed significantly improved electrochemical performance, reaching capacities of up to  $316 \text{ mAh g}^{-1}$  (89% of the reported theoretical capacity based on one layer of  $\text{Li}^+$  intercalating followed by a second lithiation layer undergoing a conversion reaction), which is the highest capacity reported so far for  $\text{Mo}_2\text{TiC}_2$ . Since the gallery height in the pillared MXene was 0.75 nm, much larger than four  $\text{Li}^+$  ions ( $0.7 \text{ \AA}$  each), these results imply that the intercalation of multiple layers of  $\text{Li}^+$  may not occur for  $\text{Mo}_2\text{TiC}_2$ , and that the reported theoretical capacity of  $356 \text{ mAh g}^{-1}$  may be a realistic value. As had been seen in the previous chapter, the pillaring process not only increases the capacity of the MXene, but also the cycling stability (possibly by providing free space for the reversible formation of  $\text{Li}_2\text{O}$  without allowing layers to restack) and rate capability (since the enlarged interlayer spacing aids the  $\text{Li}^+$  diffusion to the MXene active site). The pillared material showed high coulombic efficiency (99.9%) and good stability even at a high rate of  $1 \text{ A g}^{-1}$  (a charging time of less than 8 min) returning 80% of an initial capacity of  $135 \text{ mAh g}^{-1}$  after 500 cycles, which suggests it is a promising material to develop for Li-ion capacitor applications. The reversible formation of  $\text{Li}_2\text{O}$  during cycling was confirmed by ex-situ XPS studies, which also suggested  $\text{SiO}_2$  does not undergo significant redox activity during cycling.

In a Na-ion system the capacities of the non-pillared and pillared  $\text{Mo}_2\text{TiC}_2$  MXene were both much lower than for the Li-ion system, which could be explained by the charge storage mechanism utilising only  $\text{Na}^+$  intercalation with no conversion reaction occurring. Nevertheless, the pillared material had superior performance compared to the non-pillared MXene, delivering reversible capacities up to  $109 \text{ mAh g}^{-1}$  and  $40 \text{ mAh g}^{-1}$  even at  $1 \text{ A g}^{-1}$ , over twice that of the non-pillared MXene, showing that even here pillaring led to substantial performance improvement. However, the performance is still low compared to that of other Na-ion negative electrodes, including the  $\text{SiO}_2$ -pillared  $\text{Ti}_3\text{C}_2$  MXene reported in the previous chapter.

# **Chapter Six**

## **MXenes in Zn-ion systems**

## 6.1 Introduction

This chapter reports on results obtained from studies into MXenes for zinc-ion capacitor systems. As previously mentioned, there are widespread concerns about the safety and cost of lithium-ion batteries, with worries about dendrite formation on the negative electrode and the flammability of the organic electrolyte used.<sup>254</sup> Consequently, there is an increasing focus on safer, cheaper alternative metal-ion systems based on cheaper cations which are more evenly distributed on Earth. As well as the sodium-based systems reported in previous chapters, zinc systems are gaining significant interest.<sup>255,256</sup> Zinc is relatively widespread in nature, has a large theoretical capacity greater than 800 mAh g<sup>-1</sup>) and a low potential (-0.76 vs. standard hydrogen electrode (SHE)).<sup>257,258</sup> This potential is within the stable voltage window for water, making zinc metal compatible with aqueous electrolytes, unlike most elements under consideration for rechargeable energy storage systems.<sup>41</sup> Aqueous electrolytes are inherently non-flammable, which gives them significant safety advantages over systems based on organic electrolytes. However, aqueous electrolytes have reduced voltage windows compared to organic electrolytes, due to the hydrogen and oxygen evolution reactions.<sup>49,259</sup> This gives a thermodynamically stable window of 1.23 V, which limits considerably the energy density of aqueous systems and makes the need to find high energy density electrode materials an urgent priority.

Zinc is already widely used in primary (non-rechargeable) batteries, but commercial rechargeable systems have not yet been realised. This is in part because zinc metal forms dendrites when used with certain electrolytes, making the systems non-rechargeable in the long-term. However, it is now known that in some neutral and mildly acidic aqueous electrolytes (pH 4 to 6), such as 0.1 M zinc sulphate (ZnSO<sub>4</sub>) in water, zinc can be reversibly cycled for long duration times without losing significant capacity.<sup>6</sup>

One difficulty has been that the smaller Zn ion size (0.67 Å) and 2<sup>+</sup> charge give rise to poor diffusion kinetics, which has limited the range of available materials. In addition, the materials need to contain multivalent transition metals to allow them to be redox active with Zn. Despite numerous studies on 2D materials in other metal-ion systems, there have been few reports on the use of 2D materials in zinc-ion systems so far, and no reports on the use of MXenes for Zn storage, despite their promising activity in other multivalent systems.<sup>41–43,150,260</sup>

Since Ti<sub>3</sub>C<sub>2</sub> is the most widely studied MXene, it was chosen to study the electrochemical viability of MXenes in Zn-ion systems. It was discovered that Ti<sub>3</sub>C<sub>2</sub> is active towards the reversible insertion/removal of Zn ions, showing promising reversible capacities and good capacity retention upon cycling. In addition, a simple, one-step in-situ pillaring approach in which a surfactant pillar (CTAB) was dissolved in

the electrolyte and intercalated into the MXene within the cell was developed. This increased the interlayer spacing leading to improved electrochemical performance, without the use of more time-consuming pillaring methods such as those developed in previous chapters.

The charge storage mechanism was studied using CV and a variety of ex-situ characterisation techniques. CV studies revealed that the charge storage occurs via a combination of surface-limited and diffusion-limited processes, with a significant contribution from capacitive processes. Ex-situ EDS results revealed that  $\text{Zn}^{2+}$  is the charge carrier, shown by an increase in Zn content upon discharge and a decrease in content upon charge. Ex-situ XRD shows that there are no major phase changes during cycling, and that the in-situ pillaring technique prevents changes in the interlayer spacing that otherwise occur. Ex-situ Raman spectroscopy revealed reversible changes in vibrations corresponding to the Ti-O termination groups, demonstrating that Zn reversibly binds to these sites upon discharge and is removed upon charge. This implied a change in the Ti valence state upon cycling, which was confirmed by ex-situ XPS studies, where a reversible shift in the Ti oxidation state was observed.

For comparison, some ex-situ pillaring methods using CTAB and the amine-assisted silica pillaring technique developed in the previous chapters are also studied. In addition, having established that  $\text{Ti}_3\text{C}_2$  is promising as a reversible zinc-ion host,  $\text{Mo}_2\text{TiC}_2$  was also tested to investigate the viability of Mo-based MXenes in Zn systems. Finally,  $\text{Ti}_3\text{C}_2$  was also tested in an organic electrolyte, with a wider voltage window than the aqueous electrolyte, to investigate if this would lead to a system with a higher energy density.

## 6.2 $\text{Ti}_3\text{C}_2$ in Aqueous Zn Electrolyte

### 6.2.1 Synthesis, Pillaring and Characterisation

PXRD data shows that the  $\text{Ti}_3\text{C}_2$  MXene was successfully etched from the parent  $\text{Ti}_3\text{AlC}_2$  MAX phase (Figure 6.1). This is indicated by the loss of typical  $\text{Ti}_3\text{AlC}_2$  diffraction peaks and the shift of the (002) diffraction peak to lower angles (from  $9.6$  to  $8.1^\circ 2\theta$ ), which corresponds to the increased interlayer spacing after the removal of the Al layer, as seen in previous chapters. SEM analysis confirms that the layered structure of the MXene is retained after etching (Figure 6.2), in agreement with previous reports.<sup>86,114</sup>

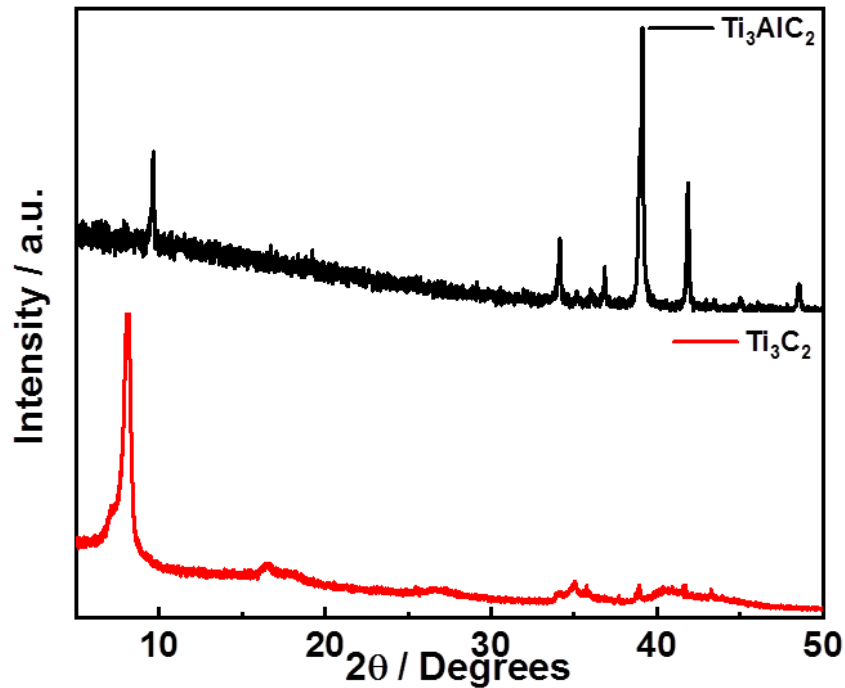


**Figure 6.1.** XRD comparison of a) the commercial  $\text{Ti}_3\text{AlC}_2$  MAX phase precursor and b) the etched  $\text{Ti}_3\text{C}_2$  MXene.

The morphology looks denser and less open than in previous chapters, which is likely to be a result of differences in the starting MAX phase material used in the different chapters. In this case a commercial  $\text{Ti}_3\text{AlC}_2$  powder (Y Carbon Ltd.) was used. SEM-EDS results show that only 0.2 wt.% of Al is present in the MXene, confirming the selective etching and transformation from  $\text{Ti}_3\text{AlC}_2$  to  $\text{Ti}_3\text{C}_2$  (Figure 6.2). EDS results also show that the  $\text{Ti}_3\text{C}_2$  contains the typical terminal elements O (11 wt.%), F (6 wt.%) and Cl (2.5 wt.%) which bind to the Ti layer during the etching process.

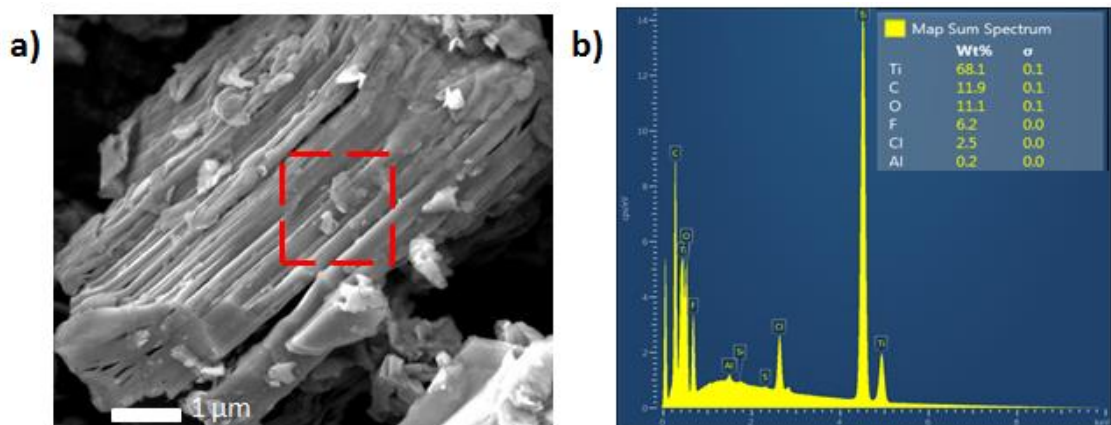


**Figure 6.2.** SEM and EDS analysis of the as-etched non-pillared  $\text{Ti}_3\text{C}_2$  MXene. a) SEM micrograph of  $\text{Ti}_3\text{C}_2$  b) EDS results of  $\text{Ti}_3\text{C}_2$ . The dashed box indicates the area the EDS spectrum was collected over.

Two sets of CTAB pillaring experiments were then carried out for investigation in the Zn-ion system. An in-situ pillaring method was developed whereby a small amount of CTAB was dissolved in the 0.1 M ZnSO<sub>4</sub> electrolyte, which was used as the active electrolyte during cell assembly, with the hypothesis of CTA<sup>+</sup> intercalating as a pillar within the cell by the end of the first discharge. Such a process would avoid the multiple intercalation and separation steps needed in standard pillaring techniques, such as those described in previous chapter and the previously reported ex-situ CTAB pillaring method described below. This process is shown schematically in Figure 6.3. This material is referred to as the in-situ pillared material for the remainder of the thesis.

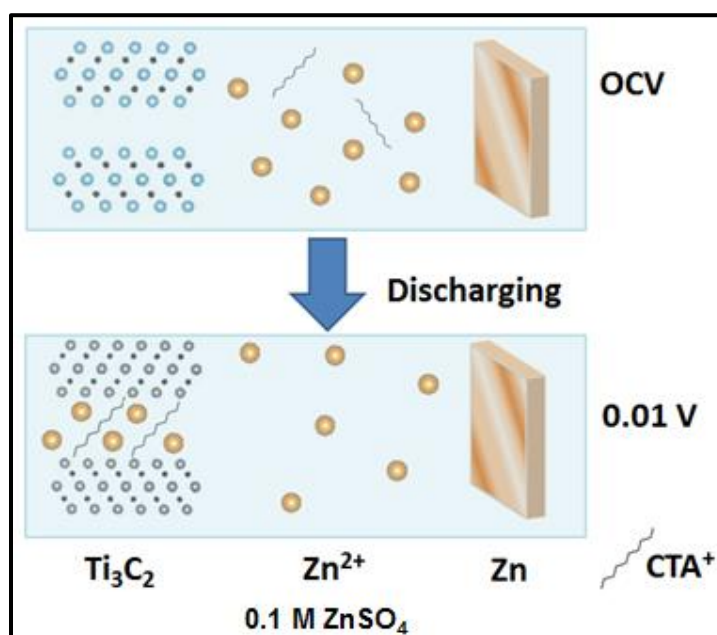


**Figure 6.3.** Schematic illustrating the in-situ pillaring process.

To help understand the in-situ pillared material and as a comparison, an ex-situ pillared MXene sample was also used. Here CTAB was pre-intercalated into Ti<sub>3</sub>C<sub>2</sub> based on the method reported by Luo et al.<sup>261</sup> Briefly, 200 mg of Ti<sub>3</sub>C<sub>2</sub> were dispersed in a solution of DI water (30 ml) and CTAB (100 mg). The dispersion was stirred for 24 h at 40 °C. The pillared MXene was then recovered by vacuum filtration and dried at 60 °C overnight. This is referred to as the ex-situ or pre-pillared material.

The XRD data for the in-situ pillared sample is shown in blue (Figure 6.4). There was a further increase in the interlayer spacing as evidenced through a shift in the (002) diffraction peak from 8.1 to 5.9° 2θ, which suggests successful pillaring. This corresponds to an increase in *d*-spacing from 1.1 nm in the as-etched MXene to 1.5 nm in the in-situ pillared material. Since a single Ti<sub>3</sub>C<sub>2</sub> layer has a reported thickness of 0.95 nm,<sup>189</sup> the pore space between the layers has increased from around 0.15 nm to 0.55 nm (ca. 3.7 fold increase). For comparison, pre-intercalating CTAB via the ex-situ pillaring approach also resulted in a shift in the (002) diffraction peak to 5.9° 2θ, albeit with a slighter broader peak, including at lower angles, showing that the two

methods give a consistent interlayer spacing. A similar shift in the (006) diffraction peak to  $18.0^\circ$   $2\theta$  in both samples also supports this, with a common  $d$ -spacing of 0.49 nm. The interlayer spacing obtained here is much smaller than the chain length of  $\text{CTA}^+$  (2.5 nm), suggesting that the cation is intercalated at an angle.<sup>261</sup> This suggests that the in-situ method is a viable technique for intercalating pillars and enlarging the interlayer spacing.

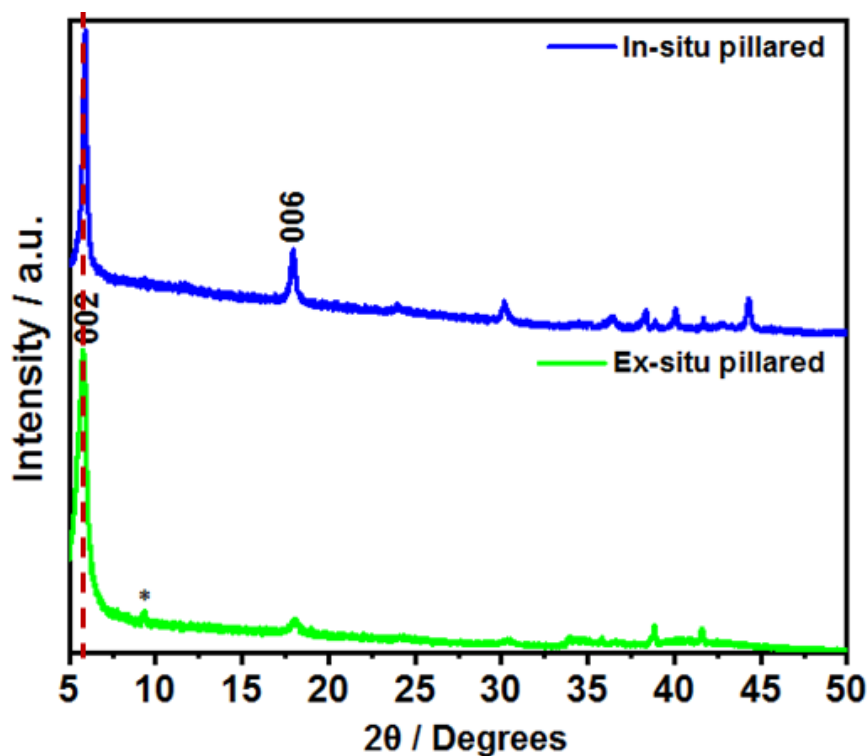


**Figure 6.4.** XRD comparison of  $\text{Ti}_3\text{C}_2$  pillared with CTAB using the a) in-situ method and b) ex-situ method. \* denotes a small amount of un-etched  $\text{Ti}_3\text{AlC}_2$  precursor remaining in the sample. The dashed red line highlights the position of the (002) diffraction peak for both samples.

TGA was then carried out to determine the total mass of CTAB which was intercalated into  $\text{Ti}_3\text{C}_2$  using the pre-intercalation ex-situ method. The as-made MXene and CTAB intercalated samples were run as powders in air inside the TGA, which included DSC as well as monitoring the mass changes (Figure 6.5). The mass change curves are very different between the two samples. The as-made MXene has a gradual loss of mass between 25 and 200 °C. This is due to the loss of intercalated water present in the samples. At temperature greater than 200 °C there is a gradual increase in mass, which becomes a rapid increase between 370 and 580 °C. This is assigned to the oxidation of the titanium in  $\text{Ti}_3\text{C}_2$  to titanium dioxide, which causes the sample to take up oxygen from the air and therefore increases the mass of the sample. Above 580 °C a mass loss is recorded which is due to the loss of carbon from the MXene as this oxidises to  $\text{CO}_2$ . The DSC curves matches well with these mass

changes, with a broad peak centred around 400 °C corresponding to the titanium oxidation and a sharp peak at just under 600 °C corresponding to the oxidation of the carbon layer to CO<sub>2</sub>. For the CTAB intercalated material, there is also a gradual mass loss up to 200 °C due to the removal of intercalated water, and a gradual increase in mass between 200 and 250 °C corresponding the titanium oxidation. However, above 250 °C the sample begins to lose mass, with a series of small steps down to a stable mass by 700 °C. This is a result of the decomposition and oxidation of CTAB intercalated within the sample. In addition, the DSC curve shows an extra peak compared to the as-made MXene also due to the decomposition of CTAB, further confirming the presence of CTAB within the sample. Figure 6.5c shows the difference in mass between the as-made MXene as the CTAB pillared MXene, ( $Ti_3C_2$  mass –  $Ti_3C_2$ -CTAB mass). It can be seen that by 700 °C, when the mass losses level off, that there is an 18.2% difference between the mass of the two samples. This suggests that the CTAB pillared material contained 18.2% by mass CTAB. This mass was used to correct the active mass used for the specific capacity results in the galvanostatic charge-discharge tests, to allow direct comparison between the non-pillared, ex-situ pillared and in-situ pillared MXenes.

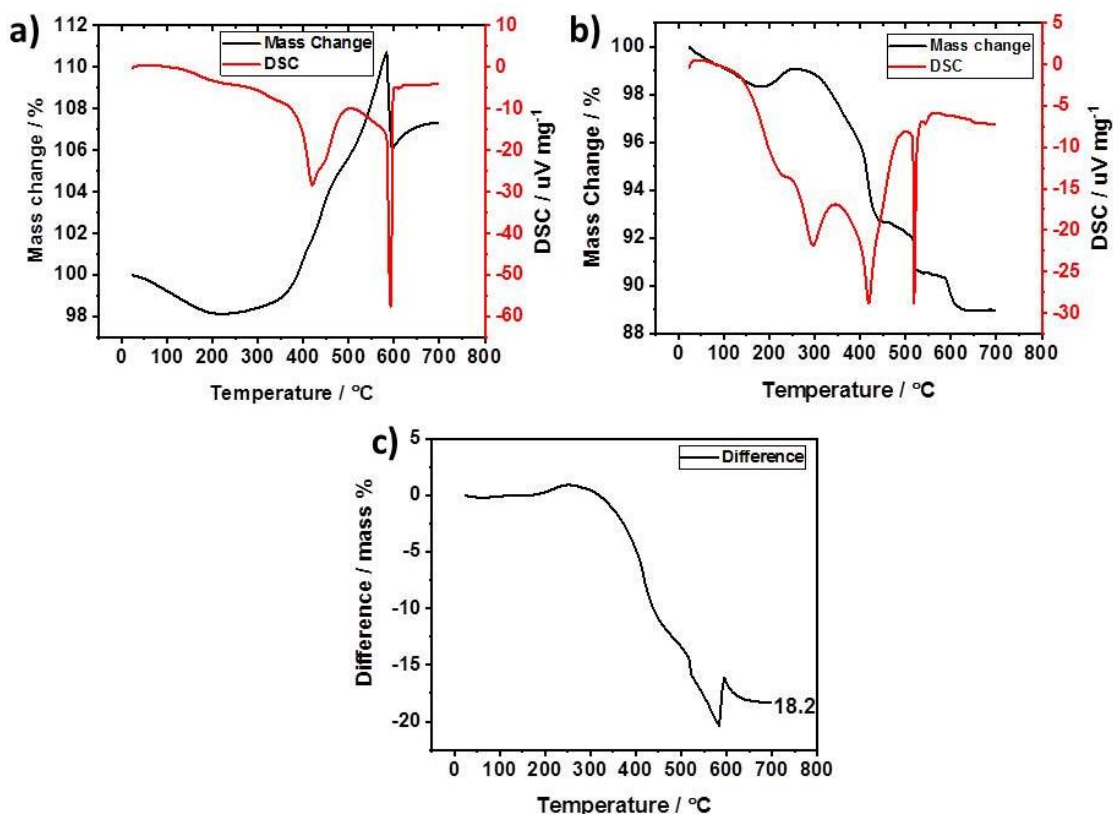


**Figure 6.5.** TGA and DSC studies comparing a) the non-pillared  $Ti_3C_2$  as-made material and b) the CTAB ex-situ pillared material. Figure c shows the difference in mass between the as-made MXene as the CTAB pillared MXene, ( $Ti_3C_2$  mass –  $Ti_3C_2$ -CTAB mass).

## 6.2.2 Electrochemical Testing

Having established that the in-situ and ex-situ pillaring methods had successfully intercalated CTAB into the MXene electrochemical testing was carried out to investigate the materials' potential as Zn-ion hosts. Since  $\text{Ti}_3\text{C}_2$  was untested in a Zn-ion system, CV analysis was carried out to determine the stable voltage window for  $\text{Ti}_3\text{C}_2$  in 0.1 M  $\text{ZnSO}_4$  using a scan rate of  $1 \text{ mV s}^{-1}$ . (Figure 6.6) The non-pillared MXene has a fairly rectangular voltammogram up to around 1.2 V, after which the current increases sharply. This was assigned to water splitting since the reaction was non-reversible. No similar distortion was seen at the lower voltage cut-off of 0.01 V. Therefore the voltage window of 0.01-1 V vs.  $\text{Zn}^{2+}/\text{Zn}$  was used for further studies, since this is well within the stable voltage window. The CTAB-pillared material does not begin to show this distortion until around 1.35 V, suggesting that the pillaring inhibits the water splitting reaction, giving this system a wider voltage window. Nevertheless, to allow for fair comparison, the window of 0.01-1 V was also used for this system.

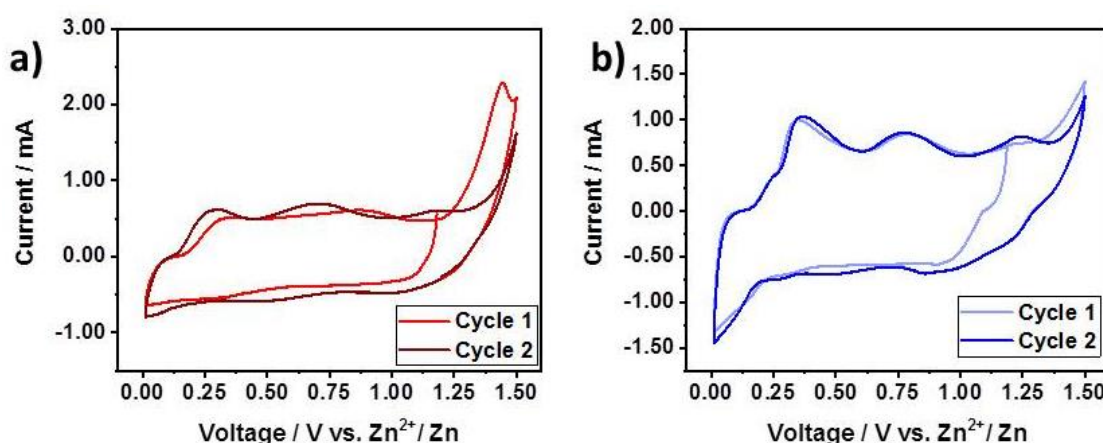


**Figure 6.6.** CV scans at  $1 \text{ mV s}^{-1}$  between 0.01 V and 1.5 V vs.  $\text{Zn}^{2+}/\text{Zn}$  to determine stable voltage window for  $\text{Ti}_3\text{C}_2$  in a) 0.1 M  $\text{ZnSO}_4$  and b) 0.1 M  $\text{ZnSO}_4$  with CTAB additive (0.1 wt.% of electrolyte).

Galvanostatic charge-discharge tests were then carried out at a rate of  $20 \text{ mA g}^{-1}$  between 0.01-1 V on the as-made MXene, the in-situ pillared MXene with CTAB as an electrolyte additive, and the ex-situ pillared CTAB containing MXene, which was prepared as a reference to compare with the in-situ pillaring method (Figure 6.7). It can be seen that all three samples show significant reversible capacity in the zinc-ion system with a similar sloping voltage profile. The voltage profile is nearly linear which is consistent with a capacitive type charge storage mechanism with no major phase changes during cycling, and is similar with those reported for  $\text{Ti}_3\text{C}_2$  in other metal-ion systems<sup>148,169,238,251</sup>. This is further supported by the ex-situ XRD results (Section 6.2.3.1), which show no phase changes occur during cycling. The as-made MXene has a 2<sup>nd</sup> cycle discharge capacity of  $76 \text{ mAh g}^{-1}$ , the pre-pillared material has a discharge capacity of  $61 \text{ mAh g}^{-1}$  and the in-situ pillared  $\text{Ti}_3\text{C}_2$  has the largest discharge capacity

at 92 mAh g<sup>-1</sup>. All three materials also show large irreversible capacity losses on the first cycle, with coulombic efficiencies of 52%, 69% and 39% respectively on the first cycle. This is also observed for Ti<sub>3</sub>C<sub>2</sub> in organic Li and Na systems, where it has been explained by the formation of a solid-electrolyte interphase (SEI) and trapping of the charge carrying cation by irreversible reaction with some surface groups on the MXene<sup>148,238</sup>. It is unlikely that a stable SEI forms here, due to the low concentration of electrolyte used, which means that any reduction products are likely dissolved.<sup>262</sup> However, the formation of any irreversible reduction products would contribute to this irreversible capacity. A more likely explanation applicable to the MXene behaviour here is irreversible Zn trapping, with the CTAB pre-pillared MXene showing the lowest capacity loss due to the CTAB already interacting with some surface groups, leaving them unable to react with Zn during cycling. The in-situ pillared material shows the largest loss, since the MXene is being opened up by the in-situ pillaring on the first cycle, exposing a greater proportion of fresh Ti<sub>3</sub>C<sub>2</sub> surface to the electrolyte for irreversible Zn trapping. This initial irreversible capacity loss is further investigated by ex-situ Raman spectroscopy and EDS (Section 6.2.3.2), where Zn trapping is demonstrated. By the 20<sup>th</sup> cycle, the coulombic efficiency had dramatically increased to over 90% in all cases, showing that the reversibility of the MXene electrodes increased upon early cycling.

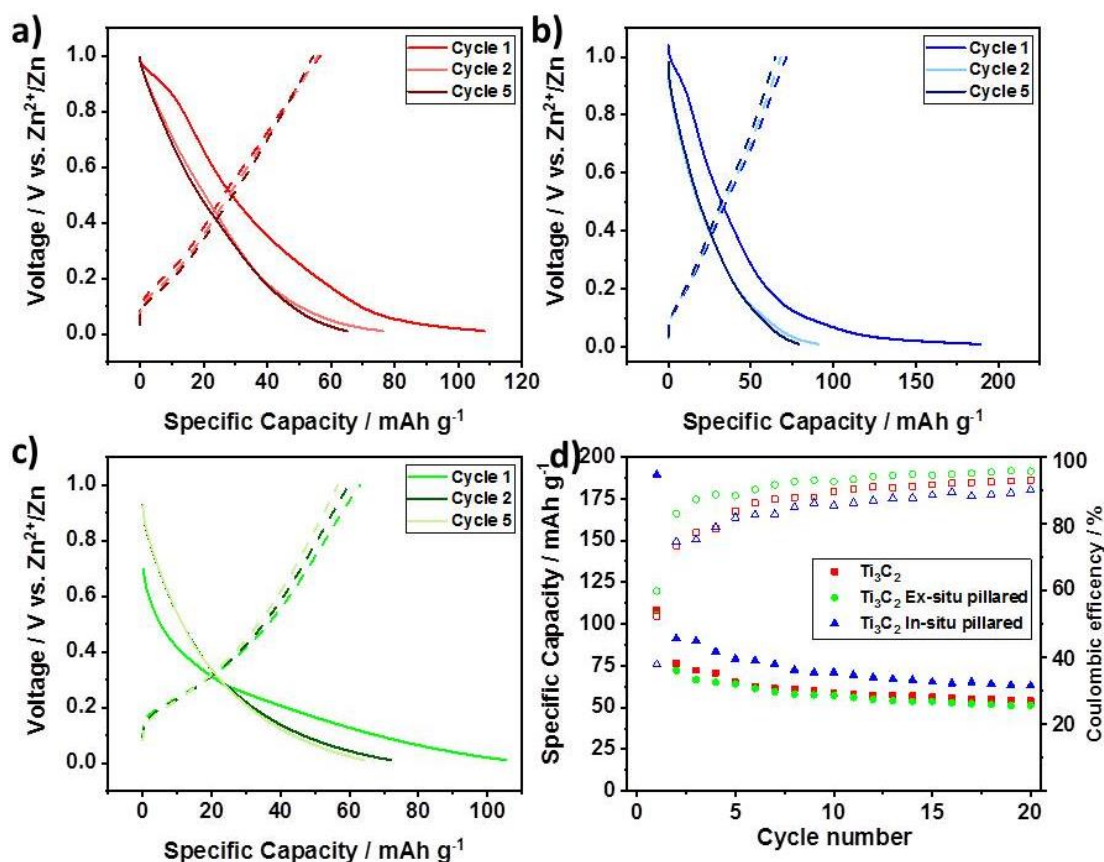


**Figure 6.7.** Galvanostatic charge-discharge testing of the Ti<sub>3</sub>C<sub>2</sub> electrodes in 0.1 M ZnSO<sub>4</sub>. a - c) Load curves at a current density of 20 mA g<sup>-1</sup> of a) Ti<sub>3</sub>C<sub>2</sub> b) the in-situ pillared Ti<sub>3</sub>C<sub>2</sub> and c) the ex-situ pillared Ti<sub>3</sub>C<sub>2</sub>. d) Discharge capacities and coulombic efficiencies over 20 cycles at

20 mA h g<sup>-1</sup> for the in-situ, ex-situ pillared and non-pillared Ti<sub>3</sub>C<sub>2</sub> materials. The capacity for the ex-situ pillared material has been corrected using the TGA results to account for the mass of CTAB in the sample, estimated to be 18.2 wt.%.

To further investigate the cycling performance of Ti<sub>3</sub>C<sub>2</sub> in the Zn-ion system, the materials were tested for 20 cycles. The in-situ pillared MXene again showed the best performance, with a discharge capacity of 62 mAh g<sup>-1</sup> being retained after 20 cycles (67% of the 2<sup>nd</sup> cycle capacity). In comparison, the as-made MXene only had a capacity of 54 mAh g<sup>-1</sup> after 20 cycles and the CTAB pre-pillared material showed only 42 mAh g<sup>-1</sup>. All three materials showed significant capacity loss over the 20 cycles, which is likely to be due to the degradation of the electrode and / or irreversible reactions with the charge carrier.

Rate capability tests were carried out on the in-situ pillared and non-pillared MXene to investigate the effect of the current density on cycling performance (Figure 6.8). The materials were cycled at 20, 50, 200, 500 and 1,000 mA g<sup>-1</sup>. It can be seen that the in-situ pillared material has the highest capacity at each rate, achieving average capacities of 86 mAh g<sup>-1</sup>, 59 mAh g<sup>-1</sup>, 52 mAh g<sup>-1</sup>, 38 mAh g<sup>-1</sup> and 27 mAh g<sup>-1</sup> at 20, 50, 200, 500 and 1,000 mA g<sup>-1</sup> respectively. After the high rate testing, the rate was switched back to 20 mA h g<sup>-1</sup> and the capacity recovered back to 67 mAh g<sup>-1</sup>. This shows that the MXene responds well to high rate cycling and is not damaged by fast charging or discharging. In comparison, the as-made MXene showed capacities of 61, 45, 40, 27 and 17 mAh g<sup>-1</sup> at the respective rates. When the rate was returned to 20 mA g<sup>-1</sup>, the capacity recovered to 56 mAh g<sup>-1</sup>, again showing that the electrode is not damaged by high rates.

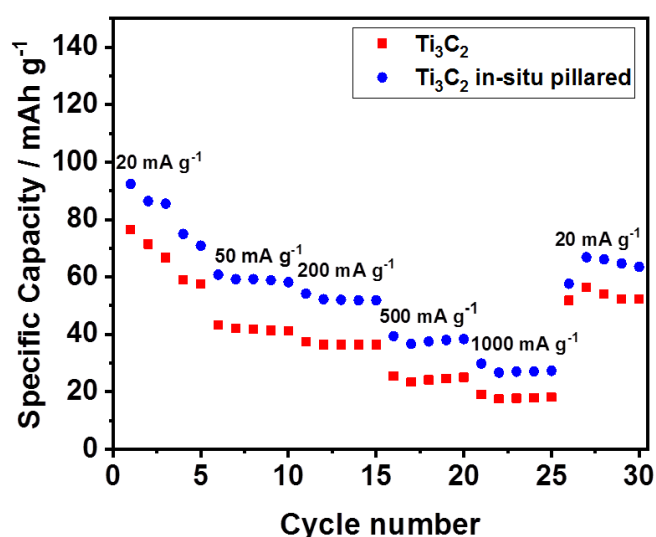


**Figure 6.8.** Rate capability tests of the non-pillared (Ti<sub>3</sub>C<sub>2</sub>) and in-situ pillared (Ti<sub>3</sub>C<sub>2</sub> in-situ pillared) materials. The cells were run at increasing rates of at rates of 20, 50, 200, 500 and 1,000 mA g<sup>-1</sup>.

To gain more insight into the charge storage on the zinc-ion cell and the kinetics of the system, cyclic voltammetry (CV) studies were carried out on the as-made MXene

and the in-situ pillared system (Figure 6.9). Cells were first cycled at a sweep rate of  $0.1 \text{ mV s}^{-1}$  for five cycles between 0.01 and 1 V before further cycling at sweep rates of 0.5, 2 and  $5 \text{ mV s}^{-1}$ . Both materials show quasi-rectangular CV plots, but with broad redox peaks at 0.2 V (vs.  $\text{Zn}^{2+}/\text{Zn}$ ) on the cathodic sweep and at just above 0.01 V on the anodic sweep. In addition, an extra broad peak is observed at around 0.7 V on the cathodic sweep after the initial cycle in the non-pillared material and in all cycles for the in-situ pillared material. This is in contrast to the reported CV plots of  $\text{Ti}_3\text{C}_2$  in other sulphate electrolytes such as  $\text{H}_2\text{SO}_4$ ,  $\text{Li}_2\text{SO}_4$  and  $\text{Na}_2\text{SO}_4$ ,<sup>114,136,160,198</sup> where no sharp redox peaks are observed and the plots are much more rectangular in shape. This suggests that the MXene behaves differently in the  $\text{ZnSO}_4$  than it does in other  $\text{SO}_4$  electrolytes, with increased redox features. Nevertheless, the quasi-rectangular shape of  $\text{Ti}_3\text{C}_2$  in the zinc-ion system suggests that there is also a large capacitive contribution to the charge storage here, which is the dominant charge storage mechanism in these other systems. When the sweep rate is increased, the CV plots for the as-made MXene become stretched, although a good rectangular shape is retained at  $0.5 \text{ mV s}^{-1}$ . At the sweep rates of 2 and  $5 \text{ mV s}^{-1}$ , it becomes difficult to distinguish the 0.2 V peak. For the in-situ pillared material, the CV plots retain the quasi-rectangular shape across all rates studied, suggesting faster kinetics, although slight distortions still occur. In addition, the broad cathodic peaks at 0.2 and 0.7 V are still noticeable at all rates, but have shifted to higher voltages as the rate increases (to 0.4 and 0.95 V respectively by  $5 \text{ mV s}^{-1}$ ).

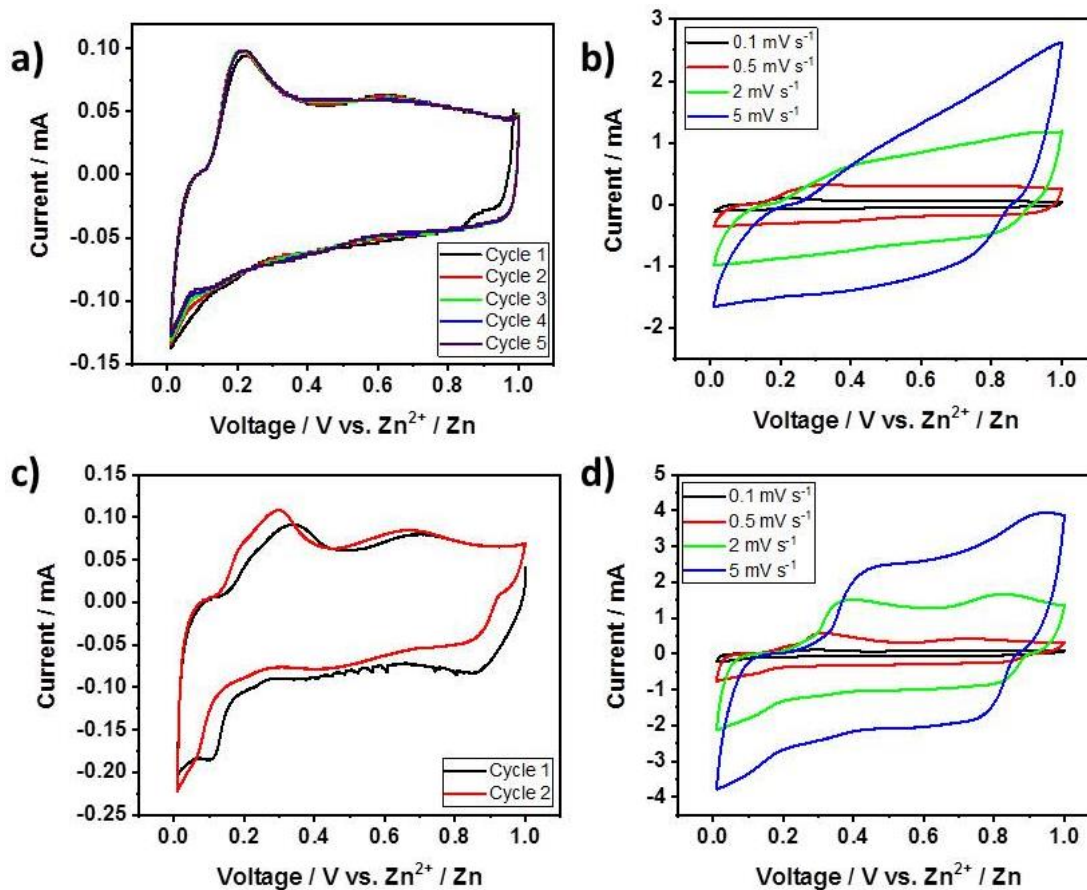


**Figure 6.9.** Cyclic voltammograms for: a) non-pillared  $\text{Ti}_3\text{C}_2$  at  $0.1 \text{ mV s}^{-1}$  for five cycles, b) non-pillared  $\text{Ti}_3\text{C}_2$  at  $0.1, 0.5, 2$  and  $5 \text{ mV s}^{-1}$ , c) in-situ pillared  $\text{Ti}_3\text{C}_2$  at  $0.1 \text{ mV s}^{-1}$  for two cycles (Only two cycles were run due to time constraints on the equipment), d) in-situ pillared  $\text{Ti}_3\text{C}_2$  at  $0.1, 0.5, 2$  and  $5 \text{ mV s}^{-1}$ .

As previously described (Section 3.2.3.13), there are three main charge storage mechanisms found in electrochemical energy storage devices: faradaic diffusion-limited redox reactions (for example, intercalation reactions found in typical battery materials), faradaic surface-controlled redox reactions (i.e. pseudocapacitance) and non-faradic electric double layer capacitance. It is known that the contribution of the diffusion limited contribution and the capacitive contribution to the charge storage can be separated out using the CV profiles at different rates. The relationship between the current ( $i$ ) and scan rate ( $v$ ) is given by Equation 6.1:

$$i = av^b \quad \text{Equation 6.1}$$

where  $a$  and  $b$  are fitting parameters.<sup>239</sup> Importantly, a  $b$ -value of  $0.5$  corresponds to a diffusion-limited process (i.e. battery-like charge storage) and a  $b$ -value of  $1$  indicates a surface-controlled process (i.e. capacitive charge storage). A plot of  $\log(i)$  against  $\log(v)$  gives a straight line with a slope of  $b$ . Analysis on the as-made MXene gives average  $b$ -values (Figure 6.10) of  $0.76$  and  $0.73$  for the cathodic and anodic currents respectively, showing that the charge storage is due to a mixture of

mechanisms with both diffusion-limited and surface-limited processes contributing to the overall capacity. For the in-situ pillared material  $b$ -values of 0.85 and 0.84 are obtained, showing that the proportion of charge storage due to capacitive processes has increased compared to the as-made MXene. In fact, the majority of the current is now derived from capacitive surface-controlled current. This is the case for both the cathodic and anodic currents. This is consistent with the rate capability tests, which showed that the in-situ pillared  $\text{Ti}_3\text{C}_2$  had a superior performance at high rates, as expected for a greater contribution from capacitive processes. This can be explained by increased interlayer spacing from the intercalation of CTAB between the nanosheets, which increases the amount of surface exposed for charge storage, and is likely to reduce the diffusion barriers at the same time. This is further studied by ex-situ XRD analysis in the next section.

When the  $b$ -value obtained at different voltages is plotted<sup>210</sup> (Figure 6.10) there is significant voltage dependence for the mechanism of charge storage. At low voltages (less than 0.4 V) the dominant contribution to the charge storage comes from diffusion-limited processes, both with and without the CTAB additive. As the voltage increases, the proportion of the capacitive contribution increases too, so that by 1 V all the charge storage comes from capacitive contributions (the  $b$ -value is equal to 1). At all voltages below 1 V, the cell containing the CTAB additive has a higher capacitive contribution than the as-made MXene, which is consistent with the average  $b$ -values. These results match the CV curves well, where there is a distinctive peak between 0.2-0.4 V depending on the scan rate, which is suggestive of a faradaic diffusion-limited battery-like reaction. Above 0.5 V, the CV curves have a rectangular shape, suggestive of a capacitive charge storage mechanism, which the  $b$ -values show to be the dominant mechanism in this voltage range. This shows that as well as there being multiple charge storage mechanisms occurring in the MXene, they contribute differently to the overall charge storage at different voltages. A similar relationship between the charge storage mechanism and voltage was reported in organic Li-ion systems by Wang et al.,<sup>263</sup> which suggests that this may be a common feature of MXenes.

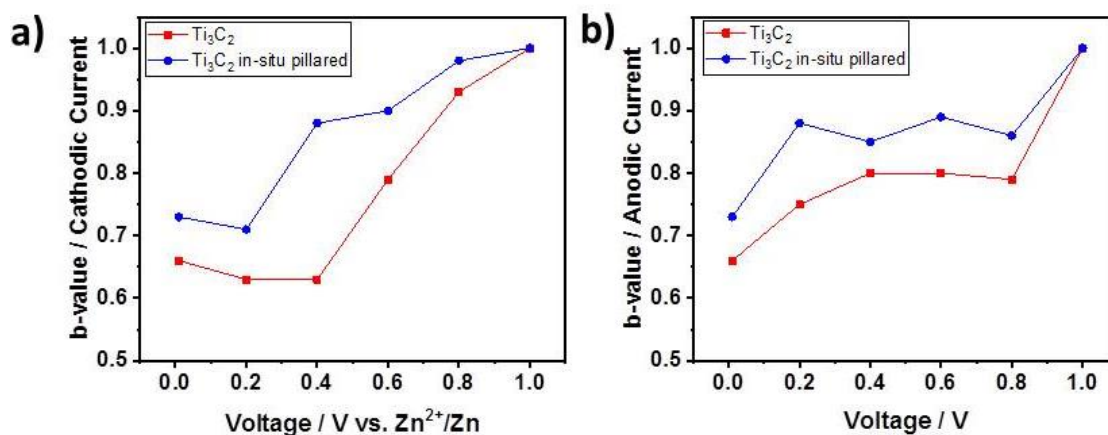


**Figure 6.10.** Plot of the  $b$ -value against voltage for the un-pillared and in-situ pillared  $\text{Ti}_3\text{C}_2$ . a) Cathodic current. b) Anodic current.

## 6.2.3 Structural Changes During Cycling

### 6.2.3.1 Ex-situ Powder X-ray Diffraction

To study the structural changes during cycling, ex-situ PXRD studies were carried out on the non-pillared (Figure 6.11) and in-situ-pillared (Figure 6.12) MXene. Figure 6.11 shows that the interlayer distance at OCV for the non-pillared  $\text{Ti}_3\text{C}_2$  is significantly enlarged compared to the pristine MXene, with a shift of the (002) diffraction peak from  $8.1^\circ 2\theta$  in the pristine material to  $5.9^\circ 2\theta$  at OCV, with a small shoulder present at higher angles leading to a small peak at  $7^\circ 2\theta$ . This is a larger interlayer spacing than reported for  $\text{Ti}_3\text{C}_2$  in organic electrolytes for Li and Na systems (which typically see the peak shift to around  $7^\circ 2\theta$ ),<sup>148,238</sup> suggesting there is a large number of water layers intercalated. Since the (002) diffraction peak relates directly to the interlayer distance in the electrode material, and gives a gallery height of around 0.55 nm, which is significantly larger than the ratio of a  $\text{Zn}^{2+}$  ion (0.074 nm),<sup>264</sup> the XRD shows that there is no size restriction for the intercalation of de-solvated  $\text{Zn}^{2+}$  ions. EDS (Table 6.1) confirms that Zn is detected in the MXene electrode after soaking, showing that it can spontaneously intercalate into  $\text{Ti}_3\text{C}_2$ . Since the interlayer spacing is so large, this must be intercalated in a solvated state ( $[\text{Zn}(\text{H}_2\text{O})_6]^{2+}$ ) with a large amount of water also between the layers. Zinc has a hydrated ionic radius of 0.43 nm<sup>255</sup>, which is still significantly smaller than the available space between the layers. No significant difference is observed between the in-situ pillared and non-pillared MXene (Figure 6.12) at this stage.

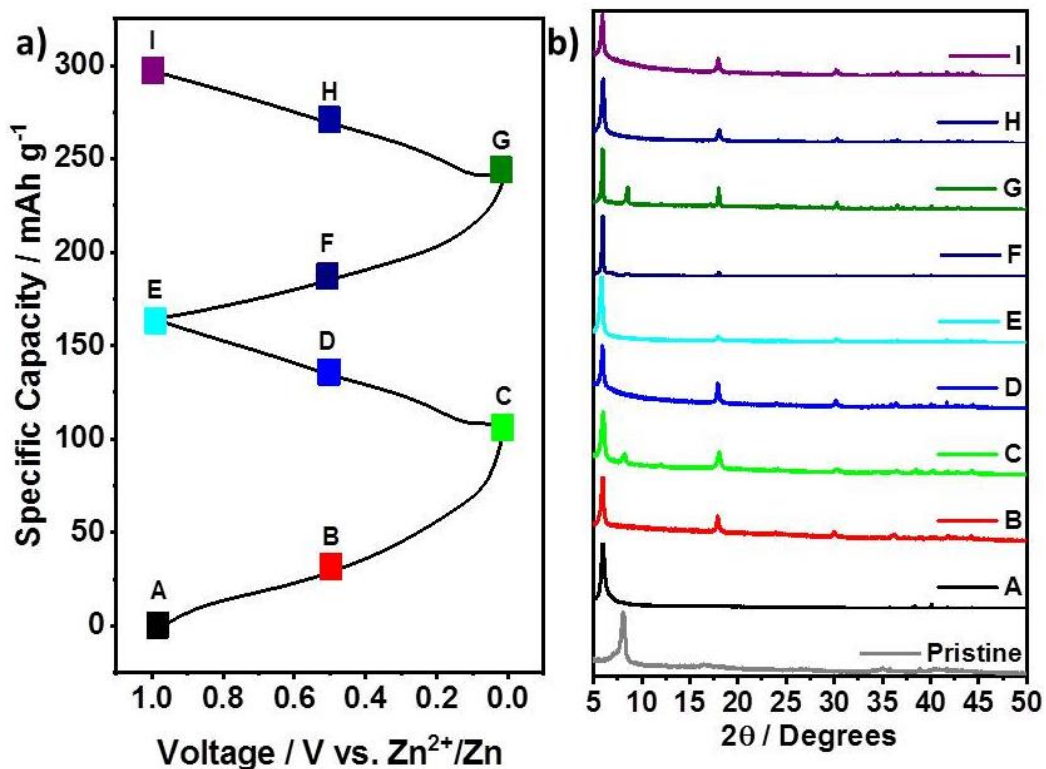


**Figure 6.11.** Ex-situ XRD of the non-pillared Ti<sub>3</sub>C<sub>2</sub>. a) Load curve showing the depth of charge each electrode was stopped at. b) Corresponding diffraction patterns.

Upon discharging to 0.5 V, almost no change is detected in the XRD compared to the material at OCV, apart from the creation of two small new peaks at 18° and 30° 2θ, which are assigned as the (004) and (006) diffraction peaks of Ti<sub>3</sub>C<sub>2</sub>. In addition, the (002) diffraction peak at 5.9° 2θ has sharpened slightly and lost a shoulder which was present at the higher angle side of the OCV electrode, suggesting an increase in the uniformity of the interlayer distances (see the inset Figure 6.12). This implies that Zn and / or water has been intercalated into Ti<sub>3</sub>C<sub>2</sub>, which has expanded previously unfilled interlayers which made up the shoulder of the (002) diffraction peak and caused a slight shift to lower angles i.e. a larger interlayer distance (see the inset of Figure 6.12). When the electrode is fully discharged to 0.01 V, a new peak appears at 8.4° 2θ. This is assigned as a split of the (002) diffraction peak with a smaller interlayer distance than the 5.9° 2θ diffraction peak. When the cell is charged to 1 V this new peak 8.4° 2θ then disappears, showing that all sheets are evenly spaced again. The same pattern is repeated on the second cycle.

**Table 6.1.** Ex-situ EDS data showing increased Zn content during discharging and decreased Zn content during charging. This supports  $\text{Zn}^{2+}$  being the charge carrier in this system.

Electrodes at different states of charge	Average Zn: Ti ratio ( $\text{Ti}_3\text{C}_2$ )	Average Zn: Ti ratio ( $\text{Ti}_3\text{C}_2$ in-situ pillared)
OCV	0.093	0.097
1 <sup>st</sup> discharge (0.01 V)	0.19	0.26
1 <sup>st</sup> Charge (1 V)	0.15	0.19
2 <sup>nd</sup> discharge (0.01 V)	0.21	0.25
2 <sup>nd</sup> Charge (1 V)	0.15	0.19

With the exception of the split of the (002) peak, no extra diffraction peaks from new phases are observed, confirming that the Zn storage occurs without a phase change, which fits well with the sloping profile of the load curve (Figure 6.7). In addition, the (002) diffraction peak is at  $5.9^\circ$   $2\theta$  for all states of charge showing that the electrode sees negligible volume change during cycling when pillared. (There is a very small variation which is likely to be due to small differences in dehydration of the samples for each run e.g. from temperature variations in the lab).

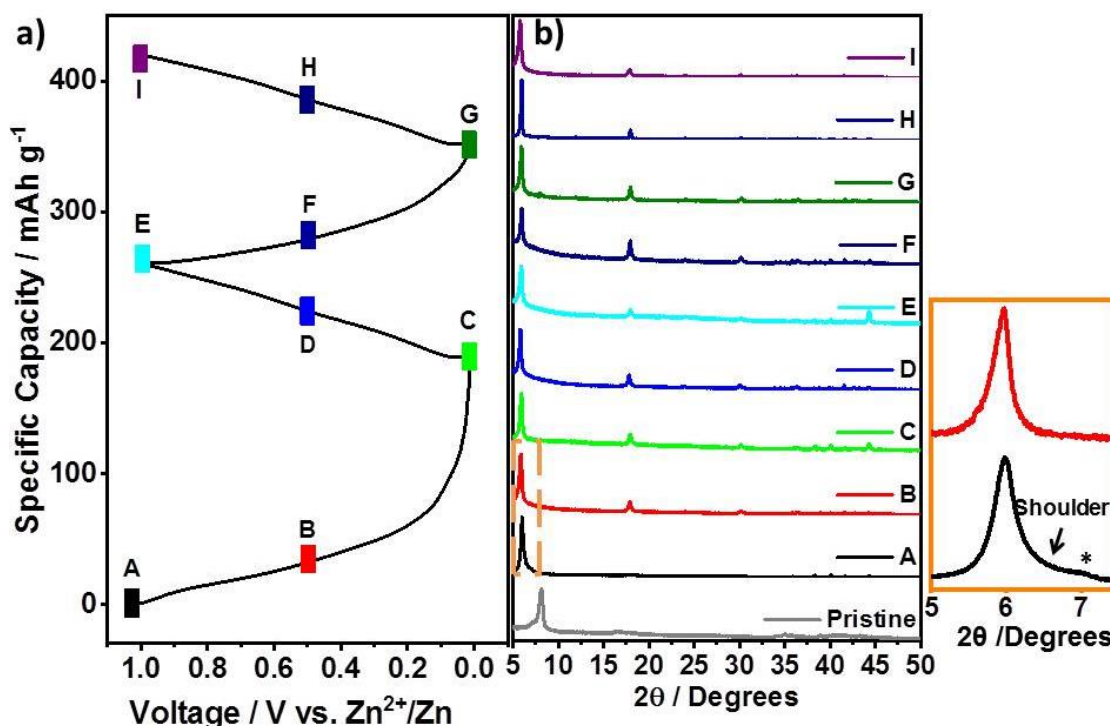


**Figure 6.12.** Ex-situ XRD data of the in-situ pillared  $\text{Ti}_3\text{C}_2$  material at different states of charge in the voltage window 0.01-1 V. a) Load curve highlighting the state of charge at which each electrode was stopped at and analysed; b) Corresponding X-ray diffraction data for each state of charge. The orange rectangle shows a zoom in region of the (002) diffraction peak at OCV state and during the first discharge to 0.5 V, highlighting the loss of the shoulder (arrow and asterisk showing small peak at  $7^\circ$ ) and sharpening of the peak as all layers appear to be intercalated.

In an ex-situ study of  $\text{Ti}_3\text{C}_2$  in an organic lithium electrolyte, Cheng et al. also found that the (002) diffraction peak split, and that the intensity of the high angle peak increased at low voltages (discharged state) and decreased in intensity when the voltage increased (charged state).<sup>238</sup> They assigned this to a sequential intercalation mechanism where the Li intercalated into  $\text{Ti}_3\text{C}_2$  with the large interlayer spaced sites preferentially (i.e. first) at the higher voltages. Once these are filled, the Li then intercalates into the smaller interlayer sites. This then reverses when the electrode is charged. An alternative explanation could be that at low voltages (as the cell discharges, and extra Zn intercalates), some solvent molecules are expelled from the interlayer space, potentially allowing  $\text{Zn}^{2+}$  to pull the layers together through electrostatic attraction. This process of pulling the sheets together and expelling water or intercalation of  $\text{Zn}^{2+}$  into smaller sites would correspond to the diffusion-limited process identified via the CV analysis at low voltages.

This split is not visible for the in-situ pillared material. Cheng et al. also noticed that when  $\text{NH}_4^+$  was pre-intercalated, the interlayer spacing enlarged, removing the sites with small interlayer spacings as shown by their PXRD results.<sup>238</sup> That the same effect is observed here with the in-situ pillaring method suggests that  $\text{CTA}^+$  was successfully intercalated between the layers and is indeed acting as an in-situ pillar for the MXene. This increased interlayer spacing means that the sheets are not pulled together which removes the volume change upon cycling, leading to improved stability of the electrode. In addition, the pillar also increases the accessibility of the surface to the solvated  $\text{Zn}^{2+}$  ions, which improves the capacity, since more storage sites are available. Furthermore, the rate capability also improves due to reduced interaction between the Zn ions and the MXene surface before reaching a storage site. This explains the reduction of current due to diffusion-limited processes seen in the CV analysis, since the diffusion barrier is likely to be lowered by this, allowing more Zn storage to occur via capacitive surface controlled processes.

### 6.2.3.2 Ex-situ Raman Spectroscopy

Raman spectroscopy was then used to investigate any changes in the bonding of the MXene materials. Figures 6.13 and 6.15 show the ex-situ Raman spectra for the first cycle of the non-pillared and in-situ pillared MXene materials respectively (see Appendix Table A.9 for peak assignments and features). In addition, Raman spectra of the pristine cast  $\text{Ti}_3\text{C}_2$  and the electrodes at OCV pre-cycling are also shown. There are common peaks in all spectra, which are consistent with those previously reported for  $\text{Ti}_3\text{C}_2$ .<sup>198,220</sup> There is a peak around  $210\text{ cm}^{-1}$  which corresponds to a Ti=O vibration. The small peak at  $740\text{ cm}^{-1}$  is also a Ti=O vibration. At  $270\text{ cm}^{-1}$  is a small broad peak which results from Ti-OH vibrations (i.e. protonated oxygen termination groups). The large and very broad peaks located between  $350\text{-}450\text{ cm}^{-1}$  and  $550\text{-}700\text{ cm}^{-1}$  result from vibrations from all the surface groups present in the MXene, which

are known to have significant overlap in their vibrational frequencies.<sup>220</sup> As such it is difficult to distinguish the different vibrations contributing to each peak, so they are not considered further in the analysis here.

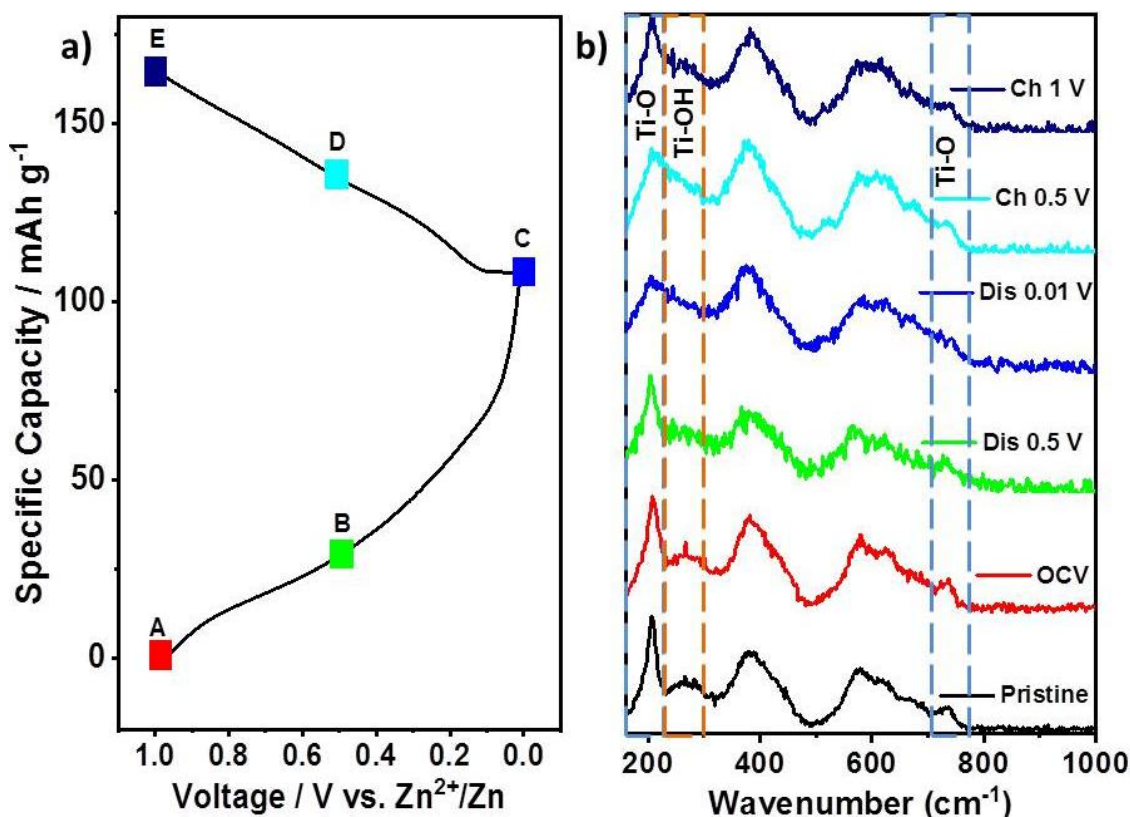


**Figure 6.13.** Ex-situ Raman spectroscopy of the non-pillared Ti<sub>3</sub>C<sub>2</sub>. a) Load curve highlighting the state of charge each electrode was stopped at. b) Corresponding Raman spectra for each state of charge. The evolution of the peaks with cycling matches that seen for the pillared material, showing that the pillared process does not change the fundamental mechanism of charge storage.

It can clearly be seen that although the ex-situ EDS and XRD results showed significant uptake of Zn into the interlayer (shown by the increase in Zn content, Table 6.1), and larger interlayer spacing even after 48 h of drying, Figure 6.14) the Raman spectrum is unchanged between the pristine electrode, and the electrode at OCV. This shows that although Zn can spontaneously intercalate into Ti<sub>3</sub>C<sub>2</sub> when the MXene is soaked in ZnSO<sub>4</sub>, no changes in the surface bonding occur, and the Zn has no covalent interaction with the termination groups.

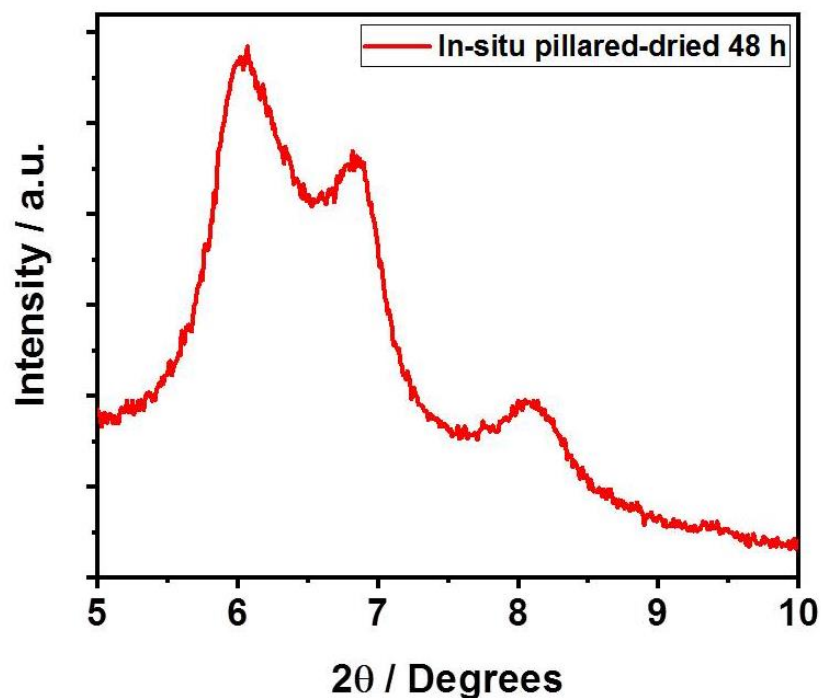


**Figure 6.14.** Ex-situ XRD of in-situ pillared  $\text{Ti}_3\text{C}_2$  at OCV after 48 h of drying for the removal of interlayer water. While some layers have still not been intercalated (shown by the diffraction peak at  $8.2^\circ 2\theta$ ) the majority of the intensity is at  $6$  and  $6.8^\circ 2\theta$ , demonstrating that CTAB and Zn have been intercalated between most layers, even at OCV. The broadness and splitting of the (002) diffraction peak between  $5.8$  and  $7^\circ 2\theta$  shows that the drying process has led to a variety of interlayer spacings caused by partial removal of CTAB.

In contrast, when current is drawn and cycling begins, there are several noticeable features in the voltage dependant evolution of the peaks corresponding to the  $-\text{O}$  and  $-\text{OH}$  surface groups. During the first discharge cycle, the  $\text{Ti}=\text{O}$  vibration at  $210\text{ cm}^{-1}$  broadens and loses intensity. In addition, a shoulder develops at higher wavenumbers on the right-hand side of this peak. By  $0.01\text{ V}$ , at the end of the first discharge cycle, this shoulder merges with the  $\text{Ti}-\text{OH}$  vibration which is visible at  $270\text{ cm}^{-1}$  in the pre-cycled electrodes and also appears to broaden upon cycling. Both peaks are significantly flattened by the end of the first discharge and the  $\text{Ti}-\text{OH}$  peak can no longer be clearly distinguished. These changes then reverse on the first charging cycle, with the  $210\text{ cm}^{-1}$  peak sharpening and seeing an increase in intensity, and a reduction of the shoulder. By the end of the first charging cycle ( $1\text{ V}$ ), the  $\text{Ti}-\text{OH}$  peak at  $270\text{ cm}^{-1}$  can be clearly distinguished from the  $210\text{ cm}^{-1}$  shoulder once more. However, it should be noted that the Raman spectrum at the end of the first charging cycle is not the same as the pre-cycled electrode at OCV (also around  $1\text{ V}$ ), suggesting that the changes in bonding are not fully reversible. This is supported by the EDS results, which showed significant amounts of Zn was retained in the material after charging to  $1\text{ V}$  (Table 6.1). This explains the substantial irreversible capacity loss observed in the galvanostatic charge-discharge cycling (Section 6.2.2); significant amounts of Zn are still bonded to the  $\text{Ti}-\text{O}$  groups by the end of the first charge to  $1$

V. It is possible that further Zn could be extracted at higher voltages, however the CV analysis of the voltage window showed that the  $\text{Ti}_3\text{C}_2$  caused significant water splitting above 1.2 V, which limits the charging voltage.

These changes are consistent with Zn ions bonding to the Ti=O terminations on the  $\text{Ti}_3\text{C}_2$  surface upon discharging the cell and the removal of them when the voltage is increased on charging. This is further supported by the broadening and sharpening of the Ti=O peak at  $740\text{ cm}^{-1}$  after discharging and charging respectively. The shoulder of the  $210\text{ cm}^{-1}$  peak suggests the formation of a Ti-O-Zn type interaction, and occurs at lower wavenumbers than the Ti-O-H vibration due to the heavier mass of Zn compared to H. This shows that -O terminations are the active sites for Zn storage in the MXene, which has also been reported for  $\text{H}^+$ ,  $\text{Li}^+$  and  $\text{Na}^+$  ion systems. This gives important guidance for the further improvement of capacity for  $\text{Ti}_3\text{C}_2$  electrodes in Zn systems, since the number of -O terminal groups can easily be increased, for example by exchanging -F groups for -O ones.<sup>239</sup> Finally, the addition of CTAB seems to have no effect on the underlying charge storage mechanism since the Raman spectra with and without CTAB show identical trends. This suggests that the improvements from the addition of CTAB are due to changes in the interlayer spacings and subsequent diffusion barriers rather than fundamentally changing the mechanisms involved.

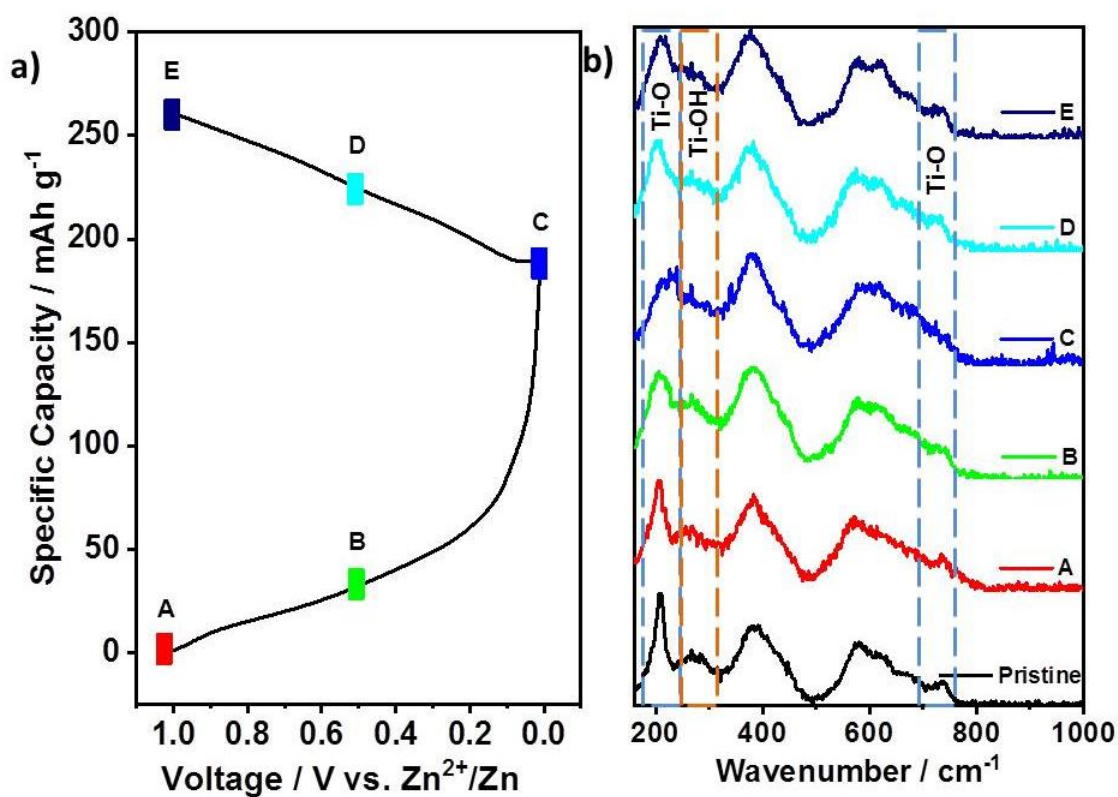


**Figure 6.15.** Ex-situ Raman spectroscopy of the in-situ pillared  $\text{Ti}_3\text{C}_2$ . a) Load curve highlighting the state of charge each electrode was stopped at. b) Corresponding Raman spectra for each state of charge. The dashed rectangles highlight key vibrations for the Zn-intercalation mechanism.

These results strongly suggest that the dominant charge storage mechanism is from the intercalation of Zn between the  $\text{Ti}_3\text{C}_2$  layers. Hu et al. studied  $\text{Ti}_3\text{C}_2$  in several sulphate-based electrolytes ( $\text{H}^+$ ,  $\text{Mg}^{2+}$  and  $\text{NH}_4^+$ ) using in-situ Raman spectroscopy and found that only  $\text{H}_2\text{SO}_4$  showed any changes in the Raman spectra on cycling, due to the pseudocapacitive  $\text{H}^+$  intercalation which saw the shift of the  $\text{Ti}=\text{O}$  vibrations to lower wavenumbers (for the peaks at around 210 and 720  $\text{cm}^{-1}$ ) when  $\text{H}^+$  intercalated.<sup>198</sup> This was explained by the formation of  $\text{Ti}-\text{O}-\text{H}$  bonds, which are accompanied by a change in the Ti valence state, thereby giving rise to pseudocapacitive charge storage. In the Mg and  $\text{NH}_4$  sulphates, no changes in the Raman spectra were seen, suggesting that no new bonds were formed, which ruled out a pseudocapacitive storage mechanism since no charge transfer occurred. Consequently, electric double layer capacitance was deemed the charge storage mechanism in those electrolytes.

This study is relevant in two ways. Firstly, Mg and Zn are both divalent cations, and therefore can be expected to have some similarities in their (electro)chemical behaviour. However, in contrast to in  $\text{MgSO}_4$ , in  $\text{ZnSO}_4$  charge storage is predominantly through the reversible binding of Zn ions to the  $-\text{O}$  termination groups on the  $\text{Ti}_3\text{C}_2$  surface, which must be accompanied by a change in the Ti valence state i.e. a pseudocapacitive intercalation reaction. Secondly, the changes shown in this chapter are not consistent with  $\text{H}^+$  as the main charge carrier, where the  $\text{Ti}=\text{O}$  peaks shift but do not flatten or disappear as they do in the results presented in this chapter. In fact, when the cell is fully discharged, and the  $\text{Ti}-\text{O}-\text{H}$  groups would be at their most abundant if this was the charge carrier; the  $\text{Ti}-\text{O}-\text{H}$  peak at 270  $\text{cm}^{-1}$  cannot be distinguished in the Raman spectra. In addition, the  $\text{Ti}=\text{O}$  vibration at 740  $\text{cm}^{-1}$  does not shift on cycling; it reduces in intensity, broadens and then re-emerges. This rules out  $\text{H}^+$  pseudocapacitance as the main charge storage mechanism, although a small contribution cannot be completely dismissed due to the obscuring of the  $\text{Ti}-\text{O}-\text{H}$  peak by the  $\text{Ti}-\text{O}-\text{Zn}$  one.  $\text{ZnSO}_4$  is only mildly acidic, (pH 4-6), so would not be expected to have  $\text{H}^+$  ions in the concentrations needed to account for the reported capacities in any case. In fact, Hu et al. showed that negligible charge was stored in  $\text{H}_2\text{SO}_4$  in this pH range.<sup>198</sup>

The third possible mechanism is  $\text{SO}_4^{2-}$  absorption via electric double layer capacitance. This was reported when  $\text{Ti}_3\text{C}_2$  was the positive electrode in  $\text{Mg}^{2+}$ ,  $\text{NH}_4^+$  and  $\text{Zn}^{2+}$  sulphates, and when nanocarbons have been used in Zn-ion capacitors.<sup>198,265</sup> However, this is clearly not the case here since no S content is detected in the EDS results at any point during the ex-situ studies (Table 6.1), and there is no  $\text{SO}_4^{2-}$  peak at 980  $\text{cm}^{-1}$  in the Raman spectra (Figures 6.13 and 6.15), both of which would be expected if this was the charge storage mechanism.

### 6.2.3.3 Ex-situ X-ray Photoelectron Spectroscopy

Ex-situ XPS was then used on the in-situ pillared  $\text{Ti}_3\text{C}_2$  to investigate the Ti oxidation state during cycling, which was implied to change by the ex-situ Raman spectroscopy studies. Samples were charged to desired state, the cells were disassembled, the electrodes were extracted and washed in DI water five times to remove any surface salts, before drying overnight under vacuum in the antechamber of a glovebox overnight. The samples were then stored in an argon filled glovebox ( $\text{O}_2$  and  $\text{H}_2\text{O} < 0.01$  ppm) until posting for analysis. The results are shown in Figure 6.16, while data on peak fitting analysis can be found in the appendix, Table A.10. There are four broad main peaks that can be observed in the Ti 2p spectra for the OCV sample (Figure 6.16, A). These centre on 455.9, 459.7, 462.0 and 465.2 eV. This is consistent with XPS spectra from previously reported studies, which show that  $\text{Ti}_3\text{C}_2$  contains predominately  $\text{Ti}^{3+}$  and  $\text{Ti}^{2+}$ .<sup>149,266</sup>  $\text{Ti}^{4+}$  oxidation states correspond to surface oxides from the oxidation of the MXene, while the other states are all expected to be found in MXenes.

For example, the peak at 455.9 eV (3/2 electrons) at OCV shifts to 455.4 eV at 0.01 V, implying reduction of Ti. A similar shift is observed for the 462.0 eV peak (1/2 electrons), which occurs at 461.5 eV at 0.01 V, further supporting the MXene Ti reduction. At 0.5 V, the corresponding peaks sit between these two end points, at 455.6 eV for the 3/2 electrons and 461.4 eV for the 1/2 electrons, suggesting that the Ti is reduced throughout the voltage window. This implies that at voltages between 0.5 and 1 V the charge storage has significant contribution from pseudocapacitive mechanisms, not just EDL capacitance (this matches data from CV plots Figure 6.9).

When the cell is charged, these changes reverse, showing that the change in valence state upon discharge is mostly reversible, revealing that the Zn storage is achieved via a Ti-based redox reaction. Interestingly, the electrode charged to 0.5 V shows very similar shifts to the electrode charged to 1 V (0.1 eV and 0.2 eV lower binding energies than at 1 V for the 3/2 and 1/2 electrons respectively). This implies that on charge most of the redox contribution has occurred by 0.5 V, which would match the distinctive redox peak observed on the CV (Figure 6.9). Reversible Ti redox is also shown by the peak deconvolution, where the concentration of  $\text{Ti}^{2+}$  increases upon discharge (from 28% at OCV to 34% at 0.01 V) and decreases on the subsequent charge (to 30%), supporting the reversible reduction of  $\text{Ti}^{4+}$  and  $\text{Ti}^{3+}$  to  $\text{Ti}^{2+}$ . This behaviour has previously been demonstrated for  $\text{Ti}_3\text{C}_2$  MXene using in-situ XANES experiments in aqueous  $\text{H}_2\text{SO}_4$  and organic Li-ion systems.<sup>98,121</sup> In both these cases the overall titanium oxidation state in the MXene was just over  $2^+$ , which would seem to match well with the results for Zn reported in this chapter.

Furthermore, the XPS results show that the surface oxides ( $\text{Ti}^{4+}$ ) also change upon cycling. As well as a reversible shift on charge and discharge as seen for the MXene

Ti, there is also a broadening on discharge (to the extent that the 1/2  $\text{Ti}^{4+}$  peak cannot be distinguished at 0.01 V and the 3/2 peak is severely flattened). The concentration of  $\text{Ti}^{4+}$  in the spectra decreases from 22% to 15% between OCV and 0.01 V, further supporting the  $\text{Ti}^{4+}$  reduction. This is then reversed on charging to 0.5 V, with little difference between the 0.5 and 1 V electrodes. This suggests that the surface oxides also contribute to reversible Zn storage, and that the oxidation on charge occurs almost entirely between 0.01 and 0.5 V. However, it may be that these surface oxides are still not desirable for MXene performance, since a previous study on nanosized anatase  $\text{TiO}_2$  for Zn-ion batteries reported low capacities of  $25 \text{ mAh g}^{-1}$ , much less than  $\text{Ti}_3\text{C}_2$  reported here.<sup>250</sup> Further work on the role of titanium-based oxides in Zn-ion systems is needed to fully determine their performance and contribution here.

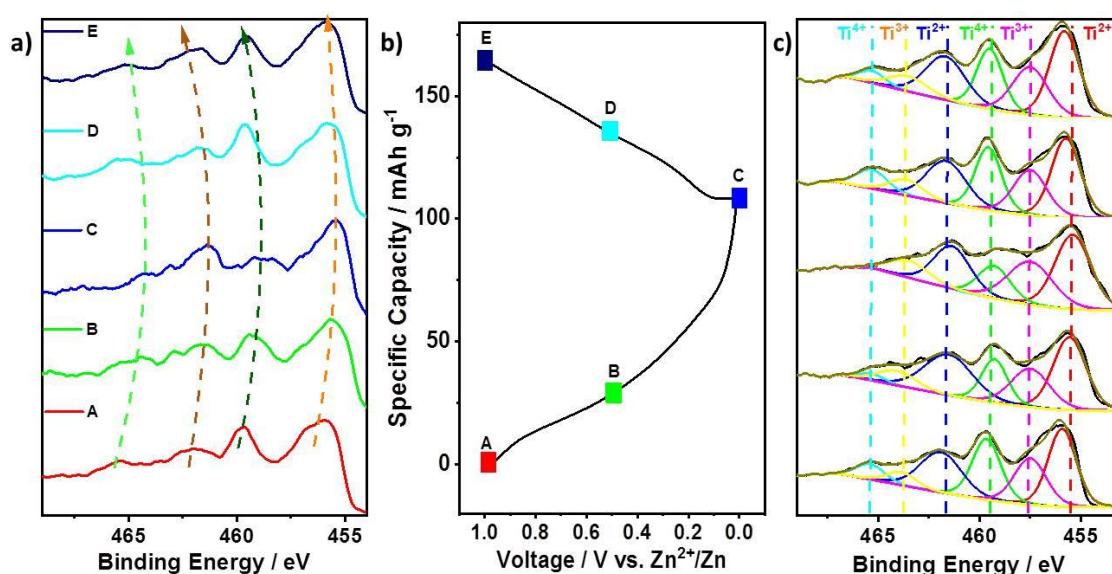


**Figure 6.16.** Ex-situ XPS Ti 2p spectra of in-situ pillared  $\text{Ti}_3\text{C}_2$  at selected states of charge during the first cycle. a) Raw data at selected states of charge, with arrows illustrating the reversible shift upon charge and discharge. b) Load curve highlighting the states of charge electrodes were extracted at. c) De-convoluted peaks showing the contribution from the various Ti oxidation states present in the sample at each state of charge.

Overall, these ex-situ studies show that when used with an initial discharged from OCV in a zinc-ion system,  $\text{Ti}_3\text{C}_2$  MXene stores charge predominantly via the reversible intercalation of  $\text{Zn}^{2+}$  ions, which bind to the terminal Ti-O groups on the surface of the MXene, with a corresponding change in the Ti oxidation state. There is minimal contribution of  $\text{H}^+$  pseudocapacitance and no contribution from  $\text{SO}_4^{2-}$  EDL capacitance. However, there is also a likely contribution from  $\text{Zn}^{2+}$  EDL capacitance, which cannot be ruled out from the current study.

### 6.3 SiO<sub>2</sub>-pillared Ti<sub>3</sub>C<sub>2</sub> in Aqueous Zn Electrolyte

To further investigate the effect of pillaring on Ti<sub>3</sub>C<sub>2</sub>, the amine-assisted pillaring method developed in the previous chapters was applied to the aqueous Zn-ion system. The pillaring conditions were the same as reported in Chapter 4, and the electrodes and cells were prepared identically to the other Zn cells reported so far in this chapter. Figure 6.17 shows the load curves for the 1<sup>st</sup>, 2<sup>nd</sup> and 5<sup>th</sup> charge-discharge cycles between 0.01-1 V at a current density of 20 mA g<sup>-1</sup>. The performance can be seen to be similar to the CTAB pillared materials on discharge, with a large first discharge capacity of 196 mAh g<sup>-1</sup>, which is close to the CTAB-pillared MXene and supports the opening up of the layers seen in those materials. However, as for the CTAB pillared material, the majority of this capacity is irreversible, with only 50 mAh g<sup>-1</sup> recovered on subsequent charge; a coulombic efficiency of only 26%. This is lower than was seen for the CTAB pillared material, despite a slightly larger interlayer spacing. This could be due to the SiO<sub>2</sub> pillars being bulkier than the CTAB ones, or a higher concentration of pillars in the interlayer, making it challenging to remove intercalated Zn.

The discharge capacity continues to decrease slightly with further cycling, to 81 mAh g<sup>-1</sup> and 62 mAh g<sup>-1</sup> on the second and fifth cycles respectively. However, the charge capacity barely changes across these cycles, dropping from 50 mAh g<sup>-1</sup> on the first cycle to 45 mAh g<sup>-1</sup> on the fifth cycle. The load curve of the charging steps are very linear, suggesting capacitive type charge storage, whereas the discharge curves deviate from linearity at lower voltages. This suggests that the capacitive charging process is actually very stable, but irreversible faradaic processes occur at low voltages on discharge (below about 0.1 V). This is supported by the low coulombic efficiencies, which do however increase across the five cycles tested (to 73% by the fifth cycle, which is still very low). Changing the voltage window to 0.1-1.2V may offer a more stable performance. In addition, it is possible that the pillaring process could be altered for this application, by using a lower concentration of Si pillars, which should be achievable by using an MXene with a lower proportion of -OH surface groups to bind to DDA. Investigating different calcination temperatures and atmospheres may also allow for the performance to be improved. Further electrochemical and spectroscopic analysis would be needed to fully understand the performance of this material.

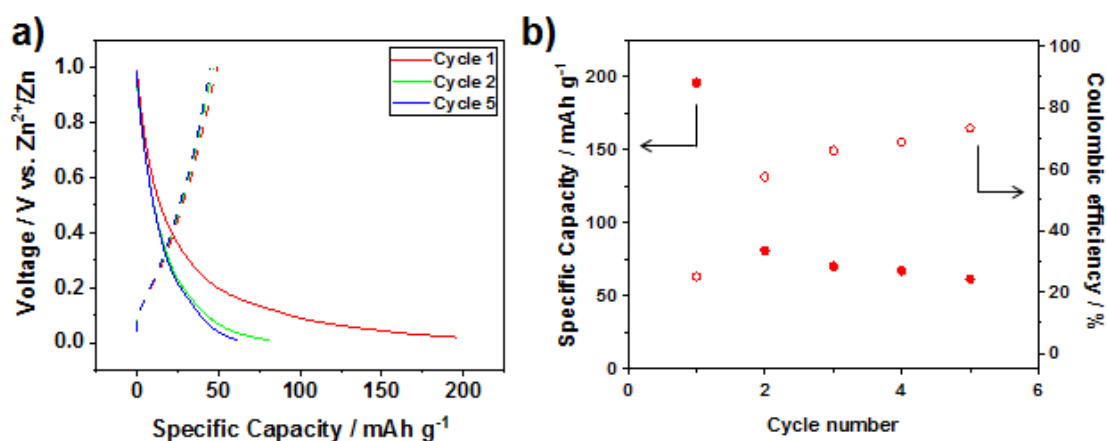


**Figure 6.17.** Galvanostatic charge-discharge testing of SiO<sub>2</sub>-pillared Ti<sub>3</sub>C<sub>2</sub> in 0.1 M ZnSO<sub>4</sub> at 20 mA g<sup>-1</sup> in a voltage window of 0.01-1 V vs. Zn<sup>2+</sup>/Zn. a) Load curves of the 1<sup>st</sup>, 2<sup>nd</sup> and 5<sup>th</sup> cycles. b) Discharge capacity and coulombic efficiency over five cycles.

#### 6.4 Mo<sub>2</sub>TiC<sub>2</sub> in Aqueous Zn Electrolyte

Since Ti<sub>3</sub>C<sub>2</sub> MXene had shown promise as an electrode in aqueous Zn-ion systems, Mo<sub>2</sub>TiC<sub>2</sub> was then tested for Zn-ion storage in 0.1 M ZnSO<sub>4</sub> against a Zn metal counter and reference electrode. Figure 6.18 shows the load curves and coulombic efficiencies over 10 cycles at 20 mA g<sup>-1</sup> between 0.2-1.2 V (note that below 0.2 V an irreversible plateau was observed with a capacity of 242 mAh g<sup>-1</sup>). Whilst there is some electrochemical activity, the capacities are very small (discharge capacities are around 5 mAh g<sup>-1</sup>) suggesting that this MXene is not a promising electrode material for Zn-ion storage. The discharge load curve is non-linear, suggesting there may be a limited faradic contribution to the capacity. The charging profile is linear up to between 1 and 1.2 V, after which point it severely deviates. This suggests that the capacity between 0.2 and 1 V is capacitive in nature, but there is some irreversible faradic contribution over 1.1 V. This leads to coulombic efficiencies over 100%, showing that this high voltage capacity is from irreversible processes. A possible cause of this irreversible capacity could be water splitting, suggesting that Mo<sub>2</sub>TiC<sub>2</sub> could be a promising candidate as a catalyst for the oxygen evolution reaction in water electrolyzers. An upper voltage cut-off of 1 or 1.1 V would give more stable performance.

However, while the discharge capacities are stable across 10 cycles, and Mo<sub>2</sub>TiC<sub>2</sub> shows some reversible charge storage, the capacities are not high enough for it to be considered a promising material for rechargeable zinc-ion batteries in 0.1 M ZnSO<sub>4</sub>. It is possible that performance could be improved by optimising parameters such as electrode architecture, particle size and by testing in different electrolyte compositions and concentrations, but these were not studied further in this work. MoO<sub>3</sub> has been shown to have high Zn capacities in aqueous systems, but suffers from low electrical conductivity like most transition metal oxides. A further area of

investigation could be to partially oxidise the Mo to form anchored MoO<sub>3</sub> nanoparticles on conductive TiC<sub>2</sub> supports, which could give a material with an open and conductive structure for high performance in Zn-ion systems.

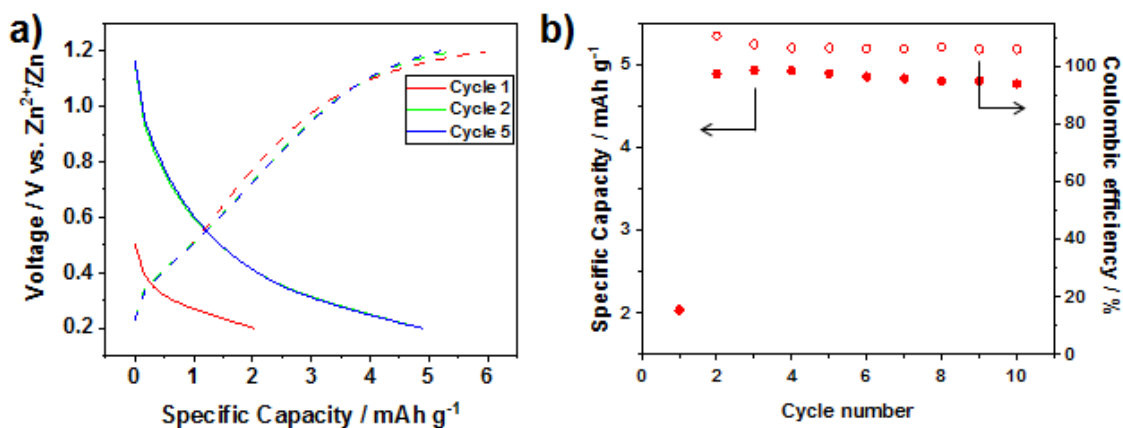


**Figure 6.18.** Galvanostatic charge-discharge testing of Mo<sub>2</sub>TiC<sub>2</sub> in 0.1 M ZnSO<sub>4</sub> at 20 mA g<sup>-1</sup> in a voltage window of 0.01-1 V vs. Zn<sup>2+</sup>/Zn. a) Load curves of the 1<sup>st</sup>, 2<sup>nd</sup> and 5<sup>th</sup> cycles. b) Discharge capacity and coulombic efficiency over five cycles.

## 6.5 MXenes in Organic Zn Electrolytes

While aqueous electrolytes have several advantages over organic ones, as discussed previously, the limited voltage window caused by thermodynamic stability window of water severely limits the energy density of cells which utilise them. This is a major drawback for their use in practical applications. In addition, for capacitive materials such as MXenes charge can be stored at a wide voltage range, including outside the stability window of water. Widening this range by using an organic electrolyte may give higher capacities by allowing this extra charge storage to be accessed, in addition to the energy gains from using a higher working voltage. Therefore, Ti<sub>3</sub>C<sub>2</sub> MXene was also tested for Zn storage in an organic electrolyte, 1 M Zn(TFSI)<sub>2</sub> in acetonitrile, which has a wider stability window than water.

Unfortunately, no capacity was recorded on the as-made Ti<sub>3</sub>C<sub>2</sub> MXene. Therefore, a variety of pillaring methods were used to attempt active the MXene, in a similar way that Ti<sub>3</sub>C<sub>2</sub> had been shown to active for Mg<sup>2+</sup> storage in organic electrolytes by pillaring with CTAB, which increased the interlayer spacing and lowered the diffusion barrier for Mg<sup>2+</sup> migration.<sup>260</sup> Ti<sub>3</sub>C<sub>2</sub> MXene was pillared with a cationic surfactant (CTAB) and using the amine-assisted pillaring method to pillar with SiO<sub>2</sub>.

### 6.5.1 CTAB-pillared Ti<sub>3</sub>C<sub>2</sub>

Ti<sub>3</sub>C<sub>2</sub> was pillared with CTAB using the ex-situ pillaring method previously described in this chapter. The load curves after electrochemical testing are shown in Figure 6.19. It can be seen that the MXene now shows some reversible capacity in the organic zinc-ion system, with capacities up to 37 mAh g<sup>-1</sup> now achievable. The

discharge load curves show a sloping plateau below 0.7 V on the 2<sup>nd</sup> cycle and 0.5 V on the 5<sup>th</sup> cycle, which suggests a faradaic charge storage reaction is occurring. The charge profiles also show non-linear behaviour. This shows that pillaring with CTAB and the subsequent enlarging of the interlayer spacing has activated the MXene for Zn-ion storage. However, the capacities are still very low, and fade rapidly over 20 cycles, with only 4 mAh g<sup>-1</sup> being retained by the 20<sup>th</sup> cycle. In addition, some of the initial capacity is from an irreversible process above 1.8 V, which is not useful for rechargeable energy storage devices. An upper voltage cut-off of 1.8 V would likely give rise to more stable cycling performance for future studies. The capacities here are much lower than was reported for CTAB pillared Ti<sub>3</sub>C<sub>2</sub> in organic Mg-ion batteries, where around 100 mAh g<sup>-1</sup> was achieved. This shows that different methods will have to be developed to improve MXene performance in organic Zn-ion systems.

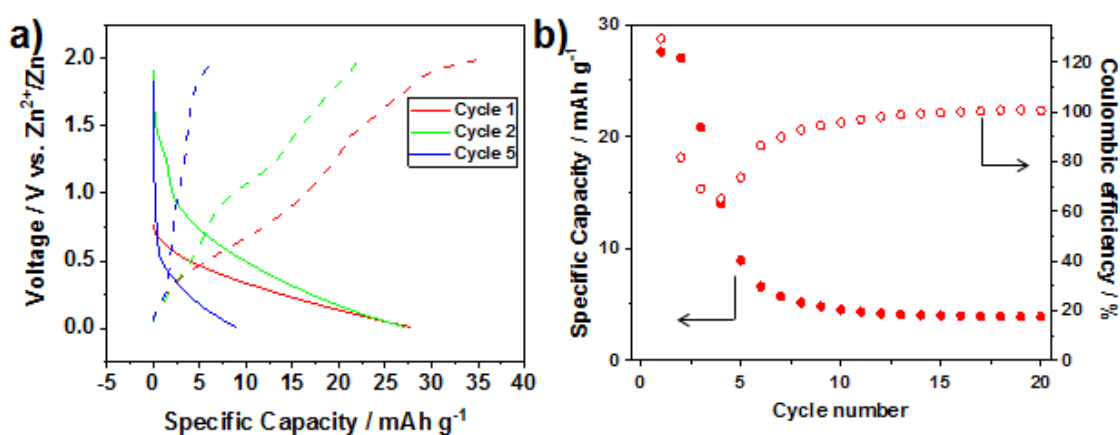


**Figure 6.19.** Galvanostatic charge-discharge testing of CTAB-pillared Ti<sub>3</sub>C<sub>2</sub> in 1 M Zn(TFSI)<sub>2</sub> at 20 mA g<sup>-1</sup> in a voltage window of 0.01-2 V vs. Zn<sup>2+</sup>/Zn. a) Load curves of the 1<sup>st</sup>, 2<sup>nd</sup> and 5<sup>th</sup> cycles. b) Discharge capacity and coulombic efficiency over ten cycles.

### 6.5.2 SiO<sub>2</sub>-pillared Ti<sub>3</sub>C<sub>2</sub>

The results from the CTAB pillaring experiments showed that Ti<sub>3</sub>C<sub>2</sub> could be activated for Zn-ion storage in organic electrolyte by pillaring methods, but that further work was required to further improve capacities to reasonable levels. Therefore, the SiO<sub>2</sub>-pillared Ti<sub>3</sub>C<sub>2</sub> was tested next. The pillaring method used was the same as reported in previous chapters. The results of the electrochemical testing are shown in Figure 6.20. The shape of the load curve is similar to that seen for CTAB-pillared Ti<sub>3</sub>C<sub>2</sub>, with a sloping plateau at low voltages (below 0.6 V), and irreversible processes above 1.8 V, which gives rise to coulombic efficiencies above 100% after 15 cycles, as well as the initial cycle. Between cycles 4-14, the coulombic efficiency increases with cycling. However, the capacities are even lower than when pillaring with CTAB, with 7 mAh g<sup>-1</sup> being the highest achieved (1<sup>st</sup> charge), some of which is irreversible, and only 2 mAh g<sup>-1</sup> being retained by the 20<sup>th</sup> cycle. This shows that although SiO<sub>2</sub> pillaring

allows for some reversible capacity to be achieved in this system, the performance is still very poor and it is not a viable electrode for this system.

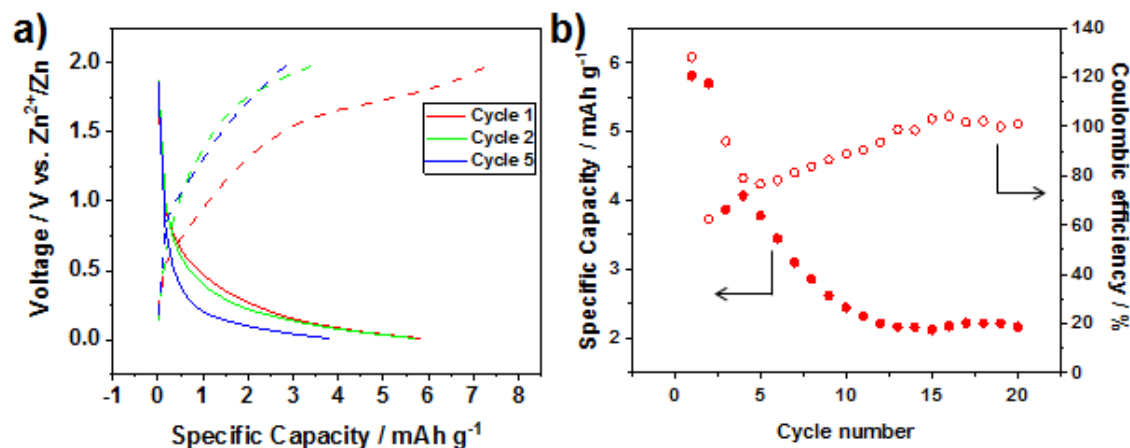


**Figure 6.20.** Galvanostatic charge-discharge testing of SiO<sub>2</sub>-pillared Ti<sub>3</sub>C<sub>2</sub> in 1 M Zn(TFSI)<sub>2</sub> at 20 mA g<sup>-1</sup> in a voltage window of 0.01-2 V vs. Zn<sup>2+</sup>/Zn. a) Load curves of the 1<sup>st</sup>, 2<sup>nd</sup> and 5<sup>th</sup> cycles b) discharge capacity and coulombic efficiency over ten cycles.

## 6.6 Conclusions

In summary, this chapter shows that Ti<sub>3</sub>C<sub>2</sub> MXene can reversibly store zinc-ions electrochemically in aqueous electrolytes. In addition, a simple proof-of-concept structuring technique based on the addition of pillars to the electrolyte that achieves a novel in-situ pillaring method was developed. This was shown to improve the electrode performance of Ti<sub>3</sub>C<sub>2</sub> MXene as a zinc-ion host for future sustainable zinc-ion batteries. The fact that Ti<sub>3</sub>C<sub>2</sub> can reversibly intercalate a significant amount of Zn<sup>2+</sup> opens up the large and growing family of MXenes as potential zinc-ion hosts, although initial results suggested that Mo<sub>2</sub>TiC<sub>2</sub> is not a promising electrode in this system. The shape of the load curve suggested that Ti<sub>3</sub>C<sub>2</sub> could be used as either a positive or negative electrode in an aqueous Zn-ion system. The kinetic and ex-situ diffraction and spectroscopic studies reveal that the Zn<sup>2+</sup> intercalation occurs with a mixture of pseudocapacitive and battery-like processes, with the -O functional groups playing a key role as the binding site for Zn ions, which is important background knowledge for the future development of MXenes for Zn-ion applications.

The in-situ pillaring successfully opens up the MXene layers, lowering the proportion of diffusion-limited charge storage and preventing volume change during cycling, without altering the underlying charge storage mechanism. The in-situ pillared material showed higher capacities than the ex-situ CTAB pillared material, and the SiO<sub>2</sub>-pillared MXene, both of which require multiple reaction and separation steps to achieve the final architecture. This demonstrates the possibility of using in-situ structural approaches to improve electrode performance, which would significantly

simplify the use of 2D materials as electrode materials, where complicated processes are often used to control the structure. The in-situ pillaring approach could be applied not just to other MXenes, but also to the wider group of 2D and layered materials.

In organic electrolytes, the as-made MXene showed no capacity, showing that it did not reversibly store  $\text{Zn}^{2+}$  in this electrolyte-solvent mixture. Limited capacities could be achieved when pillared MXenes were used, but performance was still poor compared to the aqueous systems (the highest capacity achieved was  $37 \text{ mAh g}^{-1}$ ). An enlarged stable voltage window of 0.01-1.8 V could be accessed, but this did not make up for the significantly lower capacities seen. This work does show that pillaring could be a promising method for improving the performance of MXene materials in organic Zn-ion systems, but new methods would need to be developed. A more beneficial approach for the development of MXenes for organic Zn-ion systems could be to investigate different solvents and electrolyte salts, and different MXene chemistries.

Finally, work on MXenes in other ion systems has seen substantial improvements in performance via control of the flake size and surface groups combined with careful control of the electrode architecture,<sup>114,131,238,261</sup> which implies that there is significant room to further improve the performance of in zinc-ion systems.

# **Chapter Seven**

## **Conclusions and Further Work**

## 7.1 Concluding Remarks

Overall, this thesis has shown that pillaring is a promising method for the creation of porous MXenes. Using an amine-assisted pillaring method, porous  $\text{Ti}_3\text{C}_2$  and  $\text{Mo}_2\text{TiC}_2$  MXenes were synthesised, with surface areas up to  $235 \text{ m}^2 \text{ g}^{-1}$ , which is around 60-times greater than the non-pillared MXenes. The increase in surface area does not come at the expense of the MXene structure, as has been the case with some previously reported methods to create porous MXenes such as partial oxidation. Instead, the original sheets are kept intact, and simply move further apart. This is shown by the increase in interlayer spacings which has been confirmed by XRD, TEM and pore size distribution analysis from gas sorption experiments. Interlayer spacings up to 4.2 nm were achieved, which corresponds to a gallery height of 3.25 nm. These are the highest reported distances for MXene-based materials, and some of the highest for any 2D material. The same interlayer spacings were achieved regardless of the M element in the MXene studied, since both  $\text{Mo}_2\text{TiC}_2$  and  $\text{Ti}_3\text{C}_2$  MXenes showed the same interlayer spacing after pillaring.

This is because interlayer spacing is dictated by the amine used as the co-pillar, and so long as it can intercalate, forms bilayers between the sheets which prop open the structure. This allows DDA, with a 12 carbon-long backbone, to give larger interlayer spacings than cationic surfactants such as CTAB, even when the surfactant has longer chains. This is because the cationic surfactants intercalate at angles, and have not been found to form bilayers.<sup>261</sup> If a different amine is used, such as octylamine, a smaller interlayer spacing is given. This implies that the amine-assisted pillaring method reported in this thesis can be used to give a variety of interlayer spacings that can be tuned by carefully selecting the amine co-pillar, since this appears to dictate gallery height. It was also shown, by NMR and XPS studies, that the amines intercalate by hydrogen-bonding with surface M-OH, as in layered clays, but that the identity of M has no effect on the success or gallery height achieved. This, combined with the fact that the same gallery heights are achieved with electrically insulating titanosilicates,<sup>267</sup> suggested that the amine-assisted pillaring method may be able to be applied to any MXene (or maybe even any layered material with a large enough starting interlayer spacing), so long as sufficient M-OH groups are present.

The silica precursor, TEOS, is brought into the interlayer space by solvation effects with the amine, and remains between the layers once intercalated, including during the hydrolysis step to form the  $\text{SiO}_2$  nanoparticle pillars. A calcination step can then be employed to remove the amine template, since the amine otherwise makes the MXene hydrophobic and takes up space in the pores, and weight in the material. Different calcination temperatures also give different final interlayer spacings, likely due to incomplete removal of the amine template, which gives an extra tool, alongside the choice of amine, which can be used to control the final interlayer

spacings of the pillared MXene. The calcination step is carried out under argon to prevent the oxidation of the MXene, but this means that some residual graphitic carbon remains in the structure even at 400 °C. By 500 °C, the SiO<sub>2</sub>-pillared Ti<sub>3</sub>C<sub>2</sub> MXene no longer had a layered structure crystalline enough to observe using XRD, suggesting that the material was not thermally stable at this temperature. It is also noteworthy that the intercalated and calcined pillared materials retained their porosity for one year when stored under ambient conditions, with BET surface area measurements being carried out almost one year after the pillaring process confirming that the porous nature remains in that timeframe.

The silica-pillared MXenes were then tested in a variety of metal-ion systems to investigate how the pillaring process affects the electrochemical performance. In organic electrolyte based systems used in lithium- and sodium-ion batteries the pillared material showed superior capacities, rate capability and cycling stability in each system tested. Even in an aqueous electrolyte, ZnSO<sub>4</sub>, the SiO<sub>2</sub> pillared Ti<sub>3</sub>C<sub>2</sub> showed higher capacities than the non-pillared MXene. The improved capacities are explained by increased ion access to the MXene charge storage sites as a result of the enlarged interlayer spacings and increased surface areas. The improved rate capability is likely to be due to the increased interlayer space allowing for faster ion diffusion and increased capacitive contributions as a result of higher surface areas. It also shows that the pillars do not block the interlayer space for the charge carrying ions, which would hinder ion diffusion and result in poorer rate capability. The improved cycling stability likely results from reduced trapping of the charge carrying ions due to the larger interlayer spacings keeping the charge storage sites open and the pillars preventing the restacking of the nanosheets over multiple charge-discharge cycles. The coulombic efficiency was superior in the pillared MXene compared to the non-pillared MXene in each system tested, which supports the explanation of the pillars preventing the trapping of the charge carrying ions.

For both Ti<sub>3</sub>C<sub>2</sub> and Mo<sub>2</sub>TiC<sub>2</sub>, the performance was superior in the Li-ion system compared to the Na-ion one. In addition, the improvement in capacities between pillared and non-pillared materials was greater in the Li-ion compared to the Na-ion system. In the Na-ion system, capacities were relatively low when compared to other potential negative electrodes, including some other reports on pillared MXenes, and hard carbons, which are the current standard for Na-ion negative electrodes. In addition, the improvement between the pillared and non-pillared was less than 2-fold for both Ti<sub>3</sub>C<sub>2</sub> and Mo<sub>2</sub>TiC<sub>2</sub>, while for Li-ion systems the improvements in capacities were 2-3 fold, especially after multiple cycles. The reason for this difference in improvement is however different for the two MXenes. For Ti<sub>3</sub>C<sub>2</sub>, it arises from Li being able to form multiple adsorption layers on top of the initial intercalated Li layer, with theoretical calculations predicting that up to four layers per MXene sheet may be possible,<sup>268</sup> which gives rise to much larger capacities than

Na-ion systems, where only 1-2 layers are thought to form.<sup>148,269</sup> This means that there is greater benefit to increasing the interlayer spacing to accommodate more  $\text{Li}^+$  ion compared to  $\text{Na}^+$ , since space beyond a bilayer appears to be unused for Na-ion systems.

For  $\text{Mo}_2\text{TiC}_2$ , the superior performance in Li-ion systems, is explained by the theoretically proposed mechanism which suggests that a conversion reaction to form  $\text{Li}_2\text{O}$  is viable in Li-ion systems, which provides significant extra capacity above the intercalation contribution, but this is not the case for the Na-ion system, where  $\text{Na}_2\text{O}$  does not form.<sup>100</sup> This mechanism has been partially validated in this thesis, where the reversible formation of  $\text{Li}_2\text{O}$  was detected by ex-situ XPS results in the Li-ion system. In addition, conversion reactions are typically accompanied by large volume changes upon cycling, which lead to severe capacity fade after multiple cycles. This rapid fade was observed for  $\text{Mo}_2\text{TiC}_2$  in the Li-ion system, but not the Na-ion one, which would seem to further validate this mechanism. A further benefit of pillaring  $\text{Mo}_2\text{TiC}_2$  for the Li-ion system was that the increased interlayer distance provided free space for the formation of  $\text{Li}_2\text{O}$  without causing severe volume changes / strain on the structure, which led to a more significant improvement in cycling stability than was seen for  $\text{Mo}_2\text{TiC}_2$  in the Na-ion system, or for the  $\text{Ti}_3\text{C}_2$  MXene.

It has previously been reported that  $\text{SiO}_2$ , the pillar in these materials, can itself reversibly intercalate  $\text{Li}^+$  ions and act as an electrode material for Li-ion batteries.<sup>241</sup> Therefore, it was considered possible that it could contribute to the electrochemical performance here. In addition, while there has been no report found on  $\text{SiO}_2$  for Na-ion systems, Si/  $\text{SiO}_x$  materials have been shown to be active as potential electrodes.<sup>270-272</sup> There has been no evidence found in this thesis to suggest that the  $\text{SiO}_2$  pillars contribute significantly to capacity in the pillared materials. Ex-situ XPS carried out on  $\text{SiO}_2$ -pillared  $\text{Ti}_3\text{C}_2$  in a Na-ion system and  $\text{SiO}_2$ -pillared  $\text{Mo}_2\text{TiC}_2$  in a Li-ion system showed that there was negligible change in the binding energy, and therefore the Si environment, before and after discharge. In addition, no metallic Si or  $\text{Li}_x\text{Si}$  /  $\text{Na}_x\text{Si}$  alloys were detected. Furthermore, the CV curves for each system showed far greater similarities between the pillared and non-pillared materials than between the different MXenes in a given ion system. For example, pillared and non-pillared  $\text{Mo}_2\text{TiC}_2$  MXenes in a Li-ion system had very similar CV curves, which looked very different to the CV curves recorded for pillared  $\text{Ti}_3\text{C}_2$  in the Li-ion system. If the electrochemistry was dominated by the  $\text{SiO}_2$  pillars, the CV curves for  $\text{SiO}_2$ -pillared  $\text{Mo}_2\text{TiC}_2$  and  $\text{Ti}_3\text{C}_2$  would be expected to look very similar, based on the redox behaviour of  $\text{SiO}_2$ . Nevertheless, since  $\text{SiO}_2$  and MXenes both store more charge under 1 V than above it, a small contribution from  $\text{SiO}_2$  cannot be completely ruled out by the work presented here. In addition, ex-situ XPS is a very surface sensitive technique and allows for significant time for the samples to relax between cycling

and measuring. Further work would be required to study the role SiO<sub>2</sub> pillars in more detail.

Another interesting feature of the CV curve was that after pillaring some redox peaks were no longer visible, (with the exception of those linked to the Li<sub>2</sub>O conversion reaction of the Mo<sub>2</sub>TiC<sub>2</sub> MXene, and the low voltage storage below 0.2 V). This supports previously reported assignments of these peaks as related to narrow interlayer pores, which are removed upon pillaring and the subsequent expansion of the interlayer distances. Another interesting feature of the CV analysis for all systems studied was that the charge storage mechanisms were a mixture of diffusion-limited (battery-like) and surface-limited (capacitive-like) processes. In addition, the proportion of capacitive current increased at higher voltages and the proportion of diffusion-limited current was highest at lower voltages. This was the case for the organic Li- and Na-ion systems and the aqueous Zn-ion system, suggesting that it is independent of electrolyte solvent. An effect of pillaring in organic electrolytes appeared to be that at lower voltages the proportion of diffusion-limited current increased and at higher voltages the proportion of capacitive-limited current increased. This was explained by the pillars allowing greater access to redox active sites on the electrode surface at low voltages, leading to an increase in diffusion-limited battery-like processes at these voltage ranges. At higher voltages, where capacitive processes are already the dominant charge storage mechanism, the increased interlayer spacing allows for easier ion diffusion through the layers, reducing the proportion of diffusion-limited charge transfer at these voltages.

MXenes as Zn<sup>2+</sup> hosts were previously unreported in the literature, therefore the charge storage mechanism was studied in more detail using a variety of ex-situ techniques. It was found that Ti<sub>3</sub>C<sub>2</sub> MXene can reversibly store Zn<sup>2+</sup> ions, delivering capacities comparable to other studied electrode materials. The charge storage mechanism consists of a mixture of diffusion-limited and surface-limited processes, as is the case for organic Li- and Na-ion systems. It was also found that, as for some other metal-ion systems, including organic Li-ion systems, the Ti was redox active, with redox couples involving Ti<sup>2+</sup> being the major state for Ti<sub>3</sub>C<sub>2</sub> Ti.<sup>268</sup> The terminal Ti-O groups were discovered to be the ion storage site, which is also similar to previous reports on Li- and Na-ion systems.<sup>148,268</sup> There were no major phase changes discovered during cycling, which supports a capacitive-type mechanism overall. After an initial expansion as water and Zn<sup>2+</sup> intercalate between the layers and expand the structure the interlayer distance was generally constant. At low voltages however, there was a shrinking of the interlayer spacing as water appeared to be expelled and the sheets brought closer together. A simple in-situ pillaring technique, which intercalated the cationic surfactant CTAB during the first discharge, overcame this shrinking, with the in-situ pillared material showing a consistent interlayer spacing at all cycling points after the initial expansion, and returned higher capacities, better

rate capability and improved cycling stability compared to the non-pillared material. This suggests that in-situ pillaring could be a promising alternative to other pillaring techniques, such as the amine-assisted pillaring method, which often have multiple processing steps, which adds cost, mass losses and complexity to the structuring process. The improvement in performance in the aqueous system was less significant than in the organic Li- and Na-ion ones, which may be explained by the fact that the expansion of the MXene in the aqueous ZnSO<sub>4</sub> electrolyte was larger than what has been reported for Li- and Na-ion systems. This implies that the performance in aqueous systems is less restricted by interlayer spacing than organic ones. Nevertheless, pillaring did still improve the electrochemical performance.

Pillaring also led to improved performance in an organic Zn electrolyte, but the performance was still very poor, suggesting that Ti<sub>3</sub>C<sub>2</sub> may not be a promising electrode for organic Zn-ion systems. Mo<sub>2</sub>TiC<sub>2</sub> was also tested in aqueous ZnSO<sub>4</sub>, but showed limited capacity, although techniques such as pillaring may improve the performance. However, these were not tested in this work. This shows that although Ti<sub>3</sub>C<sub>2</sub> does show promise in Zn-ion systems, suggesting that the family of MXenes are worth studying for Zn systems, each MXene may show different performance characteristics and should each be studied through a screening process.

Overall, this thesis has shown that pillaring can successfully create porous and stable MXene structures, and that these pillared materials have superior performance in electrochemical energy storage devices than their non-pillared counterparts, with capacities, rate capability, cycling stability, and coulombic efficiency all increasing. This was the case in organic Li- and Na-ion systems, and in aqueous systems, as demonstrated by the performance in ZnSO<sub>4</sub>, although the improvement here was less significant than it was for the organic systems.

## **7.2 Future work**

There are a number of areas for potential further work to expand on what has been reported in this thesis.

### **7.2.1 Amine-assisted Pillaring Method**

For the further development of the amine-assisted pillaring method, one area which should be considered is the use of other pillars. There is a variety of other organometallic compounds like which could be expected to intercalate with an amine co-pillar in the same way as TEOS. For example, using titanium isopropoxide would give TiO<sub>2</sub> pillars, and niobium ethoxide would give Nb<sub>2</sub>O<sub>5</sub>. Both of these are interesting for electrochemical energy storage, with Nb<sub>2</sub>O<sub>5</sub> in particular showing very promising rate performance, which would make them interesting to use as MXene pillars.<sup>273–275</sup>

In parallel, the amine-assisted pillaring method should be able to be applied to other MXenes, so long as surface M-OH groups are present in sufficient quantities, which based on the work presented in this thesis, appears to be the only requirement for this pillaring method for MXenes found so far. This, combined with the use of different pillars, could give a large family of materials with a wide range of chemistries which could be tested in a variety of applications including electrochemical energy storage, gas separations and storage, catalysis and water purification where pore size and surface area can have a large impact on performance. Even simply applying the pillaring method to  $\text{Ti}_2\text{C}$  would be expected to give materials with a higher specific surface area and higher specific capacities as a result of the loss of the extra inactive TiC layer in  $\text{Ti}_3\text{C}_2$ .

It is likely that the electrochemical performance could be further improved by the optimisation of the pillar concentration, surface chemistries, particle size (the particles used here typical had sizes between 1-10  $\mu\text{m}$ , as shown by SEM, which is relatively large compared to commercial battery materials). MXenes with submicron-sized lateral dimensions have already been shown to have superior performance in Li-ion batteries,<sup>238</sup> and this should be expected to be able to be combined with this pillaring method to improve the capacity and rate performance further. The use of delamination steps to reduce the number of layers in each flake may also give extra performance boosts. A further gain could be achieved through optimising the amine removal, either by changing the calcination atmosphere (such as to  $\text{H}_2/\text{N}_2$  mixtures which may allow better amine removal or higher temperatures) or by using acid-based chemical removal methods such as those reported for pillared clays.<sup>276,277</sup>

The silica pillars themselves could be studied further to increase the understanding of the size and structure of the silica particles and to characterise any bonding between the pillars and the MXene surface. One way of studying this could be through further NMR experiments, for example by collecting spectra for a longer period of time (the  $^{29}\text{Si}$  Spectra presented in this thesis were collected over a three day duration). This would increase the signal-to-noise ratio in the spectra, and could allow for any smaller peaks or asymmetries (signifying different Si environments to the main silica pillars) to be identified. This could then be combined with cross-polarisation or two-dimensional NMR experiments to determine the relationship between different Si environments and other nuclei, such as  $^1\text{H}$  and  $^{19}\text{F}$ , to characterise the pillar structure and bonding. These studies could be complemented by further advanced microscopy techniques, for example scanning probe microscopies and additional TEM related studies, which could aid in determining the size and locations of the pillars within the MXenes.

The calcination step could also be adapted to reduce the  $\text{SiO}_2$  pillars to Si (or  $\text{SiO}_x$ ) via MgO reduction, as has previously been reported to create MXene-Si composites.<sup>278</sup>

This would be expected to activate the Si electrochemically for both Li- and Na-ion systems, which could give a significant capacity boost to the electrodes. Since this would involve directly reacting the pillars, this may cause a decrease in stability over multiple cycles, but nevertheless would be interesting to investigate. This reduced pillar could then be studied alongside the SiO<sub>2</sub> pillar using techniques such as in- or ex-situ NMR, XPS and XANES to establish more comprehensively whether there is any redox contribution from the Si-based pillars. These could then be combined with in- or ex-situ XRD and TEM studies to track the interlayer distances during cycling to give a more complete understanding as to the electrochemical behaviour of these materials.

The use of different amines and calcination temperatures to give a variety of pore sizes means that the pillaring technique reported here could also be used to study ion diffusion and desolvation in battery and supercapacitor systems, as has been done with pillared carbon electrodes.<sup>179,180,226–228</sup> The role of the electrolyte solvent in the interlayer is an unexplored part of systems studied in this thesis, but has already been shown to be important for MXene performance in Li-ion systems,<sup>263</sup> and could explain some of the changes observed in the CV curves.

As well as electrochemical energy storage applications, this work could be useful for the modification of MXenes for improved performance in a range of applications, as increased interlayer spacings and porosity are critical for applications in electrochemical energy conversion, catalysis, drug delivery, water purification and gas separation, amongst others.

### 7.2.2 Mo<sub>2</sub>TiC<sub>2</sub>

In addition to the above further work suggested for the amine-assisted pillaring method, the Mo<sub>2</sub>TiC<sub>2</sub> systems in particular would benefit from more detailed mechanistic studies such as in- or ex-situ XRD, XANES, NMR, particularly in Li and Na systems, to validate the proposed intercalation-conversion mechanism, which has only been partially investigated in this thesis. If the proposed mechanism does prove to be correct, then studying alternative ion systems such as Mg-ion could be promising, since the conversion reaction is also proposed to occur in this system.<sup>100</sup>

XPS studies revealed that the Mo in Mo<sub>2</sub>TiC<sub>2</sub> is predominantly Mo<sup>4+</sup>, with small amount of Mo<sup>6+</sup> oxides. Since Mo oxides are known to have very high specific capacities, but suffer from volume expansion due to conversion reactions,<sup>57</sup> partial oxidation to increase the Mo oxidation state and form TiC supported Mo oxides could be worth investigating. This could be achieved by carrying out the calcination step for the pillaring process at 400 or 450 °C in air, which could remove more of the amine template and only partially oxidise the MXene, as shown by the TGA data. This should keep the conductive TiC backbone intact, for fast electron transport,

which is essential for electrochemical performance. In addition, the pillared material should retain large pore space for reversible  $\text{Li}_2\text{O}$  formation, to allow high capacities to be obtained.

### **7.2.3. Zinc-ion systems**

For MXenes in Zn-ion systems, the results of this thesis suggest that performance could be enhanced by increasing the proportion of active  $-\text{O}$  surface groups and creating porous stable electrode architectures such as via pillaring. Different MXenes clearly behave very differently in Zn-ion systems, therefore, there should be a systematic study of different MXene chemistries to establish which are the most promising for further development.

In addition, it would be interesting to study different aqueous electrolytes and concentrations, including the effect this has on the voltage window. If the voltage window could be expanded to fit with the metal oxide positive electrode materials, composites of these materials with MXenes could be promising electrodes where the MXenes could act as conductive supports for higher capacity oxides, whilst also contributing slightly to Zn capacity.

More generally, the area of rechargeable aqueous zinc-ion batteries is still a very new field, and the use of Zn metal as both the reference and counter electrode (as is the case for organic Li and Na systems) has not been fully assessed to date. As was discussed in Chapter 2, the stability of Zn is known to depend strongly on the local pH on the electrode surface. Therefore, it would be beneficial to the field of rechargeable aqueous zinc-ion batteries to investigate Zn metal in this role in detail. For example, using a three electrode set-up with zinc as the counter electrode, but a more established aqueous reference electrode, such as Ag/AgCl, would allow comparison of the performance and voltage profiles with the two-electrode set-up, and help determine the reliability of Zn as a reference electrode in aqueous systems. Careful characterisation of the Zn electrode (even using symmetric Zn cells initially) after cycling to check for signs of corrosion or Zn hydroxides/ oxides would also give more confidence about the stability of Zn during cycling in a given system. This may be particularly important when testing electrodes outside the thermodynamic stability window of water, when increased risk of gas evolution could significantly change the local environment on the Zn electrode.

Finally, the improvement on performance from the in-situ pillaring technique suggests that this concept could be worth studying further by applying different pillars to different MXenes (or other 2D materials) in different metal-ion systems.

# **Chapter Eight**

## **Bibliography**

## References

1. Gür, T. M. Review of electrical energy storage technologies, materials and systems: challenges and prospects for large-scale grid storage. *Energy Environ. Sci.* **11**, 2696–2767 (2018).
2. Abu-Khader, M. M. Recent advances in nuclear power: A review. *Prog. Nucl. Energy* **51**, 225–235 (2009).
3. Pérez-Díaz, J. I., Chazarra, M., García-González, J., Cavazzini, G. & Stoppato, A. Trends and challenges in the operation of pumped-storage hydropower plants. *Renew. Sustain. Energy Rev.* **44**, 767–784 (2015).
4. Holgate, S. T. ‘Every breath we take: the lifelong impact of air pollution’ - a call for action. *Clin. Med.* **17**, 8–12 (2017).
5. Li, M., Lu, J., Chen, Z. & Amine, K. 30 Years of Lithium-Ion Batteries. *Adv. Mater.* **30**, 1800561 (2018).
6. Tarascon, J.-M. & Armand, M. Issues and challenges facing rechargeable lithium batteries. *Nature* **414**, 359–367 (2001).
7. Jaiswal, A. & Chalasani, S. C. The role of carbon in the negative plate of the lead–acid battery. *J. Energy Storage* **1**, 15–21 (2015).
8. Randhawa, N. S., Gharami, K. & Kumar, M. Leaching kinetics of spent nickel–cadmium battery in sulphuric acid. *Hydrometallurgy* (2015). doi:10.1016/j.hydromet.2015.09.011
9. Takasaki, T. *et al.* Cobalt-free nickel–metal hydride battery for industrial applications. *J. Alloys Compd.* **580**, S378–S381 (2013).
10. Rao, Z. & Wang, S. A review of power battery thermal energy management. *Renew. Sustain. Energy Rev.* **15**, 4554–4571 (2011).
11. Morishita, M., Shimizu, Y., Kobayakawa, K. & Sato, Y. Suppression of the memory effect observed in alkaline secondary batteries under partial charge–discharge conditions. *Electrochim. Acta* **53**, 6651–6656 (2008).
12. Sato, Y., Takeuchi, S. & Kobayakawa, K. Cause of the memory effect observed in alkaline secondary batteries using nickel electrode. *J. Power Sources* **93**, 20–24 (2001).
13. Bruce, P. G. Energy storage beyond the horizon: Rechargeable lithium batteries. *Solid State Ionics* **179**, 752–760 (2008).
14. Rosewater, D. & Williams, A. Analyzing system safety in lithium-ion grid energy storage. *J. Power Sources* **300**, 460–471 (2015).
15. Abada, S. *et al.* Safety focused modeling of lithium-ion batteries: A review. *J. Power Sources* **306**, 178–192 (2016).

16. Lung-Hao Hu, B., Wu, F.-Y., Lin, C.-T., Khlobystov, A. N. & Li, L.-J. Graphene-modified LiFePO<sub>4</sub> cathode for lithium ion battery beyond theoretical capacity. *Nat. Commun.* **4**, 1687 (2013).
17. Kim, H. *et al.* All-graphene-battery: bridging the gap between supercapacitors and lithium ion batteries. *Sci. Rep.* **4**, 687–689 (2014).
18. Raccichini, R., Varzi, A., Passerini, S. & Scrosati, B. The role of graphene for electrochemical energy storage. *Nat. Mater.* **14**, 271–279 (2014).
19. Slater, M. D., Kim, D., Lee, E. & Johnson, C. S. Sodium-Ion Batteries. *Adv. Funct. Mater.* **23**, 947–958 (2013).
20. Yan, D. *et al.* Reduced graphene oxide/carbon nanotubes sponge: A new high capacity and long life anode material for sodium-ion batteries. *J. Power Sources* **316**, 132–138 (2016).
21. Van Nghia, N., Ou, P.-W. & Hung, I.-M. Synthesis and Electrochemical Properties of Sodium Manganese-based Oxide Cathode Material for Sodium-ion Batteries. *Electrochim. Acta* **161**, 63–71 (2015).
22. Li, X. *et al.* The design of a high-energy Li-ion battery using germanium-based anode and LiCoO<sub>2</sub> cathode. *J. Power Sources* **293**, 868–875 (2015).
23. Lin, M.-C. *et al.* An ultrafast rechargeable aluminium-ion battery. *Nature* **520**, 324–328 (2015).
24. Gu, Y. *et al.* Rechargeable magnesium-ion battery based on a TiSe<sub>2</sub>-cathode with d-p orbital hybridized electronic structure. *Sci. Rep.* **5**, 12486 (2015).
25. Demir-Cakan, R., Palacin, M. R. & Croguennec, L. Rechargeable aqueous electrolyte batteries: From univalent to multivalent cation chemistry. *Journal of Materials Chemistry A* **7**, 20519–20539 (2019).
26. Alfaruqi, M. H. *et al.* Electrochemically Induced Structural Transformation in a  $\gamma$ -MnO<sub>2</sub> Cathode of a High Capacity Zinc-Ion Battery System. *Chem. Mater.* **27**, 3609–3620 (2015).
27. Senguttuvan, P. *et al.* A High Power Rechargeable Nonaqueous Multivalent Zn/V<sub>2</sub>O<sub>5</sub> Battery. *Adv. Energy Mater.* **6**, 1600826 (2016).
28. Alfaruqi, M. H. *et al.* A layered  $\delta$ -MnO<sub>2</sub> nanoflake cathode with high zinc-storage capacities for eco-friendly battery applications. *Electrochem. commun.* **60**, 121–125 (2015).
29. Lee, J., Ju, J. B., Cho, W. Il, Cho, B. W. & Oh, S. H. Todorokite-type MnO<sub>2</sub> as a zinc-ion intercalating material. *Electrochim. Acta* **112**, 138–143 (2013).
30. Alfaruqi, M. H. *et al.* Electrochemically Induced Structural Transformation in a  $\gamma$ -MnO<sub>2</sub> Cathode of a High Capacity Zinc-Ion Battery System. *Chem. Mater.* **27**, 3609–3620 (2015).

31. Xia, C. *et al.* Rechargeable Aqueous Zinc-Ion Battery Based on Porous Framework Zinc Pyrovanadate Intercalation Cathode. *Adv. Mater.* **30**, 1705580 (2018).
32. Hu, P. *et al.* Zn/V<sub>2</sub>O<sub>5</sub> Aqueous Hybrid-Ion Battery with High Voltage Platform and Long Cycle Life. *ACS Appl. Mater. Interfaces* **9**, 42717–42722 (2017).
33. Sambandam, B. *et al.* Aqueous rechargeable Zn-ion batteries: an imperishable and high-energy Zn<sub>2</sub>V<sub>2</sub>O<sub>7</sub> nanowire cathode through intercalation regulation. *J. Mater. Chem. A* **6**, 3850–3856 (2018).
34. Zhang, L., Chen, L., Zhou, X. & Liu, Z. Towards High-Voltage Aqueous Metal-Ion Batteries Beyond 1.5 V: The Zinc/Zinc Hexacyanoferrate System. *Adv. Energy Mater.* **5**, 1400930 (2015).
35. Jia, Z., Wang, B. & Wang, Y. Copper hexacyanoferrate with a well-defined open framework as a positive electrode for aqueous zinc ion batteries. *Mater. Chem. Phys.* **149–150**, 601–606 (2015).
36. Chae, M. S., Heo, J. W., Kwak, H. H., Lee, H. & Hong, S.-T. Organic electrolyte-based rechargeable zinc-ion batteries using potassium nickel hexacyanoferrate as a cathode material. *J. Power Sources* **337**, 204–211 (2017).
37. Raccichini, R., Varzi, A., Passerini, S. & Scrosati, B. The role of graphene for electrochemical energy storage. *Nat. Mater.* **14**, 271–9 (2015).
38. Kucinskis, G., Bajars, G. & Kleperis, J. Graphene in lithium ion battery cathode materials: A review. *J. Power Sources* **240**, 66–79 (2013).
39. Ouyang, B., Wang, Y., Zhang, Z. & Rawat, R. S. MoS<sub>2</sub> anchored free-standing three dimensional vertical graphene foam based binder-free electrodes for enhanced lithium-ion storage. *Electrochim. Acta* **194**, 151–160 (2016).
40. Park, J. *et al.* Discharge mechanism of MoS<sub>2</sub> for sodium ion battery: Electrochemical measurements and characterization. *Electrochim. Acta* **92**, 427–432 (2013).
41. Shen, C. *et al.* Graphene-Boosted, High-Performance Aqueous Zn-Ion Battery. *ACS Appl. Mater. Interfaces* **10**, 25446–25453 (2018).
42. He, P. *et al.* Layered VS<sub>2</sub> Nanosheet-Based Aqueous Zn Ion Battery Cathode. *Adv. Energy Mater.* **7**, 1601920 (2017).
43. Dai, X., Wan, F., Zhang, L., Cao, H. & Niu, Z. Freestanding graphene/VO<sub>2</sub> composite films for highly stable aqueous Zn-ion batteries with superior rate performance. *Energy Storage Mater.* **17**, 143–150 (2019).
44. Simon, P. & Gogotsi, Y. Materials for electrochemical capacitors. *Nat. Mater.* **7**, 845–54 (2008).
45. González, A., Goikolea, E., Barrena, J. A. & Mysyk, R. Review on supercapacitors: Technologies and materials. *Renew. Sustain. Energy Rev.* **58**,

1189–1206 (2016).

46. Augustyn, V., Simon, P. & Dunn, B. Pseudocapacitive oxide materials for high-rate electrochemical energy storage. *Energy Environ. Sci.* **7**, 1597 (2014).
47. TAIYO YUDEN CO., L. TAIYO YUDEN CO., LTD. Available at: [https://www.yuden.co.jp/ut/solutions/lithium\\_ion/](https://www.yuden.co.jp/ut/solutions/lithium_ion/). (Accessed: 16th August 2019)
48. Wang, G., Zhang, L. & Zhang, J. A review of electrode materials for electrochemical supercapacitors. *Chem. Soc. Rev.* **41**, 797–828 (2012).
49. Suo, L. *et al.* ‘Water-in-salt’ electrolyte enables high-voltage aqueous lithium-ion chemistries. *Science* **350**, 938–43 (2015).
50. Kurzweil, P. & Chwistek, M. Electrochemical stability of organic electrolytes in supercapacitors: Spectroscopy and gas analysis of decomposition products. *J. Power Sources* **176**, 555–567 (2008).
51. Zhong, C. *et al.* A review of electrolyte materials and compositions for electrochemical supercapacitors. *Chem. Soc. Rev.* **44**, 7484–7539 (2015).
52. Aricò, A. S., Bruce, P., Scrosati, B., Tarascon, J.-M. & van Schalkwijk, W. Nanostructured materials for advanced energy conversion and storage devices. *Nat. Mater.* **4**, 366–377 (2005).
53. Masashi Okubo, *et al.* Nanosize Effect on High-Rate Li-Ion Intercalation in LiCoO<sub>2</sub> Electrode. (2007). doi:10.1021/JA0681927
54. Kim, T., Song, W., Son, D.-Y., Ono, L. K. & Qi, Y. Lithium-ion batteries: outlook on present, future, and hybridized technologies. *J. Mater. Chem. A* **7**, 2942–2964 (2019).
55. Wen, Y. *et al.* Expanded graphite as superior anode for sodium-ion batteries. *Nat. Commun.* **5**, 4033 (2014).
56. Xiao, B., Rojo, T. & Li, X. Hard Carbon as Sodium-Ion Battery Anodes: Progress and Challenges. *ChemSusChem* **12**, 133–144 (2019).
57. Cao, K., Jin, T., Yang, L. & Jiao, L. Recent progress in conversion reaction metal oxide anodes for Li-ion batteries. *Mater. Chem. Front.* **1**, 2213–2242 (2017).
58. Yu, S.-H., Feng, X., Zhang, N., Seok, J. & Abruña, H. D. Understanding Conversion-Type Electrodes for Lithium Rechargeable Batteries. *Acc. Chem. Res.* **51**, 273–281 (2018).
59. Li, Y., Lu, Y., Adelhelm, P., Titirici, M.-M. & Hu, Y.-S. Intercalation chemistry of graphite: alkali metal ions and beyond. *Chem. Soc. Rev.* **48**, 4655–4687 (2019).
60. Yu, S.-H., Lee, S. H., Lee, D. J., Sung, Y.-E. & Hyeon, T. Conversion Reaction-Based Oxide Nanomaterials for Lithium Ion Battery Anodes. *Small* **12**, 2146–2172 (2016).

61. Lu, Y., Yu, L. & Lou, X. W. (David). Nanostructured Conversion-type Anode Materials for Advanced Lithium-Ion Batteries. *Chem* **4**, 972–996 (2018).
62. Ko, M., Oh, P., Chae, S., Cho, W. & Cho, J. Considering Critical Factors of Li-rich Cathode and Si Anode Materials for Practical Li-ion Cell Applications. *Small* **11**, 4058–4073 (2015).
63. Liu, D. *et al.* Group IVA Element (Si, Ge, Sn)-Based Alloying/Dealloying Anodes as Negative Electrodes for Full-Cell Lithium-Ion Batteries. *Small* **13**, 1702000 (2017).
64. Ma, D., Cao, Z. & Hu, A. Si-Based Anode Materials for Li-Ion Batteries: A Mini Review. *Nano-Micro Lett.* **6**, 347–358 (2014).
65. Liu, Z. *et al.* Silicon oxides: a promising family of anode materials for lithium-ion batteries. *Chem. Soc. Rev.* **48**, 285–309 (2019).
66. Burt, R., Birkett, G. & Zhao, X. S. A review of molecular modelling of electric double layer capacitors. *Phys. Chem. Chem. Phys.* **16**, 6519 (2014).
67. Simon, P. & Gogotsi, Y. Materials for electrochemical capacitors. *Nat. Mater.* **7**, 845–854 (2008).
68. Piñeiro-Prado, I., Salinas-Torres, D., Ruiz-Rosas, R., Morallón, E. & Cazorla-Amorós, D. Design of Activated Carbon/Activated Carbon Asymmetric Capacitors. *Front. Mater.* **3**, 16 (2016).
69. Chmiola, J. *et al.* Anomalous increase in carbon capacitance at pore sizes less than 1 nanometer. *Science* **313**, 1760–3 (2006).
70. Largeot, C. *et al.* Relation between the ion size and pore size for an electric double-layer capacitor. *J. Am. Chem. Soc.* **130**, 2730–1 (2008).
71. García-Gómez, A., Moreno-Fernández, G., Lobato, B. & Centeno, T. A. Constant capacitance in nanopores of carbon monoliths. *Phys. Chem. Chem. Phys.* **17**, 15687–90 (2015).
72. Shi, H. Activated carbons and double layer capacitance. *Electrochim. Acta* **41**, 1633–1639 (1996).
73. Kondrat, S., Pérez, C. R., Presser, V., Gogotsi, Y. & Kornyshev, A. A. Effect of pore size and its dispersity on the energy storage in nanoporous supercapacitors. *Energy Environ. Sci.* **5**, 6474 (2012).
74. Forse, A. C., Merlet, C., Griffin, J. M. & Grey, C. P. New Perspectives on the Charging Mechanisms of Supercapacitors. *J. Am. Chem. Soc.* **138**, 5731–5744 (2016).
75. Hu, M. *et al.* High-Capacitance Mechanism for  $Ti_3C_2T_x$  MXene by *in Situ* Electrochemical Raman Spectroscopy Investigation. *ACS Nano* **10**, 11344–11350 (2016).

76. Trasatti, S. & Buzzanca, G. Ruthenium dioxide: A new interesting electrode material. Solid state structure and electrochemical behaviour. *J. Electroanal. Chem. Interfacial Electrochem.* **29**, A1–A5 (1971).
77. Zheng, J. P. Hydrous Ruthenium Oxide as an Electrode Material for Electrochemical Capacitors. *J. Electrochem. Soc.* **142**, 2699 (1995).
78. Ghodbane, O., Pascal, J.-L. & Favier, F. Microstructural effects on charge-storage properties in MnO<sub>2</sub>-based electrochemical supercapacitors. *ACS Appl. Mater. Interfaces* **1**, 1130–9 (2009).
79. Chernova, N. A., Roppolo, M., Dillon, A. C. & Whittingham, M. S. Layered vanadium and molybdenum oxides: batteries and electrochromics. *J. Mater. Chem.* **19**, 2526 (2009).
80. Jiang, Y. & Liu, J. Definitions of Pseudocapacitive Materials: A Brief Review. *ENERGY Environ. Mater.* **2**, 30–37 (2019).
81. Griffith, K. J., Forse, A. C., Griffin, J. M. & Grey, C. P. High-Rate Intercalation without Nanostructuring in Metastable Nb<sub>2</sub>O<sub>5</sub> Bronze Phases. *J. Am. Chem. Soc.* **138**, 8888–8899 (2016).
82. Wang, X., Liu, L. & Niu, Z. Carbon-based materials for lithium-ion capacitors. *Mater. Chem. Front.* **3**, 1265–1279 (2019).
83. Sun, H. *et al.* Three-dimensional holey-graphene/niobia composite architectures for ultrahigh-rate energy storage. *Science* **356**, 599–604 (2017).
84. Sandhya, C. P., John, B. & Gouri, C. Lithium titanate as anode material for lithium-ion cells: a review. *Ionics (Kiel)*. **20**, 601–620 (2014).
85. Gogotsi, Y. & Penner, R. M. Energy Storage in Nanomaterials – Capacitive, Pseudocapacitive, or Battery-like? *ACS Nano* **12**, 2081–2083 (2018).
86. Naguib, M. *et al.* Two-dimensional nanocrystals produced by exfoliation of Ti<sub>3</sub>AlC<sub>2</sub>. *Adv. Mater.* **23**, 4248–53 (2011).
87. Sokol, M., Natu, V., Kota, S. & Barsoum, M. W. On the Chemical Diversity of the MAX Phases. *Trends Chem.* **1**, 210–223 (2019).
88. MAX Phases. Available at: [https://en.wikipedia.org/wiki/MAX\\_phases](https://en.wikipedia.org/wiki/MAX_phases). (Accessed: 24th September 2019)
89. Eklund, P., Beckers, M., Jansson, U., Högberg, H. & Hultman, L. The M<sub>n+1</sub>AX<sub>n</sub> phases: Materials science and thin-film processing. *Thin Solid Films* **518**, 1851–1878 (2010).
90. Halim, J. *et al.* Transparent Conductive Two-Dimensional Titanium Carbide Epitaxial Thin Films. *Chem. Mater.* **26**, 2374–2381 (2014).
91. Naguib, M. *et al.* Two-dimensional transition metal carbides. *ACS Nano* **6**, 1322–31 (2012).

92. Rakhi, R. B., Ahmed, B., Hedhili, M. N., Anjum, D. H. & Alshareef, H. N. Effect of Postetch Annealing Gas Composition on the Structural and Electrochemical Properties of  $Ti_2CT_x$  MXene Electrodes for Supercapacitor Applications. *Chem. Mater.* **27**, 5314–5323 (2015).
93. Mashtalir, O., Naguib, M., Dyatkin, B., Gogotsi, Y. & Barsoum, M. W. Kinetics of aluminum extraction from  $Ti_3AlC_2$  in hydrofluoric acid. *Mater. Chem. Phys.* **139**, 147–152 (2013).
94. Wang, K. *et al.* Fabrication and thermal stability of two-dimensional carbide  $Ti_3C_2$  nanosheets. *Ceram. Int.* **42**, 8419–8424 (2016).
95. Alhabeb, M. *et al.* Selective Etching of Silicon from  $Ti_3SiC_2$  (MAX) To Obtain 2D Titanium Carbide (MXene). *Angew. Chemie Int. Ed.* **57**, 5444–5448 (2018).
96. Dall'Agnese, Y., Taberna, P.-L., Gogotsi, Y. & Simon, P. Two-Dimensional Vanadium Carbide (MXene) as Positive Electrode for Sodium-Ion Capacitors. *J. Phys. Chem. Lett.* **6**, 2305–9 (2015).
97. Tran, M. H. *et al.* Adding a New Member to the MXene Family: Synthesis, Structure, and Electrocatalytic Activity for the Hydrogen Evolution Reaction of  $V_4C_3T_x$ . *ACS Appl. Energy Mater.* **1**, 3908–3914 (2018).
98. Xie, Y. *et al.* Role of surface structure on Li-ion energy storage capacity of two-dimensional transition-metal carbides. *J. Am. Chem. Soc.* **136**, 6385–94 (2014).
99. Ghidui, M. *et al.* Synthesis and characterization of two-dimensional  $Nb_4C_3$  (MXene). *Chem. Commun. (Camb)*. **50**, 9517–20 (2014).
100. Anasori, B. *et al.* Two-Dimensional, Ordered, Double Transition Metals Carbides (MXenes). *ACS Nano* **9**, 9507–16 (2015).
101. Meshkian, R. *et al.* Theoretical stability and materials synthesis of a chemically ordered MAX phase,  $Mo_2ScAlC_2$ , and its two-dimensional derivate  $Mo_2ScC_2$  MXene. *Acta Mater.* **125**, 476–480 (2017).
102. Meshkian, R. *et al.* Synthesis of two-dimensional molybdenum carbide,  $Mo_2C$ , from the gallium based atomic laminate  $Mo_2Ga_2C$ . *Scr. Mater.* **108**, 147–150 (2015).
103. Yang, J. *et al.* Two-Dimensional Nb-Based  $M_4C_3$  Solid Solutions (MXenes). *J. Am. Ceram. Soc.* **99**, 660–666 (2016).
104. Halim, J. *et al.* Synthesis of Two-Dimensional  $Nb_{1.33}C$  (MXene) with Randomly Distributed Vacancies by Etching of the Quaternary Solid Solution  $(Nb_{2/3}Sc_{1/3})_2AlC$  MAX Phase. *ACS Appl. Nano Mater.* **1**, 2455–2460 (2018).
105. Zhou, J. *et al.* A Two-Dimensional Zirconium Carbide by Selective Etching of  $Al_3C_3$  from Nanolaminated  $Zr_3Al_3C_5$ . *Angew. Chem. Int. Ed. Engl.* **55**, 5008–13 (2016).
106. Zhou, J. *et al.* Synthesis and Electrochemical Properties of Two-Dimensional

- Hafnium Carbide. *ACS Nano* **11**, 3841–3850 (2017).
107. Tao, Q. *et al.* Two-dimensional  $\text{Mo}_{1.33}\text{C}$  MXene with divacancy ordering prepared from parent 3D laminate with in-plane chemical ordering. *Nat. Commun.* **8**, 14949 (2017).
  108. Persson, I. *et al.* Tailoring Structure, Composition, and Energy Storage Properties of MXenes from Selective Etching of In-Plane, Chemically Ordered MAX Phases. *Small* **14**, 1703676 (2018).
  109. Meshkian, R. *et al.* W-Based Atomic Laminates and Their 2D Derivative  $\text{W}_{1.33}\text{C}$  MXene with Vacancy Ordering. *Adv. Mater.* **30**, 1706409 (2018).
  110. Urbankowski, P. *et al.* Synthesis of two-dimensional titanium nitride  $\text{Ti}_4\text{N}_3$  (MXene). *Nanoscale* **8**, 11385–11391 (2016).
  111. Soundiraraju, B. & George, B. K. Two-Dimensional Titanium Nitride ( $\text{Ti}_2\text{N}$ ) MXene: Synthesis, Characterization, and Potential Application as Surface-Enhanced Raman Scattering Substrate. *ACS Nano* **11**, 8892–8900 (2017).
  112. Urbankowski, P. *et al.* 2D molybdenum and vanadium nitrides synthesized by ammoniation of 2D transition metal carbides (MXenes). *Nanoscale* **9**, 17722–17730 (2017).
  113. Anasori, B. *et al.*  $\text{Mo}_2\text{TiAlC}_2$ : A new ordered layered ternary carbide. *Scr. Mater.* **101**, 5–7 (2015).
  114. Ghidui, M., Lukatskaya, M. R., Zhao, M.-Q., Gogotsi, Y. & Barsoum, M. W. Conductive two-dimensional titanium carbide ‘clay’ with high volumetric capacitance. *Nature* **516**, 78–81 (2014).
  115. Urbankowski, P. *et al.* Synthesis of two-dimensional titanium nitride  $\text{Ti}_4\text{N}_3$  (MXene). *Nanoscale* **8**, 11385–11391 (2016).
  116. Li, T. *et al.* Fluorine-Free Synthesis of High-Purity  $\text{Ti}_3\text{C}_2\text{T}_x$  (T=OH, O) via Alkali Treatment. *Angew. Chemie Int. Ed.* **57**, 6115–6119 (2018).
  117. Sun, W. *et al.* Electrochemical etching of  $\text{Ti}_2\text{AlC}$  to  $\text{Ti}_2\text{CT}_x$  (MXene) in low-concentration hydrochloric acid solution. *J. Mater. Chem. A* **5**, 21663–21668 (2017).
  118. Yang, S. *et al.* Fluoride-Free Synthesis of Two-Dimensional Titanium Carbide (MXene) Using A Binary Aqueous System. *Angew. Chemie* **130**, 15717–15721 (2018).
  119. Li, M. *et al.* Element Replacement Approach by Reaction with Lewis Acidic Molten Salts to Synthesize Nanolaminated MAX Phases and MXenes. *J. Am. Chem. Soc.* **141**, 4730–4737 (2019).
  120. Hope, M. A. *et al.* NMR reveals the surface functionalisation of  $\text{Ti}_3\text{C}_2$  MXene. *Phys. Chem. Chem. Phys.* **18**, 5099–102 (2016).

121. Lukatskaya, M. R. *et al.* Probing the Mechanism of High Capacitance in 2D Titanium Carbide Using In Situ X-Ray Absorption Spectroscopy. *Adv. Energy Mater.* **5**, 1500589 (2015).
122. Zou, G. *et al.* Synthesis of urchin-like rutile titania carbon nanocomposites by iron-facilitated phase transformation of MXene for environmental remediation. *J. Mater. Chem. A* **4**, 489–499 (2016).
123. Boota, M. *et al.* Pseudocapacitive Electrodes Produced by Oxidant-Free Polymerization of Pyrrole between the Layers of 2D Titanium Carbide (MXene). *Adv. Mater.* **28**, 1517–22 (2015).
124. Dall’Agnese, Y., Rozier, P., Taberna, P.-L., Gogotsi, Y. & Simon, P. Capacitance of two-dimensional titanium carbide (MXene) and MXene/carbon nanotube composites in organic electrolytes. *J. Power Sources* **306**, 510–515 (2016).
125. Lin, Z. *et al.* Capacitance of  $Ti_3C_2T_x$  MXene in ionic liquid electrolyte. *J. Power Sources* (2016). doi:10.1016/j.jpowsour.2016.04.035
126. Zhang, H., Dong, H., Zhang, X., Xu, Y. & Fransaer, J.  $Cu_2O$  Hybridized Titanium Carbide with Open Conductive Frameworks for Lithium-ion Batteries. *Electrochim. Acta* **202**, 24–31 (2016).
127. Halim, J. *et al.* Synthesis and Characterization of 2D Molybdenum Carbide (MXene). *Adv. Funct. Mater.* **26**, 3118–3127 (2016).
128. Kajiyama, S. *et al.* Enhanced Li-Ion Accessibility in MXene Titanium Carbide by Steric Chloride Termination. *Adv. Energy Mater.* **7**, 1601873 (2017).
129. Liu, F. *et al.* Preparation of  $Ti_3C_2$  and  $Ti_2C$  MXenes by fluoride salts etching and methane adsorptive properties. *Appl. Surf. Sci.* **416**, 781–789 (2017).
130. Mashtalir, O. *et al.* Intercalation and delamination of layered carbides and carbonitrides. *Nat. Commun.* **4**, 1716 (2013).
131. Mashtalir, O., Lukatskaya, M. R., Zhao, M.-Q., Barsoum, M. W. & Gogotsi, Y. Amine-Assisted Delamination of  $Nb_2C$  MXene for Li-Ion Energy Storage Devices. *Adv. Mater.* **27**, 3501–6 (2015).
132. Naguib, M., Unocic, R. R., Armstrong, B. L. & Nanda, J. Large-scale delamination of multi-layers transition metal carbides and carbonitrides ‘MXenes’. *Dalton Trans.* **44**, 9353–8 (2015).
133. Zhao, M.-Q. *et al.* Flexible MXene/carbon nanotube composite paper with high volumetric capacitance. *Adv. Mater.* **27**, 339–45 (2015).
134. Liang, X., Garsuch, A. & Nazar, L. F. Sulfur cathodes based on conductive MXene nanosheets for high-performance lithium-sulfur batteries. *Angew. Chem. Int. Ed. Engl.* **54**, 3907–11 (2015).
135. Yan, P. *et al.* Enhanced supercapacitive performance of delaminated two-dimensional titanium carbide/carbon nanotube composites in alkaline

- electrolyte. *J. Power Sources* **284**, 38–43 (2015).
136. Lukatskaya, M. R. *et al.* Cation intercalation and high volumetric capacitance of two-dimensional titanium carbide. *Science* **341**, 1502–5 (2013).
  137. Er, D., Li, J., Naguib, M., Gogotsi, Y. & Shenoy, V. B.  $\text{Ti}_3\text{C}_2$  MXene as a high capacity electrode material for metal (Li, Na, K, Ca) ion batteries. *ACS Appl. Mater. Interfaces* **6**, 11173–9 (2014).
  138. Eames, C. & Islam, M. S. Ion intercalation into two-dimensional transition-metal carbides: global screening for new high-capacity battery materials. *J. Am. Chem. Soc.* **136**, 16270–6 (2014).
  139. Yu, X. *et al.* Mg intercalation into  $\text{Ti}_2\text{C}$  building block. *Chem. Phys. Lett.* **629**, 36–39 (2015).
  140. Naguib, M. *et al.* MXene: a promising transition metal carbide anode for lithium-ion batteries. *Electrochem. commun.* **16**, 61–64 (2012).
  141. Come, J. *et al.* A Non-Aqueous Asymmetric Cell with a  $\text{Ti}_2\text{C}$ -Based Two-Dimensional Negative Electrode. *J. Electrochem. Soc.* **159**, A1368–A1373 (2012).
  142. Cheng, R. *et al.* Understanding the Lithium Storage Mechanism of  $\text{Ti}_3\text{C}_2\text{T}_x$  MXene. *J. Phys. Chem. C* **123**, 1099–1109 (2019).
  143. Chen Jin-Feng, Hu Qian-Ku, Zhou Ai-Guo & Sun Dan-Dan. Theoretical Studies of Lithium Storage Properties of Novel Two-Dimensional Carbides. *ACTA PHYSICO-CHIMICA Sin.* **31**, 2278–2284 (2015).
  144. Sun, D. *et al.* Two-dimensional  $\text{Ti}_3\text{C}_2$  as anode material for Li-ion batteries. *Electrochem. commun.* **47**, 80–83 (2014).
  145. Wang, X. *et al.* Atomic-scale recognition of surface structure and intercalation mechanism of  $\text{Ti}_3\text{C}_2\text{T}_x$ . *J. Am. Chem. Soc.* **137**, 2715–21 (2015).
  146. Wang, X. *et al.* Pseudocapacitance of MXene nanosheets for high-power sodium-ion hybrid capacitors. *Nat. Commun.* **6**, 6544 (2015).
  147. Yu, Y.-X. Prediction of Mobility, Enhanced Storage Capacity, and Volume Change during Sodiation on Interlayer-Expanded Functionalized  $\text{Ti}_3\text{C}_2$  MXene Anode Materials for Sodium-Ion Batteries. *J. Phys. Chem. C* **120**, 5288–5296 (2016).
  148. Kajiyama, S. *et al.* Sodium-Ion Intercalation Mechanism in MXene Nanosheets. *ACS Nano* **10**, 3334–3341 (2016).
  149. Luo, J. *et al.* Tunable pseudocapacitance storage of MXene by cation pillaring for high performance sodium-ion capacitors. *J. Mater. Chem. A* **6**, 7794–7806 (2018).
  150. VahidMohammadi, A., Hadjikhani, A., Shahbazmohamadi, S. & Beidaghi, M.

- Two-Dimensional Vanadium Carbide (MXene) as a High-Capacity Cathode Material for Rechargeable Aluminum Batteries. *ACS Nano* **11**, 11135–11144 (2017).
151. Byeon, A. *et al.* Two-Dimensional Titanium Carbide MXene As a Cathode Material for Hybrid Magnesium/Lithium-Ion Batteries. *ACS Appl. Mater. Interfaces* acsami.6b04198 (2016). doi:10.1021/acsami.6b04198
  152. Xu, M. *et al.* Opening Magnesium Storage Capability of Two-Dimensional MXene by Intercalation of Cationic Surfactant. *ACS Nano* **12**, 3733–3740 (2018).
  153. Zhao, M.-Q. *et al.* Magnesium-Ion Storage Capability of MXenes. *ACS Appl. Energy Mater.* **2**, 1572–1578 (2019).
  154. Liu, F., Liu, Y., Zhao, X., Liu, X. & Fan, L.-Z. Pursuit of a high-capacity and long-life Mg-storage cathode by tailoring sandwich-structured MXene@carbon nanosphere composites. *J. Mater. Chem. A* **7**, 16712–16719 (2019).
  155. Yang, Q. *et al.* A Wholly Degradable, Rechargeable Zn–Ti<sub>3</sub>C<sub>2</sub> MXene Capacitor with Superior Anti-Self-Discharge Function. *ACS Nano* acsnano.9b03650 (2019). doi:10.1021/acsnano.9b03650
  156. Wang, Q. *et al.* MXene-Reduced Graphene Oxide Aerogel for Aqueous Zinc-Ion Hybrid Supercapacitor with Ultralong Cycle Life. *Adv. Electron. Mater.* 1900537 (2019). doi:10.1002/aelm.201900537
  157. Dong, L. *et al.* Multivalent metal ion hybrid capacitors: a review with a focus on zinc-ion hybrid capacitors. *J. Mater. Chem. A* **7**, 13810–13832 (2019).
  158. Zhan, C. *et al.* Understanding the MXene Pseudocapacitance. *J. Phys. Chem. Lett.* **9**, 1223–1228 (2018).
  159. Lin, S.-Y. & Zhang, X. Two-dimensional titanium carbide electrode with large mass loading for supercapacitor. *J. Power Sources* **294**, 354–359 (2015).
  160. Levi, M. D. *et al.* Solving the Capacitive Paradox of 2D MXene using Electrochemical Quartz-Crystal Admittance and In Situ Electronic Conductance Measurements. *Adv. Energy Mater.* **5**, n/a-n/a (2015).
  161. Li, J. *et al.* Bipolar carbide-carbon high voltage aqueous lithium-ion capacitors. *Nano Energy* **56**, 151–159 (2019).
  162. Byeon, A. *et al.* Lithium-ion capacitors with 2D Nb<sub>2</sub>CT<sub>x</sub> (MXene) – carbon nanotube electrodes. *J. Power Sources* (2016). doi:10.1016/j.jpowsour.2016.03.066
  163. Dall’Agnese, Y., Rozier, P., Taberna, P.-L., Gogotsi, Y. & Simon, P. Capacitance of two-dimensional titanium carbide (MXene) and MXene/carbon nanotube composites in organic electrolytes. *J. Power Sources* **306**, 510–515 (2016).
  164. Song, J. *et al.* Rational design of free-standing 3D porous MXene/rGO hybrid

- aerogels as polysulfide reservoirs for high-energy lithium–sulfur batteries. *J. Mater. Chem. A* **7**, 6507–6513 (2019).
165. Ma, Z., Zhou, X., Deng, W., Lei, D. & Liu, Z. 3D Porous MXene (Ti<sub>3</sub>C<sub>2</sub>)/Reduced Graphene Oxide Hybrid Films for Advanced Lithium Storage. *ACS Appl. Mater. Interfaces* **10**, 3634–3643 (2018).
  166. Zhu, J., Tang, Y., Yang, C., Wang, F. & Cao, M. Composites of TiO<sub>2</sub> Nanoparticles Deposited on Ti<sub>3</sub>C<sub>2</sub> MXene Nanosheets with Enhanced Electrochemical Performance. *J. Electrochem. Soc.* **163**, A785–A791 (2016).
  167. Hu, M. *et al.* Self-assembled Ti<sub>3</sub>C<sub>2</sub>T<sub>x</sub> MXene film with high gravimetric capacitance. *Chem. Commun. (Camb)*. **51**, 13531–3 (2015).
  168. Ren, C. E. *et al.* Porous Two-Dimensional Transition Metal Carbide (MXene) Flakes for High-Performance Li-Ion Storage. *ChemElectroChem* **689–693** (2016). doi:10.1002/celec.201600059
  169. Xie, X. *et al.* Porous Heterostructured MXene/Carbon Nanotube Composite Paper with High Volumetric Capacity for Sodium-Based Energy Storage Devices. *Nano Energy* (2016). doi:10.1016/j.nanoen.2016.06.005
  170. Zhao, D. *et al.* Alkali-induced crumpling of Ti<sub>3</sub>C<sub>2</sub>T<sub>x</sub> (MXene) to form 3D porous networks for sodium ion storage. *Chem. Commun.* **54**, 4533–4536 (2018).
  171. Bao, W. *et al.* Porous Cryo-Dried MXene for Efficient Capacitive Deionization. *Joule* **2**, 778–787 (2018).
  172. Klopogge, J. T. Synthesis of Smectites and Porous Pillared Clay Catalysts: A Review. *J. Porous Mater.* **5**, 5–41 (1998).
  173. GIL, A., GANDÍA, L. M. & VICENTE, M. A. Recent Advances in the Synthesis and Catalytic Applications of Pillared Clays. *Catal. Rev.* **42**, 145–212 (2000).
  174. Gallo, J. M. R., Teixeira, S. & Schuchardt, U. Synthesis and characterization of niobium modified montmorillonite and its use in the acid-catalyzed synthesis of β-hydroxyethers. *Appl. Catal. A Gen.* **311**, 199–203 (2006).
  175. Karaca, S., Gürses, A. & Ejder Korucu, M. Investigation of the Orientation of Ions in the Interlayer of CTAB Pillared Montmorillonite. *J. Chem.* **2013**, 1–10 (2013).
  176. Park, K.-W., Jung, J. H., Kim, J. D., Kim, S.-K. & Kwon, O.-Y. Preparation of mesoporous silica-pillared H<sup>+</sup>-titanosilicates. *Microporous Mesoporous Mater.* **118**, 100–105 (2009).
  177. Park, K.-W., Seo, H. J. & Kwon, O.-Y. Mesoporous silica-pillared titanosilicate as catalytic support for partial oxidation of methane. *Microporous Mesoporous Mater.* **195**, 191–196 (2014).
  178. Kim, B. H. *et al.* Investigation on the existence of optimum interlayer distance for H<sub>2</sub> uptake using pillared-graphene oxide. *Int. J. Hydrogen Energy* **37**,

- 14217–14222 (2012).
179. Yuan, K. *et al.* Straightforward Generation of Pillared, Microporous Graphene Frameworks for Use in Supercapacitors. *Adv. Mater.* **27**, 6714–6721 (2015).
  180. Banda, H. *et al.* Sparsely Pillared Graphene Materials for High-Performance Supercapacitors: Improving Ion Transport and Storage Capacity. *ACS Nano* **13**, 1443–1453 (2019).
  181. Hantel, M. M., Kaspar, T., Nesper, R., Wokaun, A. & Kötz, R. Persistent electrochemical pillaring of graphene ensembles. *Electrochem. commun.* **34**, 189–191 (2013).
  182. Paek, S.-M., Jung, H., Park, M., Lee, J.-K. & Choy, J.-H. An Inorganic Nanohybrid with High Specific Surface Area: TiO<sub>2</sub>-Pillared MoS<sub>2</sub>. *Chem. Mater.* **17**, 3492–3498 (2005).
  183. Shen, L. *et al.* Carbon-intercalated Ti<sub>3</sub>C<sub>2</sub>T<sub>x</sub> MXene for high-performance electrochemical energy storage. *J. Mater. Chem. A* **6**, 23513–23520 (2018).
  184. Lin, Z. *et al.* Carbon nanofiber bridged two-dimensional titanium carbide as a superior anode for lithium-ion batteries. *J. Mater. Chem. A* **3**, 14096–14100 (2015).
  185. Zhang, Y. *et al.* MXene/Si@SiO<sub>x</sub>@C Layer-by-Layer Superstructure with Autoadjustable Function for Superior Stable Lithium Storage. *ACS Nano* acsnano.8b08821 (2019). doi:10.1021/acsnano.8b08821
  186. Kong, F. *et al.* Enhanced reversible Li-ion storage in Si@Ti<sub>3</sub>C<sub>2</sub> MXene nanocomposite. *Electrochem. commun.* **97**, 16–21 (2018).
  187. Li, H. *et al.* Employing MXene as a matrix for loading amorphous Si generated upon lithiation towards enhanced lithium-ion storage. *J. Energy Chem.* **38**, 50–54 (2019).
  188. Luo, J. *et al.* Sn(4+) Ion Decorated Highly Conductive Ti<sub>3</sub>C<sub>2</sub> MXene: Promising Lithium-Ion Anodes with Enhanced Volumetric Capacity and Cyclic Performance. *ACS Nano* **10**, 2491–2499 (2016).
  189. Luo, J. *et al.* Pillared Structure Design of MXene with Ultralarge Interlayer Spacing for High-Performance Lithium-Ion Capacitors. *ACS Nano* **11**, 2459–2469 (2017).
  190. Luo, J. *et al.* Pillared MXene with Ultralarge Interlayer Spacing as a Stable Matrix for High Performance Sodium Metal Anodes. *Adv. Funct. Mater.* **29**, 1805946 (2019).
  191. Luo, J. *et al.* Atomic Sulfur Covalently Engineered Interlayers of Ti<sub>3</sub>C<sub>2</sub> MXene for Ultra-Fast Sodium-Ion Storage by Enhanced Pseudocapacitance. *Adv. Funct. Mater.* **29**, 1808107 (2019).
  192. Sun, S., Xie, Z., Yan, Y. & Wu, S. Hybrid energy storage mechanisms for sulfur-

- decorated  $\text{Ti}_3\text{C}_2$  MXene anode material for high-rate and long-life sodium-ion batteries. *Chem. Eng. J.* **366**, 460–467 (2019).
193. Xie, X. *et al.* Porous  $\text{Ti}_3\text{C}_2\text{T}_x$  MXene for Ultrahigh-Rate Sodium-Ion Storage with Long Cycle Life. *ACS Appl. Nano Mater.* **1**, 505–511 (2018).
  194. Luo, J. *et al.* Sn<sup>4+</sup> Ion Decorated Highly Conductive  $\text{Ti}_3\text{C}_2$  MXene: Promising Lithium-Ion Anodes with Enhanced Volumetric Capacity and Cyclic Performance. *ACS Nano* **10**, 2491–2499 (2016).
  195. Peng, Q. *et al.* Unique Lead Adsorption Behavior of Activated Hydroxyl Group in Two-Dimensional Titanium Carbide. *J. Am. Chem. Soc.* **136**, 4113–4116 (2014).
  196. Vandenbeeke, Peter, Ando, D. *Practical Raman Spectroscopy: An introduction.* (Wiley, 2013).
  197. Hu, T. *et al.* Vibrational properties of  $\text{Ti}_3\text{C}_2$  and  $\text{Ti}_3\text{C}_2\text{T}_2$  (T = O, F, OH) monosheets by first-principles calculations: a comparative study. *Phys. Chem. Chem. Phys.* **17**, 9997–10003 (2015).
  198. Hu, M. *et al.* High-Capacitance Mechanism for  $\text{Ti}_3\text{C}_2\text{T}_x$  MXene by *in Situ* Electrochemical Raman Spectroscopy Investigation. *ACS Nano* **10**, 11344–11350 (2016).
  199. Luo, Z. *A practical guide to transmission electron microscopy : fundamentals.* (2016).
  200. Zhang, J. Y., Hwang, J., Isaac, B. J. & Stemmer, S. Variable-angle high-angle annular dark-field imaging: application to three-dimensional dopant atom profiling. *Sci. Rep.* **5**, 12419 (2015).
  201. Newbury, D. E. & Ritchie, N. W. M. Is Scanning Electron Microscopy/Energy Dispersive X-ray Spectrometry (SEM/EDS) Quantitative? *Scanning* **35**, 141–168 (2013).
  202. Kang, F. & Konno, H. X-ray Photoelectron Spectroscopy. *Mater. Sci. Eng. Carbon* 153–171 (2016). doi:10.1016/B978-0-12-805256-3.00008-8
  203. Tavares, M. I. B. *Spectroscopic Analyses Developments and Applications.* (2017). doi:DOI: 10.5772/intechopen.71004
  204. Sing, K. S. . Adsorption methods for the characterization of porous materials. *Adv. Colloid Interface Sci.* **76–77**, 3–11 (1998).
  205. Rouquerol, J., Llewellyn, P. & Rouquerol, F. Is the bet equation applicable to microporous adsorbents? *Stud. Surf. Sci. Catal.* **160**, 49–56 (2007).
  206. Brunauer, S., Emmett, P. H. & Teller, E. Adsorption of Gases in Multimolecular Layers. *J. Am. Chem. Soc.* **60**, 309–319 (1938).
  207. Kupgan, G., Liyana-Arachchi, T. P. & Colina, C. M. NLDFT Pore Size Distribution

- in Amorphous Microporous Materials. *Langmuir* **33**, 11138–11145 (2017).
208. Elgrishi, N. N. *et al.* A Practical Beginner's Guide to Cyclic Voltammetry. (2017). doi:10.1021/acs.jchemed.7b00361
209. Gogotsi, Y. & Penner, R. M. Energy Storage in Nanomaterials – Capacitive, Pseudocapacitive, or Battery-like? *ACS Nano* **12**, 2081–2083 (2018).
210. Brezesinski, T., Wang, J., Tolbert, S. H. & Dunn, B. Ordered mesoporous  $\alpha$ - $\text{MoO}_3$  with iso-oriented nanocrystalline walls for thin-film pseudocapacitors. *Nat. Mater.* **9**, 146–151 (2010).
211. Freytag, A. I., Pauric, A. D., Jiang, M. & Goward, G. R.  $^7\text{Li}$  and  $^{29}\text{Si}$  NMR Enabled by High-Density Cellulose-Based Electrodes in the Lithiation Process in Silicon and Silicon Monoxide Anodes. *J. Phys. Chem. C* **123**, 11362–11368 (2019).
212. Ren, C. E. *et al.* Porous Two-Dimensional Transition Metal Carbide (MXene) Flakes for High-Performance Li-Ion Storage. *ChemElectroChem* **3**, 689–693 (2016).
213. Pumera, M. Graphene-based nanomaterials for energy storage. *Energy Environ. Sci.* **4**, 668–674 (2011).
214. Sun, Y., Wu, Q. & Shi, G. Graphene based new energy materials. *Energy Environ. Sci.* **4**, 1113 (2011).
215. Xue, Q. *et al.*  $\text{Mn}_3\text{O}_4$  nanoparticles on layer-structured  $\text{Ti}_3\text{C}_2$  MXene towards the oxygen reduction reaction and zinc–air batteries. *J. Mater. Chem. A* **5**, 20818–20823 (2017).
216. Zhao, G. *et al.* Self-Assembled Sandwich-like MXene-Derived Nanocomposites for Enhanced Electromagnetic Wave Absorption. *ACS Appl. Mater. Interfaces* **10**, 42925–42932 (2018).
217. Bao, W. *et al.* Porous Cryo-Dried MXene for Efficient Capacitive Deionization. *Joule* **2**, 778–787 (2018).
218. Liu, Z. *et al.* Silicon oxides: a promising family of anode materials for lithium-ion batteries. *Chem. Soc. Rev.* **48**, 285–309 (2019).
219. Peng, C., Wang, C.-A., Song, Y. & Huang, Y. A novel simple method to stably synthesize  $\text{Ti}_3\text{AlC}_2$  powder with high purity. *Mater. Sci. Eng. A* **428**, 54–58 (2006).
220. Hu, T. *et al.* Vibrational properties of  $\text{Ti}_3\text{C}_2$  and  $\text{Ti}_3\text{C}_2\text{T}_2$  (T = O, F, OH) monosheets by first-principles calculations: a comparative study. *Phys. Chem. Chem. Phys.* **17**, 9997–10003 (2015).
221. Peng, Q. *et al.* Unique lead adsorption behavior of activated hydroxyl group in two-dimensional titanium carbide. *J. Am. Chem. Soc.* **136**, 4113–6 (2014).
222. Da, Y. *et al.* Engineering 2D Architectures toward High-Performance Micro-

- Supercapacitors. *Adv. Mater.* **31**, 1802793 (2019).
223. Xue, Y. *et al.* Opening Two-Dimensional Materials for Energy Conversion and Storage: A Concept. *Adv. Energy Mater.* **7**, 1602684 (2017).
  224. Gong, S., Zhao, G., Lyu, P. & Sun, K. A Pseudolayered MoS<sub>2</sub> as Li-Ion Intercalation Host with Enhanced Rate Capability and Durability. *Small* **14**, 1803344 (2018).
  225. Bourlinos, A. B. *et al.* Graphite Oxide: Chemical Reduction to Graphite and Surface Modification with Primary Aliphatic Amines and Amino Acids. *Langmuir* **19**, 6050–6055 (2003).
  226. Banda, H. *et al.* Investigation of ion transport in chemically tuned pillared graphene materials through electrochemical impedance analysis. *Electrochim. Acta* **296**, 882–890 (2019).
  227. Margarita Herrera-Alonso, Ahmed A. Abdala, Michael J. McAllister, Ilhan A. Aksay, A. & Prud'homme, R. K. Intercalation and Stitching of Graphite Oxide with Diaminoalkanes. *Langmuir* **23**, 10644–10649 (2007).
  228. Banda, H. *et al.* Ion Sieving Effects in Chemically Tuned Pillared Graphene Materials for Electrochemical Capacitors. *Chem. Mater.* **30**, 3040–3047 (2018).
  229. Hanaor, D. A. H. & Sorrell, C. C. Review of the anatase to rutile phase transformation. *J. Mater. Sci.* **46**, 855–874 (2011).
  230. Cao, M. *et al.* Room Temperature Oxidation of Ti<sub>3</sub>C<sub>2</sub> MXene for Supercapacitor Electrodes. *J. Electrochem. Soc.* **164**, A3933–A3942 (2017).
  231. Thommes, M. *et al.* Physisorption of gases, with special reference to the evaluation of surface area and pore size distribution (IUPAC Technical Report). *Pure Appl. Chem.* **87**, 1051–1069 (2015).
  232. Chae, Y. *et al.* An investigation into the factors governing the oxidation of two-dimensional Ti<sub>3</sub>C<sub>2</sub> MXene. *Nanoscale* **11**, 8387–8393 (2019).
  233. Harris, K. J., Bugnet, M., Naguib, M., Barsoum, M. W. & Goward, G. R. Direct Measurement of Surface Termination Groups and Their Connectivity in the 2D MXene V<sub>2</sub>CT<sub>x</sub> Using NMR Spectroscopy. *J. Phys. Chem. C* **119**, 13713–13720 (2015).
  234. Li, Y., Deng, X., Tian, J., Liang, Z. & Cui, H. Ti<sub>3</sub>C<sub>2</sub> MXene-derived Ti<sub>3</sub>C<sub>2</sub>/TiO<sub>2</sub> nanoflowers for noble-metal-free photocatalytic overall water splitting. *Appl. Mater. Today* **13**, 217–227 (2018).
  235. Su, X. *et al.* Effects of etching temperature and ball milling on the preparation and capacitance of Ti<sub>3</sub>C<sub>2</sub> MXene. *J. Alloys Compd.* **752**, 32–39 (2018).
  236. Kwon, O.-Y., Shin, H.-S. & Choi, S.-W. Preparation of Porous Silica-Pillared Layered Phase: Simultaneous Intercalation of Amine-Tetraethylorthosilicate into the H<sup>+</sup>-Magadiite and Intragallery Amine-Catalyzed Hydrolysis of

- Tetraethylorthosilicate. *Chem. Mater.* **12**, 1273–1278 (2000).
237. Pang, J. *et al.* Applications of 2D MXenes in energy conversion and storage systems. *Chem. Soc. Rev.* **48**, 72–133 (2019).
  238. Cheng, R. *et al.* Understanding the Lithium Storage Mechanism of Ti<sub>3</sub>C<sub>2</sub>T<sub>x</sub> MXene. *J. Phys. Chem. C* **123**, 1099–1109 (2019).
  239. Augustyn, V. *et al.* High-rate electrochemical energy storage through Li<sup>+</sup> intercalation pseudocapacitance. *Nat. Mater.* **12**, 518–522 (2013).
  240. Nita, C. *et al.* Eco-friendly synthesis of SiO<sub>2</sub> nanoparticles confined in hard carbon: A promising material with unexpected mechanism for Li-ion batteries. *Carbon N. Y.* **143**, 598–609 (2019).
  241. Liu, Z. *et al.* Silicon oxides: a promising family of anode materials for lithium-ion batteries. *Chem. Soc. Rev.* **48**, 285–309 (2019).
  242. Guo, B. *et al.* Electrochemical reduction of nano-SiO<sub>2</sub> in hard carbon as anode material for lithium ion batteries. *Electrochem. commun.* **10**, 1876–1878 (2008).
  243. Sharma, A., Jain, H. & Miller, A. C. Surface modification of a silicate glass during XPS experiments. *Surf. Interface Anal.* **31**, 369–374 (2001).
  244. Mekki, A., Holland, D., McConville, C. F. & Salim, M. An XPS study of iron sodium silicate glass surfaces. *J. Non. Cryst. Solids* **208**, 267–276 (1996).
  245. Zhang, J. *et al.* Single platinum atoms immobilized on an MXene as an efficient catalyst for the hydrogen evolution reaction. *Nat. Catal.* **1**, 985–992 (2018).
  246. Chen, C. *et al.* MoS<sub>2</sub>-on-MXene Heterostructures as Highly Reversible Anode Materials for Lithium-Ion Batteries. *Angew. Chemie Int. Ed.* **57**, 1846–1850 (2018).
  247. Kim, H., Anasori, B., Gogotsi, Y. & Alshareef, H. N. Thermoelectric Properties of Two-Dimensional Molybdenum-Based MXenes. *Chem. Mater.* **29**, 6472–6479 (2017).
  248. Gao, Y. *et al.* Mo<sub>2</sub>TiC<sub>2</sub> MXene: A Promising Catalyst for Electrocatalytic Ammonia Synthesis. *Catal. Today* (2018). doi:10.1016/J.CATTOD.2018.12.029
  249. Meshkian, R. *et al.* Synthesis of two-dimensional molybdenum carbide, Mo<sub>2</sub>C, from the gallium based atomic laminate Mo<sub>2</sub>Ga<sub>2</sub>C. *Scr. Mater.* **108**, 147–150 (2015).
  250. Liu, W. *et al.* Investigation of zinc ion storage of transition metal oxides, sulfides, and borides in zinc ion battery systems. *Chem. Commun.* **53**, 6872–6874 (2017).
  251. Sun, D. *et al.* Two-dimensional Ti<sub>3</sub>C<sub>2</sub> as anode material for Li-ion batteries. *Electrochem. commun.* **47**, 80–83 (2014).

252. Tu, J. *et al.* Straightforward Approach toward SiO<sub>2</sub> Nanospheres and Their Superior Lithium Storage Performance. *J. Phys. Chem. C* **118**, 7357–7362 (2014).
253. Dedryvère, R. *et al.* XPS Identification of the Organic and Inorganic Components of the Electrode/Electrolyte Interface Formed on a Metallic Cathode. (2019). doi:10.1149/1.1861994
254. Mauger, A. & Julien, C. M. Critical review on lithium-ion batteries: are they safe? Sustainable? *Ionics (Kiel)*. **23**, 1933–1947 (2017).
255. Song, M., Tan, H., Chao, D. & Fan, H. J. Recent Advances in Zn-Ion Batteries. *Adv. Funct. Mater.* **28**, 1802564 (2018).
256. Fang, G., Zhou, J., Pan, A. & Liang, S. Recent Advances in Aqueous Zinc-Ion Batteries. *ACS Energy Lett.* **3**, 2480–2501 (2018).
257. Wei, T., Li, Q., Yang, G. & Wang, C. Highly reversible and long-life cycling aqueous zinc-ion battery based on ultrathin (NH<sub>4</sub>)<sub>2</sub>V<sub>10</sub>O<sub>25</sub>·8H<sub>2</sub>O nanobelts. *J. Mater. Chem. A* **6**, 20402–20410 (2018).
258. Kundu, D., Adams, B. D., Duffort, V., Vajargah, S. H. & Nazar, L. F. A high-capacity and long-life aqueous rechargeable zinc battery using a metal oxide intercalation cathode. *Nat. Energy* **1**, 16119 (2016).
259. Kim, H. *et al.* Aqueous Rechargeable Li and Na Ion Batteries. *Chem. Rev.* **114**, 11788–11827 (2014).
260. Xu, M. *et al.* Opening Magnesium Storage Capability of Two-Dimensional MXene by Intercalation of Cationic Surfactant. *ACS Nano* **12**, 3733–3740 (2018).
261. Luo, J. *et al.* Pillared Structure Design of MXene with Ultralarge Interlayer Spacing for High-Performance Lithium-Ion Capacitors. *ACS Nano* **11**, 2459–2469 (2017).
262. Verma, V., Kumar, S., Manalastas, W., Satish, R. & Srinivasan, M. Progress in Rechargeable Aqueous Zinc- and Aluminum-Ion Battery Electrodes: Challenges and Outlook. *Adv. Sustain. Syst.* **3**, 1800111 (2019).
263. Wang, X. *et al.* Influences from solvents on charge storage in titanium carbide MXenes. *Nat. Energy* **4**, 241–248 (2019).
264. Yoder, C. H. *Ionic compounds : applications of chemistry to mineralogy*. (Wiley-Interscience, 2006).
265. Wang, H., Wang, M. & Tang, Y. A novel zinc-ion hybrid supercapacitor for long-life and low-cost energy storage applications. *Energy Storage Mater.* **13**, 1–7 (2018).
266. Halim, J. *et al.* X-ray photoelectron spectroscopy of select multi-layered transition metal carbides (MXenes). *Appl. Surf. Sci.* **362**, 406–417 (2016).

267. Park, K.-W., Jung, J. H., Kim, J. D., Kim, S.-K. & Kwon, O.-Y. Preparation of mesoporous silica-pillared H<sup>+</sup>-titanosilicates. *Microporous Mesoporous Mater.* **118**, 100–105 (2009).
268. Xie, Y. *et al.* Role of Surface Structure on Li-Ion Energy Storage Capacity of Two-Dimensional Transition-Metal Carbides. *J. Am. Chem. Soc.* **136**, 6385–6394 (2014).
269. Xie, Y. *et al.* Prediction and characterization of MXene nanosheet anodes for non-lithium-ion batteries. *ACS Nano* **8**, 9606–15 (2014).
270. Qiu, D.-F., Ma, X., Zhang, J.-D., Lin, Z.-X. & Zhao, B. Mesoporous Silicon Microspheres Produced from In Situ Magnesiothermic Reduction of Silicon Oxide for High-Performance Anode Material in Sodium-Ion Batteries. *Nanoscale Res. Lett.* **13**, 275 (2018).
271. Zeng, L. *et al.* Preparation of a Si/SiO<sub>2</sub> -Ordered-Mesoporous-Carbon Nanocomposite as an Anode for High-Performance Lithium-Ion and Sodium-Ion Batteries. *Chem. A Eur. J.* **24**, 4841–4848 (2018).
272. Shimizu, M., Usui, H., Fujiwara, K., Yamane, K. & Sakaguchi, H. Electrochemical behavior of SiO as an anode material for Na-ion battery. *J. Alloys Compd.* **640**, 440–443 (2015).
273. Kim, J. W., Augustyn, V. & Dunn, B. The Effect of Crystallinity on the Rapid Pseudocapacitive Response of Nb<sub>2</sub>O<sub>5</sub>. *Adv. Energy Mater.* **2**, 141–148 (2012).
274. Zhu, G.-N., Wang, Y.-G. & Xia, Y.-Y. Ti-based compounds as anode materials for Li-ion batteries. *Energy Environ. Sci.* **5**, 6652 (2012).
275. Augustyn, V. *et al.* High-rate electrochemical energy storage through Li<sup>+</sup> intercalation pseudocapacitance. *Nat. Mater.* **12**, 518–522 (2013).
276. Zhao, D. *et al.* On the Controllable Soft-Templating Approach to Mesoporous Silicates. (2007). doi:10.1021/CR068020S
277. Nakatsuji, M., Ishii, R., Wang, Z.-M. & Ooi, K. Preparation of porous clay minerals with organic–inorganic hybrid pillars using solvent-extraction route. *J. Colloid Interface Sci.* **272**, 158–166 (2004).
278. Zhang, Y. *et al.* MXene/Si@SiO<sub>x</sub>@C Layer-by-Layer Superstructure with Autoadjustable Function for Superior Stable Lithium Storage. *ACS Nano* acsnano.8b08821 (2019). doi:10.1021/acsnano.8b08821

# Appendix

**Table A.1.** Raman Spectroscopy band assignments and peak fittings for  $\text{Ti}_3\text{C}_2$  at selected stages of pillaring.

	<b>Assignment</b>	<b>Position (<math>\text{cm}^{-1}</math>)</b>	<b>FWHM (<math>\text{cm}^{-1}</math>)</b>
<b>Alkali Treated (<math>\text{Ti}_3\text{C}_2\text{-O}</math>)</b>	Ti-O ( $E_g$ )	207	36
	Ti-OH ( $E_g$ )	n/a	n/a
	Ti-O/F/OH	379	70
	Ti-O/F/OH	589	151
	Ti-O ( $A_{1g}$ )	737	26
<b>Acid Treated (<math>\text{Ti}_3\text{C}_2\text{-OH}</math>)</b>	<b>Ti-O</b>	<b>200</b>	<b>27</b>
	<b>Ti-OH</b>	<b>272</b>	<b>23</b>
	<b>Ti-O/F/OH</b>	<b>377</b>	<b>78</b>
	<b>Ti-O/F/OH</b>	<b>565</b>	<b>123</b>
	<b>Ti-O (<math>A_{1g}</math>)</b>	<b>723</b>	<b>18</b>
	<b>C</b>	<b>1564</b>	<b>129</b>
<b>Intercalated (<math>\text{Ti}_3\text{C}_2\text{-OH-Si}</math>)</b>	Ti-O ( $E_g$ )	203	26
	Ti-OH ( $E_g$ )	266	48
	Ti-O/OH/F	388	73
	Ti-O/OH/F	567	101
	Ti-O ( $A_{1g}$ )	737	19
	DDA-Carbon	1234	251
	DDA-Carbon	1411	267
	DDA-Carbon	1607	50
<b>Calcined (<math>\text{Ti}_3\text{C}_2\text{-OH-Si-400}</math>)</b>	<b>Ti-O (<math>E_g</math>)</b>	<b>207</b>	<b>20</b>
	<b>Ti-OH (<math>E_g</math>)</b>	<b>259</b>	<b>45</b>
	<b>Ti-O/OH/F</b>	<b>384</b>	<b>69</b>
	<b>Ti-O/OH/F</b>	<b>575</b>	<b>154</b>
	<b>Ti-O (<math>A_{1g}</math>)</b>	<b>735</b>	<b>13</b>
	<b>DDA-Carbon</b>	<b>1216</b>	<b>177</b>
	<b>DDA-Carbon</b>	<b>1358</b>	<b>291</b>
	<b>DDA-Carbon</b>	<b>1568</b>	<b>109</b>

**Table A.2.** Ex-situ Si 2p XPS peak assignments and fitting errors for  $\text{Ti}_3\text{C}_2\text{-OH-Si-400}$  at selected states-of-charge in a Na-ion half-cell.

	<b>Position (eV)</b>	<b>FWHM (eV)</b>	<b>Residual</b>
<b>OCV</b>	103.1	2.5	1.05
<b>0.01 V</b>	102	1.8	0.99
<b>3 V</b>	102.2	2.4	0.95

**Table A.3.** Mo 3d XPS peak assignments and fitting errors for Mo<sub>2</sub>TiC<sub>2</sub>.

	Position (cm <sup>-1</sup> )	Assignment	FWHM (cm <sup>-1</sup> )
<b>Mo<sub>2</sub>TiC<sub>2</sub></b> <b>Residual: 1.0</b>	229.8	Mo <sup>4+</sup> (5/2)	1
	233	Mo <sup>4+</sup> (3/2)	1.2
	235.9	Mo <sup>6+</sup> (3/2)	1.4

**Table A.4.** Mo 3d XPS peak assignments and fitting errors for Mo<sub>2</sub>TiC<sub>2</sub>-Si-400.

	Position (cm <sup>-1</sup> )	Assignment	FWHM (cm <sup>-1</sup> )
<b>Mo<sub>2</sub>TiC<sub>2</sub>-Si-400</b> <b>Residual: 1.1</b>	229.7	Mo <sup>4+</sup> 5/2	0.9
	232.6	Mo <sup>6+</sup> 5/2	1.1
	232.9	Mo <sup>4+</sup> 3/2	0.95
	235.8	Mo <sup>6+</sup> 3/2	1.6

**Table A.5.** Ti 2p XPS peak assignments and fitting errors for Mo<sub>2</sub>TiC<sub>2</sub>.

	Position (cm <sup>-1</sup> )	Assignment	FWHM (cm <sup>-1</sup> )
<b>Mo<sub>2</sub>TiC<sub>2</sub></b> <b>Residual: 0.83</b>	456.2	Ti <sup>3+</sup> 3/2	1.8
	459.0	Ti <sup>4+</sup> 3/2	2.0
	461.9	Ti <sup>3+</sup> 1/2	2
	464.6	Ti <sup>4+</sup> 1/2	2

**Table A.6.** Ti 2p XPS peak assignments and fitting errors for Mo<sub>2</sub>TiC<sub>2</sub>-Si-400.

	Position (cm <sup>-1</sup> )	Assignment	FWHM (cm <sup>-1</sup> )
<b>Mo<sub>2</sub>TiC<sub>2</sub></b> <b>Residual: 0.61</b>	455.9	Ti <sup>3+</sup> 3/2	1.7
	458.8	Ti <sup>4+</sup> 3/2	2.2
	461.5	Ti <sup>3+</sup> 1/2	2.1
	464.3	Ti <sup>4+</sup> 1/2	2.0

**Table A.7.** Ex-situ O 1s XPS peak assignments and fitting errors for Mo<sub>2</sub>TiC<sub>2</sub>-Si-400 at selected states-of-charge in a Li-ion half-cell.

	Carbonate			MXene (Ti-O)			Li <sub>2</sub> O		
	Position (cm <sup>-1</sup> )	FWHM (cm <sup>-1</sup> )	Residual	Position (cm <sup>-1</sup> )	FWHM (cm <sup>-1</sup> )	Residual	Position (cm <sup>-1</sup> )	FWHM (cm <sup>-1</sup> )	Residual
<b>OCV</b>	531.7	1.7	0.62	530	1.5	0.62			
<b>0.01 V</b>	531.7	1.8	0.14	530.2	1.4	1.4	528.5	1.4	1.4
<b>3 V</b>	531.9	1.8	0.27	530.2	1.2	0.27			

**Table A.8.** Ex-situ Si 2p XPS peak assignments and fitting errors for Mo<sub>2</sub>TiC<sub>2</sub>-Si-400 at selected states-of-charge in a Li-ion half-cell.

	Position (cm <sup>-1</sup> )	FWHM (cm <sup>-1</sup> )	Residual
<b>OCV</b>	100.9	1.78	0.89
<b>0.01 V</b>	101.2	1.6	0.91
<b>3 V</b>	101.4	2.1	0.91

**Table A.9.** Raman spectroscopy band assignments and peak analysis results for Ti<sub>3</sub>C<sub>2</sub> at selected states-of-charge in the aqueous Zn-ion battery system.

	Ti-O ( $E_g$ )		Ti-OH ( $E_g$ )		Ti-O ( $A_{1g}$ )	
	Position (cm <sup>-1</sup> )	FWHM (cm <sup>-1</sup> )	Position (cm <sup>-1</sup> )	FWHM (cm <sup>-1</sup> )	Position (cm <sup>-1</sup> )	FWHM (cm <sup>-1</sup> )
<b>OCV</b>	207	25	259	59	733	30
<b>0.5</b>	201	56	267	70	734	27
<b>0.01</b>	207	65	n/a	n/a	734	41
<b>0.5</b>	207	43	267	147	734	36
<b>1 V</b>	206	27	256	93	738	24

**Table A.10.** Ex-situ Ti 2p XPS peak assignments and fitting errors for Mo<sub>2</sub>TiC<sub>2</sub>-Si-400 at selected states-of-charge in a Li-ion half-cell.

	Ti <sup>2+</sup> (3/2)	Ti <sup>3+</sup> (3/2)	Ti <sup>4+</sup> (3/2)	Ti <sup>2+</sup> (1/2)	Ti <sup>3+</sup> (1/2)	Ti <sup>4+</sup> (1/2)
OCV	Residual: 1.2					
Position	455.9	457.5	459.7	461.9	463.9	465.4
FWHM	1.6	1.9	1.7	2.4	1.7	1.6
<b>0.5 V Discharge</b>	<b>Residual: 0.79</b>					
<b>Position</b>	<b>455.6</b>	<b>457.5</b>	<b>459.3</b>	<b>461.5</b>	<b>464.1</b>	<b>465.3</b>
<b>FWHM</b>	<b>1.9</b>	<b>2.2</b>	<b>1.5</b>	<b>2.8</b>	<b>2.2</b>	<b>1.4</b>
0.01 V Discharge	Residual: 0.39					
Position	455.4	457.5	459.3	461.4	463.5	465.3
FWHM	2.1	2.6	1.9	2.2	2.3	2
<b>0.5 V Charge</b>	<b>Residual: 1.2</b>					
<b>Position</b>	<b>455.7</b>	<b>457.5</b>	<b>459.6</b>	<b>461.7</b>	<b>463.6</b>	<b>465.3</b>
<b>FWHM</b>	<b>1.7</b>	<b>1.9</b>	<b>1.5</b>	<b>2.3</b>	<b>1.9</b>	<b>1.8</b>
1 V Charge	Residual: 0.92					
Position	455.8	457.5	459.5	461.7	463.5	465.3
FWHM	1.7	2.1	1.5	2.3	2.3	1.5